

ELUCIDATING ENERGY AND ELECTRON TRANSFER DYNAMICS WITHIN
MOLECULAR ASSEMBLIES FOR SOLAR ENERGY CONVERSION

Zachary Aaron Morseth

A dissertation submitted to the faculty of the University of North Carolina at Chapel Hill in
partial fulfillment of the requirements for the degree of Doctor of Philosophy in the Department
of Chemistry

Chapel Hill
2016

Approved by:

John Papanikolas

Yosuke Kanai

Andrew Moran

James Cahoon

Gerald Meyer

© 2016
Zachary Aaron Morseth
ALL RIGHTS RESERVED

ABSTRACT

Zachary Aaron Morseth: Elucidating Energy and Electron Transfer Dynamics within Molecular Assemblies for Solar Energy Conversion
(Under the direction of John M. Papanikolas)

The use of sunlight to make chemical fuels (i.e. solar fuels) is an attractive approach in the quest to develop sustainable energy sources. Using nature as a guide, assemblies for artificial photosynthesis will need to perform multiple functions. They will need to be able to harvest light across a broad region of the solar spectrum, transport excited-state energy to charge-separation sites, and then transport and store redox equivalents for use in the catalytic reactions that produce chemical fuels. This multifunctional behavior will require the assimilation of multiple components into a single macromolecular system. A wide variety of different architectures including porphyrin arrays, peptides, dendrimers, and polymers have been explored, with each design posing unique challenges. Polymer assemblies are attractive due to their relative ease of production and facile synthetic modification. However, their disordered nature gives rise to stochastic dynamics not present in more ordered assemblies. The rational design of assemblies requires a detailed understanding of the energy and electron transfer events that follow light absorption, which can occur on timescales ranging from femtoseconds to hundreds of microseconds, necessitating the use of sophisticated techniques. We have used a combination of time-resolved absorption and emission spectroscopies with observation times that span nine orders of magnitude to follow the excited-state evolution within single-site and polymer-based molecular assemblies. We complement experimental observations with electronic structure calculations, molecular dynamics simulations, and kinetic modeling to develop a microscopic

view of these dynamics. This thesis provides an overview of work on single-site molecular assemblies and polymers decorated with pendant chromophores, both in solution and on surfaces. This work was made possible through extensive collaboration with Dr. Kirk Schanze's and Dr. John Reynolds' research groups who synthesized the samples for study.

To my family, friends, and loving wife Tory.

ACKNOWLEDGEMENTS

First, I would like to thank my family, especially my parents Aaron and Angela Morseth, for their guidance and support throughout my life. Their value of my education and teaching me a strong work ethic has undoubtedly led me to where I am today. Second, I thank my loving wife, Tory Morseth, for her support and pushing me to be the best person I can possibly be. While graduate school has had its fair share of ups and downs, she stood by my side each and every day with a strong will to see me succeed professionally and personally.

I also would like to thank my teachers and mentors through all walks of my life. Most importantly, I thank Lowell Nelson for instilling a passion for science in me and appreciation of the scientific method. I must also thank the faculty at Minnesota State University – Moorhead for taking that passion and molding me into the scientist that I am today. I especially thank Asoka Marasinghe, Craig Jasperse, Jeffrey Bodwin, Adam Goyt, and Justin James for their mentoring and friendship during my undergraduate education.

I must also thank my advisor, John Papanikolas, for accepting me into his research group here at UNC and mentoring and supporting me during graduate school. I truly enjoyed the conversations regarding science and teaching me valuable lessons that I applied to both my professional and personal life. Lastly, I thank the members of the Papanikolas group, both past and present, for their continual support and friendship over the past years.

TABLE OF CONTENTS

LIST OF TABLES.....	xiv
LIST OF SCHEMES.....	xv
LIST OF FIGURES.....	xvi
LIST OF ABBREVIATIONS.....	xxxi
LIST OF SYMBOLS	xxxiii
CHAPTER 1. INTRODUCTION	1
1.1. INTRODUCTION.....	1
1.2. ARTIFICIAL PHOTOSYNTHESIS.....	2
1.3. PHOTOINDUCED DYNAMICS IN MOLECULAR ASSEMBLIES.....	4
1.3.1. Polymer Structures.....	5
1.3.2. Site-to-Site Energy Transport.....	7
1.3.3. Dynamics in Polymer Assemblies with π -Conjugated Polymer Backbone.....	12
1.3.4. Multifunctional Behavior.....	19
1.4. REFERENCES.....	20

CHAPTER 2. ROLE OF MACROMOLECULAR STRUCTURE IN THE ULTRAFAST ENERGY AND ELECTRON TRANSFER DYNAMICS OF A LIGHT-HARVESTING POLYMER.....	25
2.1. INTRODUCTION.....	25
2.2. EXPERIMENTAL METHODS.....	29
2.2.1. Sample Preparation.....	29
2.2.2. Steady State Techniques.....	29
2.2.3. Time-Resolved Emission Spectroscopy.....	29
2.2.4. Transient Absorption Spectroscopy.....	30
2.2.5. Electronic Structure Calculations.....	31
2.3. RESULTS AND DISCUSSION.....	33
2.3.1. Synthesis of pF-iI polymer Assembly.....	33
2.3.2. Static Spectroscopy.....	33
2.3.3. Ultrafast Spectroscopy.....	34
2.3.3.1. Isoindigo Excited-State Dynamics.....	34
2.3.3.2. Energy and Electron Transfer Quenching of the Polymer Excited State.....	37
2.3.3.3. Spectral Modeling of the pF-iI Spectra.....	41
2.3.4. Simulation of Excited State Quenching Dynamics.....	45
2.3.4.1. Macromolecular Polymer Structures.....	45
2.3.4.2. Kinetic Network.....	49
2.3.4.2. Energy Transfer.....	52

2.3.4.4. Electron Transfer.....	53
2.3.4.5. Time-Dependent Populations.....	54
2.3.4.6. Comparison of Simulation with Experimental Observation.....	55
2.3.5. Analysis of Simulation Results.....	57
2.3.5.1. Microscopic Picture.....	57
2.3.5.2. Ensemble Quenching Dynamics.....	61
2.3.5.3. Role of Macromolecular Structure.....	62
2.4. CONCLUSIONS.....	67
2.5. REFERENCES.....	68
CHAPTER 3. ELECTRON TRANSFER DYNAMICS IN AN ISOINDIGO LOADED POLY(THIOPHENE) ASSEMBLY.....	71
3.1. INTRODUCTION.....	71
3.2. EXPERIMENTAL METHODS.....	75
3.2.1. Sample Preparation.....	75
3.2.2. Steady State Techniques.....	75
3.2.3. Transient Absorption Spectroscopy.....	75
3.2.4. Electronic Structure Calculations.....	77
3.2.5. Electrochemical Measurements.....	77
3.2.6. Spectroelectrochemical Measurements.....	78

3.3. RESULTS AND DISCUSSION.....	79
3.3.1. Synthesis of Materials.....	79
3.3.2. Static Spectroscopy.....	79
3.3.3. Ultrafast Spectroscopy.....	83
3.3.3.1. Isoindigo Excited-State Dynamics.....	83
3.3.3.2. Ultrafast Quenching of the Polymer Excited State.....	85
3.3.3.3. Charge Recombination.....	91
3.3.4. Simulation of Excited State Quenching.....	92
3.3.4.1. Development of the Kinetic Model.....	94
3.3.4.2. Comparison with Experiment.....	99
3.3.4.3. Microscopic Analysis of Simulation Results.....	101
3.3.4.4. Ensemble ET Quenching Dynamics	103
3.4. CONCLUSIONS.....	107
3.5. REFERENCES.....	108
CHAPTER 4. POLYMER-BASED RUTHENIUM(II) POLYPYRIDYL CHROMOPHORES FOR SOLAR ENERGY CONVERSION APPLICATIONS.....	111
4.1. INTRODUCTION.....	111
4.2. EXPERIMENTAL METHODS.....	115
4.2.1. Sample Preparation.....	115

4.2.2. Steady State Techniques.....	115
4.2.3. Time-Resolved Emission Spectroscopy.....	115
4.2.4. Transient Absorption Spectroscopy.....	116
4.2.5. Transient Absorption Kinetics Fitting Parameters.....	117
4.2.6. Electronic Structure Calculations.....	117
4.2.7. Molecular Dynamics Simulations.....	117
4.3. RESULTS AND DISCUSSION.....	119
4.3.1. Static Spectroscopy.....	119
4.3.2. Macromolecular Polymer Structures.....	119
4.3.3. Time-Resolved Spectroscopy.....	122
4.4. CONCLUSIONS.....	130
4.5. REFERENCES.....	131
 CHAPTER 5. LIGHT-HARVESTING AND CHARGE SEPARATION IN A π -CONJUGATED ANTENNA POLYMER BOUND TO TiO ₂	
5.1. INTRODUCTION.....	134
5.2. EXPERIMENTAL METHODS.....	137
5.2.1. Sample Preparation.....	137
5.2.2. Steady State Techniques.....	137
5.2.3. Transient Absorption Spectroscopy.....	137
5.2.4. Transient Absorption Kinetics Fitting Parameters.....	139

5.2.5. Molecular Dynamics Simulations.....	139
5.3. RESULTS AND DISCUSSION.....	141
5.3.1. Polymer Structures.....	141
5.3.2. Photoexcitation of pF-Ru-A.....	142
5.3.3. Interfacial Dynamics of pF-Ru-A.....	143
5.4. CONCLUSIONS.....	151
5.5. REFERENCES.....	152
CHAPTER 6. INTERFACIAL DYNAMICS WITHIN AN ORGANIC CHROMOPHORE- BASED WATER OXIDATION MOLECULAR ASSEMBLY.....	155
6.1. INTRODUCTION.....	155
6.2. EXPERIMENTAL METHODS.....	158
6.2.1. Sample Preparation.....	158
6.2.2. Steady State Techniques.....	158
6.2.3. Transient Absorption Spectroscopy.....	159
6.2.4. Electronic Structure Calculations.....	161
6.3. RESULTS AND DISCUSSION.....	162
6.3.1. Photoexcitation and Electronic Structure of T ₃ -trpy and T ₃ -trpy-Ru-L.....	162
6.3.2. Photophysics of T ₃ -trpy Chromophore.....	165
6.3.2.1. T ₃ -trpy Solution Photophysics.....	165

6.3.2.2. Interfacial Dynamics on TiO ₂	167
6.3.3.3. Interfacial Dynamics on SnO ₂	169
6.3.3. Photophysics of T ₃ -trpy-Ru-L Assembly.....	171
6.3.3.1. Solution Dynamics.....	171
6.3.3.2. Interfacial Dynamics on TiO ₂	174
6.3.3.3. Interfacial Dynamics on SnO ₂	177
6.4. CONCLUSIONS.....	179
6.5. REFERENCES.....	180

LIST OF TABLES

Table 1.1. Energy and electron transfer data for π -conjugated polymer assemblies with pendant Ru ^{II} chromophores.....	17
Table 2.1. Simulation parameters used in the kinetic modeling of pF-iI.....	51
Table 3.1. Simulation parameters used in the kinetic modeling for photoinduced dynamics of the pT-iI assembly.....	98
Table 4.1. TRES decay fits for TiO ₂ //pS-Ru-A and ZrO ₂ //pS-Ru-A films monitored at 660 nm following 440 nm excitation.....	124

LIST OF SCHEMES

Scheme 2.1. (Top) Depiction of the pF-iI ₁₀ polymer assembly with the indices of the fluorene monomers (F _i) and the iI pendants (iI _j). (Bottom) Illustration of the kinetic network used to describe the photoinduced dynamics in the pF-iI polymer assemblies following excitation centered on a fluorene monomer.....	50
Scheme 3.1. Illustration of the fundamental photophysical events occurring within the pT-iI assembly.....	97
Scheme 4.1. Cartoon of pS-Ru-A (obtained from molecular dynamics simulations) anchored onto a TiO ₂ surface, displaying the primary photophysical events.....	112
Scheme 4.2. Schematic representation of the photophysical events of the pS-Ru-A assembly at the surface of TiO ₂ . The blue circles represent Ru(L) ₃ ²⁺ chromophores while the green and red circles correspond to Ru(L) ₃ ³⁺ and Ru(L) ₃ ^{2+*}	114
Scheme 5.1. Cartoon of pF-Ru-A anchored onto a TiO ₂ surface.....	136
Scheme 5.2. Schematic representation of photophysical events of pF-Ru-A on the surface of TiO ₂ . Balls represent Ru(L) ₃ ²⁺ chromophores, and the grey ribbon the poly(fluorene) backbone.....	144
Scheme 6.1. (Left) Energy level diagram of the relevant states present in the T ₃ -trpy chromophore and T ₃ -trpy-Ru-L assemblies in relation to the metal oxide conduction band density of states for TiO ₂ (top) and SnO ₂ (bottom). (Right) Illustration of the interfacial dynamics within the T ₃ -trpy-Ru-MeCN (top) and T ₃ -trpy-Ru-OH ₂ (bottom) assemblies.....	157

LIST OF FIGURES

Figure 1.1. Schematic diagram of a tandem DSPEC for solar-driven splitting of CO ₂ into CO and O ₂	3
Figure 1.2. Condensed phase polymer assembly structures obtained from molecular dynamics simulations. Structures were calculated using periodic boundary conditions in the presence of explicit acetonitrile solvent and PF ₆ ⁻ counter ions. The polymer scaffold is shown in green color and the Ru atoms are depicted as orange spheres with enlarged diameters. A portion of the solvent is shown in the pF-Ru ₁₆ structure.....	6
Figure 1.3. (Left) Time resolved emission monitoring Os ^{II} photoluminescence in pS-Ru ₁₇ Os ₃ and pF-Ru ₆₀ Os ₁₀ . (Right) Illustration of site-to-site energy transport within a subsection of pS-Ru ₁₇ Os ₃ (upper) and pF-Ru ₆₀ Os ₁₀ (lower). The initial Ru excited state (blue) undergoes energy transfer to adjacent Ru complexes and is ultimately transferred to the Os trap (red)....	11
Figure 1.4. Condensed phase structure of a 40-repeat unit pF in explicit acetonitrile solvent obtained from molecular dynamics simulations. Most of the solvent is omitted for clarity, but a portion is shown for scale. The conformational subunits are colored based on the energy level with darker shades indicating subunits with shorter lengths and hence higher energies. The enlarged section shows a zoomed-in view of adjacent conformational subunits with a conjugation break.....	13
Figure 1.5. (Left) Illustration of excitonic energy transfer (top) and excited-state self-trapping by torsional relaxation (bottom) along a π -conjugated polymer backbone following excitation into a high-energy conformational subunit. (Right) Transient absorption difference spectra of unfunctionalized pF (upper) and pT (lower) from 300 fs to 1.4 ns following 388 nm excitation.....	14
Figure 1.6. Transient absorption spectra following primary excitation of the polymer backbone at 388 nm for pF-Ru (upper left) and pT-Ru (upper right). (Bottom) Ru ^{II} absorbance ($\epsilon_A(\lambda)$) and normalized (to unit area) polymer emission spectra ($F_D(\lambda)$). The shaded grey area reflects the integrand, $F_D(\lambda)\epsilon_A(\lambda)\lambda^4$, which is scaled for clarity. (Right) Kinetic traces of the polymer assemblies showing the initial polymer excited-state quenching during the first 10ps following excitation.....	16
Figure 2.1. (A) Chemical structures of the pF-iI repeat unit and iI-Model. (B) Snapshot of a pF-iI ₁₀ polymer assembly from fully atomistic molecular dynamics simulations in explicit dichloromethane solvent. The polymer backbone is depicted in green and the iI pendants in orange.	

The solvent is excluded for clarity.....	28
Figure 2.2. Ground state absorbance spectra of the pF-iI assembly (dark grey), pF (blue), and iI-Model (red) in room temperature DCM solution. Also shown is the superposition of the iI-Model and pF absorbance spectra (dashed black).....	34
Figure 2.3. (Left) Absorbance spectrum of iI-Model complex in DCM (red) and theoretical transitions predicted from TD-DFT calculations (gray bars). The primary orbitals corresponding to each transition are also shown for the dominant visible transitions. (Right) Calculated isodensity plots of the frontier molecular orbitals (LUMO+1, LUMO, HOMO, HOMO-1, HOMO-2, and HOMO-3) of the iI-Model complex (isodensity value = 0.03).....	35
Figure 2.4. Femtosecond transient absorption spectra following photoexcitation at 595 nm (150 fs, 280 nJ with a 120 μ m spot size) in DCM at 0.3, 1, 2, 5, 15, and 20 ps for iI-Model (A) and pF-iI (B). Also shown in (A) is the inverted ground-state absorbance spectrum of iI-Model in DCM, normalized to the 410 nm GSB (shaded orange) (C) Decays of the transient signals at 640 nm for iI-Model (orange circles) and pF-iI (red triangles). Both transients exhibit single exponential decays with $\tau = 5.8 \pm 0.1$ ps. All spectra were measured in argon saturated DCM solution at room temperature.....	36
Figure 2.5. (A) Transient absorption spectra of pF in DCM at 0.2, 1, 15, 50, 150, 500, and 1000 ps. Excitation was at 388 nm and the pulse energy was 10 nJ/pulse. (B) Transient absorption spectra of pF-iI in DCM at 0.15, 0.3, 0.5, 1, 1.5, and 3 ps. Excitation was at 388 nm and the pulse energy was 60 nJ/pulse. (C) Transient absorption spectra of pF-iI in DCM at 1.5, 3, 5, 25, 50, 300, and 1000 ps. (D) Evolution of the pF SE bands, as indicated in (A). (E) Evolution of the SE bands in pF-iI, as indicated in (B). (F) Comparison of the decays of the transient signals at 440 nm for pF-iI (red circles) and pF (black circles) show significant quenching of pF* in pF-iI within 10 ps of excitation. Both exhibit bi-exponential decays: pF-iI ($\tau_1 = 0.52 \pm 0.1$ ps and $\tau_2 = 1.4 \pm 0.2$ ps) and pF ($\tau_1 = 25 \pm 5$ ps and $\tau_2 = 325 \pm 15$ ps).....	38
Figure 2.6. (Left) Time-resolved fluorescence spectra of the unfunctionalized pF homopolymer in argon saturated DCM following 388 nm excitation. (Right) Singlet lifetime of the unfunctionalized pF homopolymer following 388 nm excitation. The fsTA transient at 780 nm (black circles) and tri-exponential fit (red line) are shown along with the scaled time-resolved fluorescence decay integrated across the 400-550 nm wavelength region (blue line).....	39

- Figure 2.7.** (Left) Spectroelectrochemical difference spectrum of iI (black) and pF (red) following quantitative reduction and oxidation, respectively. The pF⁺ spectrum has been scaled by a factor of 4.5 to account for the polaron length resulting from oxidation of the pF backbone. (Right) Predicted spectrum for the CS state obtained by adding the pF⁺ and iI- difference spectra (grey dashed line) scaled to match the 1000 ps spectra following excitation of pF-iI at 388 nm (dark red line). Shown in the inset is a zoomed in view of the pF⁺ absorption, as indicated by the black dashed line.....40
- Figure 2.8.** (Top, left) Spectral contributions from pF* (0.2 ps), iI*, and the CS state used in the spectral modeling, normalized at 580 nm. (Top, right) Time-resolved coefficients for pF* (black), iI* (blue), and the CS state (red) spectral contributions obtained from least-squares analysis of the modeled pF-iI transient absorption spectrum. The iI* and CS populations have been scaled for clarity. Overlaid on the pF* and iI* populations are bi-exponential fits while a tri-exponential fit is overlaid on the CS state population. (Bottom, left to right) Modeled pF-iI spectra at 0.2, 1, 3, and 30 ps with the modeled spectrum (green) overlaid on the pF-iI assembly spectrum (black). The individual spectral contributions for pF* (gray), iI* (blue), and the CS state (red) are shown as dashed lines.....44
- Figure 2.9.** Snapshot of the orthorhombic (100x55x55 Å) simulation cell consisting of 10 fluorene monomers (green), 10 isoindigo pendants (orange), and 2,500 dichloromethane molecules used for molecular dynamics (MD) simulations of the pF-iI₁₀ polymer assembly. The MD simulations were collected on relaxed polymer structures for 1 ns with periodic boundary conditions.....46
- Figure 2.10.** (Left) Distance distributions for fluorene-isoindigo from the ensemble of pF-iI polymer structures obtained from the MD simulations. The bars represent the total distribution while the lines represent the successive nearest acceptors. (Right) Illustration of the fluorene-isoindigo through-space distance (R_{ij}), where the distance is computed between centroids placed on each unit.....48
- Figure 2.11.** iI-Model absorbance (red) and pF emission spectrum (blue) normalized to unity area showing the scaled Förster overlap integrand shaded in gray.....53
- Figure 2.12.** Comparison of the pF*, iI*, and CS state populations obtained from experiment (black circles) with the simulated populations (red line). The spectral amplitudes for each species were scaled to match the magnitude of the simulated populations.....56
- Figure 2.13.** (Left) Model isoindigo and fluorene oligomer pair used for the estimation of the electron transfer parameter V_0 with the ADF

computational package. ⁶ The distance is computed from centroids placed on each unit. (Right) Plot of log(coupling) versus distance obtained from calculation of the charge transfer integrals of the model systems for pF-iI.....	57
Figure 2.14. (A, B) Pictorial representation of the kinetic model applied to representative pF-iI ₁₀ polymer structures obtained from molecular dynamics simulations. The initial exciton is shown as a red cloud along the polymer backbones, in which the energy and electron transfer rates are computed from the distances and orientation factors. The total quenching rate of the i^{th} monomer ($k_{Q,i}$) is then expressed as the sum of the individual computed rates. The magnitude of the EnT rate constant to the nearest pendant (i.e., k_{EnT}^{NP}) is given as the cross-hatched rectangle for each configuration.....	60
Figure 2.15. Distribution of rate constants from the pF-iI kinetic simulations, showing the total quenching rate distribution (black line). Also shown is the mean energy transfer efficiency computed as a function of the total quenching rate constant ($k_{Q,i}$) from each configuration. The total rates were computed for each configuration and binned on a logarithmic scale ranging from 10^{10} to 10^{15} s ⁻¹ with a total of 500 bins.....	62
Figure 2.16. (A) Median energy transfer rate constants as a function of the total energy transfer rate constant to the nearest pendant (purple line) and to the pendant with the largest rate (green line). (B) Mean number of acceptors (orange circles) that are needed to achieve 80% of the total energy transfer quenching rate in the kinetic simulations. (C) Mean donor-acceptor distance as a function of the total EnT quenching rate constant to the nearest pendant (purple) and to the pendant with the largest rate (green). (D) Mean orientation factor that gives rise to the computed EnT rates in pF-iI. The rates were computed for each configuration and binned on a logarithmic scale ranging from 10^{10} to 10^{15} s ⁻¹ with a total of 500 bins.....	64
Figure 2.17. Average fraction of the total energy transfer rate constant ($k_{EnT,i}$) computed as a function of $k_{EnT,i}$ for the pendant with the largest rate (k_{EnT}^M) and for the nearest pendant (k_{EnT}^{NP}) in each initial polymer configuration.....	66
Figure 3.1. (Top) Chemical structures of the pT-iI monomer (left) and iI-Model (right). (Bottom) Snapshot of a 15 repeat unit pT-iI polymer assembly (i.e., pT-iI ₁₅) obtained from fully atomistic molecular dynamics simulations in explicit dichloromethane (DCM) solvent. The polymer backbone is depicted in green and the iI pendants in orange. The solvent has been excluded for clarity.....	74

- Figure 3.2.** Ground state absorbance spectra of the pT-iI polymer assembly (grey), unfunctionalized pT polymer (blue), iI-Model (red), and the sum of the iI and pT absorbance spectra (dashed black).81
- Figure 3.3.** Frontier orbitals (HOMO and LUMO) of geometry optimized isoindigo dimers at varying separations obtained from density functional theory calculations using the B3LYP functional and the 6-31(d,p) basis sets, as implemented in Gaussian09 (Revision E.01).....82
- Figure 3.4.** (A) Femtosecond transient absorption difference spectra of iI-Model in DCM at 0.3, 1, 2, 5, 15, and 20 ps. Shown shaded in orange is the inverted ground-state absorbance spectrum for iI-Model, normalized to the GSB at 410 nm. (B) Decay of the transient signal for iI-Model at 640 nm. The transient exhibits a single exponential decay with $\tau = 5.8 \pm 0.2$ ps. (C) Femtosecond transient absorption difference spectra of pT-iI in DCM at 0.3, 2, 5, 15, 30, and 100 ps. (D) Decay of the transient signal for pT-iI at 640 nm. The transient exhibits a single exponential decay with $\tau = 12.2 \pm 1.0$ ps. All spectra were measured in argon saturated DCM and excited with a 150 fs, 100 nJ pulse at 595 nm with a 120 μm spot size.....84
- Figure 3.5.** Franck-Condon mode analysis for the alkyl-substituted pT emission spectra. The emission spectrum (red line) was fit to a sum of 4 Gaussian functions with constant width and mode spacing (light purple line).....86
- Figure 3.6.** (A) Transient absorption spectra of pT in DCM at 0.2, 3, 10, 100, 250, 500, 1000, and 1500 ps. Excitation was at 460 nm and the pulse energy was 15 nJ/pulse. (B) Transient absorption spectra of pT-iI in DCM at 0.25, 0.45, 1, 3, 7, 18, 25, 35, 95, 200, and 1500 ps. Excitation was at 460 nm and the pulse energy was 60 nJ/pulse. (C) Spectral modeling of the 1500 ps pT-iI spectrum (light red). The dashed red line, labeled CS State, is the sum of the iI⁻ and pT⁺ spectra acquired from spectroelectrochemical measurements (Figure 3.9). The dashed green line, labeled ³pT, is the 1500 ps pT spectrum from panel (A). The dark red line represents the sum of the CS State and ³pT spectra to produce the modeled 1500 ps spectrum. (D) Kinetics trace at 575 nm for pT-iI fit to a bi-exponential function that exhibits a growth ($\tau_1 = 0.23 \pm 0.08$ ps) and a decay ($\tau_2 = 22.9 \pm 0.6$ ps).....87
- Figure 3.7.** Decay of the pT* stimulated emission band at 620 nm versus time. The transient was fit to a sum of two exponentials, with characteristic time constants of $\tau_1 = 1 \pm 0.03$ ps and $\tau_2 = 490 \pm 5$ ps.....88
- Figure 3.8.** (Left) Transient absorption spectra of pT in DCM from 1 ns to 10 μs following 388 nm excitation. (Right) Kinetics trace at 750 nm monitoring the triplet exciton absorption band. The decay of the triplet exciton is fit to

a single exponential decay with $\tau=13.7\pm0.8$ μ s.....	89
Figure 3.9. (Top) Spectroelectrochemical difference spectrum of pT ⁺ . (Middle) Spectroelectrochemical difference spectrum of iI-Model. (Bottom) Modeled CS state obtained by adding the pT ⁺ spectrum to 25% of the intensity of the iI ⁻ difference spectrum. The factor of 0.25 has been introduced to properly account for the relative contributions of pT ⁺ and iI ⁻ to the CS state spectrum. This stems from the fact that approximately 4 times as many reduced iI complexes can be accommodated by a single positive polaron along an individual polymer chain. ³²	90
Figure 3.10. Transient absorption decay for pT-iI following 460 nm excitation monitoring the charge recombination kinetics at 800 nm. The signal was fit to a tri-exponential function, in which the fast time components ($\tau_1 = 2.6$ ps and $\tau_2 = 21$ ps) are attributed to the quenching dynamics and relaxation of iI*. The slower component ($\tau_3 = 215$ ps) is ascribed to charge recombination between pT ⁺ and iI ⁻	92
Figure 3.11. Snapshot of the orthorhombic simulation cell with dimensions of 85x50x50 Å consisting of 15 thiophene monomers (green), 15 isoindigo pendants (orange), and 1,800 dichloromethane molecules used for molecular dynamics (MD) simulations of the pT-iI ₁₅ polymer assembly. The MD simulations were collected on relaxed polymer structures for 1 ns with periodic boundary conditions.....	93
Figure 3.12. (A) Total distance distributions for thiophene-isoindigo (T-iI) and (B) isoindigo-isoindigo (iI-iI) from the ensemble of polymer structures obtained from MD simulations. The bars represent the total distribution while the shaded areas are the nearest isoindigo distance distributions from the perspective of each thiophene monomer (A) and each isoindigo pendant (B).....	94
Figure 3.13. iI-Model absorbance (red) and pF emission spectrum (blue) normalized to unity area showing the scaled Förster overlap integrand shaded in gray.....	95
Figure 3.14. Comparison between the pT-iI experimental kinetics at 575 nm (black circles) and the linear combination of the simulated photoinduced populations (red line) described by equation 3.4.....	100
Figure 3.15. (Left) Model isoindigo and tetrathiophene oligomer pair used for the estimation of the close-range electronic coupling (V_0) with the ADF computational package. The distance is computed from centroids placed on each unit. (Right) Plot of ln(Coupling) versus distance obtained from calculation of the charge transfer integrals of the model system.....	101
Figure 3.16. Graphical illustration of the kinetic model applied to a representative pT-iI polymer structure obtained from MD simulations. The initial	

exciton is shown as a red cloud along the polymer backbone, in which the energy and electron transfer rates are computed using the distances and orientation factors. The total quenching rate is expressed as the sum of the individual computed rates.....103

Figure 3.17. (Top) Distribution of total quenching rate constants from the pT-iI kinetic simulations (black line). The gray shaded area reflects quenching rates that lie outside of the ultrafast transient absorption instrument response. The total rates were computed for each configuration and binned on a logarithmic scale ranging from 10^8 to 10^{15} s^{-1} with 500 bins. (Middle) Average electron transfer efficiency (red circles) computed as a function of the total quenching rate constant from each configuration. (Bottom) Average number of acceptors that are needed to achieve 80% of the total electron transfer quenching rate (black squares). The standard deviation for each measurement is shown as the light gray bar.....106

Figure 4.1. Ground state absorbance spectrum of the pS-Ru-A assembly on the surface of TiO_2 (blue line) and the emission spectrum of the pS-Ru-A assembly on ZrO_2 following 480 nm excitation (red line). All films were immersed in acetonitrile with 100 mM LiClO_4 . Also shown is the absorbance spectrum contribution from TiO_2 (shaded gray area).....119

Figure 4.2. Optimized geometry of the pS-Ru monomer along with calculated isodensity plots of the frontier molecular orbitals (LUMO+2, LUMO+1, LUMO, HOMO) (isodensity value = 0.03)120

Figure 4.3. (Left) Ensemble radial distribution functions for distances computed between Ru pendants from molecular dynamics simulations of pS-Ru-A in MeCN (top) and MeOH (bottom). (Right) Snapshot of a solvated pS-Ru-A chain in MeCN solvent, revealing the close-packed structure facilitated by the flexible pS backbone (green). Solvent molecules and counter ions have been omitted for clarity.....121

Figure 4.4. Radius of gyration computed from molecular dynamics simulations of pS-Ru-A in MeCN (blue) and MeOH (red). The radii are centered at 16.9 and 20.9 Å for MeCN and MeOH, respectively.....122

Figure 4.5. Time-resolved emission for TiO_2 //pS-Ru-A and ZrO_2 //pS-Ru-A monitored at 660 nm following 444 nm excitation. The decays are fit to a tri-exponential function, with time constants and amplitudes listed in Table 4.1.....123

Figure 4.6. (A) Transient absorption spectra following 420 nm excitation of TiO_2 //Ru-A at 1, 10, 100, 500 and 1200 ps. (B) Transient absorption spectra following 420 nm excitation of TiO_2 //pS-Ru-A at 1, 10, 100, 500 and 1200 ps. (C) Transient absorption spectra following 420 nm excitation of ZrO_2 //Ru-A at 1, 10, 100, 500 and 1200 ps. (D) Kinetics at 385 nm for

TiO ₂ //Ru-A (green circles) and TiO ₂ //pS-Ru-A (red circles) with the bi-exponential fits overlain.....	127
Figure 4.7. Kinetics traces at 480 nm on timescales ranging from 200 fs to 100 μ s for ZrO ₂ //Ru-A (black triangles), TiO ₂ //Ru-A (blue triangles), and TiO ₂ //pS-Ru-A (red triangles).....	129
Figure 5.1. Chemical structures of Model-Ru-A, pF-Ru and pF-Ru-A.....	142
Figure 5.2. Ground-state absorbance spectrum of pF-Ru-A on TiO ₂ (blue) and emission spectrum of pF-Ru-A on ZrO ₂ in MeCN with 0.1 M LiClO ₄ . The emission spectrum was acquired following excitation at 450 nm.....	143
Figure 5.3. (A) Transient absorption spectra following 450 nm laser excitation for the Model-Ru-A complex on TiO ₂ at 0.25, 1, 5, 10, 100, and 1400 ps. (B) Model-Ru-A//TiO ₂ kinetics trace at 385 nm. (C) Transient absorption spectra of pF-Ru-A//TiO ₂ at 0.25, 1, 5, 10, 100, and 1400 ps. (D) pF-Ru-A//TiO ₂ kinetics trace at 385 nm. The films were immersed in argon-saturated acetonitrile with 0.1 M LiClO ₄	146
Figure 5.4. Transient absorption spectra of pF-Ru-A//ZrO ₂ following photoexcitation at 450 nm on time scales of 250 fs to 1.2 ns. The slight spectral changes that are observed between 450 and 600 nm are not observed in the Model-Ru-A//ZrO ₂ transient spectra and are attributed to Ru ^{II*} →Ru energy hopping.....	147
Figure 5.5. (A) Nanosecond transient absorption spectra of pF-Ru-A//TiO ₂ films following excitation at 450 nm from 1 ns to 2 μ s. (B) Nanosecond transient absorption spectra of pF-Ru-A//TiO ₂ films from 2 μ s to 100 μ s. The shaded region is the spectrum at 100 μ s. (C) Kinetics traces for pF-Ru-A//TiO ₂ films at probe wavelengths 400 nm (blue), 485 nm (red) and 580 nm (black) from 250 fs to 150 μ s following 450 nm excitation. The gray-filled points represent the femtosecond and picosecond kinetic traces. The films were immersed in argon-saturated acetonitrile with 0.1 M LiClO ₄	149
Figure 5.6. Kinetics trace monitored at 430 nm for Model-Ru-A//TiO ₂ (red) and 400 nm for the pF-Ru-A//TiO ₂ assembly (black) following 450 nm excitation. Charge recombination between the polaron on the pF backbone is much longer lived than back electron transfer in Model-Ru-A//TiO ₂	150
Figure 6.1. (Top) Ground-state absorption (red) and emission (blue) spectra for T ₃ -trpy in DMSO. The emission spectrum was collected following 390 nm excitation. Frontier orbitals corresponding to the lowest energy π → π^* transition in T ₃ -trpy computed by DFT (isovalue = 0.03). (Bottom) Ground-state absorption spectrum (red) for T ₃ -trpy-Ru-L in MeCN. Frontier orbitals corresponding to the	

lowest energy intra-ligand charge transfer (ILCT) transition in T ₃ -trpy-Ru-MeCN computed by DFT (isovalue = 0.03).....	163
Figure 6.2. (Top) Optimized ground-state (bottom) and excited-state (top) geometries of T ₃ -trpy. (Bottom) Emission spectrum of T ₃ -trpy in DMSO following 390 nm excitation. The light purple spectrum corresponds to the simulated fit of a one-mode Franck-Condon progression with a mode-spacing of 1,220 cm ⁻¹ and E ₀₋₀ energy of 21,150 cm ⁻¹	164
Figure 6.3. (Top Left) Transient absorption difference spectrum of T ₃ -trpy in DMSO on time scales ranging from 0.5 ps to 1.2 ns. (Top Right) Kinetic traces at 505 (black triangles) and 760 nm (blue circles) fit to a single exponential function with $\tau=575$ ps. (Bottom Left) Transient absorption difference spectrum of T ₃ -trpy in DMSO on time scales ranging from 1.5 ns to 200 μ s. (Bottom Right) Kinetics trace at 620 nm with $\tau=58$ μ s.....	166
Figure 6.4. (A) Transient absorption difference spectrum of TiO ₂ //T ₃ -trpy in H ₂ O with 0.1 M HClO ₄ on time scales ranging from 1 to 1300 ps. (B) Transient absorption difference spectrum of TiO ₂ //T ₃ -trpy on TiO ₂ in H ₂ O with 0.1 M HClO ₄ on time scales ranging from 1 ns to 50 μ s. (C) Kinetics trace monitoring the T ₃ ⁺ -trpy absorption centered at 655 nm. The decay, which spans 9 decades of time, exhibits five distinct time components: $\tau_1=0.79$ ps, $\tau_2=114$ ps, $\tau_3=20$ ns, $\tau_4=1$ μ s, and $\tau_5=50$ μ s. (D) Illustration of the primary photophysical events in the TiO ₂ //T ₃ -trpy assembly, where electron injection is followed by either fast or slow BET.....	168
Figure 6.5. (Left) Transient absorption difference spectrum of SnO ₂ //T ₃ -trpy in H ₂ O with 0.1 M HClO ₄ on time scales ranging from 1 ps to 1300 ps. (Right) Kinetics trace at 520 nm monitoring the SE band of T ₃ [*] -trpy. The band decays with two distinct time components: $\tau_1=2.3$ ps and $\tau_2=15$ ps.....	170
Figure 6.6. (A) Transient absorption difference spectrum of T ₃ -trpy-Ru-MeCN on time scales ranging from 200 fs to 5 ps. (B) Transient absorption difference spectrum of T ₃ -trpy-Ru-MeCN on time scales ranging from 10 ps to 1000 ps. (C) Kinetics trace at 655 nm fit to a tri-exponential function with characteristic time constants of $\tau_1=0.25$ ps, $\tau_2=14.6$ ps, and $\tau_3=2950$ ps.....	172
Figure 6.7. (Left) Transient absorption difference spectrum of T ₃ -trpy-Ru-MeCN on time scales ranging from 1 ns to 2400 ns. (Right) Kinetics trace at 655 nm fit to a tri-exponential function with $\tau_1=2.3$ ns, $\tau_2=47$ ns, and $\tau_3=4.3$ μ s.....	173

Figure 6.8. (A) Transient absorption difference spectrum of $\text{TiO}_2//\text{T}_3\text{-trpy-Ru-MeCN}$ in MeCN with 0.1 M LiClO_4 on time scales ranging from 0.9 ps to 1300 ps. (B) Transient absorption difference spectrum of $\text{TiO}_2//\text{T}_3\text{-trpy-Ru-MeCN}$ in MeCN with 0.1 M LiClO_4 on time scales ranging from 1.5 ns to 500 ns. (C) Kinetics trace at 650 nm. The transient is fit to a tri-exponential function with $\tau_1=25$ ns, $\tau_2=1$ μs , and $\tau_3=50$ μs175

Figure 6.9. (A) Transient absorption difference spectrum of $\text{TiO}_2//\text{T}_3\text{-trpy-Ru-OH}_2$ in pH 1 HClO_4 on time scales ranging from 1.5 ps to 1300 ps. (B) Transient absorption difference spectrum of $\text{TiO}_2//\text{T}_3\text{-trpy-Ru-OH}_2$ in pH 1 HClO_4 on time scales ranging from 1.5 ns to 500 ns. (C) Kinetics trace at 520 nm for $\text{TiO}_2//\text{T}_3\text{-trpy-Ru-OH}_2$ in pH 1 HClO_4 . The transient spans 6 decades of time and exhibits four distinct time components: $\tau_1=2$ ns, $\tau_2=45$ ns, $\tau_3=3.2$ μs , and $\tau_4=88$ μs177

Figure 6.10. (Left) Transient absorption difference spectrum of $\text{SnO}_2//\text{T}_3\text{-trpy-Ru-MeCN}$ in MeCN with 0.1 M LiClO_4 on time scales ranging from 1 ps to 1300 ps. (Middle) Transient absorption difference spectrum of $\text{SnO}_2//\text{T}_3\text{-trpy-Ru-OH}_2$ in 0.1 M HClO_4 on time scales ranging from 1 ps to 1300 ps. (Right) Kinetics trace at 520 nm for $\text{SnO}_2//\text{T}_3\text{-trpy-Ru-OH}_2$. The band exhibits an ultrafast growth ($\tau_1=0.3$ ps) followed by a bi-exponential decay ($\tau_1=35$ ps and $\tau_2=130$ ps).....178

LIST OF ABBREVIATIONS

bpy	2,2'-bipyridine
CaF ₂	calcium fluoride
CMOS	complementary metal oxide semiconductor
CO ₂	carbon dioxide
CPA	chirped pulse amplification
DFT	density functional theory
DNA	deoxyribonucleic acid
DSPEC	dye-sensitized photoelectrochemical cell
DSSC	dye-sensitized solar cell
e ⁻	electron
FWHM	full width at half maximum
H ⁺	proton
H ₂ O	water
HClO ₄	perchloric acid
iI	isoindigo
¹ ILCT	singlet intra-ligand charge transfer
³ ILCT	triplet intra-ligand charge transfer
IR	infrared
LiClO ₄	lithium perchlorate
MD	molecular dynamics
MeCN	acetonitrile
MeOH	methanol

$^1\text{MLCT}$	singlet metal to ligand charge transfer
$^3\text{MLCT}$	triplet metal to ligand charge transfer
OD	optical density
OPA	optical parametric amplifier
Os^{II}	osmium (II)
pF	poly(fluorene)
pFT	poly(fluorene-co-thiophene)
pF2T	poly(fluorene-co-bithiophene)
pS	poly(styrene)
pT	poly(thiophene)
Ru^{II}	ruthenium (II)
Ru^{III}	ruthenium (III)
SnO_2	tin oxide
T_3	terthiophene
TCSPC	time-correlated single photon counting
trpy	terpyridine
TiO_2	titanium dioxide
UV-Vis	ultraviolet-visible
ZrO_2	zirconium dioxide

LIST OF SYMBOLS

A	absorbance
\approx	approximately
$\langle \tau \rangle$	average lifetime
$\langle P_{\text{EnT},i} \rangle$	average energy transfer efficiency of donor i
k_B	Boltzman's constant
ΔA	change in absorbance
H_{ij}	electronic coupling between donor i and acceptor j
Φ_{inj}	electron injection efficiency
β	electron transfer attenuation parameter
k_{ET}	electron transfer rate constant
$k_{\text{ET},ij}$	electron transfer rate constant from donor i to acceptor j
E_{0-0}	0-0 emission energy
Φ_F	emission quantum yield
k_{EnT}	energy transfer rate constant
$k_{\text{EnT},ij}$	energy transfer rate constant from donor i to acceptor j
ν	frequency
ΔG	Gibb's free energy
ϵ_A	molar absorptivity
\hbar	Planck's constant divided by two times pi
k	rate constant

k_{ET}	energy transfer rate constant
$k_{\text{ET},ij}$	energy transfer rate constant from donor i to acceptor j
τ	lifetime
κ_{ij}	orientation factor between donor i and acceptor j
$\pi\text{-}\pi^*$	pi to pi* electronic transition
λ	solvent reorganization energy
t	time
T	temperature
R_{ij}	through-space distance between donor i and acceptor j
$k_{\text{Q},i}$	total quenching rate constant of donor i

CHAPTER 1. INTRODUCTION

1.1 INTRODUCTION

The growing concern over depleting fossil fuels reserves and increased global energy demand has prompted efforts to find sustainable, alternative energy sources capable of replacing or supplementing fossil fuels. These sources include wind, solar, geothermal, bio-based fuels, and nuclear energy. Of these, solar energy is promising given the large amount of sunlight incident upon the earth in a single day ($\sim 3 \times 10^{20}$ J); more than the entire planet consumes in a year. Capturing and harnessing this energy is a formidable task, as the amount of land needed for a 10% efficient solar cell is roughly the land area of the state of North Carolina. Moreover, even if all of the sunlight could be efficiently captured, the intermittent nature of the sun calls for a means to store this energy on a massive scale.

Through billions of years of evolution, plants discovered how to use sunlight to reduce CO_2 to carbohydrates with water. The reaction for natural photosynthesis is:



Natural photosynthesis employs highly complex macromolecular assemblies (e.g., photosystem II) to absorb light and convert the energy into chemical fuels.¹⁻² These assemblies utilize several different light-absorbing complexes (i.e., chromophores) tuned such that the collective sum of their absorption energies resembles the energies of the solar spectrum, spanning from the visible into the near infrared region. In addition, the assemblies arrange and orient the chromophores such that intra-assembly energy and electron transport to the reaction centers for chemical fuel catalysis is

efficient. While these assemblies have been highly useful for natural photosynthesis, the goal of artificial photosynthesis is to use the lessons learned from natural photosynthesis and develop a device (i.e., artificial leaf) that is efficient and simple in design.³⁻⁶

1.2. ARTIFICIAL PHOTOSYNTHESIS

One such artificial leaf is the dye-sensitized photoelectrochemical cell (DSPEC), which consists of two separate electrodes (photoanode and photocathode).⁶⁻⁹ At the photoanode, water is split to form oxygen and protons and at the other electrode, the protons can form hydrogen gas or be used with carbon dioxide to generate carbon-based fuels. The emergence of the DSPEC provides a promising approach for the generation of solar fuels, where a key feature of DSPECs is the assimilation of molecular components that harvest solar energy, separate redox equivalents and use these redox equivalents to drive solar fuels half reactions. A typical DSPEC is shown in Figure 1.1, where the device employs a chromophore-catalyst assembly covalently attached to a mesoporous, wide-bandgap metal oxide semiconductor. In the case of the photoanode, the chromophore serves to absorb light and undergo charge separation at the metal oxide interface, while the redox equivalent is transferred to the catalyst. The transfer of four redox equivalents is necessary for the oxidation of water, underscoring the need for attachment to multiple reaction centers via supramolecular assemblies. Meanwhile, the previously injected electrons can be transferred through an external circuit to the cathode to drive the reduction half reactions.

Recently, there has been significant progress in the development of Ru^{II} catalysts capable of performing water oxidation.^{10,11} Initial photoactivation of the catalyst involves the oxidation of $[\text{Ru}^{\text{II}}\text{-OH}_2]^{2+}$ to $[\text{Ru}^{\text{III}}\text{-OH}_2]^{3+}$ followed by proton loss to give $[\text{Ru}^{\text{II}}\text{-OH}]^{2+}$ above the pK_a of the coordinated water. Further photoactivation of the catalyst results in e^-/H^+ loss to give $[\text{Ru}^{\text{IV}}\text{=O}]^{2+}$. The transfer of the third oxidative equivalent leads to the formation of $[\text{Ru}^{\text{V}}\text{=O}]^{3+}$. At this point,

the complex is active towards water oxidation by O-O bond formation and proton loss to give $[\text{Ru}^{\text{III}}-\text{OO}]^{2+}$; this is, however, the rate limiting step in the cycle. Transfer of the fourth oxidative equivalent occurs with H^+ loss to give $[\text{Ru}^{\text{IV}}-\text{OO}]^{2+}$, where O_2 is replaced by H_2O in a reductive substitution step to regenerate the initial catalyst, $[\text{Ru}^{\text{II}}-\text{OH}_2]^{2+}$.

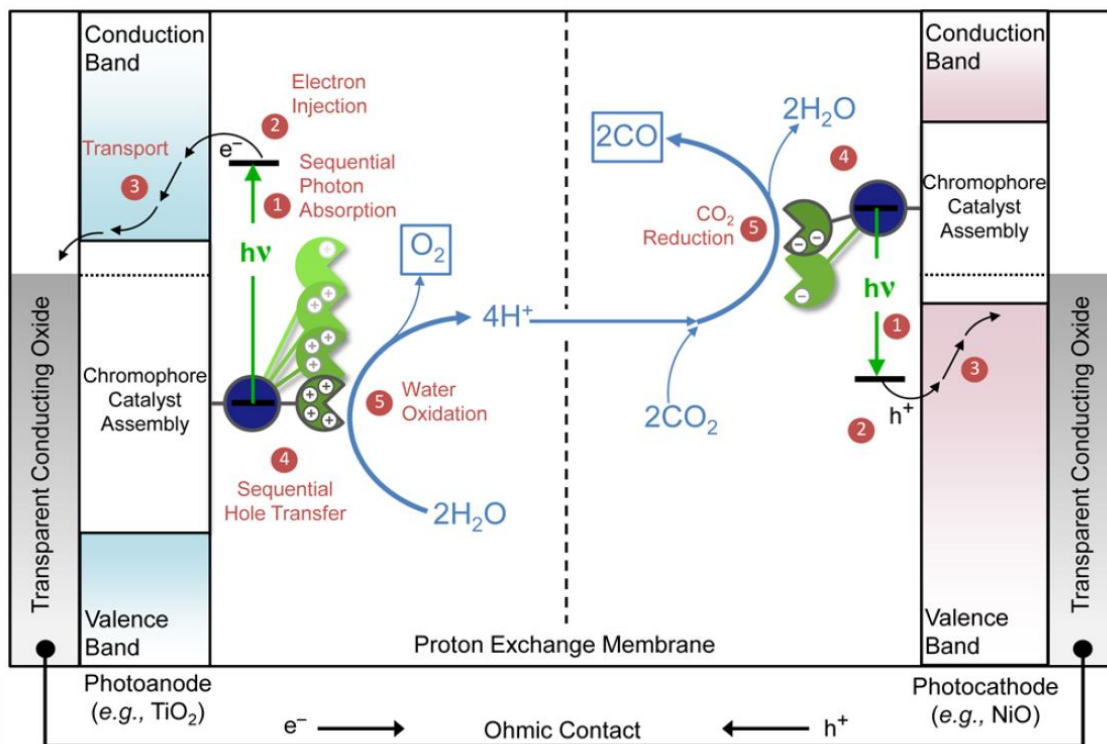


Figure 1.1. Schematic diagram of a tandem DSPEC for solar-driven splitting of CO_2 into CO and O_2 .

1.3. PHOTOINDUCED DYNAMICS IN MOLECULAR ASSEMBLIES

Multifunctional molecular and macromolecular assemblies that are able to harvest light, separate charge, and utilize the resulting redox equivalents to drive solar fuels reactions are an integral component in many artificial photosynthetic strategies.^{5, 12} Multifunctional behavior is achieved through a combination of fundamental energy and electron transfer events. While both of these processes have been extensively characterized in simple, well-defined systems consisting of only a few (often only two) molecular components, the structural complexity arising from the integration of multiple components in polymer assemblies leads to dynamical phenomena that are not found in dyads and triads. Thus, functionality in large molecular assemblies cannot be understood through studies of individual components or small model systems.

The characterization of dynamical phenomena (e.g. charge and energy migration) in large polymer-based assemblies is a challenging problem. Transport phenomena, for example, depend upon the macromolecular structure, which in turn depends upon the polymer support and the chemical structure of the monomer. The spatial relationship of the monomer's excited-state wavefunction to other assembly components, rigidity of the polymer, solvent polarity, and the nature of the counter ion can influence the structure and affect the exciton dynamics. In large macromolecular systems,¹³⁻²³ the separation between adjacent components is described not by a single distance, but rather a distribution of distances that, in turn, results in a distribution of electron and energy transfer rates. Furthermore, the presence of flexible linkages can give rise to large-scale conformational motions that can occur on timescales similar to the transfer rates,²⁴ leading to rate constants that may be more influenced by molecular motions than the quantities normally associated with electron and energy transfer, including electronic couplings, reorganization energies, and driving forces.²⁵ Thus, even the relatively simple process of site-to-site energy

transport will exhibit highly non-exponential kinetics, and disentangling contributions from the various dynamical phenomena can oftentimes only be accomplished through the use of sophisticated simulations and modeling to extract intrinsic rates from experimental data.

1.3.1 Polymer Structures

The fundamental photophysical processes of energy and electron transfer that take place in these complex assemblies depend on the separation and relative orientation of the individual components. The macromolecular structure is determined by a number of factors, including the torsional flexibility of the backbone, the size and spacing of the pendant groups, the length of the side chains, and the solvent, which vary amongst the five different assemblies shown in Figure 1. In pS-Ru, for example, each repeat unit of the polymer scaffold is functionalized by a metal complex that is connected to the backbone by a short side chain (Figure 1.2). This dense chromophore loading combined with the flexible nature of the poly(styrene) causes significant twisting of the polymer backbone in order to accommodate the large pendant metal complexes. Monte Carlo and molecular dynamics simulations indicate the structure is close-packed, with each complex lying within 2-3 Å of its neighbors.¹⁴ Whereas the macromolecular structure of the pS-Ru system is determined primarily by steric considerations and packing, the poly(fluorene)-Ru (pF-Ru) and poly(thiophene)-Ru (pT-Ru) structures are more heavily influenced by intramolecular and intermolecular forces (Figure 1.2). The conjugated π -network present in pF and pT reduces the torsional flexibility of scaffold, resulting in more extended structures, and this combined with the significantly longer side chains leads to larger average separations between adjacent complexes compared with pS-Ru. Solvent can also play a significant role, particularly in the more open pF-Ru and pT-Ru systems. Polar solvents have favorable interactions with the pendant complexes but not the polymer backbone, and as a result the assembly may adopt a structure where the side-chains

extend out into the solvent, or one in which the metal complexes take positions near the polymer to shield it from the more polar environment.

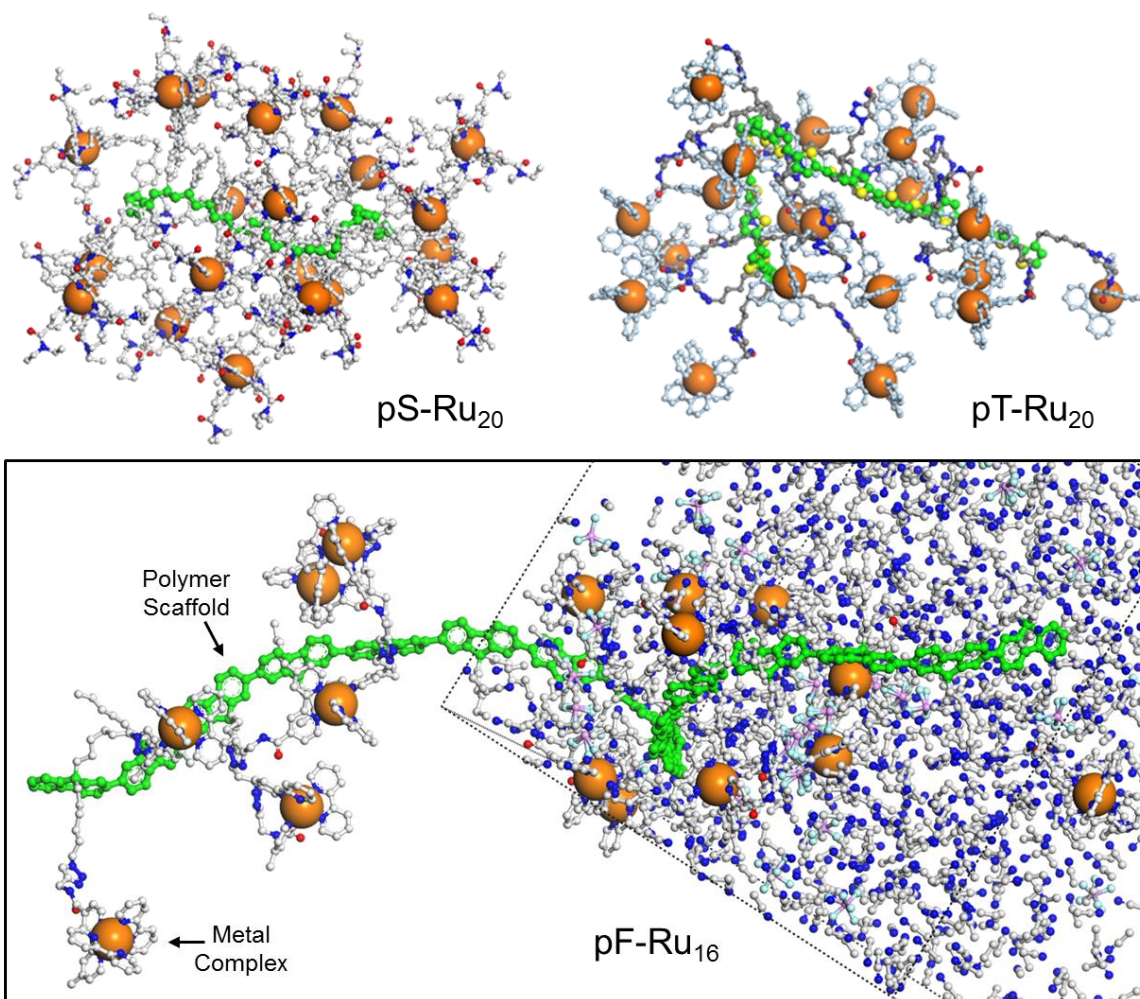


Figure 1.2. Condensed phase polymer assembly structures obtained from molecular dynamics simulations. Structures were calculated using periodic boundary conditions in the presence of explicit acetonitrile solvent and PF₆⁻ counter ions. The polymer scaffold is shown in green color and the Ru atoms are depicted as orange spheres with enlarged diameters. A portion of the solvent is shown in the pF-Ru₁₆ structure.

1.3.2 Site-to-Site Energy Transport

Site-to-site energy migration is initiated through metal-to-ligand charge transfer (MLCT) excitation of one of the pendant Ru^{II} complexes. The singlet MLCT state decays rapidly into a long-lived triplet MLCT, whose lifetime can extend from hundreds of nanoseconds to microseconds.²⁶ Because of the close proximity of the neighboring complexes, $\text{Ru}^{\text{II}*}$ excitation migrates along the chain in a random-walk like fashion through a series of isoenergetic triplet-triplet (i.e. Dexter) energy transfer events between adjacent complexes. Previous work from our laboratory has shown that energy transport is observed by replacing a small fraction of the Ru^{II} sites with Os^{II} complexes, i.e. pS- $\text{Ru}_{17}\text{Os}_3$ and pF- $\text{Ru}_{60}\text{Os}_{10}$. Because the Os^{II} sites have a lower energy excited state, they serve as traps that terminate the site-to-site random walk.^{14, 27-29} Thus, photoexcitation of the Ru^{II} sites is followed by a delayed rise in the $\text{Os}^{\text{II}*}$ emission, which is a clear signature of the transport of excited-state energy to the Os^{II} traps (Figure 1.3). (Note that the instantaneous rise in the emission intensity at $t=0$ is not the result of $\text{Ru}^* \rightarrow \text{Os}$ energy transfer, but rather reflects a combination of emission resulting from both direct excitation of the Os sites and weak Ru emission that is also detected at the monitored wavelength, ~ 780 nm).

The energy transport process includes a series of $\text{Ru}^{\text{II}*} \rightarrow \text{Ru}^{\text{II}}$ hops followed by a terminating $\text{Ru}^{\text{II}*} \rightarrow \text{Os}^{\text{II}}$ energy transfer event. The growth in the $\text{Os}^{\text{II}*}$ emission reflects the *total* time for this process, and thus reflects both the hopping time (τ) and the number of hops needed to reach the trap. The latter depends upon the fraction of Os^{II} sites; the greater the Os^{II} loading, the fewer the number of hops needed and the faster the rise in the photoluminescence intensity. Thus, while the growth indicates the presence of energy transport, the rise time itself is not a direct measure of the intrinsic $\text{Ru}^{\text{II}*} \rightarrow \text{Ru}^{\text{II}}$ hopping time.

Stochastic kinetic simulations provide a means of extracting the microscopic details of energy transport from the experimental data. The first step involves determining the macromolecular structure of the assembly using Monte Carlo simulation methods.¹⁴ A structure is selected from the ensemble and each site is assigned to be Ru or Os according to the loading statistics. One of the Ru sites is selected as the initial location of the excited state and energy transfer rate constants (k_{EnT}) are calculated to its nearest neighbors using a Dexter formalism, i.e. $k_{\text{EnT}}(\mathbf{R}) = k_0 \exp(-\beta R)$, where R is the separation between sites, k_0 is the rate constant at closest contact, and β is an attenuation parameter that determines the falloff of the electronic coupling with distance.²⁵ Because the chemical linkage connecting adjacent complexes contains a significant number of saturated carbons, the electronic coupling between sites arises primarily from direct orbital overlap between the donor and acceptor complexes. In this limit β is $\sim 1\text{-}2 \text{ \AA}^{-1}$, making energy transfer extremely short range.

Energy migration “trajectories” are propagated using a stochastic kinetic algorithm. The simulation averages many trajectories, each obtained by sampling different structures and loading configurations, to produce an output that is “fit” to the experimental data in an *ad hoc* fashion.³⁰ The simulations of energy transport in the pS-Ru₁₇Os₃ assembly reveals a distribution of hopping times ($\tau_{\text{avg}} = 1\text{-}3 \text{ ns}$) with a broad distribution in the number of hops needed to reach the Os trap.

The wide variation in the number of hops needed to reach an Os site is (in part) a reflection of the significant chain-to-chain variation in the Os loading. The fraction of Os sites in pS-Ru₁₇Os₃ is 15%, but this represents an average of the entire ensemble of chains. We estimate that only a quarter of the chains have three Os complexes, while many ($\sim 20\%$) have only one or none, and about 10% have six or more. For chains with a large fraction of Os sites, the number of hops needed to reach the trap may be as small as 2-3, but for chains with only a single Os site it may

take tens or even hundreds of hops. The presence of migration trajectories with a large number of $\text{Ru}^* \rightarrow \text{Ru}$ hops is suggested by the persistence of sensitized Os emission 200-400 ns after excitation, well beyond the ~ 50 ns excited-state lifetime of the Os complex (Figure 3).

The energy transfer times observed in the pS-Ru₁₇Os₃ assembly (1-3 ns) are long compared to singlet-singlet (i.e. Förster) energy transfer times observed in many systems,³¹⁻³³ In spite of the slower energy transfer time, the transport of the excited state to the Os trap sites is extremely efficient. We estimate that about 95% of the Ru^* excited states created on polymer chains with at least one Os complex are eventually transported to a trap site. The high transport efficiency in the pS-Ru assembly stems in part from the dense packing of the metal complexes, which ensures that a Ru^* excited state is always in close contact with one of its neighbors. While this dense packing is important, the long lifetime of the Ru^* excited state (~ 1 μs) also plays a role. Thus, even though the energy transfer time is long (1-3 ns), it is fast compared to the Ru^* lifetime, suggesting that the efficiency of a single energy transfer step is greater than 99.7%.

Transient photoluminescence data collected from the pF-Ru₆₀Os₁₀ assembly also exhibits the delayed rise in the Os* emission that is characteristic of site-to-site transport (Figure 3). While we have not yet performed Monte Carlo simulations on this system, analysis of the emission spectra suggests $\sim 80\%$ of the Ru^* excited states produced by photoexcitation are transferred to one of the Os sites. This relatively high efficiency is remarkable, especially given the low packing density of the metal complexes compared to pS-Ru₁₇Os₃ (Figure 3) and the close contact needed for triplet-triplet energy transfer. The high efficiency observed in the pF-Ru₆₀Os₁₀ assembly may be an indication that energy transport is facilitated by the conformational fluctuations that bring two complexes into close proximity where the short-range triplet-triplet energy transfer is possible.

Conformational flexibility may not only help overcome the limitations of short triplet-triplet energy transfer distances, but it may also mitigate effects of energetic disorder. The highly charged nature of the polymer and corresponding counter ions gives rise to a heterogeneous electrostatic environment that lifts the degeneracy of neighboring sites. The lower energy sites act as shallow traps that impede energy transport. In fluid solution, conformational motion is constantly changing this environment, and the effects of energetic disorder are masked. When polymer assemblies are dispersed in rigid matrices, this conformational motion is frozen out on the timescale of energy hopping. As a result, energy transfer is biased towards lower energy, and once the lowest energy sites are reached, transport of the excited state slows considerably.³⁴ Transient photoluminescence experiments performed on assemblies embedded in rigid environments show evidence of the loss of conformational flexibility. Whereas emission spectra in fluid solution show little (or no) time-dependent shift in the band position, experiments on pS-Os₂₀ exhibit a clear red shift in the emission band with increasing time after excitation that results from this energetic disorder.²⁸ The exploitation of conformational flexibility could be a powerful design concept in the development of multifunctional assemblies.

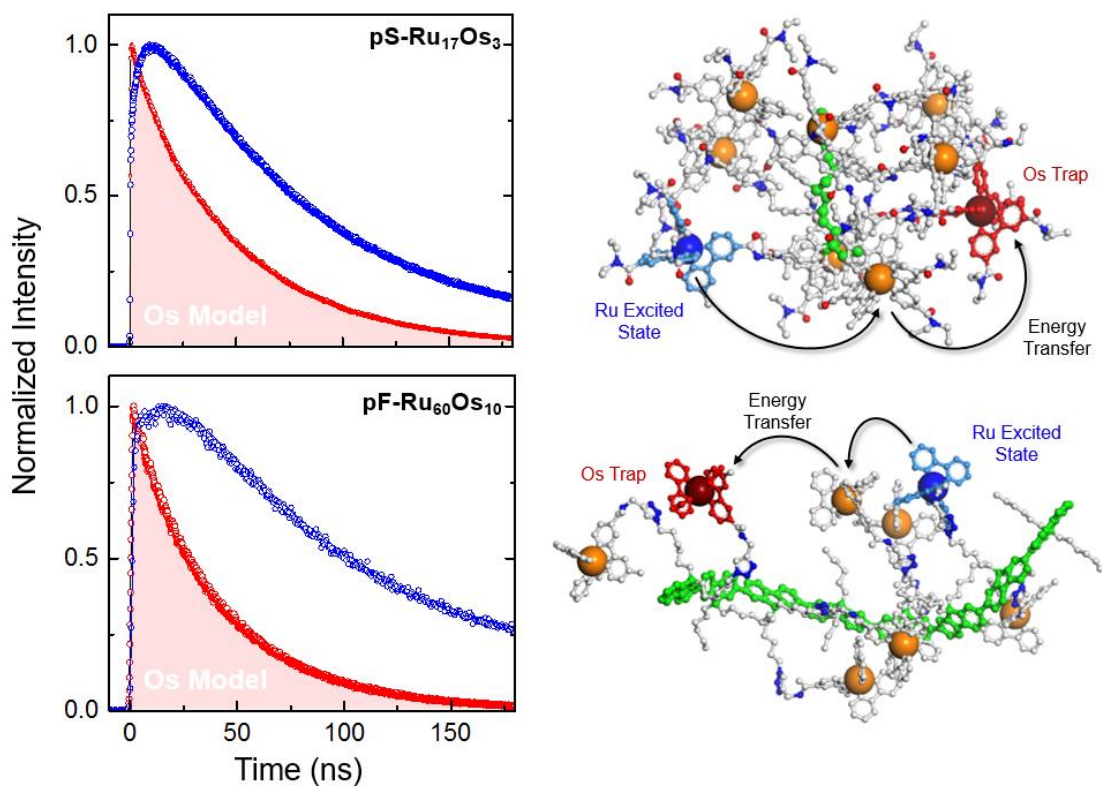


Figure 1.3. (Left) Time resolved emission monitoring Os^{II} photoluminescence in $\text{pS-Ru}_{17}\text{Os}_3$ and $\text{pF-Ru}_{60}\text{Os}_{10}$. (Right) Illustration of site-to-site energy transport within a subsection of $\text{pS-Ru}_{17}\text{Os}_3$ (upper) and $\text{pF-Ru}_{60}\text{Os}_{10}$ (lower). The initial Ru excited state (blue) undergoes energy transfer to adjacent Ru complexes and is ultimately transferred to the Os trap (red).

1.3.3 Dynamics in Polymer Assemblies with π -Conjugated Polymer Backbones

In assemblies utilizing π -conjugated polymers, photoexcitation of delocalized $\pi \rightarrow \pi^*$ transitions in the visible gives rise to additional dynamical phenomena. The excited-state dynamics of conjugated polymers have been studied extensively, both in solution and as thin films.³⁵⁻³⁹ Conformational disorder breaks up the conjugation along the backbone as a result of relatively low energy barriers for bond rotations between subunits, resulting in a chain of linked chromophores of varying conjugation lengths,⁴⁰⁻⁴¹ as depicted in the pF structure in Figure 1.4. The final structure is an energetic compromise between the entropic gain associated with producing a disordered structure and the energetic destabilization that occurs upon breaking the conjugation. The broad absorbance spectrum of the solvated polymer is a manifestation of this disorder, with longer conjugation lengths contributing to the red edge of the spectrum and shorter to the blue.³⁹

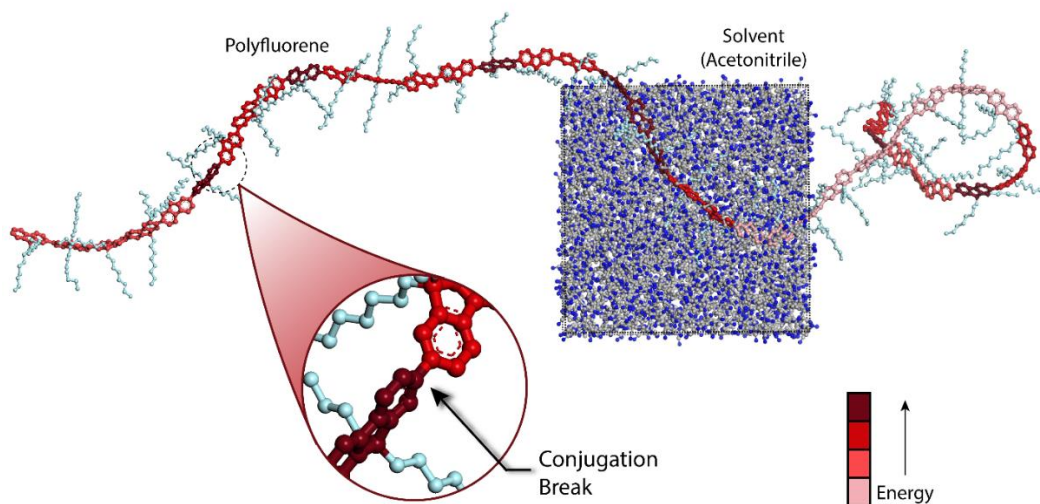


Figure 1.4. Condensed phase structure of a 40-repeat unit pF in explicit acetonitrile solvent obtained from molecular dynamics simulations. Most of the solvent is omitted for clarity, but a portion is shown for scale. The conformational subunits are colored based on the energy level with darker shades indicating subunits with shorter lengths and hence higher energies. The enlarged section shows a zoomed-in view of adjacent conformational subunits with a conjugation break.

Photoexcitation of pF and pT polymers results in a rich set of dynamical phenomena. On very short timescales (<100 fs), coupling of the excitation to small-scale torsional motions cause rapid relaxation and localization of the exciton onto a small number of monomer units.^{37, 42} Transient spectra obtained on longer timescales from pF and pT (i.e. unfunctionalized) chains in solution are dominated by a series of negative-amplitude features in the blue that arise from a combination of ground-state bleach and stimulated emission, as well as a low-energy absorption associated with the singlet excited state of the polymer (Figure 1.5). The stimulated emission bands decay in amplitude (due to excited-state relaxation) and shift to lower energy with increasing time. The red shift is indicative of torsional relaxation and/or exciton migration.^{37, 39, 43-44} In pF, the stimulated

emission shifts a few nanometers over several hundreds of picoseconds, due to a combination of large-scale conformational rearrangements and intrachain energy transfer to lower energy sites (Figure 1.5).³⁷⁻³⁸ In pT, the spectral changes are much more extensive, reflecting slow torsional relaxation that results in large-scale planarization of the backbone, such that by 100 ps, the fully relaxed excitons are formed. It has been previously shown that additional exciton stabilization is achieved through the presence of strongly-coupled low-frequency torsional degrees of freedom,⁴⁵ which is consistent with the greater spectral evolution (Stokes shift) observed in pT compared to pF. In both pF and pT, the exciton decays through either emission or intersystem crossing to form longer-lived triplet excitons.³⁶⁻³⁷

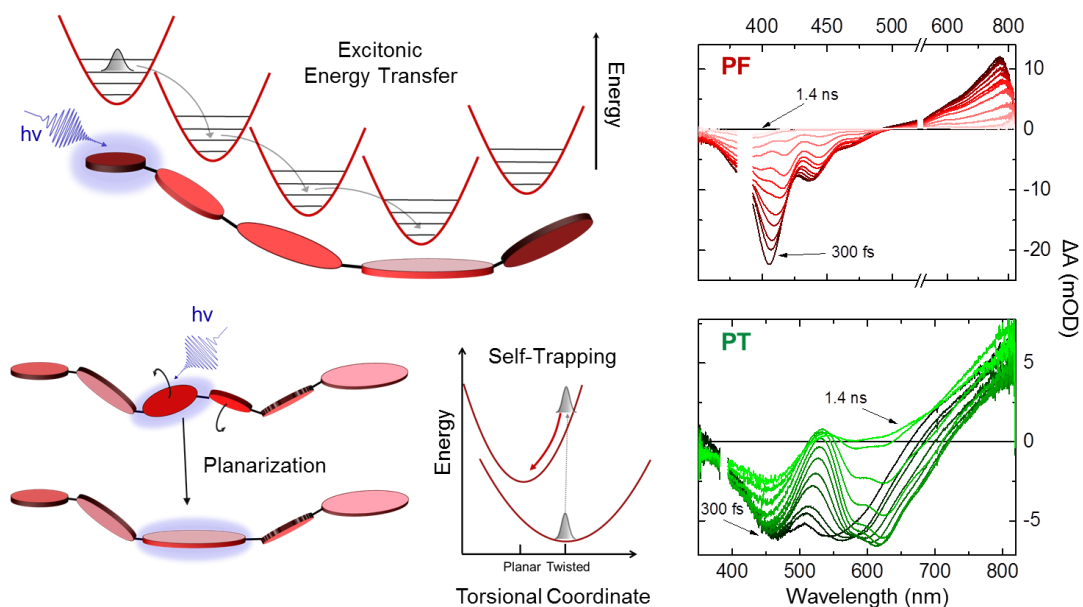


Figure 1.5. (Left) Illustration of excitonic energy transfer (top) and excited-state self-trapping by torsional relaxation (bottom) along a π -conjugated polymer backbone following excitation into a high-energy conformational subunit. (Right) Transient absorption difference spectra of unfunctionalized pF (upper) and pT (lower) from 300 fs to 1.4 ns following 388 nm excitation.

The transient spectra obtained from pF-Ru following excitation of the pF backbone are dramatically altered by the presence of the pendant Ru^{II} complexes (Figure 1.6). The stimulated emission feature observed at early times resembles that seen in pF, but in pF-Ru it is quenched within several picoseconds. The transient spectra are also qualitatively different. Whereas in pF the stimulated emission shifts continuously to the red, in pF-Ru this band initially shifts to the red, but after a few picoseconds shifts back to higher energy, leaving behind the spectrum of pF⁺. This behavior is the result of pF* quenching through a combination of energy and electron transfer mechanisms. Energy transfer to give a singlet Ru excited state (*i.e.* $^1\text{pF}^* + \text{Ru}^{+2} \rightarrow \text{pF} + ^1\text{Ru}^{+2*}$) occurs with a time constant of 450 fs, accounting for ~85% of the pF* quenching events in pF-Ru, while electron transfer to produce a charge-separated state (*i.e.* $^1\text{pF}^* + \text{Ru}^{+2} \rightarrow \text{pF}^+ + \text{Ru}^{+1}$) takes place on a slower timescale, $\tau = 1.5$ ps. In pF-Ru, the apparent blue-shift of the stimulated emission is due to the formation of pF⁺.

Assemblies incorporating pT, as well as scaffolds with mixed thiophene and fluorene content, pFT and pF2T, also show competitive energy and electron transfer. Like pF-Ru, all of these assemblies exhibit negative-going stimulated emission features that are quenched in the presence of the pendant Ru^{II} complexes. Analysis of the quenching kinetics reveals that the electron transfer time across this series of polymers is relatively constant, varying between 1-2 ps (Figure 1.6).⁴⁶⁻⁴⁸ The energy transfer times, on the other hand, increase with greater thiophene content and as a result the fraction of polymer excited states that decay through the energy transfer pathway also decreases across the series (Table 1.1).

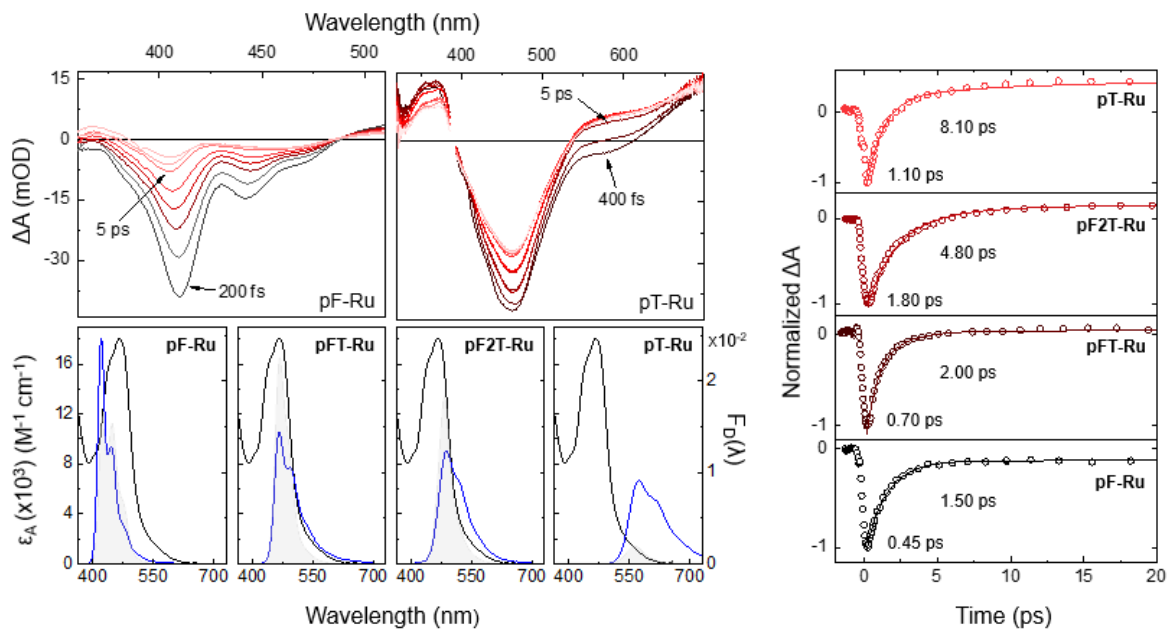


Figure 1.6. Transient absorption spectra following primary excitation of the polymer backbone at 388 nm for pF-Ru (upper left) and pT-Ru (upper right). (Bottom) Ru^{II} absorbance ($\epsilon_A(\lambda)$) and normalized (to unit area) polymer emission spectra ($F_D(\lambda)$). The shaded grey area reflects the integrand, $F_D(\lambda)\epsilon_A(\lambda)\lambda^4$, which is scaled for clarity. (Right) Kinetic traces of the polymer assemblies showing the initial polymer excited-state quenching during the first 10 ps following excitation.

Table 1.1. Energy and electron transfer data for π -conjugated polymer assemblies with pendant Ru^{II} chromophores.

		Energy Transfer		Electron Transfer		
Assembly	Energy Transfer: Electron Transfer Ratio	τ (ps)	τ_{RET} (ps)	τ (ps)	$-\Delta G^0$ (eV)	λ (eV)
pF-Ru	85:15	0.45	0.45	1.5	0.72	0.50-0.75 ↑ ↓
pFT-Ru	75:25	0.7	1.2	2.0	0.45	
pF2T-Ru	25:75	4.8	4.0	1.8	0.46	
pT-Ru	15:85	8.1	10.0	1.1	0.50	

The trend in energy transfer rates across the polymer series can be understood in terms of the absorption and emission properties of assemblies. The rate constant for resonant energy transfer (RET) between a donor (D) and acceptor (A) separated by a distance R is given by:

$$\frac{1}{\tau_{\text{RET}}} = \frac{1}{\tau_D} \left(\frac{R_0}{R} \right)^6 \quad (1.2)$$

where τ_D is the excited-state lifetime of the donor, and R_0 is the Förster distance, the distance at which energy transfer is 50% efficient. The Förster distance can be estimated from independent spectroscopic measurements of the donor and acceptor according to:

$$R_0^6 = A \Phi_D \kappa^2 \int_0^\infty F_D(\lambda) \epsilon_A(\lambda) \lambda^4 d\lambda \quad (1.3)$$

where Φ_D is the quantum yield of the donor in the absence of the acceptor, and κ is a factor describing the relative orientations of the donor and acceptor. The constant A is given by $A = 9000(\ln 10)/(128\pi^5 n^4 N_A)$, where n is the refractive index and N_A is Avogadro's number. The integral in Eq. 1.3 describes the product of the emission spectrum of the donor normalized to unity area and the absorption spectrum of the acceptor, as illustrated in Figure 1.6.

The large energy transfer rate constant observed in the pF-Ru assembly results from the significant spectral overlap between the pF emission and the Ru absorption (Figure 1.6) and large

quantum yield of pF*. The decrease in the energy transfer rate across the series is attributed to a systematic shift in the emission spectrum to lower energy with increasing thiophene content, which results in an overall decrease in the overlap between the donor emission and acceptor absorption, as well as a decrease in the quantum yield of the polymer (Φ_D). Energy transfer rates predicted using Eq. 1.2 are in good agreement with the experimentally observed values (Table 1).⁴⁶⁻⁴⁸

The lifetimes of the charge-separated state produced by electron transfer also depends upon the polymer backbone. While the charge-separated state in pF-Ru undergoes recombination (i.e. back electron transfer) to reform the ground state with $\tau=6$ ns, in pT-Ru it decays with $\tau\sim 20$ μ s. The dramatic difference between these two assemblies may be a consequence of the high hole mobility of the pT polymer backbone, which could quickly and efficiently separate the electron and the hole.

While the identity of the polymer backbone has a dramatic influence on the partitioning between energy and electron transfer (Table 1.1), the macromolecular structure also plays a role to direct the preferred quenching pathway. In pF and pT assemblies with pendant isoindigo (iI) chromophores (pF-iI and pT-iI, respectively), computational modeling in conjunction with ultrafast experiments reveal the role of the macromolecular structure. In pF-iI, the large fluorene monomer size spreads the pendants in solution, with average donor-acceptor distances of ~ 15.8 Å. Given the exponential fall-off for the electronic coupling in electron transfer and significant spectral overlap between the iI absorption and pF emission, energy transfer dominates overall.⁴⁹ In the case of pT-iI, the small thiophene monomer leads to a close-packed structure with donor-acceptor distances < 12 Å. This, in conjunction with the small spectral overlap between the iI absorption and pT emission leads to fast (< 200 fs) ET accounting for over 95% of the quenching events in pT-iI.

1.3.4 Multifunctional Behavior

The eventual utilization of molecular assemblies in artificial photosynthetic applications will require that they perform multiple functions, including light-harvesting and charge separation, as well as storage and transport of redox equivalents to catalytic sites. Multifunctional behavior is observed in the excited-state photophysics of pS-Ru (Chapter 4) and pF-Ru (Chapter 5) assemblies anchored to TiO₂ through carboxylate groups placed on 100% of the Ru^{II} complexes in pS-Ru and ~30% of the Ru complexes in pF-Ru.⁵⁰ The result is a composite structure, in which the assembly is attached to the surface through a few complexes, while the remaining chromophores serve as antennas for light absorption and excited-state transport.

The photophysics of these assemblies on TiO₂ were studied across 9 decades of time using transient absorption spectroscopy (TA) and time-resolved emission spectroscopy (TRES). Photoexcitation of surface-bound Ru^{II} sites results in prompt electron injection into the TiO₂ conduction band, producing a Ru^{III} species at the surface. In both pS-Ru and pF-Ru, site-to-site energy transport is observed, where delayed electron injection on the ns time scale is observed, revealing the antenna nature of these assemblies to transport the excited-state energy to the surface. Following electron injection in pS-Ru, the hole on the surface-bound Ru^{III} complex is transferred to the Ru^{II} sites away from the metal oxide surface, giving rise to a long-lived charge-separated state. In pF-Ru, we observe hole transfer to quickly occur to the pF backbone, which shuttles and stores the redox equivalent for hundreds of microseconds. The formation of a long-lived charge-separated state is a desirable property for the production of solar fuels as it enables effective transfer of redox equivalents to be used in multi-electron catalytic reactions.

REFERENCES

1. Renger, G., Oxidative Photosynthetic Water Splitting: Energetics, Kinetics and Mechanism. *Photosynth Res* **2007**, *91*, 186-186.
2. Ferreira, K. N.; Iverson, T. M.; Maghlaoui, K.; Barber, J.; Iwata, S., Architecture of the Photosynthetic Oxygen-Evolving Center. *Science* **2004**, *303*, 1831-1838.
3. House, R. L.; Iha, N. Y. M.; Coppo, R. L.; Alibabaei, L.; Sherman, B. D.; Kang, P.; Brennaman, M. K.; Hoertz, P. G.; Meyer, T. J., Artificial Photosynthesis: Where Are We Now? Where Can We Go? *J Photoch Photobio C* **2015**, *25*, 32-45.
4. Meyer, T. J., Chemical Approaches to Artificial Photosynthesis. *Accounts Chem Res* **1989**, *22*, 163-170.
5. Alstrum-Acevedo, J. H.; Brennaman, M. K.; Meyer, T. J., Chemical Approaches to Artificial Photosynthesis. 2. *Inorg Chem* **2005**, *44*, 6802-6827.
6. Song, W. J.; Chen, Z. F.; Brennaman, M. K.; Concepcion, J. J.; Patrocinio, A. O. T.; Iha, N. Y. M.; Meyer, T. J., Making Solar Fuels by Artificial Photosynthesis. *Pure Appl Chem* **2011**, *83*, 749-768.
7. Treadway, J. A.; Moss, J. A.; Meyer, T. J., Visible Region Photooxidation on TiO₂ with a Chromophore-Catalyst Molecular Assembly. *Inorg Chem* **1999**, *38*, 4386.
8. Gerischer, H., Photocatalysis in Aqueous-Solution with Small TiO₂ Particles and the Dependence of the Quantum Yield on Particle-Size and Light-Intensity. *Electrochim Acta* **1995**, *40*, 1277-1281.
9. Gerischer, H., Photoelectrochemical Catalysis of the Oxidation of Organic-Molecules by Oxygen on Small Semiconductor Particles with TiO₂ as an Example. *Electrochim Acta* **1993**, *38*, 3-9.
10. Ashford, D. L.; Gish, M. K.; Vannucci, A. K.; Brennaman, M. K.; Templeton, J. L.; Papanikolas, J. M.; Meyer, T. J., Molecular Chromophore-Catalyst Assemblies for Solar Fuel Applications. *Chem Rev* **2015**, *115*, 13006-13049.
11. Concepcion, J. J.; Jurss, J. W.; Brennaman, M. K.; Hoertz, P. G.; Patrocinio, A. O. T.; Iha, N. Y. M.; Templeton, J. L.; Meyer, T. J., Making Oxygen with Ruthenium Complexes. *Accounts Chem Res* **2009**, *42*, 1954-1965.
12. Gust, D.; Moore, T. A.; Moore, A. L., Mimicking Photosynthetic Solar Energy Transduction. *Accounts Chem Res* **2001**, *34*, 40-48.
13. Sykora, M.; Maxwell, K. A.; DeSimone, J. M.; Meyer, T. J., Mimicking the Antenna-Electron Transfer Properties of Photosynthesis. *Proceedings of the National Academy of Sciences of the United States of America* **2000**, *97*, 7687-7691.

14. Fleming, C. N.; Maxwell, K. A.; DeSimone, J. M.; Meyer, T. J.; Papanikolas, J. M., Ultrafast Excited-State Energy Migration Dynamics in an Efficient Light-Harvesting Antenna Polymer Based on Ru(II) and Os(II) Polypyridyl Complexes. *J Am Chem Soc* **2001**, *123*, 10336-10347.
15. Fang, Z.; Ito, A.; Stuartt, A. C.; Luo, H. L.; Chen, Z. F.; Vinodgopal, K.; You, W.; Meyer, T. J.; Taylor, D. K., Soluble Reduced Graphene Oxide Sheets Grafted with Polypyridylruthenium-Derivatized Polystyrene Brushes as Light Harvesting Antenna for Photovoltaic Applications. *Acs Nano* **2013**, *7*, 7992-8002.
16. Devadoss, C.; Bharathi, P.; Moore, J. S., Energy Transfer in Dendritic Macromolecules: Molecular Size Effects and the Role of an Energy Gradient. *J Am Chem Soc* **1996**, *118*, 9635-9644.
17. Balzani, V.; Campagna, S.; Denti, G.; Juris, A.; Serroni, S.; Venturi, M., Designing Dendrimers Based on Transition Metal Complexes. Light-Harvesting Properties and Predetermined Redox Patterns. *Accounts Chem Res* **1998**, *31*, 26-34.
18. Nantalaksakul, A.; Reddy, D. R.; Bardeen, C. J.; Thayumanavan, S., Light Harvesting Dendrimers. *Photosynth Res* **2006**, *87*, 133-150.
19. McCafferty, D. G.; Friesen, D. A.; Danielson, E.; Wall, C. G.; Saderholm, M. J.; Erickson, B. W.; Meyer, T. J., Photochemical Energy Conversion in a Helical Oligoproline Assembly. *Proceedings of the National Academy of Sciences of the United States of America* **1996**, *93*, 8200-8204.
20. Knorr, A.; Galoppini, E.; Fox, M. A., Photoinduced Intramolecular Electron Transfer in Dichromophore-Appended Alpha-Helical Peptides: Spectroscopic Properties and Preferred Conformations. *J Phys Org Chem* **1997**, *10*, 484-498.
21. Serron, S. A.; Aldridge, W. S.; Fleming, C. N.; Danell, R. M.; Baik, M. H.; Sykora, M.; Dattelbaum, D. M.; Meyer, T. J., Evidence for through-Space Electron Transfer in the Distance Dependence of Normal and Inverted Electron Transfer in Oligoproline Arrays. *J Am Chem Soc* **2004**, *126*, 14506-14514.
22. Wilger, D. J.; Bettis, S. E.; Materese, C. K.; Minakova, M.; Papoian, G. A.; Papanikolas, J. M.; Waters, M. L., Tunable Energy Transfer Rates Via Control of Primary, Secondary, and Tertiary Structure of a Coiled Coil Peptide Scaffold. *Inorg Chem* **2012**, *51*, 11324-11338.
23. Bettis, S. E.; Ryan, D. M.; Gish, M. K.; Alibabaei, L.; Meyer, T. J.; Waters, M. L.; Papanikolas, J. M., Photophysical Characterization of a Helical Peptide Chromophore–Water Oxidation Catalyst Assembly on a Semiconductor Surface Using Ultrafast Spectroscopy. *The Journal of Physical Chemistry C* **2014**, *118*, 6029-6037.
24. Davis, W. B.; Ratner, M. A.; Wasielewski, M. R., Conformational Gating of Long Distance Electron Transfer through Wire-Like Bridges in Donor-Bridge-Acceptor Molecules. *J Am Chem Soc* **2001**, *123*, 7877-7886.

25. Barbara, P. F.; Meyer, T. J.; Ratner, M. A., Contemporary Issues in Electron Transfer Research. *J Phys Chem-Us* **1996**, *100*, 13148-13168.
26. McCusker, J. K., Femtosecond Absorption Spectroscopy of Transition Metal Charge-Transfer Complexes. *Accounts Chem Res* **2003**, *36*, 876-887.
27. Fleming, C. N.; Dupray, L. M.; Papanikolas, J. M.; Meyer, T. J., Energy Transfer between Ru(II) and Os(II) Polypyridyl Complexes Linked to Polystyrene. *J Phys Chem A* **2002**, *106*, 2328-2334.
28. Fleming, C. N.; Jang, P.; Meyer, T. J.; Papanikolas, J. M., Energy Migration Dynamics in a Ru(II)- and Os(II)-Based Antenna Polymer Embedded in a Disordered, Rigid Medium. *J Phys Chem B* **2004**, *108*, 2205-2209.
29. Fleming, C. N.; Brennaman, M. K.; Papanikolas, J. M.; Meyer, T. J., Efficient, Long-Range Energy Migration in Ru-II Polypyridyl Derivatized Polystyrenes in Rigid Media. Antennae for Artificial Photosynthesis. *Dalton T* **2009**, 3903-3910.
30. Gillespie, D. T., Exact Stochastic Simulation of Coupled Chemical-Reactions. *J Phys Chem-Us* **1977**, *81*, 2340-2361.
31. Chen, Z.; Grumstrup, E. M.; Gilligan, A. T.; Papanikolas, J. M.; Schanze, K. S., Light-Harvesting Polymers: Ultrafast Energy Transfer in Polystyrene-Based Arrays of Pi-Conjugated Chromophores. *J Phys Chem B* **2014**, *118*, 372-378.
32. Yeow, E. K. L.; Ghiggino, K. P.; Reek, J. N. H.; Crossley, M. J.; Bosman, A. W.; Schenning, A. P. H. J.; Meijer, E. W., The Dynamics of Electronic Energy Transfer in Novel Multiporphyrin Functionalized Dendrimers: A Time-Resolved Fluorescence Anisotropy. *J Phys Chem B* **2000**, *104*, 2596-2606.
33. Kleiman, V. D.; Melinger, J. S.; McMorro, D., Ultrafast Dynamics of Electronic Excitations in a Light-Harvesting Phenylacetylene Dendrimer. *J Phys Chem B* **2001**, *105*, 5595-5598.
34. Akselrod, G. M.; Deotare, P. B.; Thompson, N. J.; Lee, J.; Tisdale, W. A.; Baldo, M. A.; Menon, V. M.; Bulovic, V., Visualization of Exciton Transport in Ordered and Disordered Molecular Solids. *Nat Commun* **2014**, *5*.
35. Bredas, J. L.; Beljonne, D.; Coropceanu, V.; Cornil, J., Charge-Transfer and Energy-Transfer Processes in Pi-Conjugated Oligomers and Polymers: A Molecular Picture. *Chem Rev* **2004**, *104*, 4971-5003.
36. Banerji, N.; Cowan, S.; Vauthey, E.; Heeger, A. J., Ultrafast Relaxation of the Poly(3-Hexylthiophene) Emission Spectrum. *J Phys Chem C* **2011**, *115*, 9726-9739.
37. Hintschich, S. I.; Dias, F. B.; Monkman, A. P., Dynamics of Conformational Relaxation in Photoexcited Oligofluorenes and Polyfluorene. *Phys Rev B* **2006**, *74*, 045210-045219.

38. Nelson, T.; Fernandez-Alberti, S.; Roitberg, A. E.; Tretiak, S., Nonadiabatic Excited-State Molecular Dynamics: Modeling Photophysics in Organic Conjugated Materials. *Accounts Chem Res* **2014**, *47*, 1155-1164.
39. Hwang, I.; Scholes, G. D., Electronic Energy Transfer and Quantum-Coherence in Pi-Conjugated Polymers. *Chem Mater* **2011**, *23*, 610-620.
40. Bredas, J. L.; Heeger, A. J., Theoretical Investigation of Gas-Phase Torsion Potentials Along Conjugated Polymer Backbones - Polyacetylene, Polydiacetylene, and Polythiophene. *Macromolecules* **1990**, *23*, 1150-1156.
41. Chen, H. L.; Huang, Y. F.; Lim, T. S.; Su, C. H.; Chen, P. H.; Su, A. C.; Wong, K. T.; Chao, T. C.; Chan, S. I.; Fann, W., Excited-State Backbone Twisting of Polyfluorene as Detected from Photothermal after-Effects. *J Phys Chem B* **2009**, *113*, 8527-8531.
42. Wells, N. P.; Blank, D. A., Correlated Exciton Relaxation in Poly(3-Hexylthiophene). *Physical review letters* **2008**, *100*, 086403-086406.
43. Busby, E.; Carroll, E. C.; Chinn, E. M.; Chang, L. L.; Moule, A. J.; Larsen, D. S., Excited-State Self-Trapping and Ground-State Relaxation Dynamics in Poly(3-Hexylthiophene) Resolved with Broadband Pump-Dump-Probe Spectroscopy. *J Phys Chem Lett* **2011**, *2*, 2764-2769.
44. Westenhoff, S.; Beenken, W. J. D.; Friend, R. H.; Greenham, N. C.; Yartsev, A.; Sundstrom, V., Anomalous Energy Transfer Dynamics Due to Torsional Relaxation in a Conjugated Polymer. *Physical review letters* **2006**, *97*, 166804-166807.
45. Heimel, G.; Daghofer, M.; Gierschner, J.; List, E. J. W.; Grimdsale, A. C.; Mullen, K.; Beljonne, D.; Bredas, J. L.; Zojer, E., Breakdown of the Mirror Image Symmetry in the Optical Absorption/Emission Spectra of Oligo(Para-Phenylene)S. *J. Chem. Phys.* **2005**, *122*, 54501-54511.
46. Wang, L.; Puodziukynaite, E.; Vary, R. P.; Grumstrup, E. M.; Walczak, R. M.; Zolotarskaya, O. Y.; Schanze, K. S.; Reynolds, J. R.; Papanikolas, J. M., Competition between Ultrafast Energy Flow and Electron Transfer in a Ru(II)-Loaded Polyfluorene Light-Harvesting Polymer. *J Phys Chem Lett* **2012**, *3*, 2453-2457.
47. Wang, L.; Puodziukynaite, E.; Grumstrup, E. M.; Brown, A. C.; Keinan, S.; Schanze, K. S.; Reynolds, J. R.; Papanikolas, J. M., Ultrafast Formation of a Long-Lived Charge-Separated State in a Ru-Loaded Poly(3-Hexylthiophene) Light-Harvesting Polymer. *J Phys Chem Lett* **2013**, *4*, 2269-2273.
48. Puodziukynaite, E.; Wang, L.; Schanze, K. S.; Papanikolas, J. M.; Reynolds, J. R., Poly(Fluorene-Co-Thiophene)-Based Ionic Transition-Metal Complex Polymers for Solar Energy Harvesting and Storage Applications. *Polym Chem-Uk* **2014**, *5*, 2363-2369.
49. Morseth, Z. A.; Pho, T. V.; Gilligan, A. T.; Dillon, R. J.; Schanze, K. S.; Reynolds, J. R.; Papanikolas, J. M., Role of Macromolecular Structure in the Ultrafast Energy and Electron Transfer Dynamics of a Light-Harvesting Polymer. *J Phys Chem B* **2016**, *120*, 7937-7948.

50. Leem, G.; Morseth, Z. A.; Puodziukynaite, E.; Jiang, J.; Zhen, F.; Gilligan, A. T.; Reynolds, J. R.; Papanikolas, J. M.; Schanze, K. S., Light-Harvesting and Charge-Separation in a Pi-Conjugated Antenna Polymer Bound to Tio₂. *J. Phys. Chem. C*. **2014**, *118*, 28535-28541.

CHAPTER 2. ROLE OF MACROMOLECULAR STRUCTURE IN THE ULTRAFAST ENERGY AND ELECTRON TRANSFER DYNAMICS OF A LIGHT-HARVESTING POLYMER

This chapter previously appeared as an article in the Journal of Physical Chemistry B. The original citation is as follows: Morseth, Z.A.; Pho, T.V.; Gilligan, A.T.; Dillon, R.J.; Schanze, K.S.; Reynolds, J.R.; Papanikolas, J.M.; *J. Phys. Chem. B.*, 2016, *120*, 7937-7948.

2.1 INTRODUCTION

One strategy towards the realization of molecular materials capable of solar fuels production is the design of complex macromolecular structures whose underlying architecture facilitates efficient excited-state transport, charge separation, and catalytic functions by combining a series of basic energy transfer (EnT) and electron transfer (ET) events.^{1,2} While the fundamentals of EnT and ET have been well-studied in model systems where the parameters that influence the transfer rate (e.g. distance, orientation, and free energy) are known, multichromophoric systems present new distinct challenges.³ The structural disorder results in a distribution of donor-acceptor separations, which in turn leads to a distribution of transfer rates. Furthermore, the presence of multiple acceptors give rise to parallel quenching pathways, and structural fluctuations can couple transport phenomena with low-frequency, large-scale conformational motions.⁴ The result of this dynamical complexity is oftentimes multimodal kinetics that requires the incorporation of structural information into the analysis of transient experiments in order to reach clear and meaningful conclusions.

The approach used in our group combines structural information from molecular simulations (e.g. Monte Carlo or molecular dynamics) with kinetic network models composed of the individual energy and electron transfer events to describe the photoinduced dynamics of functionalized

polymers. Early work from our group examined site-to-site excited state energy transport in macromolecular assemblies consisting of multiple pendant Ru(II) complexes linked together by a polystyrene chain (pS-Ru).⁵ In that work, coarse-grained Monte Carlo simulations provided an ensemble of structures that were then used as input into a stochastic kinetic model. More recent efforts have examined Ru(II) loaded assemblies based on π -conjugated polymers, including poly(fluorene) (pF),⁶ poly(thiophene) (pT),⁷ and poly(fluorene-co-thiophene) (pFT, pF2T)⁸. Structural modeling of these systems is more challenging compared to pS-Ru, however. Whereas the dense packing in the pS-Ru system made it possible to model the macromolecular structure using a relatively simplistic potential (i.e. freely-rotating chains, hard spheres, continuum solvent), the more rigid polymer structure and lower chromophore density requires more sophisticated potentials and explicit solvent representation.

We report here a combined experimental and theoretical effort to characterize the EnT and ET processes occurring within a light harvesting polymer assembly based on a pF polymer functionalized with pendant isoindigo (iI) chromophores (Figure 2.1A) in dichloromethane (DCM) solution. Ultrafast transient absorption spectroscopy shows that excitation of the π -conjugated backbone in pF-iI is followed by quenching of the polymer excited state on the fs-ps time scale through a combination of EnT to produce iI*, and ET to form a charge-separated state consisting of a reduced isoindigo (iI⁻) and a positive polaron on the polymer. A detailed microscopic picture of the quenching dynamics is developed by combining the spectroscopic experiments with large-scale computer simulation. Fully-atomistic molecular dynamics (MD) simulations of the assemblies in explicit solvent indicate that the pF-iI assembly adopts complex macromolecular structures in which the pendant groups extend into the solvent at the end of their flexible tethers (Figure 2.1B). These structures are then used as input into a kinetic model that

accounts for the primary dynamical events (i.e., energy transfer, excited-state relaxation, electron transfer, and charge recombination). Several underlying themes emerge from the simulations that illustrate the intricate details governing the quenching dynamics. Large spectral overlap between the polymer emission and pendant absorption bands ensure efficient, long-range resonant EnT to the pendants. However, the macromolecular structure, which dictates the distances and orientations of the pendants in relation to the backbone, also plays a profound role. In structures where the side chains are bent back towards the backbone, ET dominates while in open structures where the side chains are extended away from the backbone, the quenching proceeds primarily by EnT. The presence of two dynamic quenching regimes stems from the distance dependence for EnT and ET. For ET, the large electronic coupling and subsequent exponential falloff of the electronic coupling with distance restricts ET to short donor-acceptor separations, while for EnT the R^{-6} dependence on distance enables efficient energy transfer to a wide range of donor-acceptor separations. Although the donor-acceptor separation strongly governs the overall quenching rate, the orientation of the pendant in relation to the backbone is also a significant factor. In the pF-iI assemblies, the side chain structure leads to a significant number of molecular configurations in which the orientation of the nearest pendant is unfavorable for EnT. In these configurations, the overall EnT quenching rate is spread amongst multiple acceptors that lie further from the backbone. The combination of ultrafast spectroscopy and computer simulations provide insight into the excited-state quenching dynamics and the relationship to the macromolecular structure of the light-harvesting polymer.

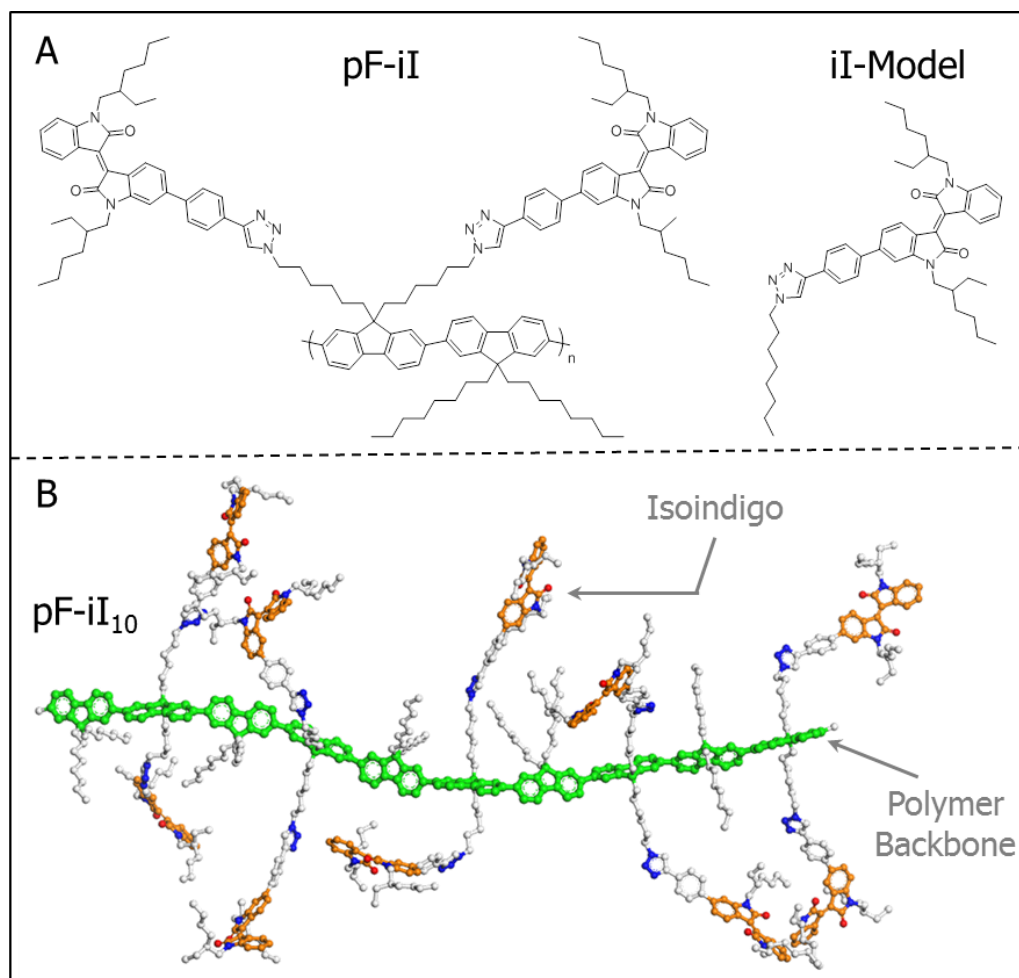


Figure 2.1. (A) Chemical structures of the pF-iI repeat unit and iI-Model. (B) Snapshot of a pF-iI₁₀ polymer assembly from fully atomistic molecular dynamics simulations in explicit dichloromethane solvent. The polymer backbone is depicted in green and the iI pendants in orange. The solvent is excluded for clarity.

2.2 EXPERIMENTAL METHODS

2.2.1. Sample Preparation

All spectroscopic experiments were performed in spectroscopic grade dichloromethane. Ground-state absorption and emission measurements were performed in 1 cm quartz cuvettes whereas transient measurements were performed in 2 mm quartz cuvettes in sufficiently dilute solution (optical density (OD) between 0.3 and 0.4 at the excitation wavelength) to minimize interchain effects. All samples were sparged with argon for 20 minutes and sealed prior to use.

2.2.2. Steady State Techniques

UV-Visible spectra were recorded on an HP 8543 Diode Array Spectrophotometer. UV-Visible spectra were recorded on all samples before and after excited state measurements to ensure that samples did not undergo photodecomposition.

Emission spectra were measured on Photon Technology International (PTI 4SE-NIR) Quantamaster™ spectrofluorometer equipped with a continuous xenon arc lamp as the excitation source. The emitting light was collected at 90° to the excitation beam and detected by a Multi-mode 814 photomultiplier tube (PMT) in photon counting mode (digital).

2.2.3. Time-Resolved Emission Spectroscopy

Time-resolved emission measurements of the pF homopolymer in DCM were performed with a Coherent Chameleon laser system and a Hamamatsu streak camera. The laser fundamental was tuned to 775 nm and pulse-picked to 1.7 MHz. The power was attenuated using a Conoptics 350-80 Electro-Optic Modulator. The 775 nm output was frequency doubled with a BBO crystal and the residual fundamental was removed with a BG40 colored glass bandpass filter. Experiments were performed with magic angle detection using a calcite polarizer on the 388 nm excitation beam and a wire-grid polarizer on the fluorescence signal. A 400 nm dielectric long pass filter was used

on the fluorescence signal to remove any pump scatter. Samples were contained in a sealed 2 mm fused silica cuvette and degassed with argon for 10 minutes prior to measurements. The concentration of the solution was adjusted such that it had a maximum absorbance of 0.1 in the 2 mm cuvette.

2.2.4. Transient Absorption Spectroscopy

Femtosecond-picosecond transient absorption measurements were performed using a home-built transient absorption spectrometer. The spectrometer is based on a commercially available ultrafast laser system (Clark MXR CPA-2210). The system consists of an erbium-doped fiber ring oscillator pumped by a solid-state fiber coupled laser diode operating at 980 nm and a chirped pulse Ti:Sapphire regenerative amplifier pumped by a frequency-doubled, Q-switched Nd:YAG laser. Following pulse compression, the amplifier produces pulses centered at 775 nm with 120 fs fwhm duration at 1 kHz with pulse energies of 1.6 mJ/pulse.

The amplified output is initially split into two fractions, where the larger fraction (80%) is further split to pump several optical parametric amplifiers (OPA) for frequency tunability. 50% (650 μ J/pulse) of this fraction pumps a collinear near-IR OPA (White Light Conversion TOPAS-C) that is tuned to 1070 nm and mixed with the residual fundamental in a 1 mm thick BBO crystal to produce 450 nm pulses by sum-frequency generation with energies of approximately 1 μ J/pulse. A smaller portion (20%) is used to drive a home-built collinear near-IR OPA tuned to 1200 nm. The femtosecond probe pulse is generated by focusing either the 1200 nm signal output or 775 nm fundamental (5 μ J/pulse) into a translating 5 mm thick CaF₂ window, giving spectral coverage across the visible region. The smaller fraction of the amplifier output (20%) is further split using a 90:10 window, where the larger fraction is frequency doubled in a 1 mm BBO crystal and coupled into a home-built, hollow fiber waveguide filled with argon at 20 psig for spectral broadening.

Prism compression results in 388 nm pump pulses (200 nJ/pulse) with a duration of approximately 35 fs fwhm.

The pump beam is directed through a mechanical chopper to modulate between pump-on and pump-off spectra and focused onto the sample using a 300 mm lens. The probe beam is focused and overlapped with the pump pulse using a 250 mm spherical aluminum mirror. After the sample, the probe beam is dispersed by a 0.15 m spectrograph with a 600 g/mm grating and detected on a diode array. Time-resolved spectra were collected by varying the delay between pump and probe pulses using a computer controlled delay stage with a resolution of 1 μ m. Spectra were collected on a shot-by-shot (1 kHz) basis over the range of 350 to 820 nm with a sensitivity of up to 0.1 mOD. The angle between the pump and probe polarization vectors was set to magic angle ($\sim 54.7^\circ$) to avoid polarization effects and ensure that only excited-state population dynamics were being monitored. The sample was stirred with a magnetic stirrer to provide for a fresh sample volume between laser pulses and a steady-state absorbance spectrum was acquired before and after transient experiments to confirm the absence of photoproduct formation. Following data collection, the frequency chirp in the probe pulse was characterized using the optical Kerr response of liquid CCl_4 in a 2 mm cuvette in a polarization gating geometry. The spectra were chirp corrected using a data processing program written in LabVIEW.

2.2.5. Electronic Structure Calculations

The ground-state geometry of the iI-Model complex was optimized using the B3LYP DFT functional and the 6-31G** basis sets, as implemented in Gaussian09 (v09e01).¹ Solvation effects for dichloromethane (DCM) were included with a polarizable continuum model in Gaussian. A vibrational analysis was performed to verify that the optimized structure was at a potential energy minimum.

Time-dependent density functional theory (TD-DFT) calculations were performed on the optimized ground-state geometry using the B3LYP DFT functional and the 6-31G** basis sets, as implemented in Gaussian09 (v09e01), with solvation effects for dichloromethane included with a polarizable continuum model. A total of 10 singlet states were computed.

2.3 RESULTS AND DISCUSSION

2.3.1 Synthesis of pF-iI Polymer Assembly

The pF-iI₄₀ polymer assembly has 20 repeat units ($M_n = 39.4$ kDa), with each consisting of two fluorene monomers – one of which is functionalized with two isoindigo (iI) chromophores and the other with two C₈ alkyl chains (Figure 2.1). The synthesis of the pF-iI polymer followed a route analogous to our previously reported Ru^{II} chromophore-loaded polymers,^{6,7} where an alkyne-terminated chromophore is attached to azide-functionalized polymer backbones via “Click” chemistry. The alkyne-terminated isoindigo was prepared via a Stille coupling of 6-bromo-*N,N'*-(2-ethylhexyl)-isoindigo⁹ with trimethyl((4-(trimethylstannyl)phenyl)ethynyl)silane,^{10,11} and the trimethylsilyl group was subsequently deprotected via treatment with basic methanol. Azide-functionalized poly(fluorene)⁶ was then coupled to the isoindigo unit via a Cu-catalyzed Click reaction to afford the poly(fluorene)-isoindigo adduct (pF-iI) (Figure 2.1A). The completion of the reaction was monitored by the disappearance of the azide groups by FTIR spectroscopy, and ¹H NMR spectroscopy revealed the quantitative conversion of the azide groups to triazole moieties. Finally, a control isoindigo compound (iI-Model) was synthesized via a Click reaction between 1-azidooctane¹² and the alkyne-terminated isoindigo.

2.3.2 Static Spectroscopy

The ground-state absorbance spectrum of the pF-iI assembly in DCM solution extends from 350 to 650 nm and exhibits three primary absorption features. The low energy transitions at 410 nm and 520 nm correspond to $\pi \rightarrow \pi^*$ absorptions on the isoindigo subunits, while the intense absorption at 395 nm largely results from $\pi \rightarrow \pi^*$ excitation of the pF backbone. The absorbance spectrum for the pF-iI assembly is well-described by a superposition of the constituent spectra,

indicating that the electronic structure of the polymer and isoindigo pendants are not significantly perturbed upon formation of the assembly (Figure 2.2).

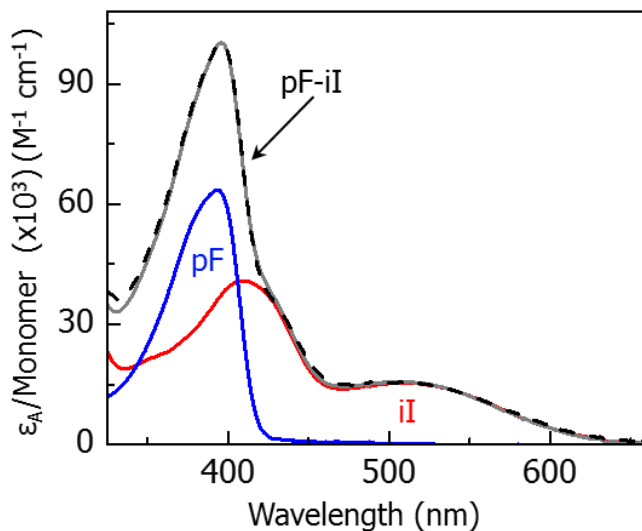


Figure 2.2. Ground state absorbance spectra of the pF-iI assembly (dark grey), pF (blue), and iI-Model (red) in room temperature DCM solution. Also shown is the superposition of the iI-Model and pF absorbance spectra (dashed black).

2.3.3 Ultrafast Spectroscopy

2.3.3.1. Isoindigo Excited-State Dynamics

Photoexcitation of iI into the low energy absorption band produces a short-lived, non-emissive excited state,^{13,14} whose transient absorption spectra are comprised of two ground-state bleach (GSB) features centered at 410 and 520 nm, as well as a broad excited state absorption (ESA) that extends across the visible and near-infrared (Figure 2.4A). The spectrum decays rapidly with simultaneous loss of the ESA (750 nm) and GSB (400 nm) features, which occurs with single-exponential kinetics ($\tau \sim 5$ –7 ps), consistent with similar isoindigo complexes.¹⁵ Given the underlying structural similarity to trans-stilbene, it has been proposed that the rapid excited-state

decay in iI occurs through a conical intersection that is accessed through rotation about the central ethylene bond.¹⁴ This hypothesis is supported by density functional theory (DFT) and time-dependent density functional theory (TD-DFT) calculations, which show that the $\pi \rightarrow \pi^*$ excitation likely weakens this bond by shifting electron density from the C=C bond at its core into the rest of the π framework (Figure 2.3).

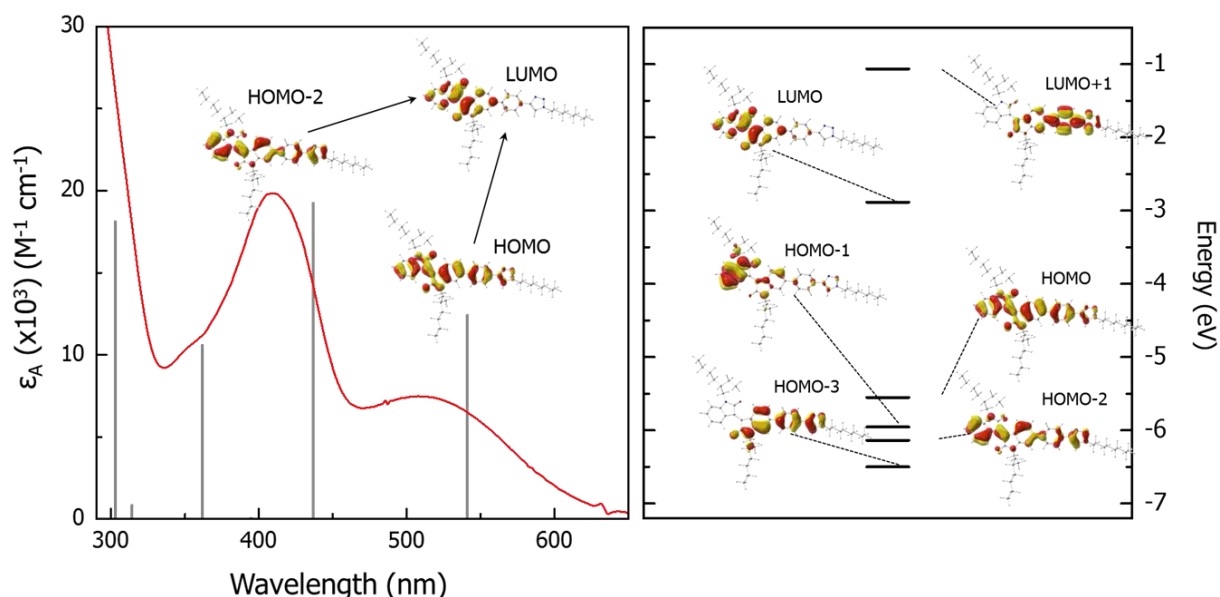


Figure 2.3. (Left) Absorbance spectrum of iI-Model complex in DCM (red) and theoretical transitions predicted from TD-DFT calculations (gray bars). The primary orbitals corresponding to each transition are also shown for the dominant visible transitions. (Right) Calculated isodensity plots of the frontier molecular orbitals (LUMO+1, LUMO, HOMO, HOMO-1, HOMO-2, and HOMO-3) of the iI-Model complex (isodensity value = 0.03).

While passage through a conical intersection may explain the rapid excited state decay, complete rotation to form the cis-isomer does not appear to take place to any significant extent, as evidenced by the lack of new absorption bands in the transient spectra, suggesting that the crossing

point lies closer to the trans-isomer along the bond rotation coordinate. The excited-state dynamics of the iI pendants embedded in the pF-iI assembly are remarkably similar to the iI-Model, both in the shape of the transient spectra (Figure 2.4B) and their rate of decay ($\tau=5\text{-}6$ ps) (Figure 2.4C), providing further evidence that the iI electronic structure remains unchanged upon incorporation into the pF-iI assembly.

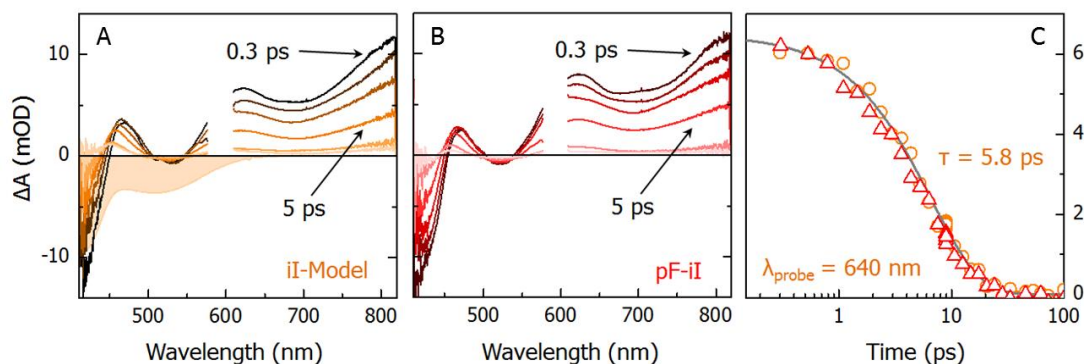


Figure 2.4. Femtosecond transient absorption spectra following photoexcitation at 595 nm (150 fs, 280 nJ with a 120 μm spot size) in DCM at 0.3, 1, 2, 5, 15, and 20 ps for iI-Model (A) and pF-iI (B). Also shown in (A) is the inverted ground-state absorbance spectrum of iI-Model in DCM, normalized to the 410 nm GSB (shaded orange) (C) Decays of the transient signals at 640 nm for iI-Model (orange circles) and pF-iI (red triangles). Both transients exhibit single exponential decays with $\tau = 5.8 \pm 0.1$ ps. All spectra were measured in argon saturated DCM solution at room temperature.

2.3.3.2. *Energy and Electron Transfer Quenching of the Polymer Excited State*

Transient absorption spectra obtained from the unfunctionalized pF polymer and the pF-iI assembly following 388 nm excitation are displayed in Figure 2.5. At early pump-probe delays, the pF transient spectra (Figure 2.5A) are characterized by a structured, negative-going feature in the blue that results from a combination of GSB and stimulated emission (SE), as well as a broad, intense ESA extending through the red wavelengths that is ascribed to the singlet exciton absorption ($S_1 \rightarrow S_n$).¹⁶ The conjugated polymer gives rise to a much more intense photoresponse compared to the iI pendants, with the intensity of the pF* transient absorption signal being about 10 times greater than the iI* spectrum obtained under similar conditions. Close inspection of the SE feature (Figure 2.5D) shows that it red-shifts as the pump-probe delay increases, which reflects evolution of the exciton due to conformational rearrangements and interchain excitonic energy transfer (EET) to lower energy sites (i.e., longer conjugation lengths).^{16,17} The spectral shift is accompanied by a decrease in intensity of both the SE and ESA features, which decay with $\tau_1=25$ ps and $\tau_2=325$ ps. The longer component is close to the pF* excited state lifetime (329 ps) determined from the singlet exciton decay at 780 nm and time-resolved emission measurements (Figure 2.6). Although the pF-iI spectra at early times are similar to those observed for pF, the subsequent evolution of the spectra in the two systems are considerably different (Figure 2.5B). The SE feature in pF-iI decays completely in the first 5 ps, about 100 times faster than the lifetime of the pF polymer (Figure 2.5F). There are a number of potential mechanisms that could be responsible for the rapid quenching of the pF* excited state. One possibility involves the interaction of two (or more) excited states on the same chain. This possibility can be eliminated, however, since the transients are independent of pulse energy at the fluences used, indicating that the observed dynamics are a result of single photon absorptions.

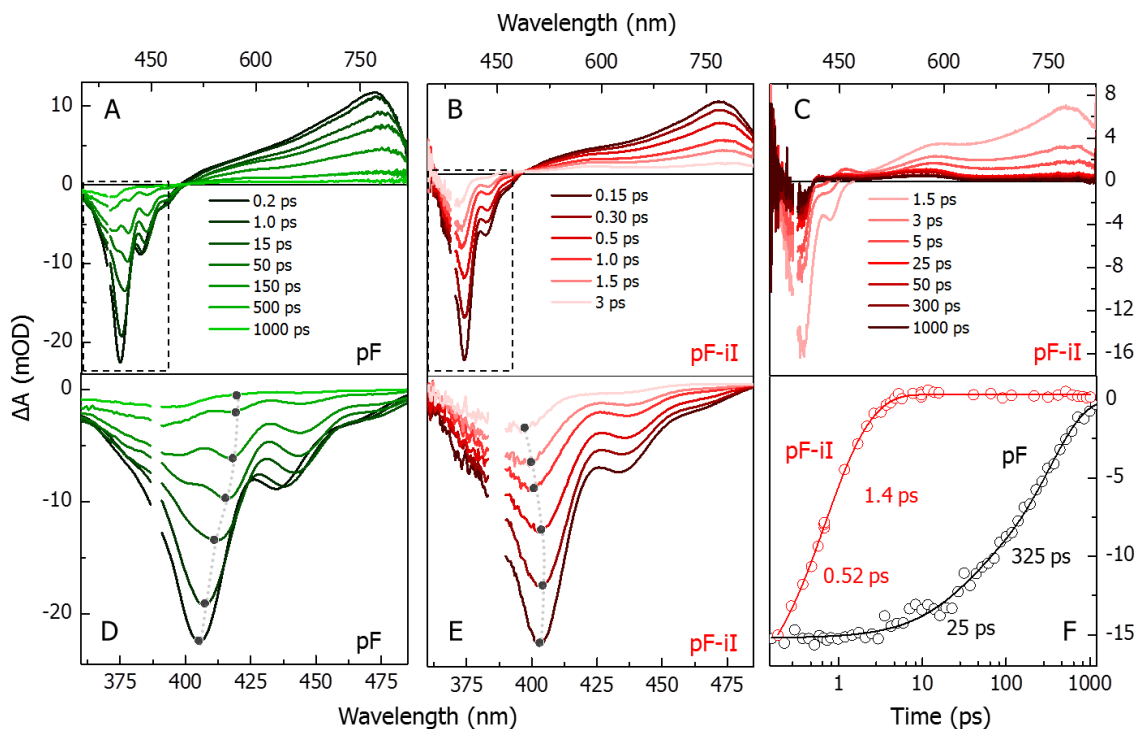


Figure 2.5. (A) Transient absorption spectra of pF in DCM at 0.2, 1, 15, 50, 150, 500, and 1000 ps. Excitation was at 388 nm and the pulse energy was 10 nJ/pulse. (B) Transient absorption spectra of pF-iI in DCM at 0.15, 0.3, 0.5, 1, 1.5, and 3 ps. Excitation was at 388 nm and the pulse energy was 60 nJ/pulse. (C) Transient absorption spectra of pF-iI in DCM at 1.5, 3, 5, 25, 50, 300, and 1000 ps. (D) Evolution of the pF SE bands, as indicated in (A). (E) Evolution of the SE bands in pF-iI, as indicated in (B). (F) Comparison of the decays of the transient signals at 440 nm for pF-iI (red circles) and pF (black circles) show significant quenching of pF* in pF-iI within 10 ps of excitation. Both exhibit bi-exponential decays: pF-iI ($\tau_1 = 0.52 \pm 0.1$ ps and $\tau_2 = 1.4 \pm 0.2$ ps) and pF ($\tau_1 = 25 \pm 5$ ps and $\tau_2 = 325 \pm 15$ ps).

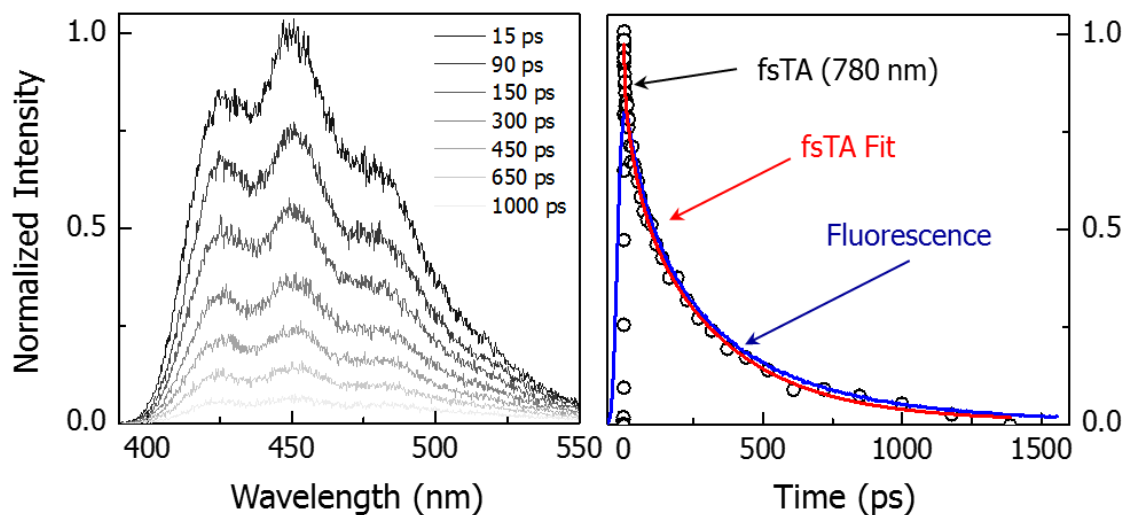


Figure 2.6. (Left) Time-resolved fluorescence spectra of the unfunctionalized pF homopolymer in argon saturated DCM following 388 nm excitation. (Right) Singlet lifetime of the unfunctionalized pF homopolymer following 388 nm excitation. The fsTA transient at 780 nm (black circles) and tri-exponential fit (red line) are shown along with the scaled time-resolved fluorescence decay integrated across the 400-550 nm wavelength region (blue line).

Instead, the rapid quenching of the pF^* is attributed to a combination of EnT and ET quenching. The pF-iI transient absorption spectra decay in amplitude during the first 1 ps, but do not show significant changes in shape, consistent with rapid EnT of the pF^* excited state to give the weaker absorbing iI^* , i.e. $pF^* + iI \rightarrow pF + iI^*$. In addition, the 400 nm bleach and 575 nm absorption features observed at later times do not resemble the bands in the transient spectra of either the pF^* produced by photoexcitation, or the iI^* resulting from EnT. Instead, spectroelectrochemistry suggests that these spectral features correspond to a charge-separated (CS) state formed by ET quenching of the pF^* to give a positive polaron on the pF and a reduced iI pendant, i.e. $pF^* + iI \rightarrow pF^+ + iI^-$ (Figure 2.7).

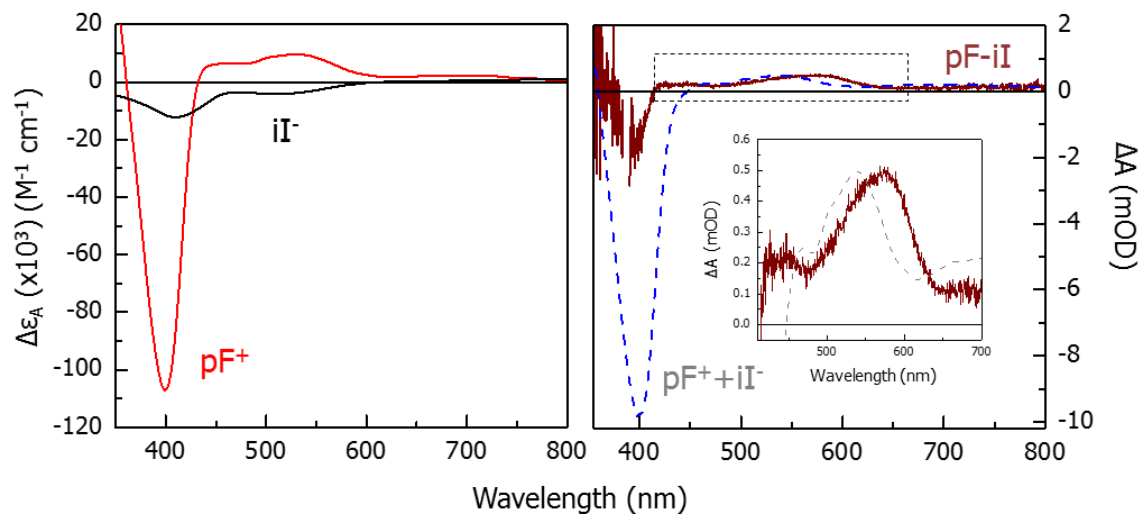


Figure 2.7. (Left) Spectroelectrochemical difference spectrum of iI^- (black) and pF^+ (red) following quantitative reduction and oxidation, respectively. The pF^+ spectrum has been scaled by a factor of 4.5 to account for the polaron length resulting from oxidation of the pF backbone. (Right) Predicted spectrum for the CS state obtained by adding the pF^+ and iI^- difference spectra (grey dashed line) scaled to match the 1000 ps spectra following excitation of $pF-iI$ at 388 nm (dark red line). Shown in the inset is a zoomed in view of the pF^+ absorption, as indicated by the black dashed line.

2.3.3.3. Spectral Modeling of the pF-iI Spectra

Given the presence of both EnT and ET quenching, the pF-iI transient spectra at time Δt_i ($\Delta A_{pF-iI}(\Delta t_i)$) can be represented by a superposition of three spectral components that correspond to the pF* ($\Delta \tilde{A}_{pF}(\Delta t_i)$), iI* ($\Delta \tilde{A}_{iI}$), and the CS ($\Delta \tilde{A}_{CS}$) states:

$$\Delta A_{pF-iI}(\Delta t_i) = C_{pF,t_i} \Delta \tilde{A}_{pF}(\Delta t_i) + C_{iI,t_i} \Delta \tilde{A}_{iI} + C_{CS,t_i} \Delta \tilde{A}_{CS}, \quad (2.1)$$

where C_{pF,t_i} , C_{iI,t_i} , and C_{CS,t_i} are the corresponding spectral amplitudes for each species at the time point t_i . The three component spectra were determined from experimental observation. The iI* contribution ($\Delta \tilde{A}_{iI}$) is given by the 1 ps spectrum of the iI-Model when excited at 388 nm and the spectrum of the CS state ($\Delta \tilde{A}_{CS}$) is represented by the pF-iI transient spectrum at 1000 ps (Figure 2.5C). Both were taken to be independent of time and normalized at 580 nm. The pF* spectra, on the other hand, show complicated spectral evolution that reflects the relaxation of the exciton. This evolution is most dramatic in the SE band in the blue region of the spectrum (400-480 nm), and for this reason we have limited the spectral modeling to the visible and near IR region (480–785 nm) where there are distinct spectral features associated with pF*, iI*, and the CS state. However, even in the near IR the pF* spectra exhibit spectral changes, albeit to a lesser degree. In order to account for this, the pF* component at Δt_i ($\Delta \tilde{A}_{pF}(t_i)$) is selected from experimentally observed pF* spectra, each of which was also normalized at 580 nm. The 0.2 ps spectrum of pF* is shown along with the iI* and CS spectral components in Figure 2.8A. The time-dependent coefficients of the three species (C_{pF,t_i} , C_{iI,t_i} , and C_{CS,t_i}) were then determined by fitting the transient spectra of the pF-iI assembly at each time delay to eq. 2.1.

The three coefficients show the time-evolution of the pF*, iI*, and CS state populations following photoexcitation of the pF-iI assembly (Figure 2.8). The decay of the pF* population

occurs with both fast ($\tau_1=0.7$ ps) and slow ($\tau_2=2.0$ ps) time components, and coincides with the growth of the iI^* and CS state populations that result from EnT and ET. The appearance of the iI^* component reflects the EnT pathway. It grows in with a time constant of 0.5 ps and reaches a maximum by about 3 ps. The iI^* formed by EnT decays rapidly ($\tau=8.2$ ps) and thus contributes minimally to the spectra after ~ 30 ps. Formation of the CS state by ET quenching is evident in even the earliest spectra, implying that a fraction of ET events occur within the instrument response (200 fs). The remaining fraction grows in over hundreds of femtoseconds and then decays with both fast (1.3 ps) and slow (600 ps) time components. Estimates of the driving force ($\Delta G_{CR}=-2.21$ eV) and solvent reorganization energy ($\lambda\sim 0.8$ eV) suggest that charge recombination lies deep within the Marcus inverted regime (Supporting Information), resulting in a recombination rate that is expected to be several orders of magnitude slower than charge separation.

While the slower component is consistent with inverted ET, the origin of the fast component is unclear. One possible explanation is that it arises when one of the iI pendants lies close to the backbone. In this scenario, weakened electrostatic screening in the non-polar DCM solvent gives rise to a strong Coulombic attraction between the pF^+ and iI^- formed by ET. This strong intermolecular interaction facilitates the formation of a stable contact ion-pair that that exhibits fast back electron transfer due to the strong electronic coupling. The role of contact ion pairs has also been implicated in the fast ET recombination dynamics observed in synthetic DNA hairpins in solvent environments with low effective dielectric constants.¹⁸

Similar (but opposite) solvent forces may also be responsible for the slower charge recombination ($\tau\sim 6$ ns) that is observed in the analogous pF -Ru assembly.^{6,7} While this order of magnitude difference cannot be rationalized by differences in the ET energetics (i.e. ΔG and λ), which are similar for the pF - iI and pF -Ru assemblies, it can be explained by the differences in the

solvent polarity. Whereas DCM is ineffective at screening the electrostatic interaction, the pF^+ and Ru^{I} are well-shielded by the polar nitrile solvents used in the pF-Ru studies.⁶ As a consequence, the solvent is more able to separate the electron and hole and this leads to a longer recombination time.

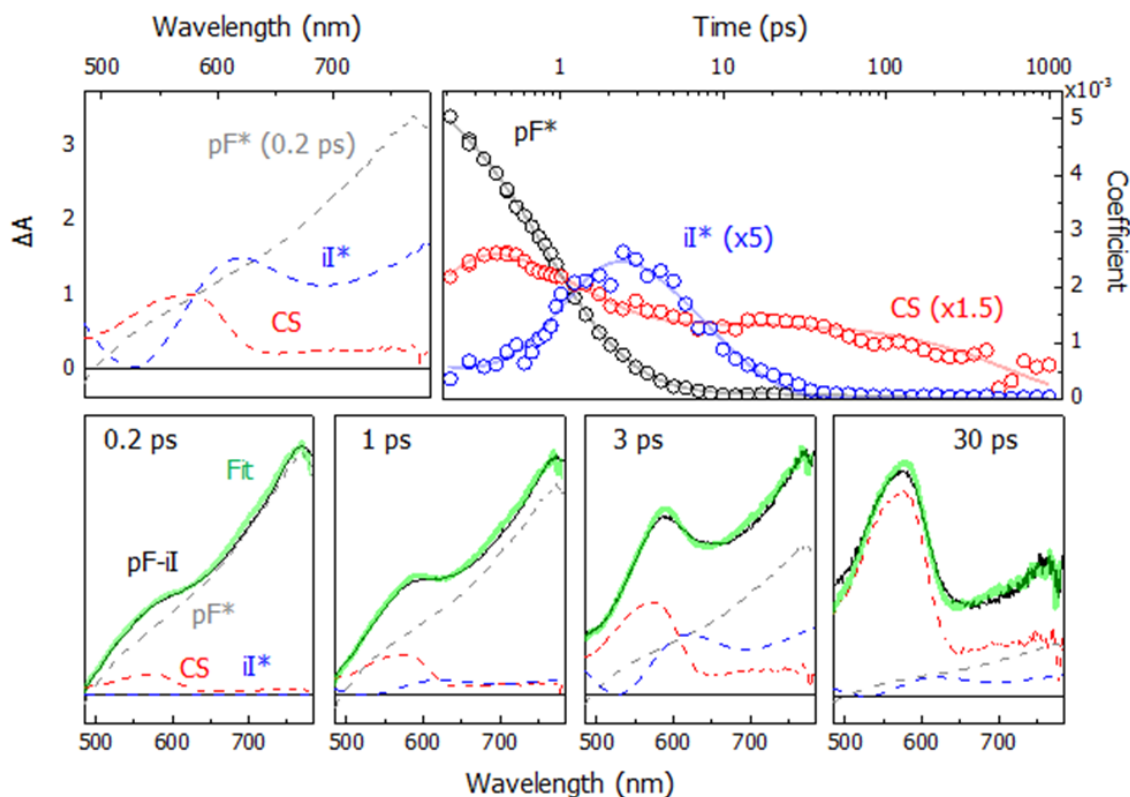


Figure 2.8. (Top, left) Spectral contributions from pF* (0.2 ps), iI*, and the CS state used in the spectral modeling, normalized at 580 nm. (Top, right) Time-resolved coefficients for pF* (black), iI* (blue), and the CS state (red) spectral contributions obtained from least-squares analysis of the modeled pF-iI transient absorption spectrum. The iI* and CS populations have been scaled for clarity. Overlaid on the pF* and iI* populations are bi-exponential fits while a tri-exponential fit is overlaid on the CS state population. (Bottom, left to right) Modeled pF-iI spectra at 0.2, 1, 3, and 30 ps with the modeled spectrum (green) overlaid on the pF-iI assembly spectrum (black). The individual spectral contributions for pF* (gray), iI* (blue), and the CS state (red) are shown as dashed lines.

2.3.4 Simulation of Excited State Quenching Dynamics

The photoinduced EnT and ET dynamics are characterized not by a single rate constant, but rather a distribution of rates that reflects the range of orientations and separations of the iI acceptors with respect to the location of the excitation along the pF backbone. We have developed a computational model of the quenching dynamics that combines structural information obtained from fully-atomistic MD simulation with a kinetic network simulation that describes the individual EnT and ET events between the photoexcited polymer and the iI pendants. Direct comparison of the simulation with experimental observation provides a means of parameterizing the kinetic model, and through analysis of the simulation results we obtain a microscopic view of the photoinduced dynamics that take place following photoexcitation.

2.3.4.1. *Macromolecular Polymer Structures*

Macromolecular structures of the pF-iI₁₀ assembly are obtained from MD simulation of the assembly in explicit DCM solvent (Figure 2.9). The simulation cell was constructed as follows. First, the geometry of the pF-iI monomer was optimized by DFT methods employing the B3LYP functional and the 6-31G** basis sets, as implemented in Gaussian09 (v09e01).¹⁹ Next, atomic charges obtained from a natural bond order (NBO) analysis were applied to the monomer unit and the pF-iI₁₀ polymer was constructed. The assembly was optimized in the absence of solvent using the Universal Force Field (UFF) and relaxed through a series of annealing cycles.²⁰ The annealed polymer chain was placed in a periodic simulation cell along with 2,500 DCM molecules and subjected to 6 annealing cycles in which the temperature was initially increased to 1200 K and after 60 ps was reduced back to 298 K for 20 ps. The structures obtained at the end of each annealing cycle were used as initial conditions for constant NVT molecular dynamics trajectories

with $T=298$ K. Dynamics were collected on each structure for a total of 1 ns with snapshots taken every 2.5 ps, resulting in an ensemble of 2,406 configurations.

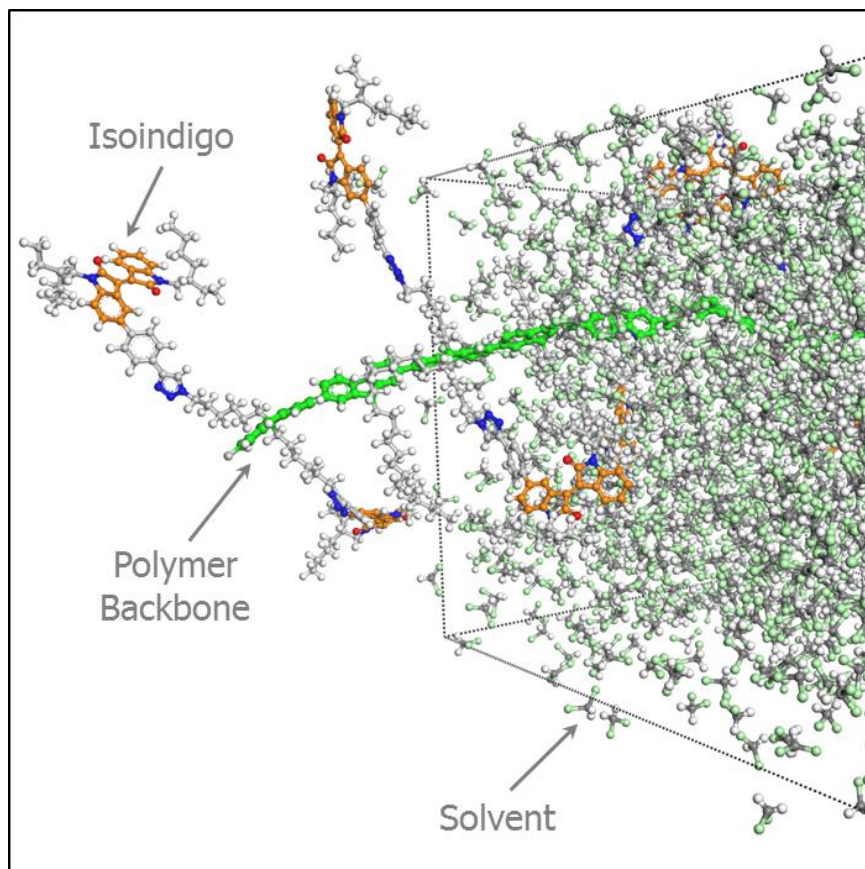


Figure 2.9. Snapshot of the orthorhombic ($100 \times 55 \times 55$ Å) simulation cell consisting of 10 fluorene monomers (green), 10 isoindigo pendants (orange), and 2,500 dichloromethane molecules used for molecular dynamics (MD) simulations of the pF-iI₁₀ polymer assembly. The MD simulations were collected on relaxed polymer structures for 1 ns with periodic boundary conditions.

The polymer assemblies adopt complex macromolecular structures where relatively low barriers to bond rotation between monomers results in significant twisting of the polymer chain (Figure 2.9). In addition, the large size of the fluorene monomer and the long side-chain tethers gives rise to a sparse packing of the pendants, and the resulting structures are characterized by a wide distribution of separations between the iI pendants and the polymer backbone (Figure 2.10).

Because the rates of EnT and ET depend sensitively on distance, quenching of the pF^* is dominated by iI chromophores that lie closest to the polymer. Analysis of the MD structures shows that the nearest iI pendant to a particular monomer (i.e., R_{NP}) lies between 9.6 Å and 21 Å from the polymer (Figure 2.10). The largest distances are constrained by the length of the hydrocarbon tether, while the shortest are the result of pendants whose side chains bend back towards the polymer backbone. As is discussed below, the macromolecular polymer structure plays a profound role in the overall quenching dynamics of the assembly.

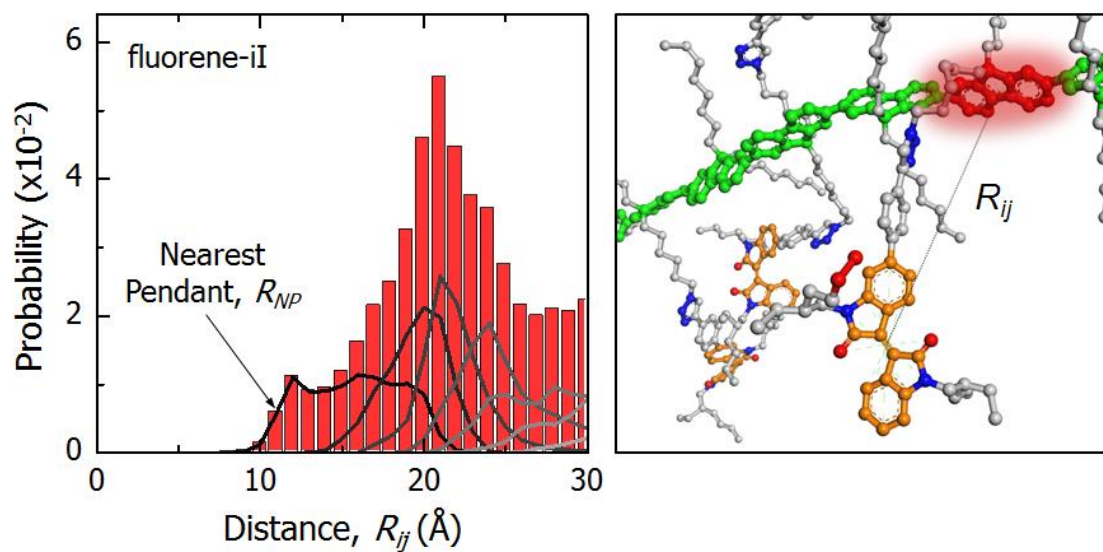


Figure 2.10. (Left) Distance distributions for fluorene-isoindigo from the ensemble of pF-iI polymer structures obtained from the MD simulations. The bars represent the total distribution while the lines represent the successive nearest acceptors. (Right) Illustration of the fluorene-isoindigo through-space distance (R_{ij}), where the distance is computed between centroids placed on each unit.

2.3.4.2. Kinetic Network

The excited state relaxation dynamics are described by a set of first order decay pathways that can be divided into five groups, indicated by the different colors in Scheme 2.1. The polymer excitation is centered at one of the pF monomer units (e.g. F_i) and relaxes back to its ground state (k_{pF^*}), or undergoes energy transfer (k_{EnT}) or electron transfer (k_{ET}) to one of the iI acceptors (e.g. iI_j , iI_{j+1} , iI_{j+2} , etc.), which are followed by either iI* excited state decay (k_{iI^*}) or charge recombination (k_{CR}), respectively. The rate constants associated with three of the groups (k_{pF^*} , k_{iI^*} , and k_{CR}) are determined from experimental observation and treated as fixed parameters (Table 2.1). Charge recombination is treated by assigning k_{CR} to be either $(1.3 \text{ ps})^{-1}$ ($k_{CR,fast}$) or $(600 \text{ ps})^{-1}$ ($k_{CR,slow}$) with probabilities determined by the amplitudes of the fast and slow components observed experimentally. The energy transfer and electron transfer rates (k_{EnT} and k_{ET}) are computed for each iI acceptor using structural information (i.e. distances and orientation) obtained from the MD configuration, as discussed in more detail below. Exciton migration along the pF backbone is excluded from the model based on the separation of time scales for $pF^* \rightarrow pF$ transport ($\sim 10\text{-}100 \text{ ps}$) and pF^* quenching ($\sim 1 \text{ ps}$).

Scheme 2.1. (Top) Depiction of the pF-iI₁₀ polymer assembly with the indices of the fluorene monomers (F_i) and the iI pendants (iI_j). (Bottom) Illustration of the kinetic network used to describe the photoinduced dynamics in the pF-iI polymer assemblies following excitation centered on a fluorene monomer.

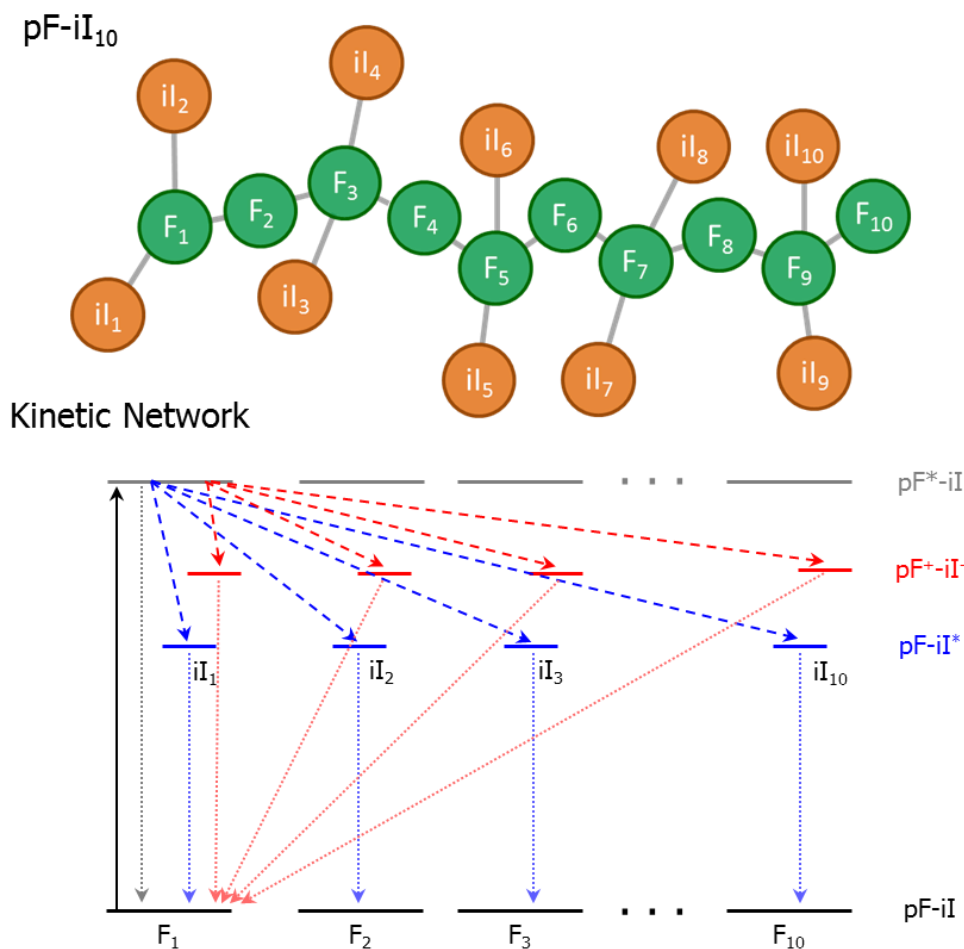


Table 2.1. Simulation parameters used in the kinetic modeling of pF-iI.

Kinetic Process	Simulation Parameter		Value	Origin
Energy Transfer (k_{ET})	pF* lifetime	τ_D	329 ps	fixed ^a
	pF* quantum yield	Φ_D	0.51	fixed ^a
	Orientation factor	κ_{ij}	-	MD ^b
	D-A separation	R_{ij}	-	MD ^b
Electron Transfer (k_{ET})	Attenuation Parameter	β	1.0 \AA^{-1}	fixed ^c
	Coupling	V_0	50 meV	adj. ^c
	Driving Force	ΔG^0	-0.76 eV	fixed ^a
	D-A separation	R_{ij}	-	MD ^b
	Reorganization Energy	λ	0.8 eV	MD ^b
pF* Excited State Decay	Decay Constant	k_{pF^*}	$(329 \text{ ps})^{-1}$	fixed ^a
Charge Recombination	Decay Constant	$k_{\text{CR,fast}}$	$(1.3 \text{ ps})^{-1}$	fixed ^a
		$k_{\text{CR,slow}}$	$(600 \text{ ps})^{-1}$	fixed ^a
iI* Excited State Decay	Decay Constant	k_{iI^*}	$(5.8 \text{ ps})^{-1}$	fixed ^a

^aMeasured experimentally and treated as fixed parameter in simulation

^bCalculated from MD structure.

^cDetermined by fit of kinetic simulation to transient absorption data.

2.3.4.3. Energy Transfer

The rate constant for resonant energy transfer ($k_{EnT,ij}$) from the polymer excited state (donor) centered on the i^{th} fluorene monomer unit (F_i) to the j^{th} pendant isoindigo (acceptor) (iI_j) is given by the Förster expression:

$$k_{EnT,ij} = A \frac{\Phi_D \kappa_{ij}^2}{\tau_D R_{ij}^6} \int_0^\infty F_D(\lambda) \epsilon_A(\lambda) \lambda^4 d\lambda \quad (2.2a)$$

where τ_D and Φ_D are the lifetime and quantum yield of the donor, respectively, and A is constant given by $A = 9000(\ln 10) / 128 \pi^5 n^4 N_A$, where n is the refractive index of the medium and N_A is Avogadro's number. The integral describes the product of the emission spectrum of the donor (normalized to unity area) and the absorption spectrum of the acceptor, where the integrand for the pF-iI assembly is illustrated in Figure 2.11.

The rate of energy transfer is also sensitive to the through space donor-acceptor distance (R_{ij}) and relative orientations of the donor and acceptor transition dipoles (κ_{ij}), both of which are determined from the assembly structures obtained by MD simulation. The donor-acceptor separation (R_{ij}) is measured from the center of F_i to the midpoint of the C=C bond in the iI_j , and κ_{ij}^2 is given by

$$\kappa_{ij}^2 = (\cos \theta_{ij} - 3 \cdot \cos \delta_i \cos \gamma_j)^2 \quad (2.2b)$$

where θ_{ij} is the angle between the transition dipoles of the polymer (μ_D) and iI (μ_A) chromophores, and δ_i and γ_j are the angles between μ_D and μ_A and a vector joining the dipoles, respectively. In evaluating κ_{ij}^2 , μ_D is oriented parallel to the polymer backbone, while μ_A is directed along the C=C bond between the 6 and 6' carbons in the iI.²¹ It is important to note that all of the parameters

needed to calculate $(k_{ET,ij})$ using Eqn. 2.2a are determined either from experiment or extracted from the MD simulation.

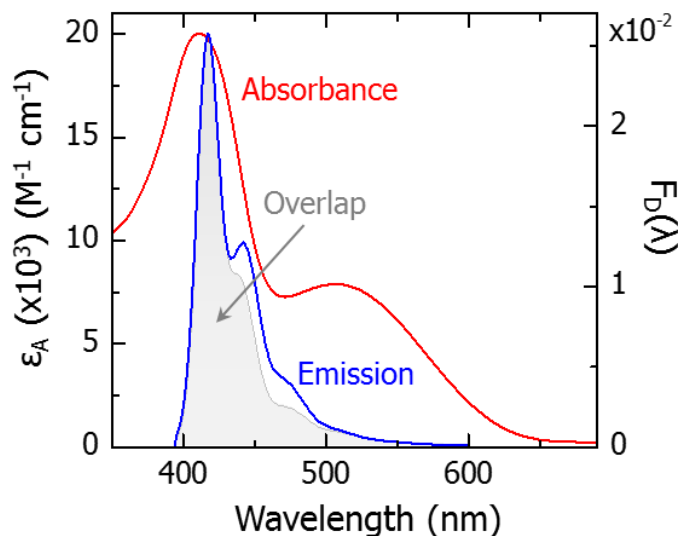


Figure 2.11. iI-Model absorbance (red) and pF emission spectrum (blue) normalized to unity area showing the scaled Förster overlap integrand shaded in gray.

2.3.4.4. Electron Transfer

The rate constant for electron transfer $(k_{ET,ij})$ between the F_i monomer unit and the iI_j pendant is computed using

$$k_{ET,ij} = \sqrt{\frac{\pi}{\hbar^2 \lambda k_B T}} |H_{ij}|^2 \cdot \exp \left[-\frac{(\Delta G^0 + \lambda)^2}{4\lambda k_B T} \right] \quad (2.3a)$$

where λ is the total solvent reorganization energy, H_{ij} is the electronic coupling, and ΔG^0 is the thermodynamic driving force.²² ΔG^0 and λ are estimated from the measured redox potentials, emission spectra, donor/acceptor radii and separation, and solvent dielectric properties to be -0.76 eV and 0.8 eV, respectively,^{23,24} suggesting that there is a small barrier for charge separation. The electronic coupling, H_{ij} , depends upon the donor-acceptor separation, i.e.

$$H_{ij} = V_0 \exp \left[-\beta \left(\frac{R_{ij} - R_0}{2} \right) \right] \quad (2.3b)$$

where V_0 is the electronic coupling at the van der Waals separation R_0 , and β is an attenuation parameter that reflects the decrease in orbital overlap with increasing separation.²⁵ For purely through-space electron transfer, experimentally determined values of β lie between 0.9-1.1 Å⁻¹.²⁶ The value of R_0 is estimated from the chemical structures to be 9.6 Å while the value for V_0 was treated as an adjustable parameter, as described below.

2.3.4.5. Time-Dependent Populations

The time-dependent populations of the polymer excited state ($\rho_{F_i^*}$), pendant excited state ($\rho_{il_j^*}$), and charge-separated state (ρ_{CS_i}) are computed from the following rate equations:

$$\frac{d\rho_{F_i^*}}{dt} = - \left(\sum_{i=1}^n k_{ET,ij} + \sum_{i=1}^n k_{ET,ij} + k_{F^*} \right) \rho_{F_i^*} \quad (2.4a)$$

$$\frac{d\rho_{il_j^*}}{dt} = \sum_{i=1}^n k_{ET,ij} \cdot \rho_{F_i^*} - k_{il^*} \cdot \rho_{il_j^*} \quad (2.4b)$$

$$\frac{d\rho_{CS_i}}{dt} = \sum_{i=1}^n k_{ET,ij} \cdot \rho_{F_i^*} - k_{CR} \cdot \rho_{CS_i} \quad (2.4c)$$

There is a separate rate equation for each species, which for a polymer with n ii acceptors is $3n$ total equations. This set of equations can be expressed concisely in matrix form as:

$$\frac{d\mathbf{P}}{dt} = \mathbf{K} \cdot \mathbf{P} \quad (2.5)$$

where \mathbf{K} is a $3n \times 3n$ matrix of rate constants and \mathbf{P} is the composition vector containing the populations of each species. The numerical solution to Eq. 2.5 is obtained through matrix

diagonalization of \mathbf{K} . The solution vector at time t is then given by $\mathbf{P}(t)=\mathbf{Q}\cdot\exp[\mathbf{\Lambda}t]\cdot\mathbf{Q}^{-1}\mathbf{P}_0$ where $\exp[\mathbf{\Lambda}t]$ is a diagonal matrix containing the eigenvalues (Λ), \mathbf{Q} is a matrix of the eigenvectors, and \mathbf{P}_0 is the population vector at $t=0$ that describes the initial location of the photoexcitation.

Simulation of the ensemble average of the quenching dynamics starts with the random selection of one of the 2,406 configurational snapshots from the MD trajectories. The location of the photoexcitation is then randomly chosen to be either one of the monomer units in the polymer chain ($\text{pF}^*-\text{iI}_{10}$) or one of the pendant chromophores ($\text{pF}-\text{iI}_{10}^*$), with probabilities given by the relative extinction coefficients at 388 nm (i.e. about 65:35 $\text{pF}^*:\text{iI}^*$). The time-dependent populations are computed and the results from 100,000 different starting initial configurations are combined to yield the quenching dynamics of the ensemble.

2.3.4.6. Comparison of Simulation with Experimental Observation

The composition vector (\mathbf{P}) describes the time evolution of the pF^* , iI^* , and CS species. With β set to 1.0 \AA^{-1} , the only adjustable parameter in the model is V_0 , which was varied to obtain agreement with the amplitudes determined by spectral modeling. Because we do not know the absolute extinction coefficients for each species, these amplitudes only reveal how the population varies with time, and do not provide information about the relative populations of the three different components. As a result, in comparing the simulation with experiment, we scaled the spectral amplitudes to match the magnitude of the populations determined by simulations. Reasonable agreement with experiment is obtained for $V_0 = 50 \text{ meV}$ (Figure 2.12).

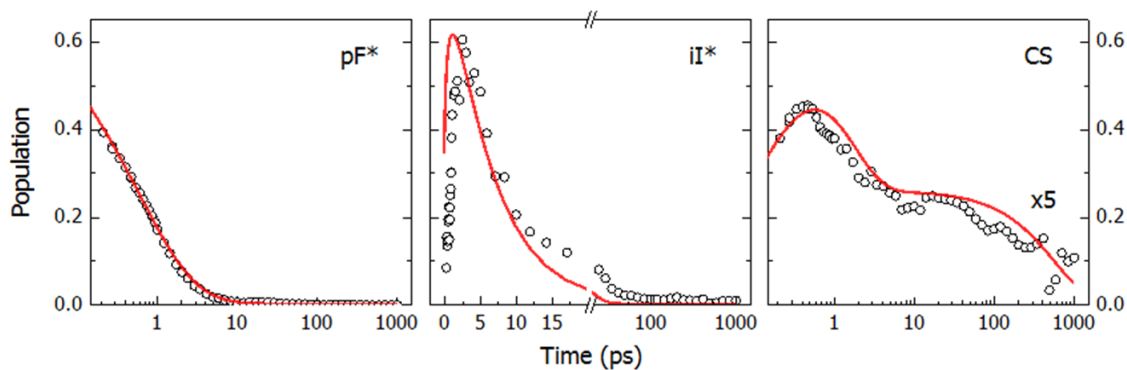


Figure 2.12. Comparison of the pF^* , iI^* , and CS state populations obtained from experiment (black circles) with the simulated populations (red line). The spectral amplitudes for each species were scaled to match the magnitude of the simulated populations.

This value reproduces the growth of the CS at early times (200-500 fs). It is also consistent with estimates of the charge transfer integrals computed using the Amsterdam Density Functional (ADF) package,²⁷ which suggest that the ground-state electronic coupling for pF-iI at the closest point of approach (9.6 Å) is ~25 meV (Figure 2.13). The simulations indicate that EnT dominates over ET for a large number of configurations, owing to the relatively large Förster radius of 40 Å.

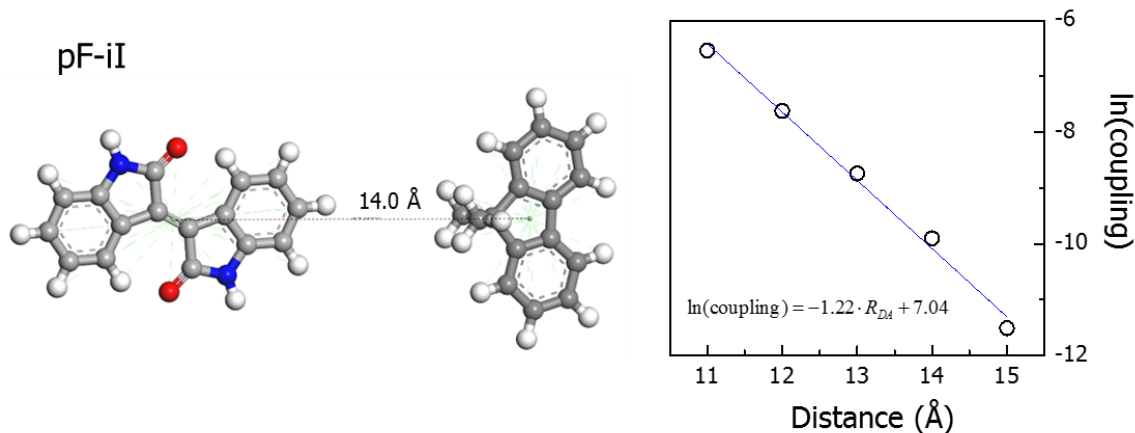


Figure 2.13. (Left) Model isoindigo and fluorene oligomer pair used for the estimation of the electron transfer parameter V_0 with the ADF computational package.⁶ The distance is computed from centroids placed on each unit. (Right) Plot of log(coupling) versus distance obtained from calculation of the charge transfer integrals of the model systems for pF-iI.

2.3.5. Analysis of Simulation Results

2.3.5.1. Microscopic Picture

We first consider the analysis of the EnT and ET rate constants present within a representative configuration. Shown in Figure 2.14A is a configuration selected from the MD trajectories, where the polymer excited state is centered at the i^{th} monomer unit, shaded in red. Because the EnT and ET quenching processes occur through multiple parallel kinetic pathways, the total rate constant for each is represented by the sum of the individual EnT and ET rates to all the iI acceptors, i.e. $k_{EnT,i} = \sum_j k_{EnT,ij}$ and $k_{ET,i} = \sum_j k_{ET,ij}$. The total height of the bar reflects the total quenching rate (i.e. $k_{Q,i} = k_{ET,i} + k_{EnT,i}$), which is $(0.25 \text{ ps})^{-1}$. The bar is divided into two

smaller bars that depict the total energy transfer (blue) and electron transfer (red) rate constants, $k_{EnT,i}$ and $k_{ET,i}$, respectively.

In this configuration there are 7 pendants within 35 Å of the excited state. The nearest pendant (iI₆) lies 15.2 Å from the exciton with $\kappa^2 = 0.67$, while the next nearest pendant (iI₅) is 21.9 Å away with $\kappa^2 = 0.17$. Thus, in this particular case, the total EnT rate (i.e., $k_{EnT,i}$) is dominated by iI₆ due to its short separation and favorable orientation, and as a consequence iI₆ accounts for 81% of $k_{EnT,i}$. While the other pendants lie 21.9 Å or further from the backbone, collectively they contribute to the remaining 19% of $k_{EnT,i}$. On the other hand, ET occurs almost solely to iI₆ due to the rapid attenuation of the electronic coupling with distance, and as a result the rate constant for ET to iI₆ accounts for 99.8% of $k_{ET,i}$. The probability of energy transfer (i.e. the energy transfer efficiency) for a single configuration with excitation centered at the i^{th} fluorene monomer ($P_{EnT,i}$) is given by the relative magnitudes of its energy and electron transfer rate constants, i.e.

$$P_{EnT,i} = \frac{k_{EnT,i}}{k_{ET,i} + k_{EnT,i}} . \quad (2.6)$$

For the configuration shown in Figure 2.14A, $k_{EnT,i}$ and $k_{ET,i}$ are $1.20 \times 10^{12} \text{ s}^{-1}$ and $1.85 \times 10^{11} \text{ s}^{-1}$, respectively, resulting in a total quenching rate ($k_{Q,i}$) of $1.39 \times 10^{12} \text{ s}^{-1}$ and an energy transfer efficiency of 87%.

While the rate of EnT to a particular iI acceptor increases at shorter separations, the largest EnT rate does not always occur to the nearest pendant. In the configuration shown in Figure 2.14B, the nearest pendant resides at a distance of 14.7 Å from the initial excited state and is situated with its transition dipole oriented orthogonal to the donor transition dipole on the

polymer, resulting in a small orientation factor (i.e. $\kappa^2 = 0.06$). This orientation suppresses EnT to the nearest iI acceptor and as a consequence the pendant with the largest EnT rate constant (i.e., k_{EnT}^M) lies further away (i.e., 17.6 Å) as a result of the parallel orientation of the pendant in relation to the backbone (i.e., $\kappa^2 = 0.94$). Furthermore, even though the distance to the acceptors that contribute to the overall quenching rate is increased — leading to a smaller EnT rate constant to an individual acceptor — the presence of multiple acceptors gives rise to an appreciable total EnT quenching rate. In fact, the magnitude of $k_{EnT,i}$ ($1.2 \times 10^{12} \text{ s}^{-1}$) is still significantly larger than $k_{ET,i}$ ($2.8 \times 10^{11} \text{ s}^{-1}$), giving rise to a large efficiency for energy transfer (80%).

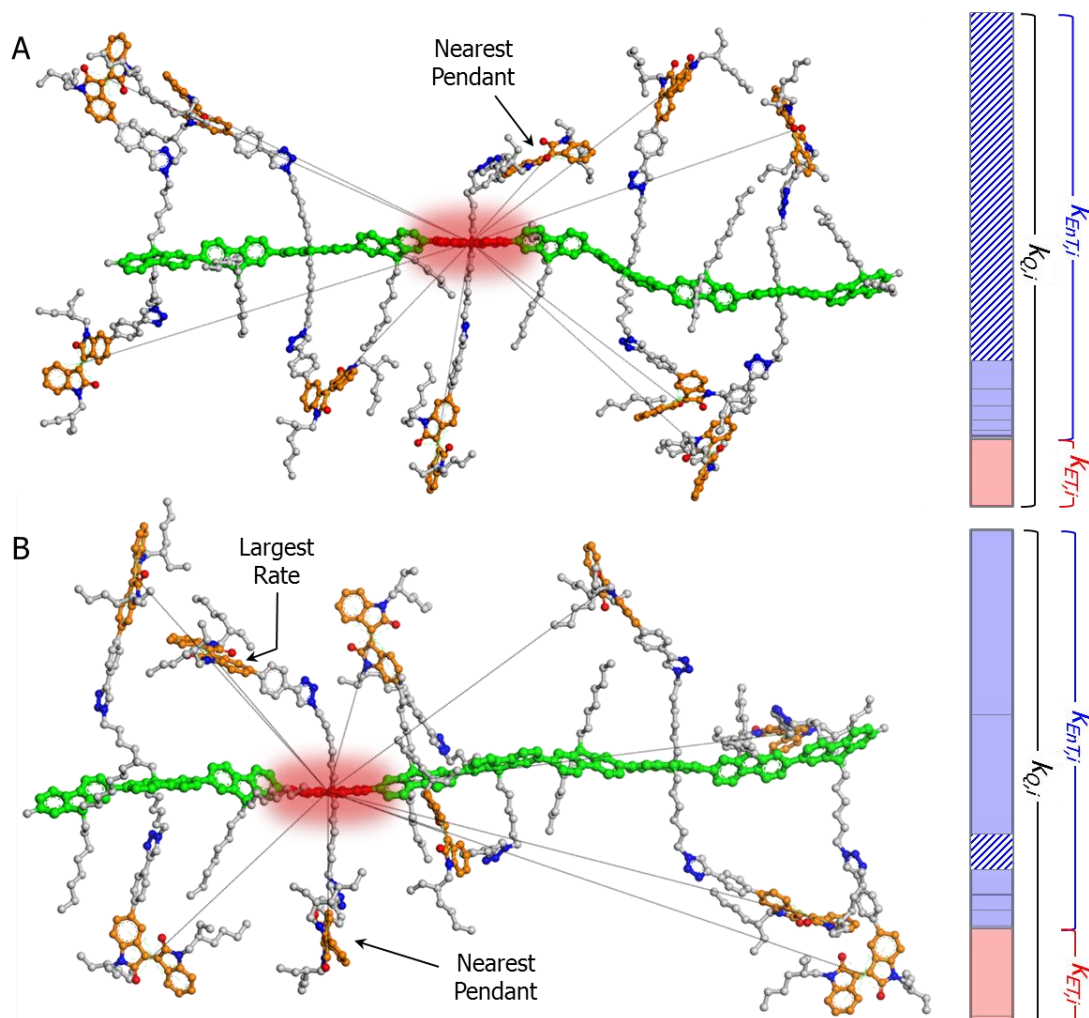


Figure 2.14. (A, B) Pictorial representation of the kinetic model applied to representative pF-iI₁₀ polymer structures obtained from molecular dynamics simulations. The initial exciton is shown as a red cloud along the polymer backbones, in which the energy and electron transfer rates are computed from the distances and orientation factors. The total quenching rate of the i^{th} monomer ($k_{Q,i}$) is then expressed as the sum of the individual computed rates. The magnitude of the EnT rate constant to the nearest pendant (i.e., k_{ET}^{NP}) is given as the cross-hatched rectangle for each configuration.

2.3.5.2. Ensemble Quenching Dynamics

The qualitative observations made in the examination of the individual structures are reinforced by the analysis of the entire ensemble. Shown in Figure 2.15 is the distribution of total quenching rate constants (i.e. $k_{Q,i} = k_{EnT,i} + k_{ET,i}$) that is obtained from the ensemble of configurations. The distribution reveals a large heterogeneity in the total quenching rates, extending from 10^{11} - 10^{14} s⁻¹. The average energy transfer efficiency ($\langle P_{EnT,i} \rangle$), which is depicted as a function of the total quenching rate in Figure 2.15, suggests the presence of two quenching regimes. The fastest quenching events are dominated by the ET pathway, whereas the slower quenching events proceed via EnT. This partitioning is a consequence of the differences in the distance dependence of the rate constants for EnT and ET. The exponential falloff of H_{ij} with separation (Eq. 2.3b) causes the ET rate to be determined largely by transfer to the nearest pendant, and is only appreciable for small donor-acceptor separations (< 18 Å). This is in contrast to the long-range dipole-dipole coupling for EnT, which exhibits an R^{-6} dependence, resulting in appreciable values of EnT rate constants for iI acceptors that are 10 to 25 Å from the polymer excited state. Thus, even though the EnT rate constants are smaller in magnitude compared to the fastest ET events, the large Förster radius makes it active over much greater distances. This extended range enables EnT to more iI acceptors in the assembly, which results in EnT being the dominant quenching pathway, accounting for ~80% of the quenching events.

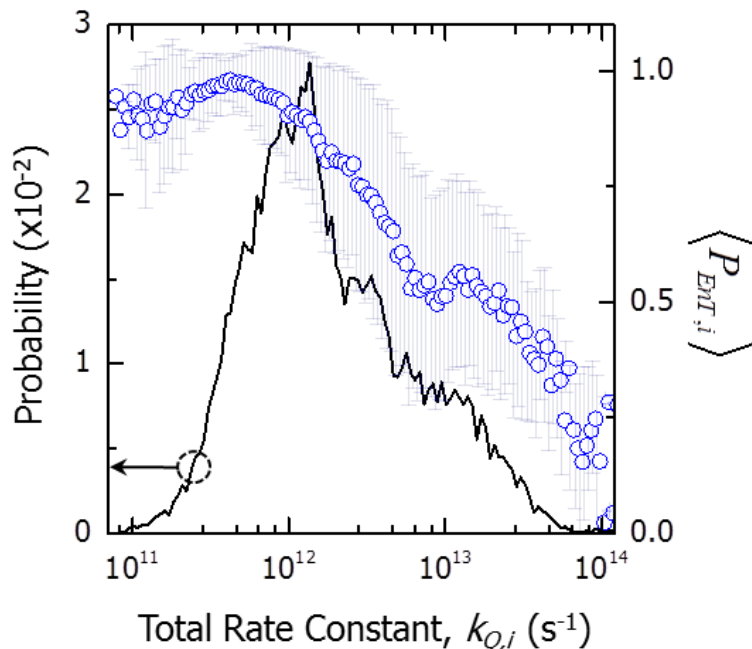


Figure 2.15. Distribution of rate constants from the pF-iI kinetic simulations, showing the total quenching rate distribution (black line). Also shown is the mean energy transfer efficiency computed as a function of the total quenching rate constant ($k_{Q,i}$) from each configuration. The total rates were computed for each configuration and binned on a logarithmic scale ranging from 10^{10} to 10^{15} s^{-1} with a total of 500 bins.

2.3.5.3. Role of Macromolecular Structure

The positions and orientations of the iI acceptors also lead to configurations in which the nearest pendant does not possess the largest energy transfer rate constant (i.e., $k_{EnT}^{NP} \neq k_{EnT}^M$).

Shown in Figure 2.16A are ensemble averages of k_{EnT}^{NP} as well as k_{EnT}^M as a function of the *total* energy transfer rate, $k_{EnT,i}$. For $k_{EnT,i}$ greater than $3 \times 10^{12} \text{ s}^{-1}$, the rate constant to the nearest pendant is nearly equal to the total energy transfer rate, signifying that energy transfer quenching

is dominated by the nearest acceptor. However, as $k_{EnT,i}$ decreases, the total EnT rate constant becomes larger than the EnT rate to the il pendant with the largest EnT rate constant on average (i.e., $k_{EnT,i} > \langle k_{EnT}^M \rangle$), indicating that the total rate for energy transfer quenching has contributions from multiple acceptors. To quantify this effect, we have computed the average number of acceptors that are needed to make up 80% of $k_{EnT,i}$ for each configuration (Figure 2.16B). From the analysis, for $k_{EnT,i} > 1 \times 10^{13} \text{ s}^{-1}$, the total EnT quenching rate is dominated by a single pendant, while for $k_{EnT,i} < 1 \times 10^{12} \text{ s}^{-1}$, $k_{EnT,i}$ contains significant contributions from 2 or more pendants. Physically, this implies that in structures where the side chains are extended away from the backbone, the number of pendants that communicate strongly with the polymer excited state increases overall, underscoring the multichromophore effect. However, as the dominant acceptor becomes strongly coupled to the polymer excited state (i.e., small R_{ij} and large κ_{ij}^2) this pendant will dominate, and thus the number of acceptors that participate in the EnT quenching decreases.

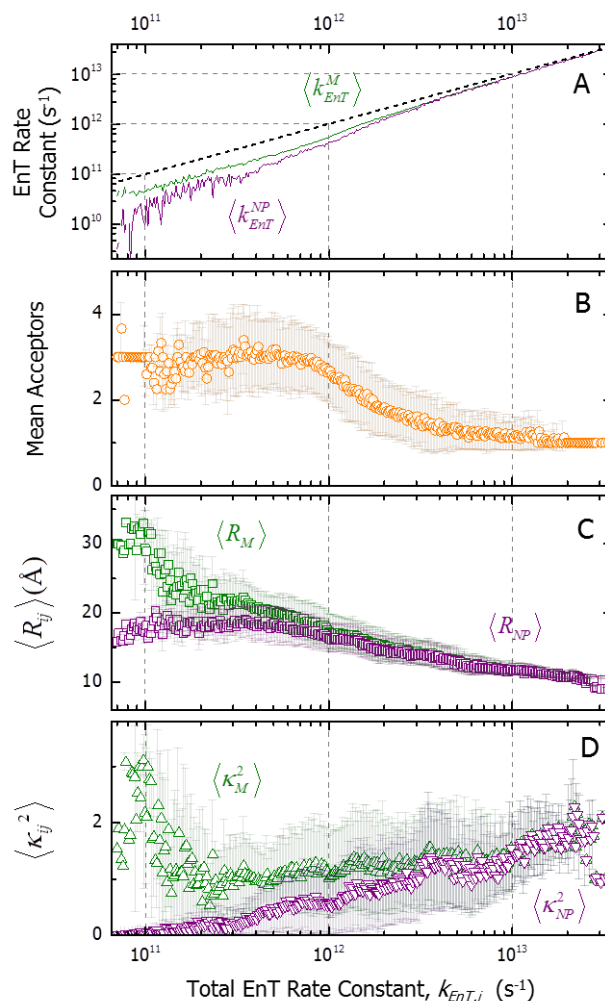


Figure 2.16. (A) Median energy transfer rate constants as a function of the total energy transfer rate constant to the nearest pendant (purple line) and to the pendant with the largest rate (green line). (B) Mean number of acceptors (orange circles) that are needed to achieve 80% of the total energy transfer quenching rate in the kinetic simulations. (C) Mean donor-acceptor distance as a function of the total EnT quenching rate constant to the nearest pendant (purple) and to the pendant with the largest rate (green). (D) Mean orientation factor that gives rise to the computed EnT rates in pF-iL. The rates were computed for each configuration and binned on a logarithmic scale ranging from 10^{10} to $10^{15} s^{-1}$ with a total of 500 bins.

Furthermore, for $k_{EnT,i}$ less than $\sim 2 \times 10^{12} \text{ s}^{-1}$, the pendant with the largest rate constant is not the pendant that is closest to the excitation. This difference is slight for $k_{EnT,i}$ near $2 \times 10^{12} \text{ s}^{-1}$ but becomes more significant as $k_{EnT,i}$ approaches 10^{11} s^{-1} . The physical origin of this effect can be understood by examining the average separations ($\langle R_{ij} \rangle$) and orientation factors ($\langle \kappa_{ij}^2 \rangle$) as a function of the total energy transfer rate. The fast EnT rates ($\sim 10^{13} \text{ s}^{-1}$) occur in configurations where the nearest pendant is close the excitation ($R_{ij} \sim 10\text{-}15 \text{ \AA}$, Figure 2.16C) with a favorable orientation factor ($\kappa_{ij}^2 \sim 1$, Figure 2.16D). The slowest rates ($\sim 10^{10} \text{ s}^{-1}$), on the other hand, correspond to configurations in which the nearest pendants have orientations that result in $\kappa_{ij}^2 \sim 0$. As a consequence, even though the distance to other iI pendants may be further, the more favorable orientation makes EnT to those sites possible. In addition, even though the rate constant for EnT to any single acceptor may be small, multiple acceptors contribute to the total EnT rate. At the low-end of the distribution, for example, the total EnT rate is distributed amongst an average of 3 acceptors, with the largest rate constant accounting for about 50% of the total (Figure 2.17).

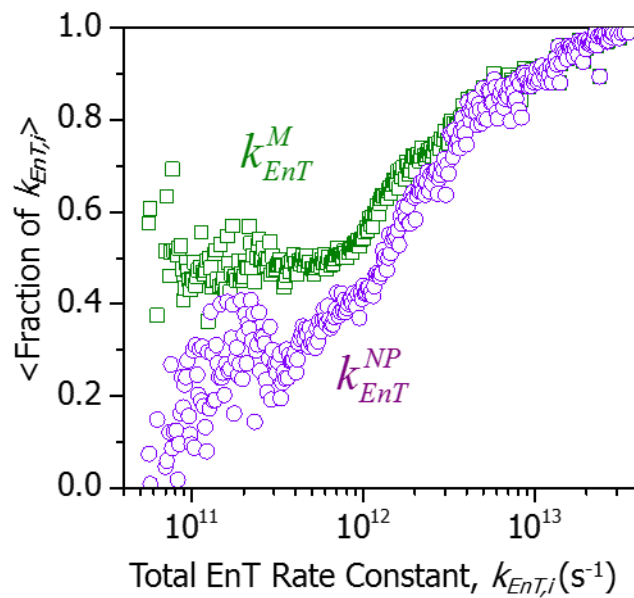


Figure 2.17. Average fraction of the total energy transfer rate constant ($k_{EnT,i}$) computed as a function of $k_{EnT,i}$ for the pendant with the largest rate (k_{EnT}^M) and for the nearest pendant (k_{EnT}^{NP}) in each initial polymer configuration.

2.4 CONCLUSIONS

In summary, we have examined the excited state quenching dynamics in a multichromophore assembly combining the functional elements of both broadly-absorbing organic chromophores and a π -conjugated polymer. With the use of femtosecond transient absorption spectroscopy, photoexcitation of the polymer backbone reveals multi-exponential quenching kinetics of the polymer excited state on the fs-ps time scale through a combination of electron and energy transfer processes. Energy transfer is the dominant quenching pathway, where the excited iI pendants rapidly relax within 30 ps owing to the short excited-state lifetime of iI*. Electron transfer, on the other hand, yields a CS state consisting of a reduced iI pendant and a positively charged polaron on the polymer backbone. This CS state persists for several hundreds of picoseconds before complete recombination occurs. The quenching dynamics were analyzed using a kinetic model that incorporates assembly structures determined by all-atom molecular dynamics simulations of the pF-iI assembly. These simulations show that the combination of donor-acceptor separations, pendant density, and orientation of the pendants relative to the backbone dictate the quenching pathway.

REFERENCES

- (1) Gust, D.; Moore, T. A.; Moore, A. L.: Solar Fuels via Artificial Photosynthesis. *Acc. Chem. Res.* **2009**, *42*, 1890-1898.
- (2) Alstrum-Acevedo, J. H.; Brennaman, M. K.; Meyer, T. J.: Chemical Approaches to Artificial Photosynthesis. 2. *Inorg. Chem.* **2005**, *44*, 6802-6827.
- (3) Morseth, Z. A.; Wang, L.; Puodziukynaite, E.; Leem, G.; Gilligan, A. T.; Meyer, T. J.; Schanze, K. S.; Reynolds, J. R.; Papanikolas, J. M.: Ultrafast Dynamics in Multifunctional Ru(II)-Loaded Polymers for Solar Energy Conversion. *Acc. Chem. Res.* **2015**, *48*, 818-827.
- (4) Davis, W. B.; Ratner, M. A.; Wasielewski, M. R.: Conformational Gating of Long Distance Electron Transfer Through Wire-like Bridges in Donor-Bridge-Acceptor Molecules. *J. Am. Chem. Soc.* **2001**, *123*, 7877-7886.
- (5) Fleming, C. N.; Maxwell, K. A.; DeSimone, J. M.; Meyer, T. J.; Papanikolas, J. M.: Ultrafast Excited-State Energy Migration Dynamics in an Efficient Light-harvesting Antenna Polymer Based on Ru(II) and Os(II) Polypyridyl Complexes. *J. Am. Chem. Soc.* **2001**, *123*, 10336-10347.
- (6) Wang, L.; Puodziukynaite, E.; Vary, R. P.; Grumstrup, E. M.; Walczak, R. M.; Zolotarskaya, O. Y.; Schanze, K. S.; Reynolds, J. R.; Papanikolas, J. M.: Competition Between Ultrafast Energy Flow and Electron Transfer in a Ru(II)-loaded Polyfluorene Light-harvesting Polymer. *J. Phys. Chem. Lett.* **2012**, *3*, 2453-2457.
- (7) Wang, L.; Puodziukynaite, E.; Grumstrup, E. M.; Brown, A. C.; Keinan, S.; Schanze, K. S.; Reynolds, J. R.; Papanikolas, J. M.: Ultrafast Formation of a Long-lived Charge-separated State in a Ru-Loaded Poly(3-hexylthiophene) Light-harvesting Polymer. *J. Phys. Chem. Lett.* **2013**, *4*, 2269-2273.
- (8) Puodziukynaite, E.; Wang, L.; Schanze, K. S.; Papanikolas, J. M.; Reynolds, J. R.: Poly(fluorene-co-thiophene)-Based Ionic Transition-Metal Complex Polymers for Solar Energy Harvesting and Storage Applications. *Polym. Chem.* **2014**, *5*, 2363-2369.
- (9) Mei, J. G.; Graham, K. R.; Stalder, R.; Reynolds, J. R.: Synthesis of Isoindigo-based Oligothiophenes for Molecular Bulk Heterojunction Solar Cells. *Org. Lett.* **2010**, *12*, 660-663.
- (10) Price, D. W.; Tour, J. M.: Biphenyl- and Fluorenyl-based Potential Molecular Electronic Devices. *Tetrahedron* **2003**, *59*, 3131-3156.
- (11) Chaignon, F.; Falkenstrom, M.; Karlsson, S.; Blart, E.; Odobel, F.; Hammarstrom, L.: Very Large Acceleration of the Photoinduced Electron Transfer in a Ru(Bpy)(3)-Naphthalene Bisimide Dyad Bridged on the Naphthyl Core. *Chem. Comm.* **2007**, 64-66.

- (12) Alvarez, S. G.; Alvarez, M. T.: A Practical Procedure for the Synthesis of Alkyl Azides at Ambient Temperature in Dimethyl Sulfoxide in High Purity and Yield. *Synthesis-Stuttgart* **1997**, 413-414.
- (13) Bialas, D.; Suraru, S. L.; Schmidt, R.; Wurthner, F.: Thiophene-functionalized Isoindigo Dyes Bearing Electron Donor Substituents with Absorptions Approaching the near Infrared Region. *Org. Biomol. Chem.* **2011**, 9, 6127-6132.
- (14) Estrada, L. A.; Stalder, R.; Abboud, K. A.; Risko, C.; Bredas, J. L.; Reynolds, J. R.: Understanding the Electronic Structure of Isoindigo in Conjugated Systems: A Combined Theoretical and Experimental Approach. *Macromolecules* **2013**, 46, 8832-8844.
- (15) Goswami, S.; Gish, M. K.; Wang, J.; Winkel, R. W.; Papanikolas, J. M.; Schanze, K. S.: pi-Conjugated Organometallic Isoindigo Oligomer and Polymer Chromophores: Singlet and Triplet Excited State Dynamics and Application in Polymer Solar Cells. *ACS Appl. Mater. Interfaces* **2015**, 7, 26828-26838.
- (16) Hintschich, S. I.; Dias, F. B.; Monkman, A. P.: Dynamics of Conformational Relaxation in Photoexcited Oligofluorenes and Polyfluorene. *Phys. Rev. B.* **2006**, 74, 045210-045219.
- (17) Franco, I.; Tretiak, S.: Electron-Vibrational Dynamics of Photoexcited Polyfluorenes. *J. Am. Chem. Soc.* **2004**, 126, 12130-12140.
- (18) Lewis, F. D.; Liu, X. Y.; Miller, S. E.; Hayes, R. T.; Wasielewski, M. R.: Formation and Decay of Localized Contact Radical Ion Pairs in DNA Hairpins. *J. Am. Chem. Soc.* **2002**, 124, 14020-14026.
- (19) Frisch, M. J.; Trucks, G. W.; Schlegel, H. B.; Scuseria, G. E.; Robb, M. A.; Cheeseman, J. R.; Scalmani, G.; Barone, V.; Mennucci, B.; Petersson, G. A.; et. al.: Gaussian 09, Revision E.01. Gaussian, Inc.: Wallingford, CT, USA, 2009.
- (20) Rappe, A. K.; Casewit, C. J.; Colwell, K. S.; Goddard, W. A.; Skiff, W. M.: Uff, a Full Periodic-Table Force-Field for Molecular Mechanics and Molecular-Dynamics Simulations. *J. Am. Chem. Soc.* **1992**, 114, 10024-10035.
- (21) Estrada, L. A.; Stalder, R.; Abboud, K. A.; Risko, C.; Bredas, J. L.; Reynolds, J. R.: Understanding the Electronic Structure of Isoindigo in Conjugated Systems: A Combined Theoretical and Experimental Approach. *Macromolecules* **2013**, 46, 8832-8844.
- (22) Marcus, R. A.: Electron-Transfer Reactions in Chemistry - Theory and Experiment. *Rev. Mod. Phys.* **1993**, 65, 599-610.
- (23) Marcus, R. A.; Sutin, N.: Electron Transfers in Chemistry and Biology. *Biochim. Biophys. Acta.* **1985**, 811, 265-322.

- (24) Weller, A.: Photoinduced Electron-transfer in Solution - Exciplex and Radical Ion-Pair Formation Free Enthalpies and Their Solvent Dependence. *Z. Phys. Chem. Neue. Fol.* **1982**, *133*, 93-98.
- (25) Barbara, P. F.; Meyer, T. J.; Ratner, M. A.: Contemporary Issues in Electron Transfer Research. *J. Phys. Chem.* **1996**, *100*, 13148-13168.
- (26) Wenger, O. S.; Leigh, B. S.; Villahermosa, R. M.; Gray, H. B.; Winkler, J. R.: Electron Tunneling Through Organic Molecules in Frozen Glasses. *Science* **2005**, *307*, 99-102.
- (27) te Velde, G.; Bickelhaupt, F. M.; Baerends, E. J.; Guerra, C. F.; Van Gisbergen, S. J. A.; Snijders, J. G.; Ziegler, T.: Chemistry with ADF. *J Comput Chem* **2001**, *22*, 931-967.

CHAPTER 3. ELECTRON TRANSFER DYNAMICS IN AN ISOINDIGO LOADED POLY(THIOPHENE) ASSEMBLY

This chapter has been submitted for publication as an article in the Journal of Physical Chemistry B.

3.1 INTRODUCTION

Natural photosynthetic systems have evolved over billions of years, forming complex macromolecular structures that integrate light harvesting¹⁻² and charge separation³ with multi-electron water oxidation and carbon dioxide reduction catalysis for the production of sugars.⁴⁻⁵ Over the past several decades, researchers have worked to mimic the functionality of natural photosynthesis (i.e., light harvesting, charge separation, and energy storage) in man-made molecular assemblies.⁶⁻¹⁰ Polymers have received considerable attention due to their ability to organize multiple molecular components that can perform the basic energy and electron transfer (EnT and ET, respectively) processes needed to collect and convert solar photons into usable energy.^{8,11-12} However, their disordered chemical structures give rise to complicated, multi-exponential kinetics that are oftentimes difficult to interpret in terms of fundamental photophysical events.

We have combined time-resolved spectroscopy with computer simulations to disentangle the fundamental time scales associated with EnT and ET in molecular assemblies comprised of polymer backbones functionalized with pendant chromophores.^{8, 13-16} Early work focused on site-to-site energy transport in polystyrene-based assemblies functionalized with pendant Ru(II) and Os(II) complexes. Analysis of the transient photoluminescence using a stochastic kinetic model revealed efficient energy migration following photoexcitation of the pendant Ru(II) complexes.^{13,17} A key feature of our approach was the use of a kinetic model that provided

molecular level insight into the energy transport dynamics by incorporating macromolecular structures obtained from Monte Carlo simulations. The large size of the Ru(II) pendant groups in relation to the styrene monomer results in densely packed assemblies whose structures are dominated by the repulsive interactions of the side chains. Structures are determined largely by the excluded volume and torsional potentials and attractive interactions play only a small role, and as a consequence, the simulations used a relatively simple potential that treated the polymer as a flexible chain and the Ru(II) complexes as hard spheres. Subsequent efforts examined analogous Ru(II)-based assemblies incorporating π -conjugated polymers (e.g. poly(fluorene) or poly(thiophene)), where the polymer excitation decays through a combination of rapid EnT and ET to the pendant chromophores.^{8,14-16} As a result of their more complicated chemical architecture, modeling of the macromolecular structure in these systems requires atomistic detail and realistic potentials to describe the conformational disorder of the polymer and the interactions of the side chains.

A recent report from our group examined the excited-state dynamics in a poly(fluorene)-based assembly functionalized with pendant isoindigo (iI) chromophores (pF-iI) using a combination of ultrafast spectroscopic methods and computer simulation.¹⁸ Experiments showed that quenching of the pF* occurs through a combination of EnT and ET to the pendants. Macromolecular structures obtained from all-atom molecular dynamics (MD) simulations were input into a kinetic model, which showed the distance and orientation of the pendants in relation to the backbone play a profound role in the preferred quenching pathways. As a result, even though the rate constants for ET are larger, EnT dominates. Here we apply the same experimental and modeling methodology to the poly(thiophene) analog, pT-iI (Figure 3.1). In contrast to pF-iI, we find that a majority of the pT* excitations (~95%) undergo ET to form a charge-separated (CS) state (i.e.,

pT⁺-iF). The remaining pT* population is quenched by EnT to the pendants or undergoes intersystem crossing to form the triplet exciton, ³pT. The use of ultrafast spectroscopy in conjunction with computational methods provides a microscopic view of the photoinduced dynamics occurring within the polymer assembly.

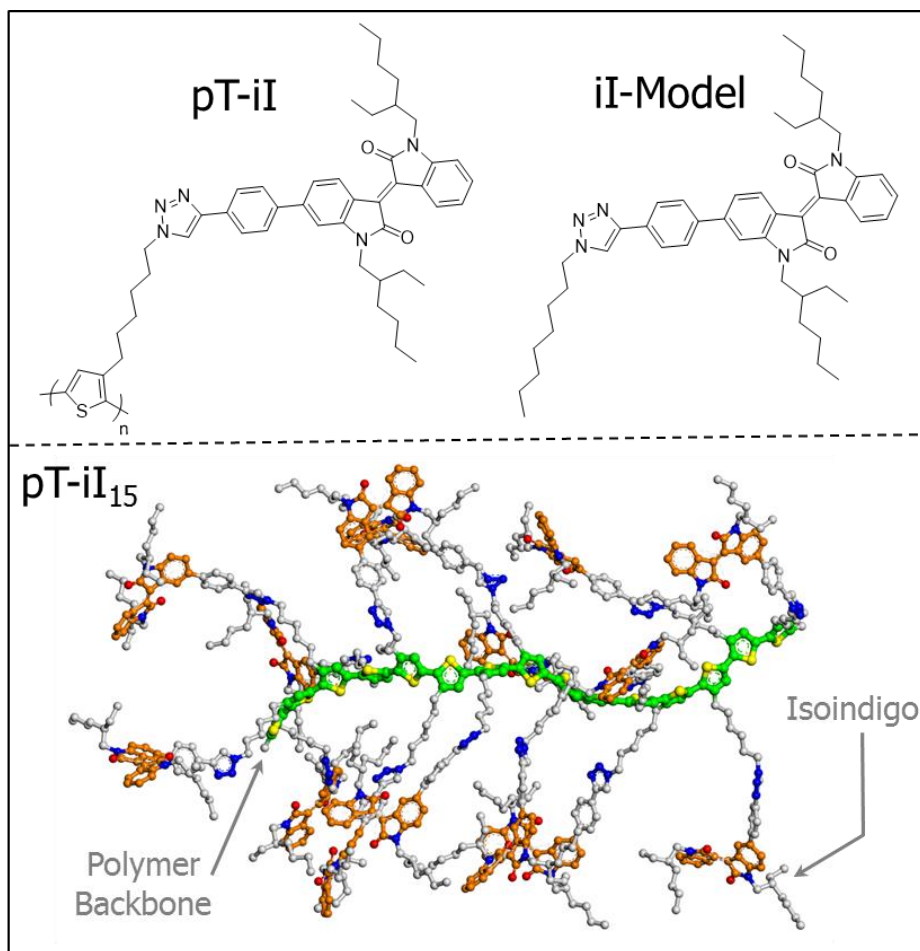


Figure 3.1. (Top) Chemical structures of the pT-iI monomer (left) and iI-Model (right). (Bottom) Snapshot of a 15 repeat unit pT-iI polymer assembly (i.e., pT-iI₁₅) obtained from fully atomistic molecular dynamics simulations in explicit dichloromethane (DCM) solvent. The polymer backbone is depicted in green and the iI pendants in orange. The solvent has been excluded for clarity.

3.2 EXPERIMENTAL METHODS

3.2.1. Sample Preparation

All spectroscopic experiments were performed in spectroscopic grade dichloromethane. Ground-state absorption and emission measurements were performed in 1 cm quartz cuvettes whereas transient measurements were performed in 2 mm quartz cuvettes in sufficiently dilute solution (optical density (OD) between 0.5 and 0.6 at the visible absorbance maximum) to minimize interchain effects. All samples were sparged with argon for 20 minutes and sealed prior to use.

3.2.2. Steady State Techniques

UV-Visible spectra were recorded on an HP 8543 Diode Array Spectrophotometer. UV-Visible spectra were recorded on all samples before and after excited state measurements to ensure that samples did not undergo photodecomposition.

Emission spectra were measured on Photon Technology International (PTI 4SE-NIR) Quantamaster™ spectrofluorometer equipped with a continuous xenon arc lamp as the excitation source. The emitting light was collected at 90° to the excitation beam and detected by a Multi-mode 814 photomultiplier tube (PMT) in photon counting mode (digital).

3.2.3. Transient Absorption Spectroscopy

Femtosecond-picosecond transient absorption measurements were performed using a home-built transient absorption spectrometer. The spectrometer is based on a commercially available ultrafast laser system (Clark MXR CPA-2210). The system consists of an erbium-doped fiber ring oscillator pumped by a solid-state fiber coupled laser diode operating at 980 nm and a chirped pulse Ti:Sapphire regenerative amplifier pumped by a frequency-doubled, Q-switched Nd:YAG

laser. Following pulse compression, the amplifier produces pulses centered at 775 nm with 120 fs fwhm duration at 1 kHz with pulse energies of 1.6 mJ/pulse.

The amplified output is initially split into two fractions, where the larger fraction (80%) is further split to pump several optical parametric amplifiers (OPA) for frequency tunability. 50% (650 μ J/pulse) of this fraction pumps a collinear near-IR OPA (White Light Conversion TOPAS-C) that is tuned to 1130 nm and mixed with the residual 775 nm fundamental in a 1 mm thick BBO crystal to produce 460 nm pulses by sum-frequency generation with energies of approximately 1 μ J/pulse. A smaller portion (20%) is used to drive a home-built collinear near-IR OPA tuned to 1200 nm. The femtosecond probe pulse is generated by focusing the 1130 nm signal output (5 μ J/pulse) into a translating 5 mm thick CaF₂ window, giving spectral coverage across the visible region.

The pump beam is directed through a mechanical chopper to modulate between pump-on and pump-off spectra and focused onto the sample using a 300 mm lens. The probe beam is focused and overlapped with the pump pulse using a 250 mm spherical aluminum mirror. After the sample, the probe beam is dispersed by a 0.15 m spectrograph with a 600 g/mm grating and detected on a diode array. Time-resolved spectra were collected by varying the delay between pump and probe pulses using a computer controlled delay stage with a resolution of 1 μ m. Spectra were collected on a shot-by-shot (1 kHz) basis over the range of 350 to 820 nm with a sensitivity of up to 0.1 mOD. The angle between the pump and probe polarization vectors was set to magic angle ($\sim 54.7^\circ$) to avoid polarization effects and ensure that only excited-state population dynamics were being monitored. The sample was stirred with a magnetic stirrer to provide for a fresh sample volume between laser pulses and a steady-state absorbance spectrum was acquired before and after transient experiments to confirm the absence of photoproduct formation. Following data collection, the frequency chirp in the probe pulse was characterized using the optical Kerr response

of liquid CCl_4 in a 2 mm cuvette in a polarization gating geometry. The spectra were chirp corrected using a data processing program written in LabVIEW.

3.2.4. Electronic Structure Calculations

The ground-state geometry of the iI-Model complex was optimized using the B3LYP DFT functional and the 6-31G** basis sets, as implemented in Gaussian09 (v09e01).¹⁹ Solvation effects for dichloromethane (DCM) were included with a polarizable continuum model in Gaussian. A vibrational analysis was performed to verify that the optimized structure was at a potential energy minimum.

Time-dependent density functional theory (TD-DFT) calculations were performed on the optimized ground-state geometry using the B3LYP DFT functional and the 6-31G** basis sets, as implemented in Gaussian09 (v09e01), with solvation effects for dichloromethane included with a polarizable continuum model. A total of 10 singlet states were computed.

3.2.5. Electrochemical Measurements

Electrochemical measurements were performed in THF solutions containing 0.1 M tetrabutylammonium hexafluorophosphate (TBAPF_6) as the supporting electrolyte using a single-compartment three-electrode cell with a platinum button, platinum flag, and non-aqueous Ag/Ag^+ electrode as the working, counter, and reference electrodes, respectively. The scan rate was 50 mV/s, and the concentration of the analyte was 1 mM. Potentials were reported vs. a ferrocene/ferrocenium (Fc/Fc^+) external standard (-5.1 eV vs. vacuum). All electrochemical measurements were performed using an EG&G Princeton Applied Research model 273A potentiostat/galvanostat in an argon-filled glove box.

3.2.6. Spectroelectrochemical Measurements

Spectroelectrochemical measurements were performed in DCM solutions containing 0.1 M tetrabutylammonium hexafluorophosphate (TBAPF₆) as the supporting electrolyte using an optically transparent thin layer electrode (OTTLE) cell. Platinum mesh, platinum wire, and a non-aqueous Ag/Ag⁺ electrode were used as the working, counter, and reference electrodes, respectively. Samples were prepared inside an argon-filled glove box, and the concentration of the analyte was 1 mM. UV-Vis spectra were recorded at 50 mV intervals using a Cary 5000 UV-Vis-NIR spectrophotometer. Potentials were reported vs. a ferrocene/ferrocenium (Fc/Fc⁺) external standard. All electrochemical measurements were performed using an EG&G Princeton Applied Research model 273A potentiostat/galvanostat.

3.3 RESULTS AND DISCUSSION

3.3.1 Synthesis of Materials

The synthesis of the ~40 repeat unit isoindigo-loaded pT polymer (pT-iI₄₀) follows a route similar to the previously reported iI-loaded pF polymer (pF-iI).¹⁸ Briefly, an alkyne-terminated iI chromophore was attached to an azide-functionalized pT backbone via “Click” chemistry. The alkyne-terminated isoindigo was prepared via a Stille coupling of 6-bromo-*N,N'*-(2-ethylhexyl)-isoindigo²⁰ with trimethyl((4-(trimethylstannyl)phenyl)ethynyl)silane,²¹⁻²² and the trimethylsilyl group was subsequently deprotected via treatment with basic methanol. Azide-functionalized poly(thiophene)¹⁵ was then coupled to the isoindigo unit via Cu-catalyzed Click reactions to afford the poly(thiophene)-isoindigo adduct (pT-iI) (Figure 3.1). The completion of the reaction was monitored by the disappearance of the azide groups by FTIR spectroscopy, and ¹H NMR spectroscopy revealed the quantitative conversion of the azide groups to triazole moieties. Finally, a control isoindigo compound (iI-Model) was synthesized via a Click reaction between 1-azidooctane²³ and the alkyne-terminated isoindigo. Detailed synthesis and characterization data are described in the Supporting Information.

3.3.2 Static Spectroscopy

The ground-state absorbance spectrum of the pT-iI assembly is (for the most part) a superposition of the absorbance spectra of the individual pT and iI components (Figure 3.2). The prominent absorption peak at 415 nm is a mixture of iI $n \rightarrow \pi^*$ and $\pi \rightarrow \pi^*$ transitions, while the low energy shoulder at 500 nm contains overlapping $\pi \rightarrow \pi^*$ absorptions of the iI pendants and pT backbone. While the superposition reproduces the general features of the spectrum, it overestimates the intensity at higher energy and underestimates it at lower energy. The magnitude of this systematic deviation is unusual when compared to similar assemblies with

pendant architectures,^{14-16, 18} suggesting that incorporation of the pT and iI into the assembly slightly alters their electronic properties. Perturbation in the pT electronic structure could result from an increase in the torsional disorder in the polymer chain induced by the presence of the iI pendants. The resulting blue shift in its absorption band would give rise to the observed differences.²⁴ Alternatively, the spectral mismatch could also result from interaction between iI pendants, an idea supported by simulation and experimental observations. In particular, the transient spectra exhibit differences in both the lifetime and spectral positions of iI* embedded in the assembly compared to the isolated iI model (Figure 3.4). Moreover, MD simulations show the smallest iI-iI separations (center to center) to be 8-10 Å, where DFT calculations suggest mixing of the orbitals on adjacent pendants is possible (Figure 3.3). Further discussion of these observations is contained in subsequent sections. While a superposition of the component spectra does not exactly describe that of the assembly spectrum, we emphasize that the magnitude of the mismatch is minor, suggesting that the electronic structure of the assembly constituents remain largely intact upon formation of the assembly.

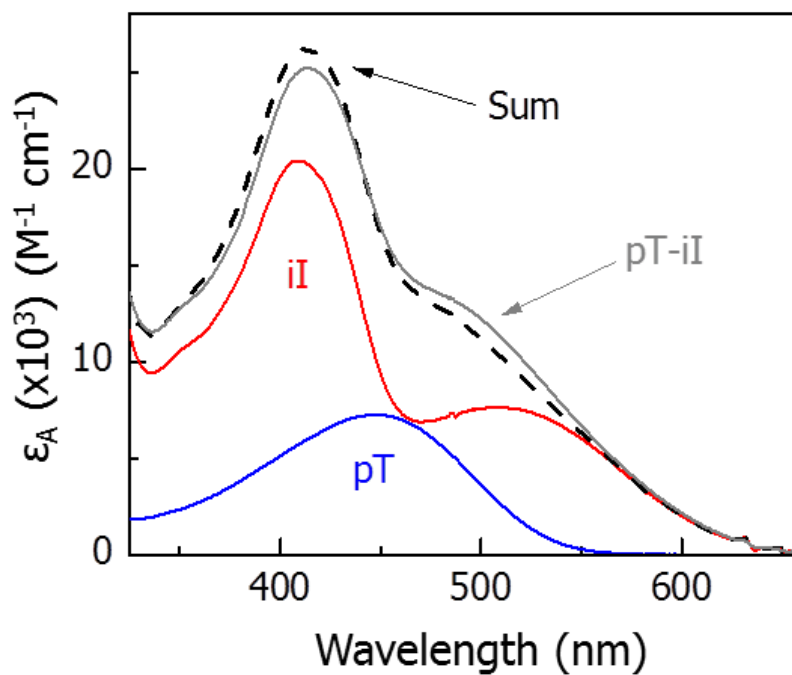


Figure 3.2. Ground state absorbance spectra of the pT-iI polymer assembly (grey), unfunctionalized pT polymer (blue), iI-Model (red), and the sum of the iI and pT absorbance spectra (dashed black).

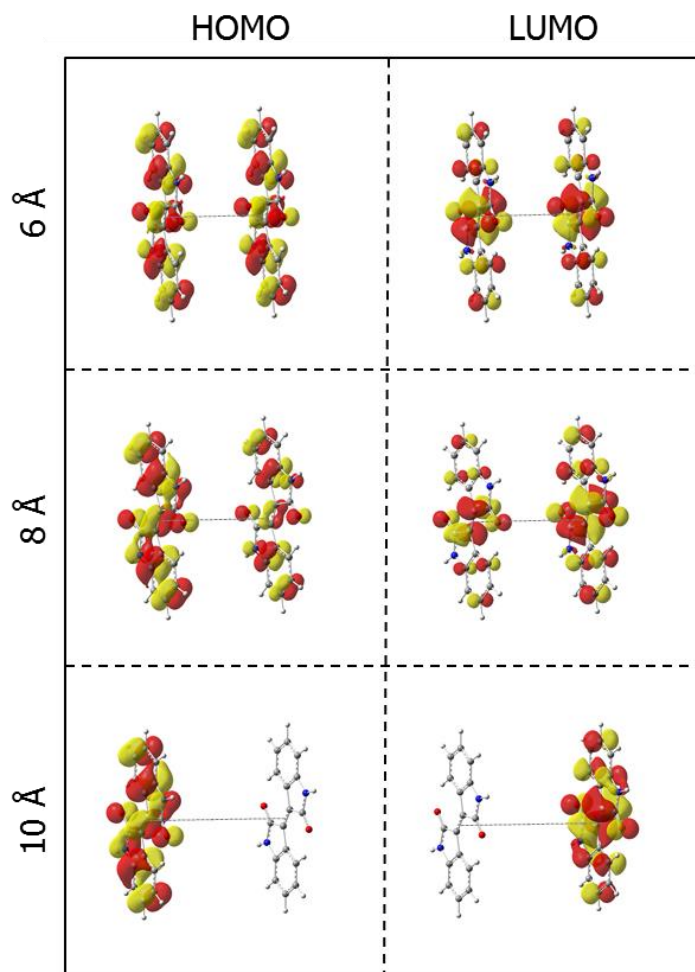


Figure 3.3. Frontier orbitals (HOMO and LUMO) of geometry optimized isoindigo dimers at varying separations obtained from density functional theory calculations using the B3LYP functional and the 6-31(d,p) basis sets, as implemented in Gaussian09 (Revision E.01).

3.3.3 Ultrafast Spectroscopy

Excitation of the polymer backbone results in complicated transient absorption spectra that reflect multiple overlapping bands associated with the polymer (pT^*) and the isoindigo (iI^*) excited states, as well as a charge-separated (CS) state (pT^+-iI^-) formed by ET quenching. We are able to disentangle contributions from these different species by performing experiments on the pT polymer and iI-Model controls, as well as the pT-iI assembly.

3.3.3.1. Isoindigo Excited-State Dynamics

The excited-state dynamics of iI are shown in Figure 3.4. The iI-Model transient spectra exhibit prominent ground-state bleach (GSB) features at 410 and 520 nm. The 520 nm bleach is offset by a broad photoinduced absorption (PA) that extends into the near IR (Figure 3.4A). The iI excited state is short-lived (Figure 3.4B), rapidly relaxing to the ground state through a conical intersection between the S_1 and S_0 potential energy surfaces with $\tau \sim 5-7$ ps.^{18, 25}

The excited-state dynamics of the iI pendants embedded in the pT-iI assembly are followed by selective excitation at the red edge of the iI absorbance spectrum at 595 nm (Figure 3.4C). The transient spectra qualitatively resemble that of the iI-Model, but with small blue shifts in the GSB features and a slight increase in the iI lifetime to ~ 12 ps, both observations suggest there is a slight perturbation in the iI electronic structure by other elements of the assembly, consistent with conclusions reached in the analysis of the ground state spectra.

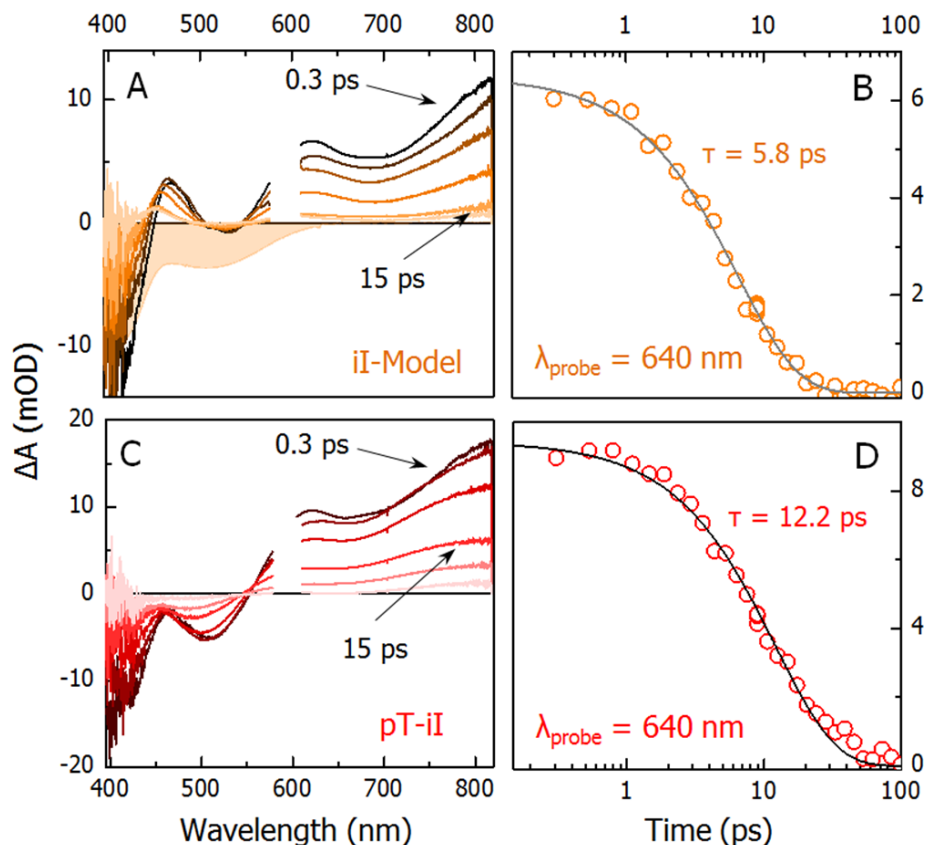


Figure 3.4. (A) Femtosecond transient absorption difference spectra of iI-Model in DCM at 0.3, 1, 2, 5, 15, and 20 ps. Shown shaded in orange is the inverted ground-state absorbance spectrum for iI-Model, normalized to the GSB at 410 nm. (B) Decay of the transient signal for iI-Model at 640 nm. The transient exhibits a single exponential decay with $\tau = 5.8 \pm 0.2$ ps. (C) Femtosecond transient absorption difference spectra of pT-iI in DCM at 0.3, 2, 5, 15, 30, and 100 ps. (D) Decay of the transient signal for pT-iI at 640 nm. The transient exhibits a single exponential decay with $\tau = 12.2 \pm 1.0$ ps. All spectra were measured in argon saturated DCM and excited with a 150 fs, 100 nJ pulse at 595 nm with a 120 μm spot size.

3.3.3.2. Ultrafast Quenching of the Polymer Excited State

The pT spectra contain a prominent stimulated emission (SE) band near 550 nm (Figure 3.5), as well as a GSB in the blue (450 nm) and a broad PA band extending into the near-IR (Figure 3.6A). During the first few ps, the SE band rapidly red shifts from 550 nm to ~650 nm as the exciton relaxes through a combination of dynamic planarization of the polymer chain near the exciton (i.e., self-trapping) and intrachain electronic energy transfer (EET).²⁶⁻²⁸ After the initial red shift, the SE decays in intensity with a lifetime of 490 ps (Figure 3.7), which corresponds primarily to relaxation back to the ground state with a small fraction (10%) of the pT* undergoing intersystem crossing (ISC)²⁹ to form a long-lived ($\tau=13.7\ \mu\text{s}$) triplet state, $^3\text{pT}^*$ (Figure 3.8).

The transient spectra of the pT-iI assembly are shown in Figure 3.6B. The most striking difference between the pT and pT-iI transient spectra is the noticeable absence of the pT* SE band, even at the earliest delay of 0.25 ps. This absence suggests rapid quenching of a substantial fraction of the pT* excitons by the pendant iI units within the first 0.25 ps, while the remaining pT* is completely quenched by several ps. The transient spectra of pT-iI at early times exhibit a GSB feature around 500 nm, as well as a shallow depression in the PA at ~650 nm, both of which correspond to the iI*. At long delays (1500 ps), the evidence of iI* dissipates, yet the spectra do not resemble pT*, but rather a combination of a CS state (pT^+-iI^-) and the triplet polymer excited state, $^3\text{pT}^*$ (Figure 3.6C). Because the ISC time constant (1200 ps)³⁰ is slow compared to the EnT and ET quenching pathways, it is a minor relaxation pathway and the quantum yield for triplet formation, determined from kinetic simulations below, is only about 0.03%.

Disentangling the different kinetic contributions is challenging given the large number of species and the extensive overlap of their transient absorption features. We can make progress, however, through judicious choice of probe wavelength. The transient at 575 nm, for example, only contains

contributions from the pT* SE, as well as the weak PA of iI* and $^3\text{pT}^*$ (Figure 3.6D).³¹ The transient shows an initial 0.23 ps growth, which reflects the loss of the pT* SE, while the subsequent decay ($\tau=22.9$ ps) results mostly from iI* excited-state relaxation. The presence of iI* suggests that pT* may be quenched through EnT. However, kinetic modeling (described in more detail below) indicates that EnT in pT-iI is suppressed due to poor spectral overlap. Instead, quenching of the pT* arises largely from ET to form the CS state.

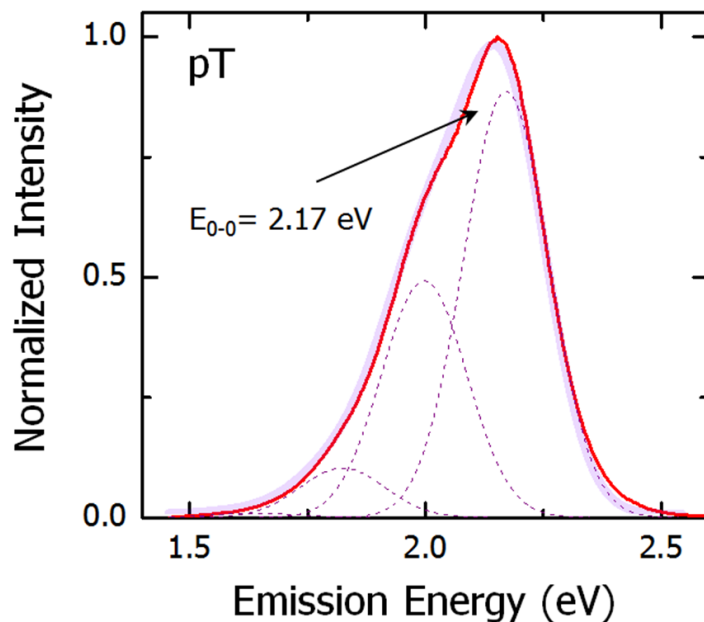


Figure 3.5. Franck-Condon mode analysis for the alkyl-substituted pT emission spectra. The emission spectrum (red line) was fit to a sum of 4 Gaussian functions with constant width and mode spacing (light purple line).

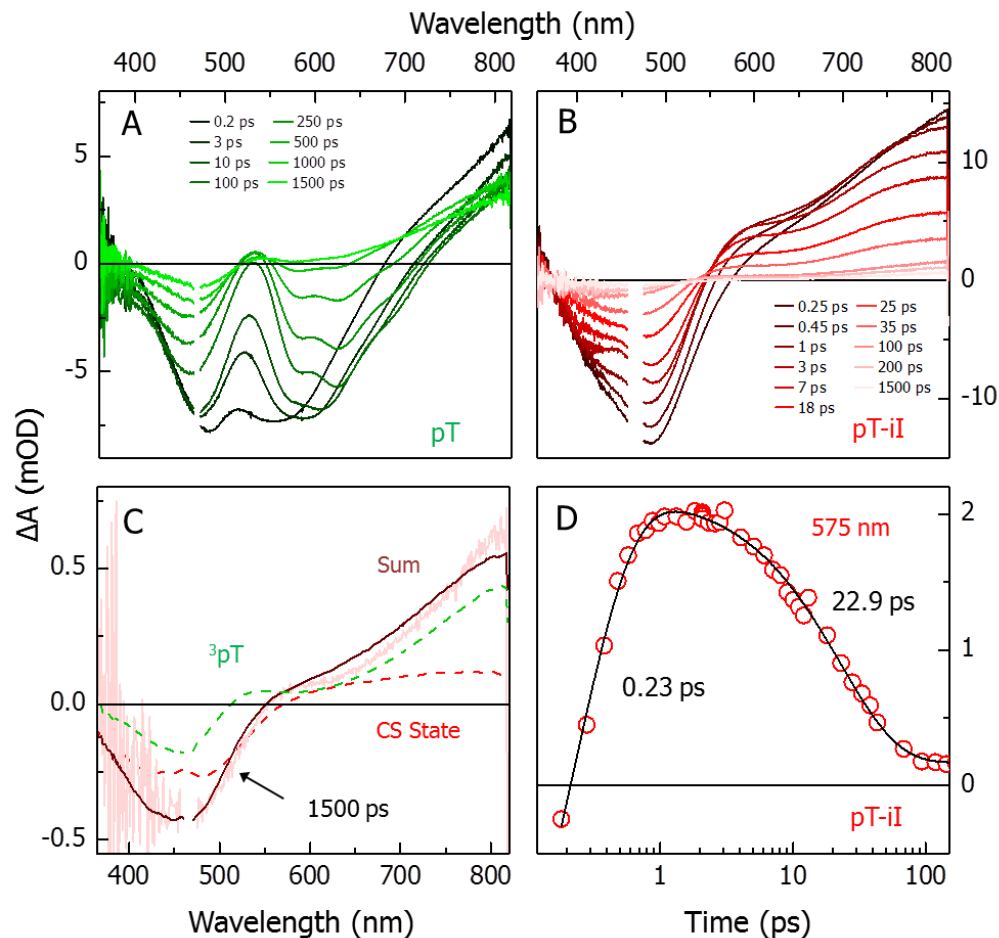


Figure 3.6. (A) Transient absorption spectra of pT in DCM at 0.2, 3, 10, 100, 250, 500, 1000, and 1500 ps. Excitation was at 460 nm and the pulse energy was 15 nJ/pulse. (B) Transient absorption spectra of pT-iI in DCM at 0.25, 0.45, 1, 3, 7, 18, 25, 35, 95, 200, and 1500 ps. Excitation was at 460 nm and the pulse energy was 60 nJ/pulse. (C) Spectral modeling of the 1500 ps pT-iI spectrum (light red). The dashed red line, labeled CS State, is the sum of the iI^- and pT^+ spectra acquired from spectroelectrochemical measurements (Figure 3.9). The dashed green line, labeled ^3pT , is the 1500 ps pT spectrum from panel (A). The dark red line represents the sum of the CS State and ^3pT spectra to produce the modeled 1500 ps spectrum. (D) Kinetics trace at 575 nm for pT-iI fit to a bi-exponential function that exhibits a growth ($\tau_1 = 0.23 \pm 0.08$ ps) and a decay ($\tau_2 = 22.9 \pm 0.6$ ps).

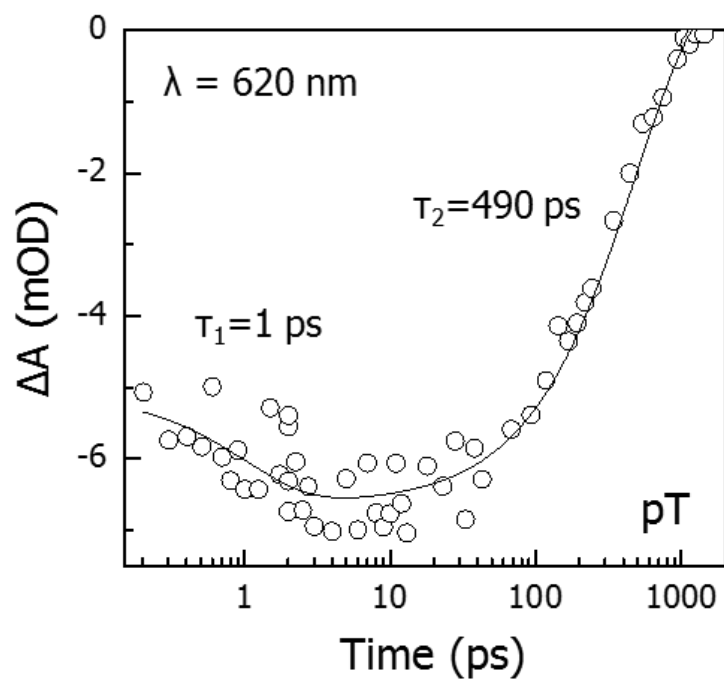


Figure 3.7. Decay of the pT* stimulated emission band at 620 nm versus time. The transient was fit to a sum of two exponentials, with characteristic time constants of $\tau_1 = 1 \pm 0.03$ ps and $\tau_2 = 490 \pm 5$ ps.

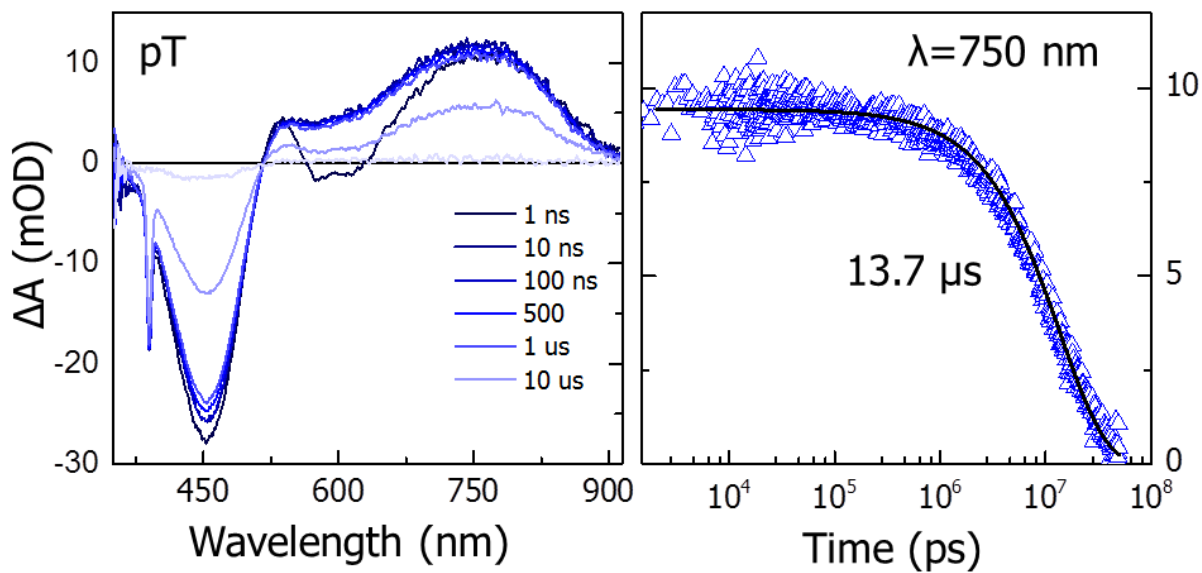


Figure 3.8. (Left) Transient absorption spectra of pT in DCM from 1 ns to 10 μ s following 388 nm excitation. (Right) Kinetics trace at 750 nm monitoring the triplet exciton absorption band. The decay of the triplet exciton is fit to a single exponential decay with $\tau=13.7\pm0.8 \mu$ s.

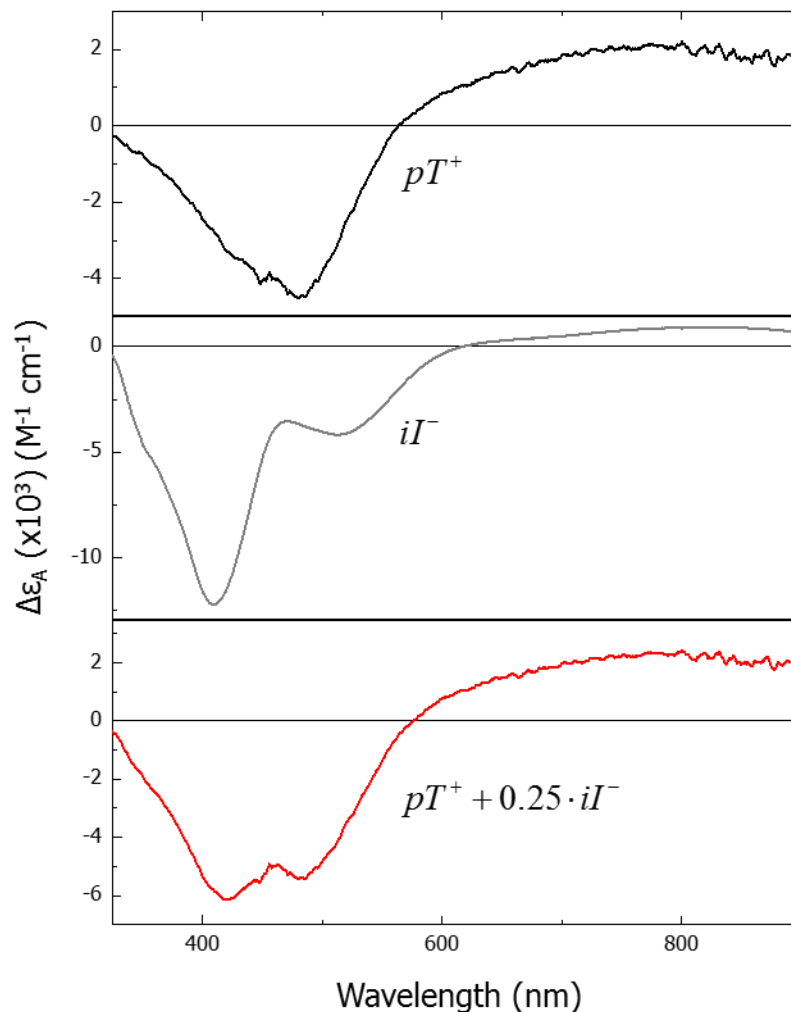


Figure 3.9. (Top) Spectroelectrochemical difference spectrum of pT^+ . (Middle)

Spectroelectrochemical difference spectrum of iI^- -Model. (Bottom) Modeled CS state obtained by adding the pT^+ spectrum to 25% of the intensity of the iI^- difference spectrum. The factor of 0.25 has been introduced to properly account for the relative contributions of pT^+ and iI^- to the CS state spectrum. This stems from the fact that approximately 4 times as many reduced iI complexes can be accommodated by a single positive polaron along an individual polymer chain.³²

3.3.3.3. Charge Recombination

The time constant for charge recombination, as measured through the decay of the PA at 800 nm, is 215 ps (Figure 3.10). Interestingly, the CS state has a significantly shorter lifetime in pT-iI compared to the analogous pT-Ru assembly, where recombination takes place with $\tau \sim 20$ μ s.¹⁵ This dramatic difference is not the result of the recombination energetics. The charge recombination driving force (ΔG_{CR}) is only slightly different in the two assemblies (-1.52 eV in pT-iI and -1.70 eV in pT-Ru) and the reorganization energies (λ) are similar, $\lambda \sim 0.5$ -1.0 eV, computed according to:

$$\lambda = \frac{e^2}{4\pi\epsilon_0} \left(\frac{1}{2R_A} + \frac{1}{2R_D} - \frac{1}{R_{DA}} \right) \left(\frac{1}{n^2} - \frac{1}{\epsilon_s} \right) \quad (3.1)$$

While one would expect some difference in recombination times, the range of expected barrier heights is not enough to account for the approximately four orders of magnitude difference between the two systems. Instead, the variation in recombination times between the pT-iI and pT-Ru systems could stem from differences in the solvent dielectric constants in conjunction with the high hole mobility of pT.³³ We attribute the long-lived CS state in pT-Ru to the ability of the hole to diffuse away from the reduced Ru pendant, which is facilitated by the ability of the polar nitrile solvent to shield the Coulombic attraction between the separated electron and hole.³⁴ Since the pT-iI assembly is not soluble in nitrile solvents, the lower dielectric DCM solvent is less effective at shielding the electron-hole pair, which in turn leads to an overall greater attraction between the electron and hole, smaller average separations, and consequently faster charge recombination.

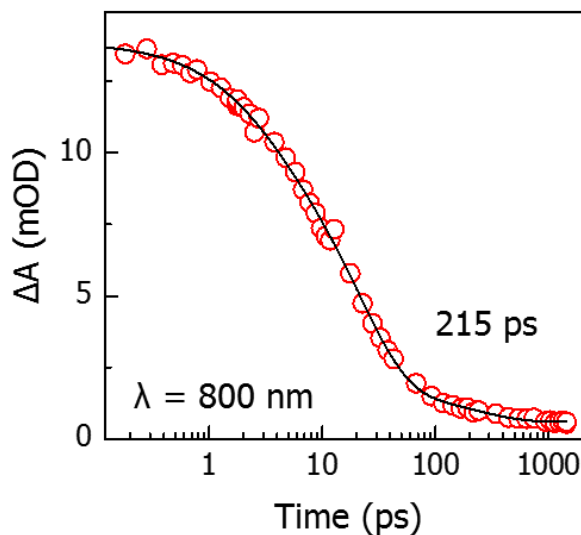


Figure 3.10. Transient absorption decay for pT-iI following 460 nm excitation monitoring the charge recombination kinetics at 800 nm. The signal was fit to a tri-exponential function, in which the fast time components ($\tau_1 = 2.6$ ps and $\tau_2 = 21$ ps) are attributed to the quenching dynamics and relaxation of iI^* . The slower component ($\tau_3 = 215$ ps) is ascribed to charge recombination between pT^+ and iI^- .

3.3.4 Simulation of Excited State Quenching

The photoinduced dynamics in the pT-iI assembly are simulated with a kinetic model that uses the macromolecular structures obtained from fully-atomistic MD simulations to compute EnT and ET rate constants between individual donor (pT^*) and acceptors (iI) pairs.¹⁸ In the sections that follow, we describe the macromolecular polymer structures obtained from MD simulations and the development of the kinetic model. We then compare the kinetic simulation with experiment and discuss the role that the polymer structures play in the overall quenching dynamics.

Macromolecular Structures. Macromolecular structures were obtained from all-atom MD simulations using an approach similar to that employed in the pF-iI studies.¹⁸ Shown in Figure

3.11 is a representative snapshot of an assembly with 15 repeat units (pT-iI₁₅) in the presence of 1800 DCM solvent molecules.

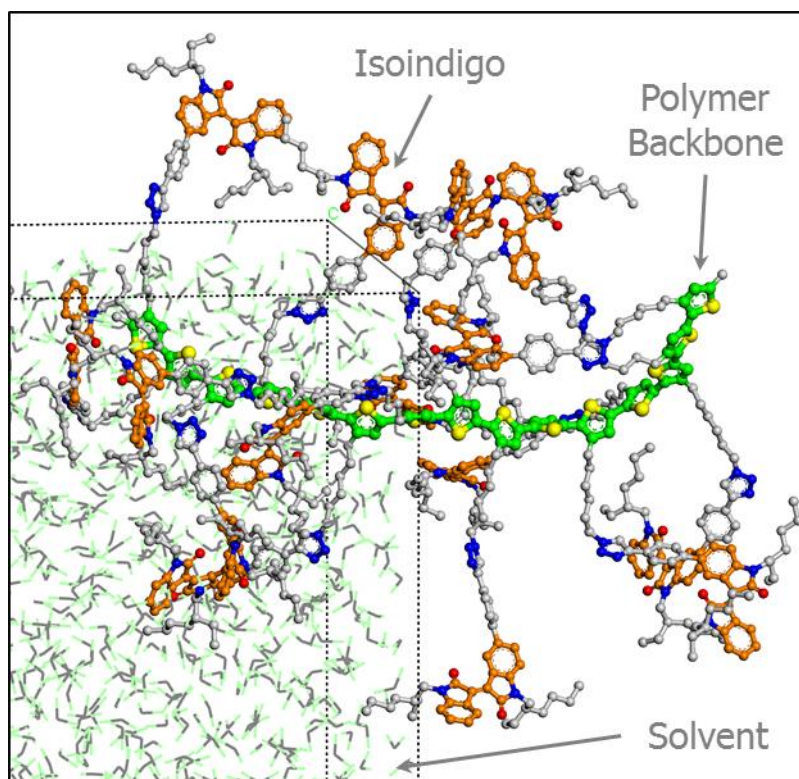


Figure 3.11. Snapshot of the orthorhombic simulation cell with dimensions of 85x50x50 Å consisting of 15 thiophene monomers (green), 15 isoindigo pendants (orange), and 1,800 dichloromethane molecules used for molecular dynamics (MD) simulations of the pT-iI₁₅ polymer assembly. The MD simulations were collected on relaxed polymer structures for 1 ns with periodic boundary conditions.

The solvated assemblies adopt structures with significant twisting of the pT chain and pendants that extend into the solvent. Furthermore, the relatively small size of the thiophene monomer

results in many configurations where 4-5 iI pendants are within 20 Å of a given thiophene (Figure 3.12A) with the nearest iI being as close as 5 Å. The small thiophene monomer also leads to a high pendant density, where the iIs are typically within 7-10 Å of each other (Figure 3.12B).

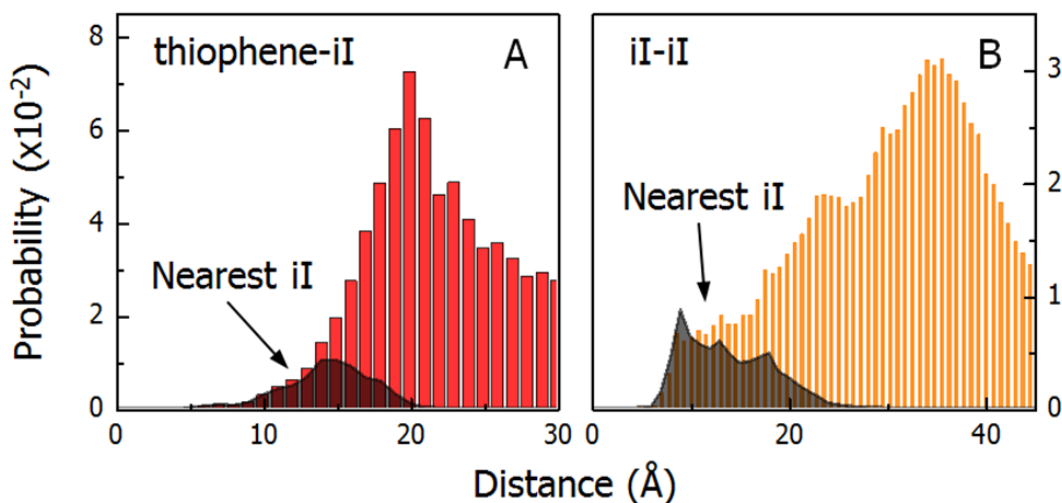


Figure 3.12. (A) Total distance distributions for thiophene-isoindigo (T-iI) and (B) isoindigo-isoindigo (iI-iI) from the ensemble of polymer structures obtained from MD simulations. The bars represent the total distribution while the shaded areas are the nearest isoindigo distance distributions from the perspective of each thiophene monomer (A) and each isoindigo pendant (B).

3.3.4.1. Development of the Kinetic Model

The elements of the kinetic model describing the photoinduced dynamics are depicted in Scheme 3.1. Several of the rate constants in the network are determined from experimental observations and set as fixed parameters. The excited state lifetime of the pT polymer (k_{pT^*}), the pT triplet state (k_{3pT^*}), and the iI pendants (k_{iI^*}), along with the charge recombination rates (k_{CR}) were determined from transient absorption measurements and set to $(490 \text{ ps})^{-1}$, $(13.7 \text{ } \mu\text{s})^{-1}$, $(12.2 \text{ ps})^{-1}$, and $(215 \text{ ps})^{-1}$, respectively, as summarized in Table 3.1. The intersystem crossing rate

constant (k_{ISC}) for formation of the $^3\text{pT}^*$ was determined by Heeger and co-workers to be $(1200 \text{ ps})^{-1}$.³⁰

The rate constant for EnT between the i^{th} thiophene donor and the j^{th} iI acceptor was calculated using the Förster expression:

$$k_{EnT,ij} = A \frac{\Phi_D \kappa_{ij}^2}{\tau_D R_{ij}^6} \int_0^\infty F_D(\lambda) \epsilon_A(\lambda) \lambda^4 d\lambda \quad (3.2)$$

The lifetime (τ_D) and quantum yield (Φ_D) are determined experimentally, while the separation and orientation factors between the donor and acceptor (R_{ij} and κ_{ij}) were extracted from MD simulations. Lastly, the Förster overlap integral was computed between the iI absorbance and pT emission (Figure 3.13).

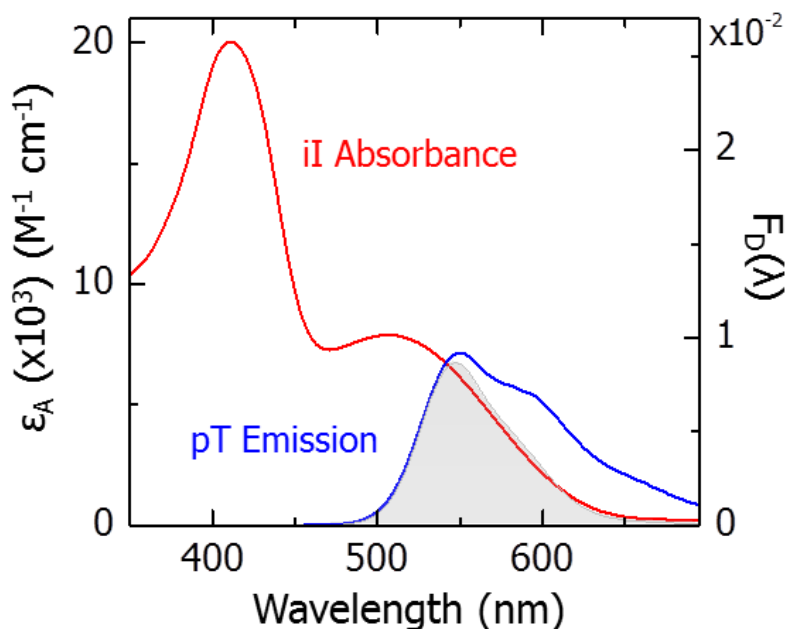


Figure 3.13. iI-Model absorbance (red) and pT emission spectrum (blue) normalized to unity area showing the scaled Förster overlap integrand shaded in gray.

The rate constants for ET were computed according to Marcus theory:

$$k_{ET,ij} = \sqrt{\frac{\pi}{\hbar^2 \lambda k_B T}} |H_{ij}|^2 \cdot \exp\left[-\frac{(\Delta G^0 + \lambda)^2}{4\lambda k_B T}\right] \quad (3.3)$$

We determined the driving force (ΔG^0) from electrochemistry to be -0.78 eV, and estimated the reorganization energy (λ) from MD simulations to be 0.8 eV (Eq. 3.1). The electronic coupling (H_{ij}) between the i^{th} donor and j^{th} acceptor depends upon their separation, i.e.

$$H_{ij} = V_0 \exp\left[-\beta\left(\frac{R_{ij} - R_0}{2}\right)\right] \quad (3.4)$$

where V_0 is the coupling at closest approach and β is the attenuation parameter. It is important to note that V_0 and β are the only adjustable parameters in the kinetic network.

The time-dependent populations for pT^* , iI^* , the CS state, and $^3pT^*$ are determined by a series of rate equations:

$$\frac{d\rho_{T_i^*}}{dt} = -\left(\sum_i k_{ET,ij} + \sum_i k_{ET,ij} + k_{pT^*}\right) \rho_{T_i^*} \quad (3.5a)$$

$$\frac{d\rho_{iI_j^*}}{dt} = \sum_{i=1}^n k_{ET,ij} \cdot \rho_{T_i^*} - k_{iI^*} \cdot \rho_{iI_j^*} \quad (3.5b)$$

$$\frac{d\rho_{CS_i}}{dt} = \sum_{i=1}^n k_{ET,ij} \cdot \rho_{T_i^*} - k_{CR} \cdot \rho_{CS_i} \quad (3.5c)$$

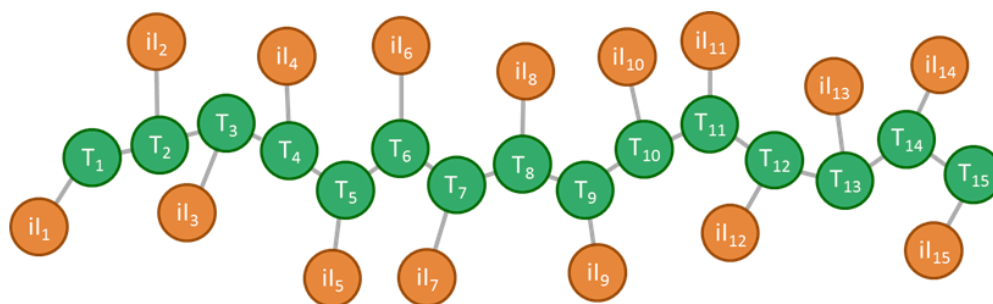
$$\frac{d\rho_{^3pT_i^*}}{dt} = k_{ISC} \cdot \rho_{pT_i^*} - k_{^3pT} \cdot \rho_{^3pT^*} \quad (3.5d)$$

which are solved using matrix methods, as described in the previously mentioned pF-iI system.¹⁸

Implementation of the kinetic model closely follows the simulation of the excited state dynamics in the pF-iI system.¹⁸ Briefly, we select one of the pT-iI₁₅ structures from the MD trajectory and then randomly choose either one of the monomer units or pendant chromophores as the center

location of the excited state. The resulting rate equations (Eq. 3.5a-d) are then solved to obtain the time-dependent populations. This process is repeated 100,000 times, averaging over different structures and initial locations of the excited state.

Scheme 3.1. Illustration of the fundamental photophysical events occurring within the pT-iI assembly.



Kinetic Network

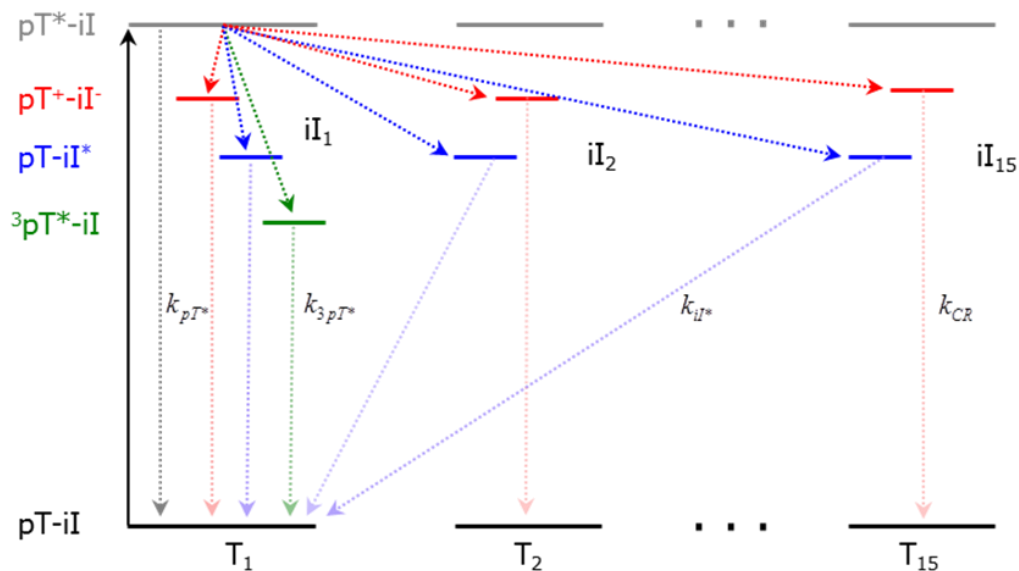


Table 3.1. Simulation parameters used in the kinetic modeling for photoinduced dynamics of the pT-il assembly.

Kinetic Process	Simulation Parameter		Value	Origin
Energy Transfer (k_{EnT})	pT* Lifetime	τ_D	490 ps	fixed ^a
	pT* Quantum Yield	Φ_D	0.12	fixed ^a
	Orientation Factor	κ_{ij}^2	-	MD ^b
	D-A Separation	R_{ij}	-	MD ^b
Electron Transfer (k_{ET})	Attenuation Parameter	β	0.6 \AA^{-1}	adj. ^c
	Coupling	V_0	0.265 eV	adj. ^c
	Driving Force	ΔG^0	-0.78 eV	fixed ^a
	D-A Separation	R_{ij}	-	MD ^b
	Reorganization Energy	λ	0.8 eV	MD ^b
Charge Recombination	Decay Constant	k_{CR}	$(215 \text{ ps})^{-1}$	fixed ^a
pT* Excited State Decay	Decay Constant	k_{pT^*}	$(490 \text{ ps})^{-1}$	fixed ^a
Intersystem Crossing	³ pT* Formation	k_{ISC}	$(1200 \text{ ps})^{-1}$	fixed ^a
	³ pT* Relaxation	$k_{3\text{pT}^*}$	$(13.7 \text{ }\mu\text{s})^{-1}$	fixed ^a
il* Excited State Decay	Decay Constant	k_{il^*}	$(12.2 \text{ ps})^{-1}$	fixed ^a

^aMeasured experimentally and treated as fixed parameter in simulation

^bCalculated from MD structure.

^cDetermined by fit of kinetic simulation to transient absorption data.

3.3.4.2. Comparison with Experiment

Simulated transients are obtained for direct comparison with experiment by first selecting values for β and V_0 (the only adjustable parameters in the model) and using those to determine the time dependent populations ($\rho_{pT^*}(t)$, $\rho_{il^*}(t)$, $\rho_{CS}(t)$, and $\rho_{3pT^*}(t)$) from the kinetic model (Eq. 3.5a-d). The kinetics obtained from transient absorption is a linear combination of these populations, i.e.

$$\Delta A_{Sim,t}^{pT-il} = -a \cdot \rho_{pT^*}(t) + b \cdot \rho_{il^*}(t) + c \cdot \rho_{3pT^*}(t) + d \cdot \rho_{CS}(t) \quad (3.6)$$

We fit Equation 3.6 to the experimental transient at 575 nm using a nonlinear least squares method to determine the amplitudes. As discussed above, at this probe wavelength the CS state does not contribute, and thus $d=0$.

We repeated this process for a series of (β , V_0) values. The attenuation parameter (β) reflects the fall-off of the wave function and for through-space ET has a value of 1.0 \AA^{-1} .³⁵ While simulations of the pF-iI assembly reproduced the data well with $\beta=1.0 \text{ \AA}^{-1}$,¹⁸ we find that setting β to 1.0 \AA^{-1} in the pT-iI system gives unacceptable fits for all values of V_0 . Instead, a smaller value ($\beta=0.6 \text{ \AA}^{-1}$) along with a larger coupling ($V_0=265 \text{ meV}$) accurately reproduce the 575 nm kinetics (Figure 3.14). The larger V_0 matches the 265 meV value predicted by the Amsterdam Density Functional (ADF) program package³⁶ (Figure 3.15). The origin of the smaller attenuation parameter in the pT-iI assembly compared to pF-iI is unclear, but may stem from differences in the conformations of the side chains. Previous studies have shown that in saturated linkers where the sp^3 carbons adopt an all-trans configuration, the electronic communication between the donor and acceptor is enhanced over large distances, leading to amplified ET rates.^{12, 37}

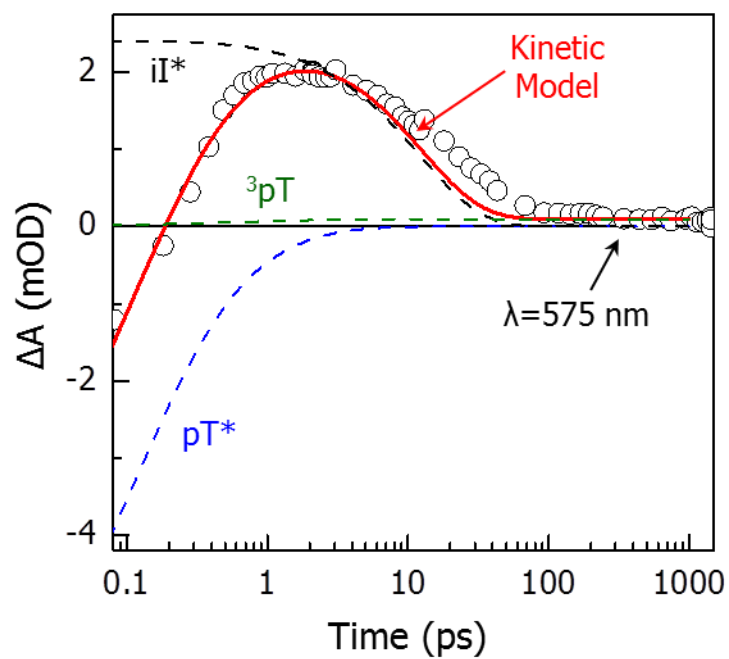


Figure 3.14. Comparison between the pT-iI experimental kinetics at 575 nm (black circles) and the linear combination of the simulated photoinduced populations (red line) described by equation 3.4.

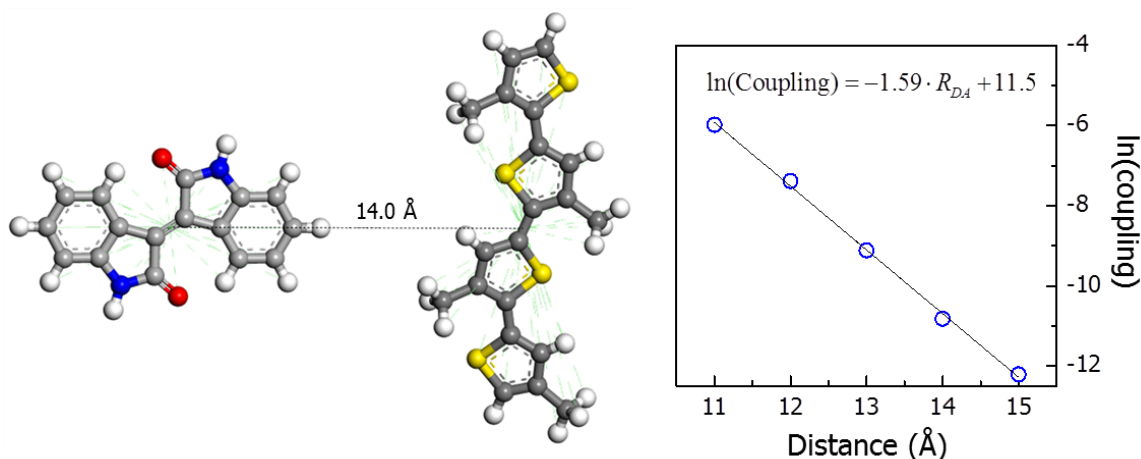


Figure 3.15. (Left) Model isoindigo and tetrathiophene oligomer pair used for the estimation of the close-range electronic coupling (V_0) with the ADF computational package. The distance is computed from centroids placed on each unit. (Right) Plot of $\ln(\text{Coupling})$ versus distance obtained from calculation of the charge transfer integrals of the model system.

3.3.4.3. Microscopic Analysis of Simulation Results

Because the polymer exciton can be quenched by any of the pendant groups, the *total* rate constants for EnT ($k_{EnT,i}$) and ET ($k_{ET,i}$) quenching of the i^{th} thiophene monomer are the sum of the individual EnT and ET rate constants to all the pendants, i.e.

$$k_{EnT,i} = \sum_j k_{EnT,ij} \quad (3.7a)$$

$$k_{ET,i} = \sum_j k_{ET,ij} \quad (3.7b)$$

The contribution of the individual EnT and ET rate constants to the total quenching rate is depicted for a typical structure in Figure 3.16. The monomer unit colored in red shows the location of the pT exciton. The red and blue bars at the right denote the magnitude of $k_{ET,i}$ and $k_{EnT,i}$, respectively. In this configuration, ET dominates with $k_{ET,i}$ being about 15 times greater than $k_{EnT,i}$

$((0.55 \text{ ps})^{-1}$ versus $(8.26 \text{ ps})^{-1}$). EnT in pT-iI is suppressed relative to ET due to a small Förster overlap integral ($3.65 \times 10^{14} \text{ M}^{-1} \text{ cm}^{-1} \text{ nm}^4$) for EnT (Figure 3.15) and a relatively large electronic coupling for ET. As a result, ET quenching is observed to be significantly faster than EnT in virtually every configuration in the ensemble. This is in contrast to the previously mentioned pF-iI assembly, where the pF emission has significant overlap with the iI absorption and the electronic coupling for ET is smaller, leading to a situation in which EnT is the dominant quenching mechanism.¹⁸

As a result of the high pendant density, $k_{\text{EnT},i}$ and $k_{\text{ET},i}$ have significant contributions from multiple pendants. In this case, ET to the nearest iI pendant accounts for 35% of $k_{\text{ET},i}$ and the next nearest iI contributes 30%. The net result is that the pT* excitation is lost with an effective rate constant that is 2 to 4 times greater than the individual rates.

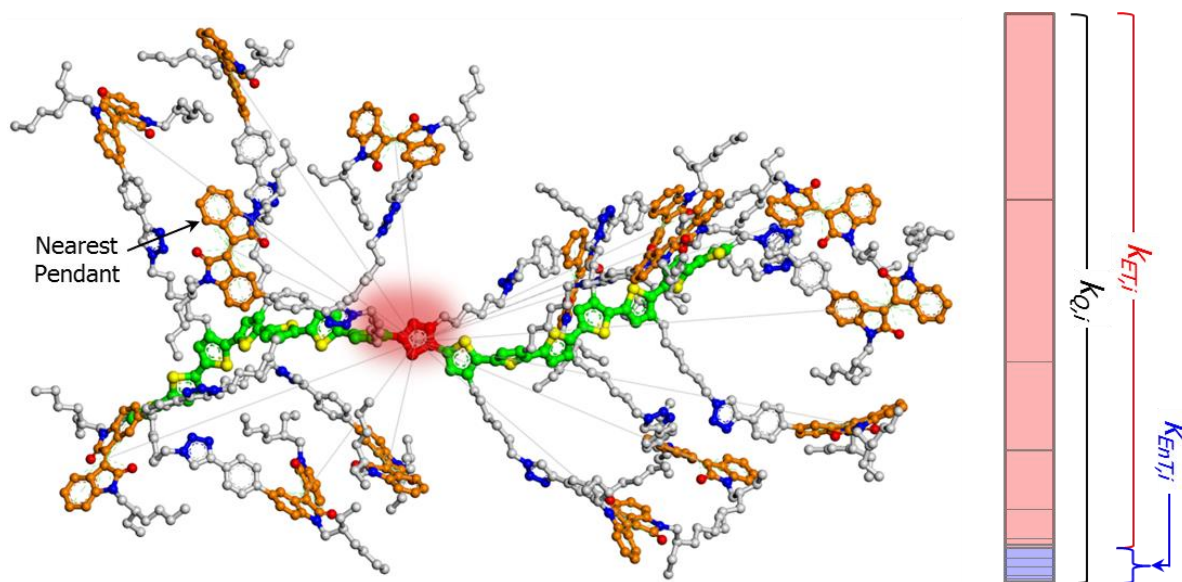


Figure 3.16. Graphical illustration of the kinetic model applied to a representative pT-iI polymer structure obtained from MD simulations. The initial exciton is shown as a red cloud along the polymer backbone, in which the energy and electron transfer rates are computed using the distances and orientation factors. The total quenching rate is expressed as the sum of the individual computed rates.

3.3.4.3. Ensemble ET Quenching Dynamics

Shown in Figure 3.17 is the distribution of total quenching rate constants ($k_{Q,i} = k_{EnT,i} + k_{ET,i}$) obtained from an ensemble of 27,090 structural configurations and exciton locations. The distribution is broad, corresponding to quenching times that range from less than 100 fs to about 10 ps. Although ET is the dominant quenching mechanism (i.e. $k_{ET,i} > k_{EnT,i}$) in all configurations, EnT does contribute when the pendant structure in the vicinity of the pT* exciton is less conducive to ET. The fraction of quenching events that proceed through ET is given by:

$$P_{ET,i} = \frac{k_{ET,i}}{k_{ET,i} + k_{EnT,i} + k_{ISC}} \quad (3.8)$$

This quantity is computed for each structure/exciton location in the ensemble and the average ET efficiency ($\langle P_{ET,i} \rangle$) is depicted as a function of $k_{Q,i}$ in Figure 3.17. The fastest quenching events (i.e., $k_{Q,i} > (100 \text{ fs})^{-1}$) are due almost entirely to ET (i.e., $P_{ET,i} > 99\%$). However, as $k_{Q,i}$ slows, EnT becomes increasingly important and $\langle P_{ET,i} \rangle$ approaches 70% for $k_{Q,i} \sim (10 \text{ ps})^{-1}$.

The number of iI pendants participating in the quenching also varies with total quenching rate, $k_{Q,i}$. The presence of multiple pendants situated near the backbone results in a larger quenching rate constant when compared to quenching by a single iI. To quantify this, we have defined the number of acceptors as the number pendants accounting for 80% of $k_{Q,i}$ (Figure 3.17). The fastest quenching events ($k_{Q,i} > (50 \text{ fs})^{-1}$) are dominated by just one or two pendants. As the quenching rate slows, the number of iIs participating grows to about 4 when $k_{Q,i} \sim (0.5\text{-}1 \text{ ps})^{-1}$. This increase is largely a result of the closest acceptor lying further from the excitation, such that no single iI pendant is favored. Even slower quenching events ($k_{Q,i} < (1\text{-}10 \text{ ps})^{-1}$) proceed by ET to a one or two iIs that lie further from the backbone.

Therefore, ET plays a dominant role in the quenching dynamics of the pT-iI assembly, where the macromolecular structure mediates short donor-acceptor distances in a majority of the configurations. EnT quenching plays a minor role due to the small spectral overlap between the pT emission and iI absorption. This is in contrast to the previously studied pF-iI system, where although ET was faster than EnT, the combination of large donor-acceptor distances in a significant fraction of the configurations and extensive spectral overlap ensured efficient long-range EnT, with EnT quenching taking place in $\sim 70\%$ of the excitations. The conclusions drawn

from these systems reveal that the macromolecular polymer structure plays an important role in directing the overall quenching dynamics in multichromophore polymer assemblies.

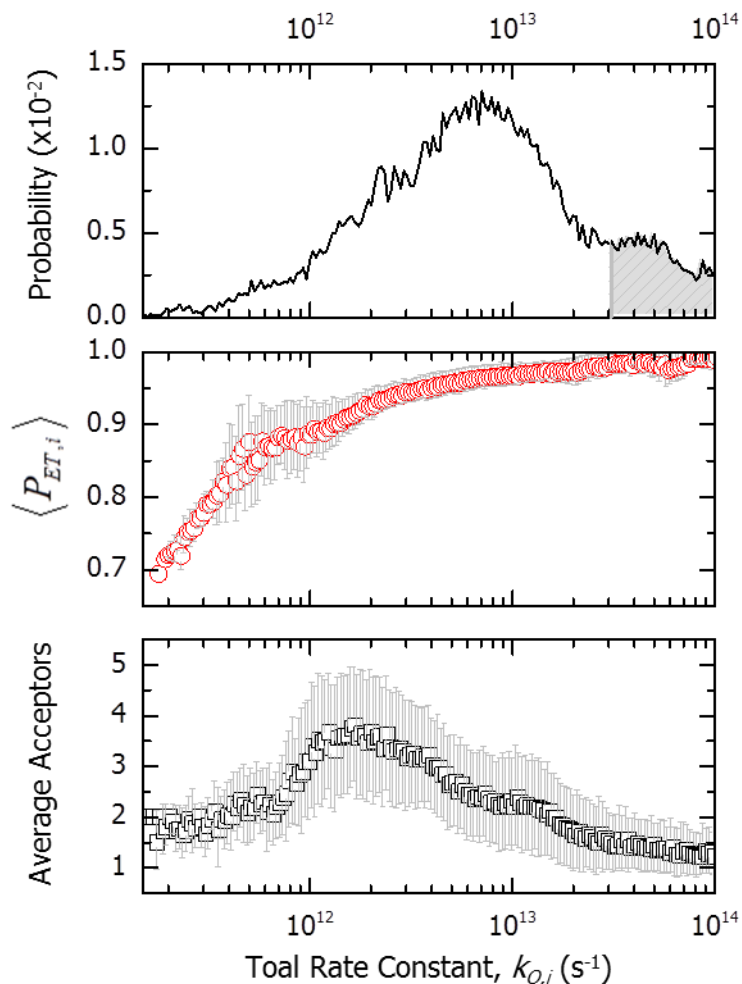


Figure 3.17. (Top) Distribution of total quenching rate constants from the pT-iI kinetic simulations (black line). The gray shaded area reflects quenching rates that lie outside of the ultrafast transient absorption instrument response. The total rates were computed for each configuration and binned on a logarithmic scale ranging from 10^8 to 10^{15} s^{-1} with 500 bins. (Middle) Average electron transfer efficiency (red circles) computed as a function of the total quenching rate constant from each configuration. (Bottom) Average number of acceptors that are needed to achieve 80% of the total electron transfer quenching rate (black squares). The standard deviation for each measurement is shown as the light gray bar.

3.4 CONCLUSIONS

We have demonstrated a multichromophore light-harvesting assembly combining a π -conjugated polymer functionalized with pendant isoindigo chromophores. Femtosecond transient absorption spectroscopy reveals that photoexcitation of the polymer backbone results in multi-exponential quenching kinetics of the polymer excited state on the fs-ps time scales, decaying primarily as a result of ET to yield a CS state, reducing the pendant iI chromophores and leaving a positively charged polaron on the polymer backbone. This CS state persists for hundreds of picoseconds before complete charge recombination occurs. A kinetic analysis in conjunction with MD simulations of the pT-iI assembly extends the spectroscopic results, revealing the complicated microscopic details that dictate the observed dynamics. The range of donor-acceptor separations of the pendants relative to the backbone control the quenching pathway. In a majority of the configurations, the polymer excited state is quenched quickly by ET. However, there are a small (~5%) number of polymer configurations in which the pendants are situated far from the polymer excited state and are thus quenched by a combination of ET and EnT on the picosecond time scale.

REFERENCES

1. Pullerits, T.; Sundstrom, V., Photosynthetic Light-Harvesting Pigment-Protein Complexes: Toward Understanding How and Why. *Acc. Chem. Res.* **1996**, *29*, 381-389.
2. van Grondelle, R.; Novoderezhkin, V. I., Energy Transfer in Photosynthesis: Experimental Insights and Quantitative Models. *Phys Chem Chem Phys* **2006**, *8*, 793-807.
3. Gust, D.; Moore, T. A.; Moore, A. L., Solar Fuels Via Artificial Photosynthesis. *Acc. Chem. Res.* **2009**, *42*, 1890-1898.
4. Concepcion, J. J.; Jurss, J. W.; Brennaman, M. K.; Hoertz, P. G.; Patrocinio, A. O. T.; Iha, N. Y. M.; Templeton, J. L.; Meyer, T. J., Making Oxygen with Ruthenium Complexes. *Accounts Chem Res* **2009**, *42*, 1954-1965.
5. Morris, A. J.; Meyer, G. J.; Fujita, E., Molecular Approaches to the Photocatalytic Reduction of Carbon Dioxide for Solar Fuels. *Acc. Chem. Res.* **2009**, *42*, 1983-1994.
6. Meyer, T. J., Chemical Approaches to Artificial Photosynthesis. *Acc. Chem. Res.* **1989**, *22*, 163-170.
7. Alstrum-Acevedo, J. H.; Brennaman, M. K.; Meyer, T. J., Chemical Approaches to Artificial Photosynthesis. 2. *Inorg. Chem.* **2005**, *44*, 6802-6827.
8. Morseth, Z. A.; Wang, L.; Puodziukynaite, E.; Leem, G.; Gilligan, A. T.; Meyer, T. J.; Schanze, K. S.; Reynolds, J. R.; Papanikolas, J. M., Ultrafast Dynamics in Multifunctional Ru(II)-Loaded Polymers for Solar Energy Conversion. *Acc. Chem. Res.* **2015**, *48*, 818-827.
9. Aratani, N.; Kim, D.; Osuka, A., Discrete Cyclic Porphyrin Arrays as Artificial Light-Harvesting Antenna. *Acc. Chem. Res.* **2009**, *42*, 1922-1934.
10. Ziessel, R.; Ulrich, G.; Haefele, A.; Harriman, A., An Artificial Light-Harvesting Array Constructed from Multiple Bodipy Dyes. *J. Am. Chem. Soc.* **2013**, *135*, 11330-11344.
11. Leem, G.; Morseth, Z. A.; Puodziukynaite, E.; Jiang, J. L.; Fang, Z.; Gilligan, A. T.; Reynolds, J. R.; Papanikolas, J. M.; Schanze, K. S., Light Harvesting and Charge Separation in a Pi-Conjugated Antenna Polymer Bound to Tio₂. *J. Phys. Chem. C* **2014**, *118*, 28535-28541.
12. Leem, G.; Morseth, Z. A.; Wee, K. R.; Jiang, J. L.; Brennaman, M. K.; Papanikolas, J. M.; Schanze, K. S., Polymer-Based Ruthenium(II) Polypyridyl Chromophores on Tio₂ for Solar Energy Conversion. *Chem-Asian J* **2016**, *11*, 1257-1267.
13. Fleming, C. N.; Maxwell, K. A.; DeSimone, J. M.; Meyer, T. J.; Papanikolas, J. M., Ultrafast Excited-State Energy Migration Dynamics in an Efficient Light-Harvesting Antenna Polymer Based on Ru(II) and Os(II) Polypyridyl Complexes. *J. Am. Chem. Soc.* **2001**, *123*, 10336-10347.

14. Puodziukynaite, E.; Wang, L.; Schanze, K. S.; Papanikolas, J. M.; Reynolds, J. R., Poly(Fluorene-Co-Thiophene)-Based Ionic Transition-Metal Complex Polymers for Solar Energy Harvesting and Storage Applications. *Polym Chem-Uk* **2014**, *5*, 2363-2369.
15. Wang, L.; Puodziukynaite, E.; Grumstrup, E. M.; Brown, A. C.; Keinan, S.; Schanze, K. S.; Reynolds, J. R.; Papanikolas, J. M., Ultrafast Formation of a Long-Lived Charge-Separated State in a Ru-Loaded Poly(3-Hexylthiophene) Light-Harvesting Polymer. *J. Phys. Chem. Lett.* **2013**, *4*, 2269-2273.
16. Wang, L.; Puodziukynaite, E.; Vary, R. P.; Grumstrup, E. M.; Walczak, R. M.; Zolotarskaya, O. Y.; Schanze, K. S.; Reynolds, J. R.; Papanikolas, J. M., Competition between Ultrafast Energy Flow and Electron Transfer in a Ru(II)-Loaded Polyfluorene Light-Harvesting Polymer. *J. Phys. Chem. Lett.* **2012**, *3*, 2453-2457.
17. Fleming, C. N.; Jang, P.; Meyer, T. J.; Papanikolas, J. M., Energy Migration Dynamics in a Ru(II)- and Os(II)-Based Antenna Polymer Embedded in a Disordered, Rigid Medium. *J. Phys. Chem. B.* **2004**, *108*, 2205-2209.
18. Morseth, Z. A.; Pho, T. V.; Gilligan, A. T.; Dillon, R. J.; Schanze, K. S.; Reynolds, J. R.; Papanikolas, J. M., Role of Macromolecular Structure in the Ultrafast Energy and Electron Transfer Dynamics of a Light-Harvesting Polymer. *J. Phys. Chem. B.* **2016**, *120*, 7937-7948.
19. Frisch, M. J.; Trucks, G. W.; Schlegel, H. B.; Scuseria, G. E.; Robb, M. A.; Cheeseman, J. R.; Scalmani, G.; Barone, V.; Mennucci, B.; Petersson, G. A., et al. *Gaussian 09*, Gaussian, Inc.: Wallingford, CT, USA, 2009.
20. Mei, J.; Graham, K. R.; Stalder, R.; Reynolds, J. R., Synthesis of Isoindigo-Based Oligothiophenes for Molecular Bulk Heterojunction Solar Cells. *Org Lett* **2010**, *12*, 660-3.
21. Price, D. W.; Tour, J. M., Biphenyl- and Fluorenyl-Based Potential Molecular Electronic Devices. *Tetrahedron* **2003**, *59*, 3131-3156.
22. Chaignon, F.; Falkenstrom, M.; Karlsson, S.; Blart, E.; Odobel, F.; Hammarstrom, L., Very Large Acceleration of the Photoinduced Electron Transfer in a Ru(Bpy)(3)-Naphthalene Bisimide Dyad Bridged on the Naphthyl Core. *Chem. Comm.* **2007**, 64-66.
23. Alvarez, S. G.; Alvarez, M. T., A Practical Procedure for the Synthesis of Alkyl Azides at Ambient Temperature in Dimethyl Sulfoxide in High Purity and Yield. *Synthesis-Stuttgart* **1997**, 413-414.
24. Vezie, M. S.; Few, S.; Meager, I.; Pieridou, G.; Dorling, B.; Ashraf, R. S.; Goni, A. R.; Bronstein, H.; McCulloch, I.; Hayes, S. C., et al., Exploring the Origin of High Optical Absorption in Conjugated Polymers. *Nat Mater* **2016**, *15*, 746-+.
25. Estrada, L. A.; Stalder, R.; Abboud, K. A.; Risko, C.; Bredas, J. L.; Reynolds, J. R., Understanding the Electronic Structure of Isoindigo in Conjugated Systems: A Combined Theoretical and Experimental Approach. *Macromolecules* **2013**, *46*, 8832-8844.

26. Busby, E.; Carroll, E. C.; Chinn, E. M.; Chang, L. L.; Moule, A. J.; Larsen, D. S., Excited-State Self-Trapping and Ground-State Relaxation Dynamics in Poly(3-Hexylthiophene) Resolved with Broadband Pump-Dump-Probe Spectroscopy. *J. Phys. Chem. Lett.* **2011**, *2*, 2764-2769.
27. Westenhoff, S.; Daniel, C.; Friend, R. H.; Silva, C.; Sundstrom, V.; Yartsev, A., Exciton Migration in a Polythiophene: Probing the Spatial and Energy Domain by Line-Dipole Forster-Type Energy Transfer. *J. Chem. Phys.* **2005**, *122*, 094903.
28. Banerji, N.; Cowan, S.; Vauthey, E.; Heeger, A. J., Ultrafast Relaxation of the Poly(3-Hexylthiophene) Emission Spectrum. *J. Phys. Chem. C* **2011**, *115*, 9726-9739.
29. Huang, Y. F.; Chen, H. L.; Ting, J. W.; Liao, C. S.; Larsen, R. W.; Fann, W., Direct Measurement of the Triplet Quantum Yield of Poly(3-Dodecylthiophene) in Solution. *J. Phys. Chem. B* **2004**, *108*, 9619-9622.
30. Kraabel, B.; Moses, D.; Heeger, A. J., Direct Observation of the Intersystem Crossing in Poly(3-Octylthiophene). *J. Chem. Phys.* **1995**, *103*, 5102-5108.
31. This probe wavelength corresponds to the zero-crossing point in the CS state spectrum and therefore the CS does not contribute to the signal.
32. Takeda, N.; Miller, J. R., Poly(3-Decylthiophene) Radical Anions and Cations in Solution: Single and Multiple Polarons and Their Delocalization Lengths in Conjugated Polymers. *J. Phys. Chem. B* **2012**, *116*, 14715-14723.
33. Sirringhaus, H.; Tessler, N.; Friend, R. H., Integrated Optoelectronic Devices Based on Conjugated Polymers. *Science* **1998**, *280*, 1741-1744.
34. Schlag, E. W.; Levine, R. D., Ionization, Charge Separation, Charge Recombination, and Electron-Transfer in Large Systems. *J. Phys. Chem.* **1992**, *96*, 10608-10616.
35. Gray, H. B.; Winkler, J. R., Long-Range Electron Transfer. *P. Natl. Acad. Sci. U.S.A.* **2005**, *102*, 3534-3539.
36. te Velde, G.; Bickelhaupt, F. M.; Baerends, E. J.; Guerra, C. F.; Van Gisbergen, S. J. A.; Snijders, J. G.; Ziegler, T., Chemistry with ADF. *J Comput Chem* **2001**, *22*, 931-967.
37. This Probe Wavelength Corresponds to the Zero-Crossing Point in the Cs State Spectrum and Therefore the Cs Does Not Contribute to the Signal.

CHAPTER 4. POLYMER-BASED RUTHENIUM(II) POLYPYRIDYL CHROMOPHORES FOR SOLAR ENERGY CONVERSION APPLICATIONS

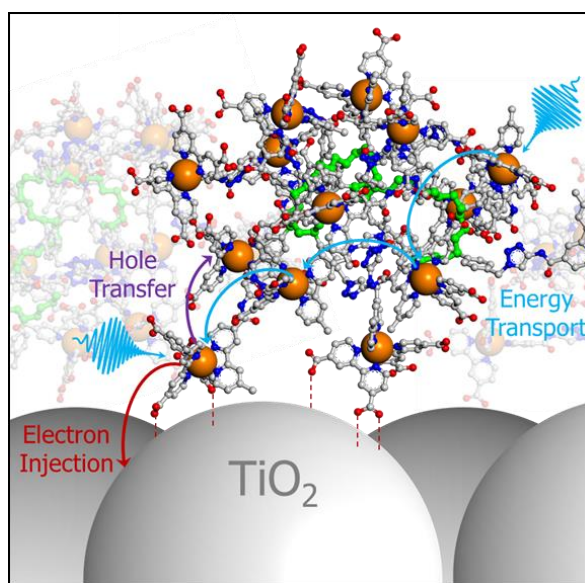
This chapter contains work that previously appeared as an article in Chemistry-An Asian Journal. The original citation is as follows: Leem, G.; Morseth, Z.A.; Wee, K.R.; Jiang, J.; Papanikolas, J.M.; Schanze, K.S. "Polymer-based Ruthenium(II) Polypyridyl Chromophores on TiO₂ for Solar Energy Conversion," *Chem. Asian J.* **2016**, *11*, 1257-1267.

4.1 INTRODUCTION

Dye-sensitized solar cells (DSSCs) are photovoltaic devices for solar energy conversion based on dye sensitization of wideband gap semiconductors, typically nanocrystalline anatase TiO₂, by molecular chromophores and have received enormous attention since their inception in 1991.¹ In these systems, a variety of chromophores serve as efficient sensitizers, extending the visible absorption spectrum of both n- and p-type metal oxides.²⁻⁴ Although "single-site" chromophores such as [cis-(dithiocyanato)- Ru-bis(2,2'-bipyridine-4,4'-dicarboxylate)] complex (N3), its doubly protonated tetrabutylammonium salt (N719), and other related sensitizers⁵⁻⁷ remain among the most commonly used in DSSCs, there has been an increased effort towards the development of multichromophoric assemblies capable of enhancing the light-absorbing properties to achieve appreciable solar efficiencies.⁸⁻¹⁰ Central to the realization of solar conversion technologies is the development of functional light-harvesting assemblies that mimic photosynthesis by coupling multi-chromophore antennas that can efficiently funnel excited state energy to locations where charge-separation can occur (Scheme 4.1). In recent years, multi-chromophore light-harvesting assemblies based on a wide range of architectures have been explored (i.e., polymers, dendrimers, peptides, porphyrin arrays).¹¹⁻¹⁴ Owing to the intrinsic heterogeneity of the mesoporous semiconductor surface and polymer assemblies, the dynamics

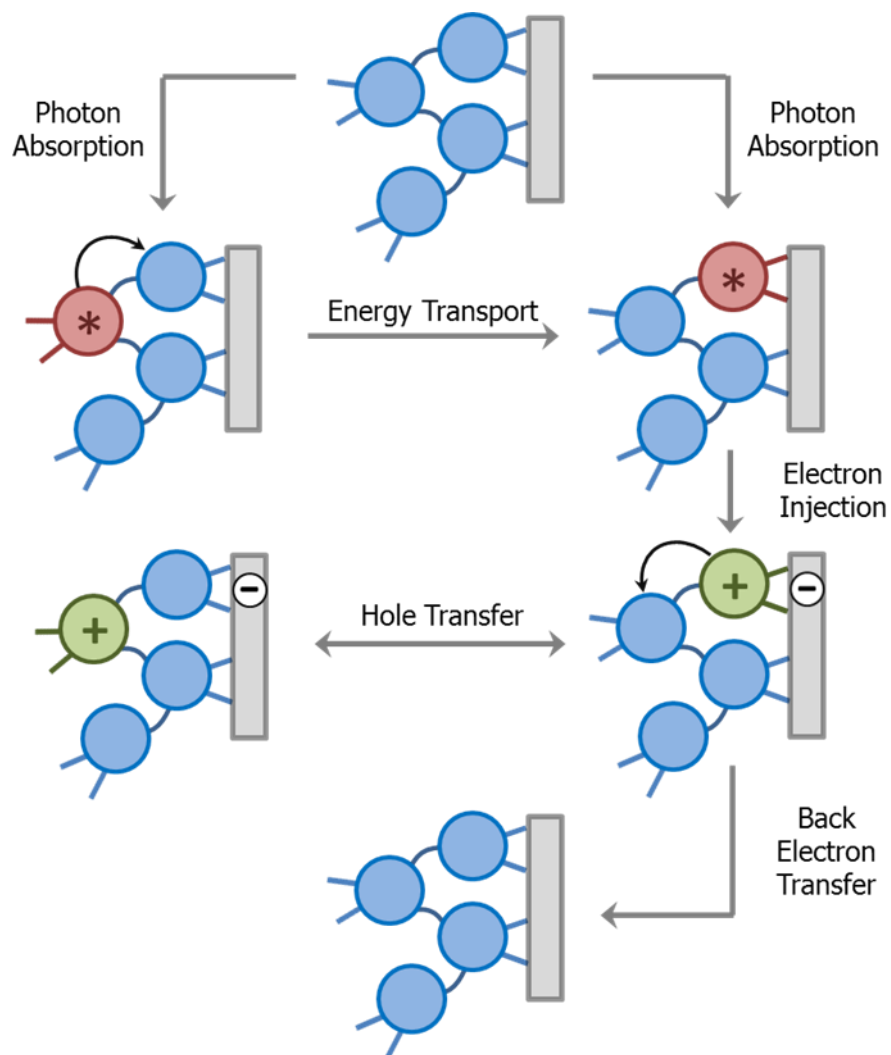
are inherently complex. Thus, a detailed understanding of the structure and dynamical phenomena that ensue following photon absorption is paramount in the rational design of these polymer assemblies.

Scheme 4.1. Cartoon of pS-Ru-A (obtained from molecular dynamics simulations) anchored onto a TiO_2 surface, displaying the primary photophysical events.



In this chapter, we describe the photophysics of a polystyrene- based assembly with pendant Ru^{II} chromophores containing carboxylic acid moieties (pS-Ru-A) anchored to mesoporous TiO₂ films (Scheme 4.2). With the use of transient absorption spectroscopy applied to the polymer-loaded TiO₂, we find that photoexcitation of the Ru^{II} complexes appended to the polymer backbone is followed by electron injection on the picosecond time scale. Time-resolved emission spectroscopy reveals evidence for a slower quenching process (20–50 ns), which is attributed to energy transport and delayed charge injection. The resulting charge-separated state is found to persist on a time scale of ~100 ns, which is longer than for monomeric Ru^{II} sensitizers. This finding could imply a combination of energy transport from unbound complexes towards the surface for electron injection and hole transfer away from the surface to spatially separate the electron-hole pair and delay recombination. Molecular dynamics simulations of pS-Ru-A assemblies in fluid solution provides insight into the relationship between the structure and the observed photoinduced dynamics within the light harvesting arrays.

Scheme 4.2. Schematic representation of the photophysical events of the pS-Ru-A assembly at the surface of TiO_2 . The blue circles represent $\text{Ru}(\text{L})_3^{2+}$ chromophores while the green and red circles correspond to $\text{Ru}(\text{L})_3^{3+}$ and $\text{Ru}(\text{L})_3^{2+*}$.



4.2. EXPERIMENTAL METHODS

4.2.1. Sample Preparation

Thin films of ZrO_2 and TiO_2 deposited on FTO glass were soaked for 48 hours in a solution containing the sensitizer dissolved in acetonitrile and were placed in a home-made 1 cm quartz cuvette at a 45 degree angle relative to the front face of the cuvette. All transient absorption experiments were performed with the sensitized films immersed in argon-saturated solutions of 100 mM LiClO_4 dissolved in acetonitrile and were raster-scanned to prevent photodegradation of the samples.

4.2.2. Steady State Techniques

UV-Visible spectra were recorded on an HP 8543 Diode Array Spectrophotometer. UV-Visible spectra were recorded on all samples before and after excited state measurements to ensure that samples did not undergo photodecomposition.

Emission spectra were measured on Photon Technology International (PTI 4SE-NIR) Quantamaster™ spectrofluorometer equipped with a continuous xenon arc lamp as the excitation source. The emitting light was collected at 90° to the excitation beam and detected by a Multi-mode 814 photomultiplier tube (PMT) in photon counting mode (digital).

4.2.3. Time-Resolved Emission Spectroscopy

Time-resolved emission measurements were collected using an Edinburgh Instruments FLS920 fluorescence spectrometer by the time-correlated single photon counting (TCSPC) technique. The excitation source was a 444.2 nm diode laser (Edinburgh Instruments EPL-445, 73 ps fwhm pulse width, 2 mm beam diameter) operated at 100 kHz. Emission measurements were monitored at 660 nm with a bandwidth of 20 nm and were detected with a Hamamatsu 2658P photomultiplier tube.

A 515 nm long-pass filter was used to reject the laser scatter. All measurements were performed with the sensitized films immersed in argon-saturated solutions of 100 mM LiClO₄ dissolved in acetonitrile.

4.2.4. Transient Absorption Spectroscopy

Transient absorption measurements were performed using a home-built transient absorption spectrometer. The spectrometer is based on a commercially available ultrafast laser system (Clark MXR CPA-2210). The system consists of an erbium-doped fiber ring oscillator pumped by a solid-state fiber coupled laser diode operating at 980 nm and a chirped pulse Ti:Sapphire regenerative amplifier pumped by a frequency-doubled, Q-switched Nd:YAG laser. Following pulse compression, the amplifier produces pulses centered at 775 nm with 120 fs fwhm duration at 1 kHz with pulse energies of 1.6 mJ/pulse. The 420 nm pump pulse was generated in a 2 mm BBO crystal by sum frequency generation of the 775 nm fundamental and the second harmonic of the 1840 nm idler from an optical parametric amplifier (Light Conversion TOPAS-C) while the femtosecond probe pulse is generated by focusing 3 mW of the 775 nm amplifier output into a translating 5 mm thick CaF₂ window. The pump beam is focused onto the sample using a 300 mm lens and the probe beam is focused and overlapped with a 250 mm spherical aluminum mirror. Spectra were collected on a shot-by-shot (1 kHz) basis over the range of 350 to 820 nm with a sensitivity of up to 0.1 mOD. The angle between the pump and probe polarization vectors was set to magic angle ($\sim 54.7^\circ$) to avoid polarization effects and ensure that only excited-state population dynamics were being monitored and the sample was raster scanned to provide for a fresh sample between laser pulses. Following data collection, the frequency chirp in the probe pulse was characterized using the optical Kerr response of liquid CCl₄ in a 2 mm cuvette in a polarization

gating geometry. The spectra were chirp-corrected using a data processing program written in LabVIEW.

Sub-nanosecond transient measurements were performed with an Ultrafast Systems EOS spectrometer. The probe pulse is generated by continuum generation from a photonic crystal fiber and detected by a fiber optic coupled multichannel spectrometer with a CMOS sensor. The pump-probe delay is electronically controlled and the kinetic window ranges from 500 ps – 400 μ s. The time resolution of the instrument is around 500 ps, dictated by the width of the probe pulse and the timing electronics.

4.2.5 Transient Absorption Kinetics Fitting Parameters

The fsTA kinetics traces at 385 nm were fit to a bi-exponential function with an x and y -offset as implemented in Origin 9.0. The instrument response function (IRF) at 385 nm from the cross-correlation determined the earliest time point in the fitting function. The fitting function was minimized using the Levenberg-Marquardt method until a reduced Chi-Square value of $1e^{-9}$ was achieved.

4.2.6. Electronic Structure Calculations

Electronic structure calculations were performed using Gaussian v09a02.¹⁵ The ground-state geometry of the pS-Ru-A monomer was optimized using the B3LYP density functional theory (DFT) functional¹⁶ with the LANL2DZ basis set for the Ru^{II} center and the 6-31G** basis set for the C, H, N, and O atoms. Solvation effects for acetonitrile were included used a polarizable continuum model (PCM), as implemented in Gaussian 09 (v09a02).

4.2.7 Molecular Dynamics Simulations

The polymer assembly was constructed and the geometries were optimized and annealed in the absence of solvent with atomic charges obtained from the Gaussian 09 electronic structure

calculations using natural bond order (NBO) population analysis.¹⁷ The annealing step consisted of a series of temperature cycles ranging from 300 to 700 K using the Universal Force Field (UFF).¹⁸ The simulation cell was comprised of a 14-repeat unit polymer with 1200 acetonitrile molecules. The cell was then annealed for 1 ns using the UFF with the temperature ranging from 300 K to 700 K. The annealed simulation cells were then used as initial conditions for constant NVT molecular dynamics trajectories at a temperature of 298 K controlled by the Nose thermostat with a Q-ratio of 0.01. Dynamics were collected for a total of 1 ns in each solvent with snapshots taken every 2.5 ps, giving a trajectory with 400 snapshots for analysis from each initial configuration.

4.3. RESULTS AND DISCUSSION

4.3.1. Static Spectroscopy

The ground-state absorbance spectrum of the pS-Ru-A assembly on TiO_2 in MeCN exhibits a distinct absorption band centered near 450 nm (Figure 4.1). This transition is assigned to the manifold of metal-to-ligand charge transfer states on the pendant Ru^{II} chromophores. In this MLCT transition, electron density is transferred from the Ru^{II} metal center to a ligand, as evidenced from DFT calculations (Figure 4.2). Following excitation on ZrO_2 , where electron injection is not possible, the pS-Ru-A assembly exhibits a broad band centered at 650 nm (Figure 4.2), characteristic of phosphorescence from the triplet MLCT excited-state formed following rapid intersystem crossing from the singlet MLCT state.

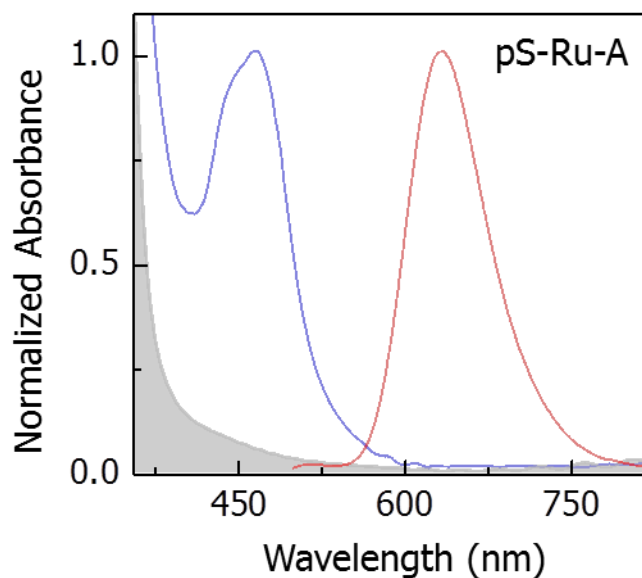


Figure 4.1. Ground state absorbance spectrum of the pS-Ru-A assembly on the surface of TiO_2 (blue line) and the emission spectrum of the pS-Ru-A assembly on ZrO_2 following 480 nm excitation (red line). All films were immersed in acetonitrile with 100 mM LiClO_4 . Also shown is the absorbance spectrum contribution from TiO_2 (shaded gray area).

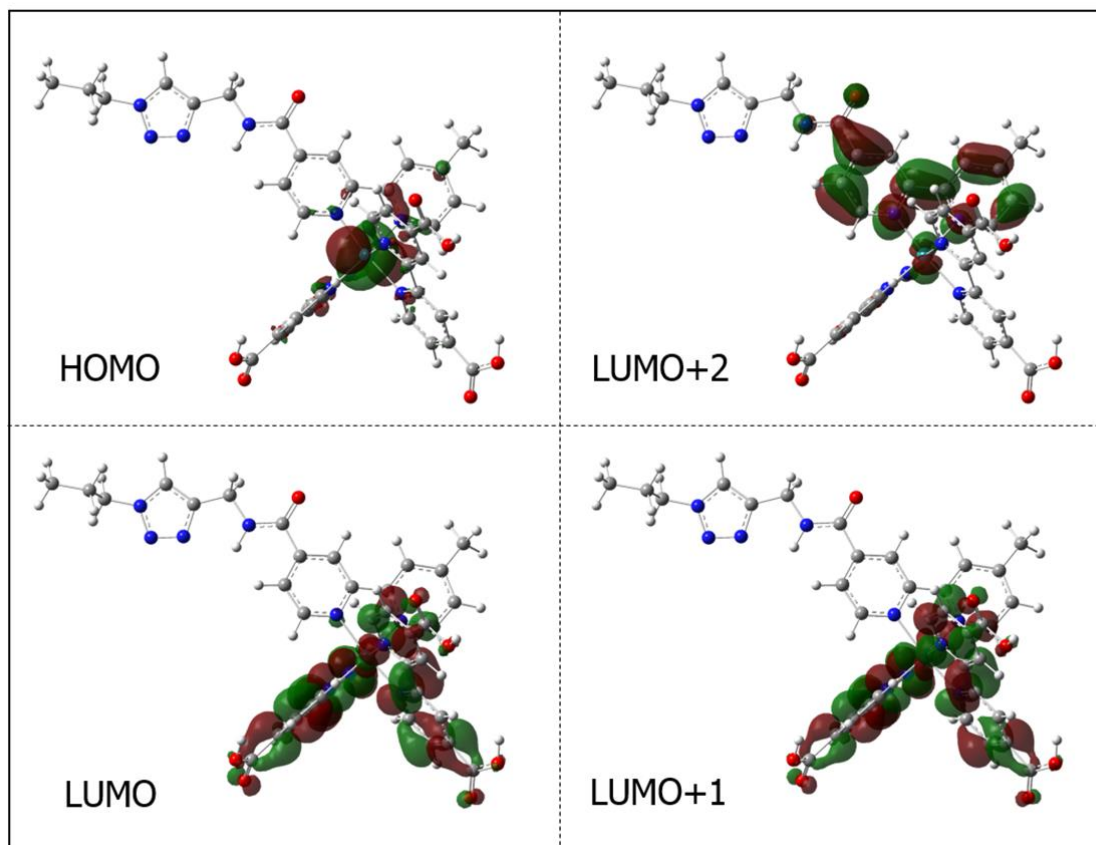


Figure 4.2. Optimized geometry of the pS-Ru monomer along with calculated isodensity plots of the frontier molecular orbitals (LUMO+2, LUMO+1, LUMO, HOMO) (isodensity value = 0.03).

4.3.2. Macromolecular Polymer Structures

In order to gain more insight into the effect of solvent on adsorption of the polymers onto the mesoporous TiO_2 films, molecular dynamics simulations were performed for a pS-Ru-A chain dissolved in MeCN and MeOH. The molecular dynamics simulations reveal that the solvated polymer chains are compact, with the majority of the center-to-center distances between the pendant complexes in the range 10–20 Å (Figure 4.3).

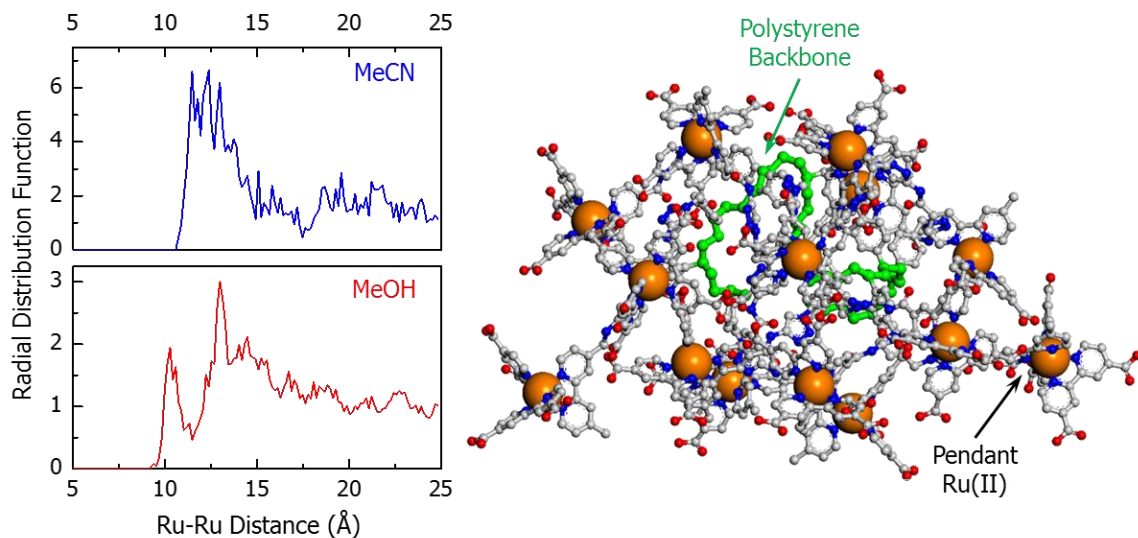


Figure 4.3. (Left) Ensemble radial distribution functions for distances computed between Ru pendants from molecular dynamics simulations of pS-Ru-A in MeCN (top) and MeOH (bottom). (Right) Snapshot of a solvated pS-Ru-A chain in MeCN solvent, revealing the close-packed structure facilitated by the flexible pS backbone (green). Solvent molecules and counter ions have been omitted for clarity.

This result stems from the flexible nature of the saturated polymer backbone which is able to bend and twist to reduce steric hindrance between the large pendant complexes. The simulation also suggests that solvent also affects the macromolecular polymer structure, where pS-Ru-A in MeOH displays slightly larger center-to-center Ru-Ru distances in comparison to MeCN. This effect is more clearly seen in the comparison of the computed radius of gyration following MD simulations in both MeCN and MeOH. As shown in Figure 4.4, the radius of gyration is centered at 16.9 Å in MeCN and 20.9 Å in MeOH, indicating that the polymer structure is more diffuse in MeOH compared to MeCN. This has been observed previously in related pS-Ru polymers and is thought to stem from differences in the solvent dielectric properties.¹⁹

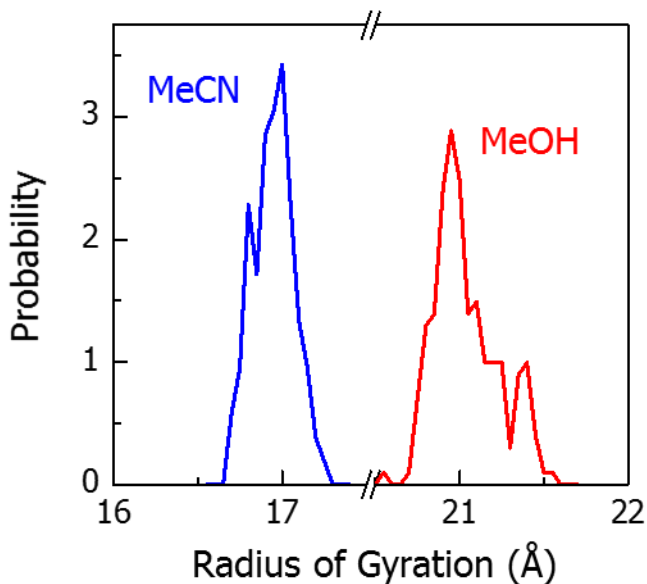


Figure 4.4. Radius of gyration computed from molecular dynamics simulations of pS-Ru-A in MeCN (blue) and MeOH (red). The radii are centered at 16.9 and 20.9 Å for MeCN and MeOH, respectively.

4.3.3. Time-Resolved Spectroscopy

To develop an understanding of the intra-assembly interfacial dynamics of the pS-Ru-A light-harvesting system at the metal oxide interface, time-resolved emission spectroscopy (TRES) in conjunction with transient absorption spectroscopy was performed for films immersed in MeCN with 0.1M LiClO₄. From the TRES data for ZrO₂//pS-Ru-A and TiO₂//pS-Ru-A (Figure 4.5), the single-wavelength emission intensity at 660 nm exhibits a multiexponential decay on both metal-oxide surfaces. The emission decay observed for ZrO₂//pS-Ru-A is assumed to be free of contributions from electron injection by the photoexcited Ru-A chromophores, which is greatly inhibited if not prohibited given the position of the excited-state oxidation potential of the pendants (0.65 V vs. NHE) in relation to the ZrO₂ conduction band (ca. 1.5 V vs. NHE).²⁰ When attached to TiO₂, however, the photoexcited pS-Ru-A assembly exhibits accelerated emission

decay, indicating a greater extent of excited- state quenching arising from electron injection by excited chromophores located nearby the nano-TiO₂ interface. This observation could arise from energy migration within the polymer assembly to surface-bound pendants, after which electron injection occurs. Previous work on similar pS-Ru complexes studied in both fluid solutions and rigid matrices revealed that the time scale for MLCT exciton hopping between chromophores (e.g., Ru*+Ru→Ru+Ru*) occurs on the 1–10 ns time scale.²¹⁻²³ The time scales associated with the emission quenching of TiO₂//pS-Ru-A are consistent with excited-state migration to the semiconductor surface through a series of energy-transfer steps after which charge separation occurs, quenching the emission.

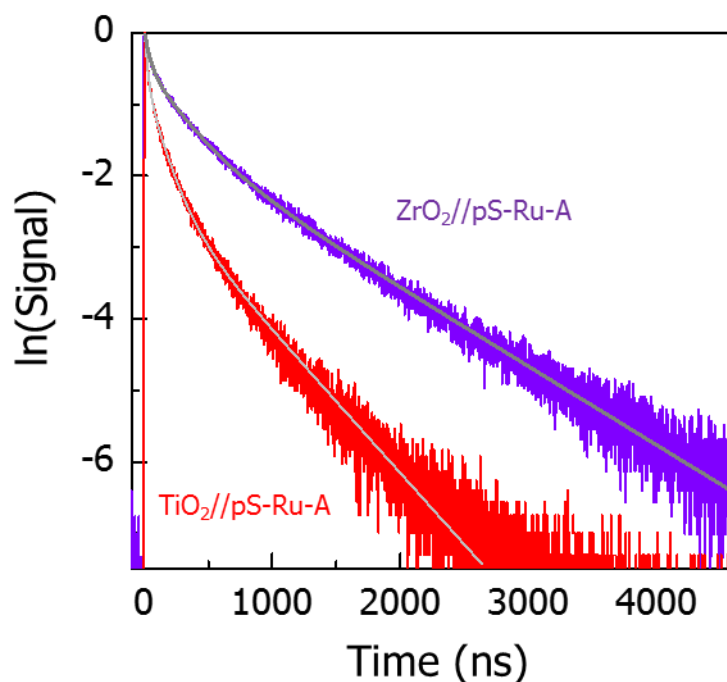


Figure 4.5. Time-resolved emission for TiO₂//pS-Ru-A and ZrO₂//pS-Ru-A monitored at 660 nm following 444 nm excitation. The decays are fit to a tri-exponential function, with time constants and amplitudes listed in Table 4.1.

Careful analysis of the TRES data reveals that the emission decays for both the ZrO₂//pS-Ru-A and TiO₂//pS-Ru-A systems are complex, but can be fit to a tri-exponential decay function. The quenching observed from tens to hundreds of nanoseconds is consistent with multiple energy-transfer steps among the pendants before reaching the surface. The results of the fitting are given below in Table 1.

Table 4.1. TRES decay fits for TiO₂//pS-Ru-A and ZrO₂//pS-Ru-A films monitored at 660 nm following 440 nm excitation.

Fitting Parameter	TiO ₂ //pS-Ru-A	ZrO ₂ //pS-Ru-A
A ₁	0.46	0.34
τ ₁ (ns)	21.6±0.3	39.6±0.5
A ₂	0.42	0.40
τ ₂ (ns)	128±1	271±2
A ₃	0.12	0.26
τ ₃ (ns)	500±0	910±0
< τ > (ns)	299	682

The decay lifetimes range from tens to hundreds of nanoseconds, and they are approximately twice as large for ZrO₂// pS-Ru-A compared to TiO₂//pS-Ru-A. Comparison of the component amplitudes is also striking—for ZrO₂//pS-Ru-A these are weighted roughly equally, while for TiO₂ a majority of the amplitude falls on the faster time constants. To quantify these results, the weighted average lifetimes <τ> for each metal-oxide (MO_x) were computed from the tri-exponential fits according to Equation (4.1):

$$\langle \tau_{MOx} \rangle = \frac{\sum_{i=1}^3 A_i \cdot \tau_i^2}{\sum_{i=1}^3 A_i \cdot \tau_i} \quad (4.1)$$

In addition, we have estimated the quantum yield (Φ) for energy transport and electron injection by Equation 4.2:

$$\Phi = 1 - \frac{\langle \tau_{TiO_2} \rangle^{-1}}{\langle \tau_{ZrO_2} \rangle^{-1}} \quad (4.2)$$

From these results, we estimate that 56% of the excitations in the pS-Ru-A assembly result in electron injection events into the TiO_2 conduction band.

To provide further insight into the interfacial electron-transfer dynamics, we have performed transient absorption spectroscopy with observation times ranging from hundreds of femtoseconds to hundreds of microseconds. To provide a point of reference, a parallel investigation was conducted on the model complex, $TiO_2//Ru-A$. First we examine the results for $TiO_2//Ru-A$. As shown in Figure 4.6A, the transient absorption spectrum following 420 nm MLCT excitation reveals a distinctive ground-state bleach near 450 nm, a prominent absorption centered at 385 nm, and a weak absorption extending to the red of 500 nm. The absorption at 385 nm is attributed to a $\pi-\pi^*$ transition of the $bpy^{\cdot-}$ radical anion while the weak, red absorption results from a combination of overlapping $\pi-\pi^*$ and ligand-metal charge transfer (LMCT) bands.^{20, 24} Loss of the $bpy^{\cdot-}$ absorption at 385 nm while retaining the ground-state bleach amplitude at 450 nm is the spectral signature of decay of the MLCT state by electron injection into TiO_2 . The decay at 385 nm (Figure 4.6D) is multi-exponential, exhibiting both fast ($t_1=60$ ps) and slow ($t_2=500$ ps) components, as has been observed in a similar light-harvesting array at TiO_2 featuring a poly(fluorene) polymer backbone, as described in Chapter 5. This photoinduced electron injection event has been shown to be a multi-exponential process,²⁵ resulting from dynamic relaxation processes that occur within the photoexcited chromophores. Furthermore,

qualitative analysis⁴ of the relative amplitudes of the 385 nm absorption and 450 nm bleach are similar for TiO₂//Ru-A compared to ZrO₂//Ru-A at 1 ps (Figure 4.6C). Taken together, this suggests that there is negligible ultrafast ($t < 200$ fs) electron injection that occurs in the TiO₂//Ru-A system. This result is notable, as most Ru^{II}-based chromophores undergo very efficient and rapid (< 1 ps) electron injection. The slower electron injection in the present system is thermodynamically driven with excited-state energetics altered by the lower-energy, amide-functionalized bipyridine ligand. As mentioned above, density functional theory (DFT) calculations performed on Ru-A (Figure 4.2) indicate that the HOMO is located on the Ru^{II} center, while the LUMO and LUMO+1 are localized primarily on the carboxylated bipyridine ligands, serving to direct the MLCT excitation to the TiO₂ surface. Given these results, we conclude that the relatively slow electron injection for TiO₂//Ru-A is a result of the ligand modifications which serve to reduce the excited-state oxidation potential of the chromophore. This gives rise to relatively low energy MLCT states that consequently do not have appreciable energetic overlap with the acceptor electronic levels within the TiO₂.

Photoexcitation of the TiO₂//pS-Ru-A film at 420 nm gives rise to similar spectral features as seen for the TiO₂//Ru-A film at early times (Figure 4.6B). The 385 nm absorption due to bpy^{*} decays with time components that are similar to the model system TiO₂//Ru-A ($t_1 = 60$ ps and $t_2 = 500$ ps) (Figure 4.6D). However, the overall electron injection yield is less during the first 1.5 ns following excitation, a conclusion that is based upon the relative amplitude of the loss of the 385 nm absorption with respect to the 450 nm bleach (Figure 4.6B). Our interpretation is that photoexcited surface-bound chromophores undergo electron injection similar to the Ru-A, while the remaining excited states distal to the surface undergo intra-assembly triplet-triplet energy

transport to surface-bound chromophores, at which point electron injection occurs, as supported by the TRES results discussed above.

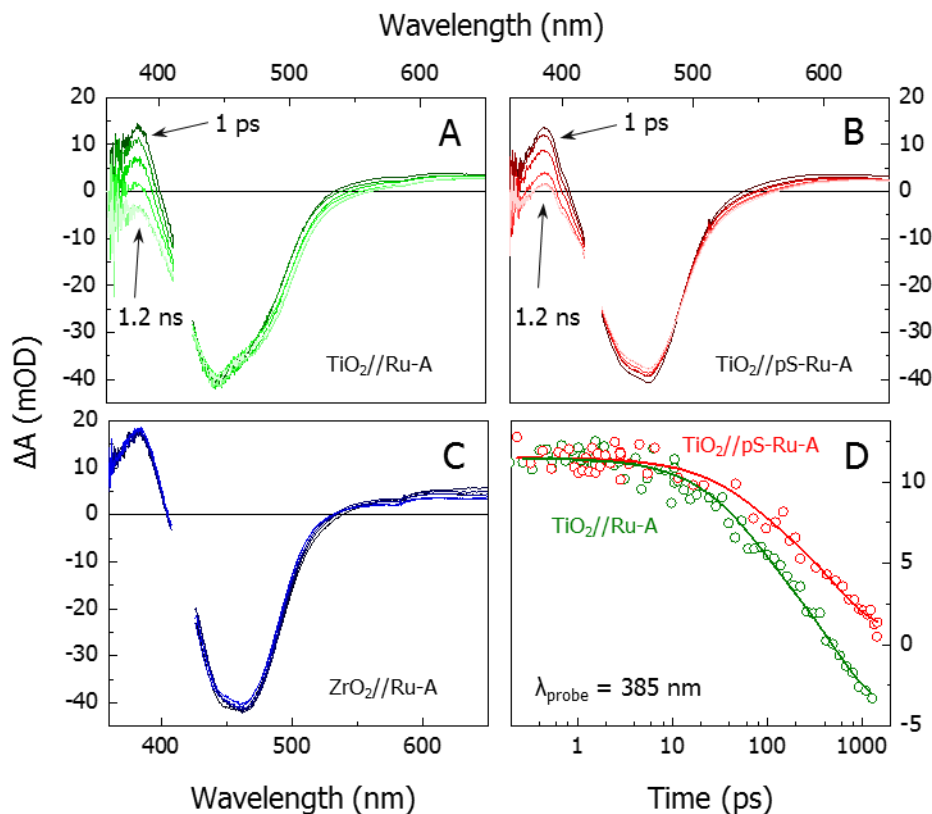


Figure 4.6. (A) Transient absorption spectra following 420 nm excitation of $\text{TiO}_2//\text{Ru-A}$ at 1, 10, 100, 500 and 1200 ps. (B) Transient absorption spectra following 420 nm excitation of $\text{TiO}_2//\text{pS-Ru-A}$ at 1, 10, 100, 500 and 1200 ps. (C) Transient absorption spectra following 420 nm excitation of $\text{ZrO}_2//\text{Ru-A}$ at 1, 10, 100, 500 and 1200 ps. (D) Kinetics at 385 nm for $\text{TiO}_2//\text{Ru-A}$ (green circles) and $\text{TiO}_2//\text{pS-Ru-A}$ (red circles) with the bi-exponential fits overlain.

To investigate the slower photoinduced dynamics within the $\text{TiO}_2//\text{Ru-A}$ and $\text{TiO}_2//\text{pS-Ru-A}$ films, we have performed transient absorption experiments on the ns– μs time scales. In these experiments, instrument limitations do not allow spectroscopic monitoring of the $\text{bpy}^{\bullet-}$ absorption at 385 nm to observe the slower electron injection events. However, these

experiments do provide a glimpse into the excited-state relaxation and $\text{TiO}_2(\text{e}^-) \rightarrow \text{Ru}^{\text{III}}$ back electron transfer (BET) dynamics occurring within both systems. As shown in Figure 4.7, for $\text{ZrO}_2//\text{Ru-A}$, $\text{TiO}_2//\text{Ru-A}$, and $\text{TiO}_2//\text{pS-Ru-A}$, the kinetics for the recovery of the ground-state bleach monitored at 480 nm are multi-exponential and occur across a range of timescales from ns to μs . The major amplitude changes occur >10 ns with longer-lived bleaches observed for TiO_2 as expected for BET slower than excited-state decay. Looking at 1–10 ns for $\text{TiO}_2//\text{Ru-A}$ and $\text{TiO}_2//\text{pS-Ru-A}$, a small but rapid decay is apparent, presumably due to BET that is occurring faster than excited-state decay for a small fraction of chromophores. Importantly, comparison of the BET kinetics between $\text{TiO}_2//\text{Ru-A}$ and $\text{TiO}_2//\text{pS-Ru-A}$ reveals that recovery of the ground-state Ru^{II} species is slower for the pS-Ru-A assembly. Complete BET in the pS-Ru-A assembly occurs within ~ 100 ms; by contrast, for the monomer, Ru-A BET is complete within ~ 10 μs . From the molecular dynamics simulations of pS-Ru-A in MeCN solution, the chromophore packing is dense within the pS-Ru-A assembly (see above). Given the dense loading, delayed BET in the polymer assembly likely arises from intra-assembly hole transport to complexes away from the electron injection site via self-exchange hopping (e.g., $\text{Ru}^{\text{III}} + \text{Ru}^{\text{II}} \rightarrow \text{Ru}^{\text{II}} + \text{Ru}^{\text{III}}$) serving to spatially separate the electron and hole ($\text{TiO}_2(\text{e}^-)$ and Ru^{III} , respectively). The transport distances are greater than would be present for Ru-A, where each chromophore is directly bound to the surface.

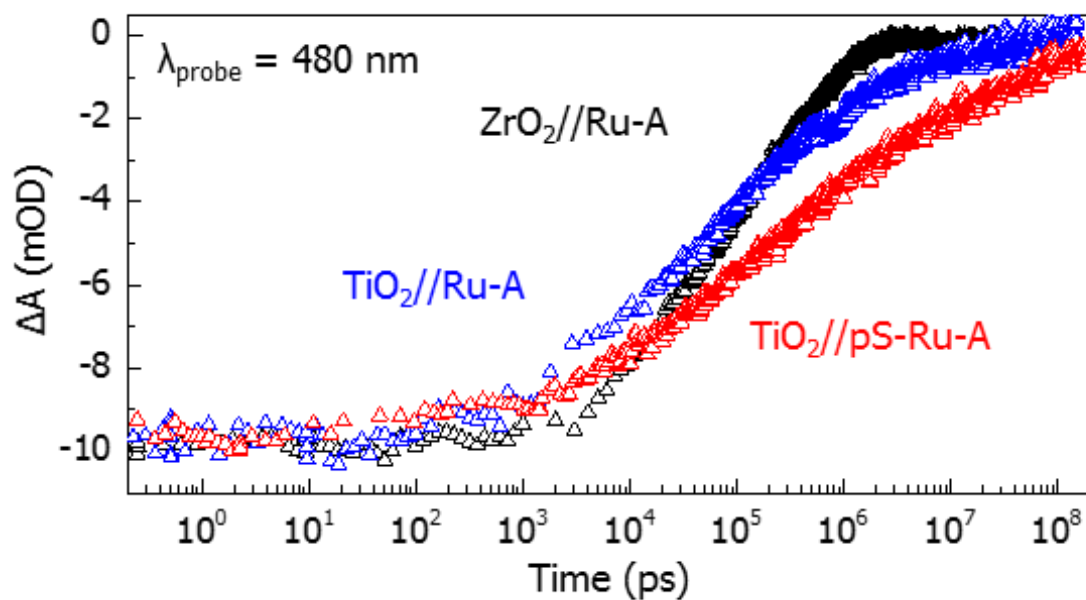


Figure 4.7. Kinetics traces at 480 nm on timescales ranging from 200 fs to 100 μs for ZrO₂//Ru-A (black triangles), TiO₂//Ru-A (blue triangles), and TiO₂//pS-Ru-A (red triangles).

4.4. CONCLUSIONS

In summary, time-resolved emission and transient absorption spectroscopy were applied to the $\text{TiO}_2//\text{Ru-A}$, $\text{ZrO}_2//\text{pS-Ru-A}$, and $\text{TiO}_2//\text{pS-Ru-A}$ films to investigate the photoinduced processes that occur following excitation of the Ru^{II} chromophores. These measurements reveal a series of energy- and electron-transfer events that occur following photoexcitation. For $\text{TiO}_2//\text{pS-Ru-A}$, photoexcitation of surface-bound Ru^{II} chromophores results in picosecond electron injection into TiO_2 , while excitation of unbound Ru^{II} chromophores leads to multiple $\text{Ru}^* \rightarrow \text{Ru}$ energy hopping events, followed by electron injection. Subsequently, hole transfer to pendant complexes away from the surface can occur, slowing back electron transfer in the polymer systems. Lastly, on longer time scales, back efficient electron transfer between Ru^{III} and $\text{TiO}_2(e^-)$ gives the original ground-state Ru^{II} species. Together, these results reveal the antenna nature of the assembly, where the combination of efficient site-to-site energy and hole transport among the pendant complexes serves to funnel excited-state energy towards the metal-oxide surface for electron injection and spatially separating the electron–hole pairs to delay BET, respectively.

REFERENCES

1. Oregan, B.; Gratzel, M., A Low-Cost, High-Efficiency Solar-Cell Based on Dye-Sensitized Colloidal Tio₂ Films. *Nature* **1991**, *353*, 737-740.
2. Bettis, S. E.; Hanson, K.; Wang, L.; Gish, M. K.; Concepcion, J. J.; Fang, Z.; Meyer, T. J.; Papanikolas, J. M., Photophysical Characterization of a Chromophore/Water Oxidation Catalyst Containing a Layer-by-Layer Assembly on Nanocrystalline Tio₂ Using Ultrafast Spectroscopy. *J Phys Chem A* **2014**, *118*, 10301-10308.
3. Bettis, S. E.; Ryan, D. M.; Gish, M. K.; Alibabaei, L.; Meyer, T. J.; Waters, M. L.; Papanikolas, J. M., Photophysical Characterization of a Helical Peptide Chromophore-Water Oxidation Catalyst Assembly on a Semiconductor Surface Using Ultrafast Spectroscopy. *J Phys Chem C* **2014**, *118*, 6029-6037.
4. Wang, L.; Ashford, D. L.; Thompson, D. W.; Meyer, T. J.; Papanikolas, J. M., Watching Photoactivation in a Ru(II) Chromophore-Catalyst Assembly on Tio₂ by Ultrafast Spectroscopy. *J Phys Chem C* **2013**, *117*, 24250-24258.
5. Juozapavicius, M.; Kaucikas, M.; Dimitrov, S. D.; Barnes, P. R. F.; van Thor, J. J.; O'Regan, B. C., Evidence for "Slow" Electron Injection in Commercially Relevant Dye-Sensitized Solar Cells by Vis-Nir and Ir Pump-Probe Spectroscopy. *J Phys Chem C* **2013**, *117*, 25317-25324.
6. Juozapavicius, M.; Kaucikas, M.; van Thor, J. J.; O'Regan, B. C., Observation of Multiexponential Pico- to Subnanosecond Electron Injection in Optimized Dye-Sensitized Solar Cells with Visible-Pump Mid-Infrared-Probe Transient Absorption Spectroscopy. *J Phys Chem C* **2013**, *117*, 116-123.
7. Chi, Y.; Wu, K. L.; Wei, T. C., Ruthenium and Osmium Complexes That Bear Functional Azolate Chelates for Dye-Sensitized Solar Cells. *Chem-Asian J* **2015**, *10*, 1098-1115.
8. Morseth, Z. A.; Wang, L.; Puodziukynaite, E.; Leem, G.; Gilligan, A. T.; Meyer, T. J.; Schanze, K. S.; Reynolds, J. R.; Papanikolas, J. M., Ultrafast Dynamics in Multifunctional Ru(II)-Loaded Polymers for Solar Energy Conversion. *Accounts Chem Res* **2015**, *48*, 818-827.
9. Leem, G.; Morseth, Z. A.; Puodziukynaite, E.; Jiang, J. L.; Fang, Z.; Gilligan, A. T.; Reynolds, J. R.; Papanikolas, J. M.; Schanze, K. S., Light Harvesting and Charge Separation in a Pi-Conjugated Antenna Polymer Bound to Tio₂. *J Phys Chem C* **2014**, *118*, 28535-28541.
10. Fang, Z.; Ito, A.; Keinan, S.; Chen, Z. F.; Watson, Z.; Rochette, J.; Kanai, Y.; Taylor, D.; Schanze, K. S.; Meyer, T. J., Atom Transfer Radical Polymerization Preparation and Photophysical Properties of Polypyridylruthenium Derivatized Polystyrenes. *Inorg Chem* **2013**, *52*, 8511-8520.
11. Ashford, D. L.; Lapides, A. M.; Vannucci, A. K.; Hanson, K.; Torelli, D. A.; Harrison, D. P.; Templeton, J. L.; Meyer, T. J., Water Oxidation by an Electropolymerized Catalyst on Derivatized Mesoporous Metal Oxide Electrodes. *J Am Chem Soc* **2014**, *136*, 6578-6581.

12. Fukuzumi, S.; Ohkubo, K., Assemblies of Artificial Photosynthetic Reaction Centres. *J Mater Chem* **2012**, *22*, 4575-4587.
13. Andrews, D. L., Light Harvesting in Dendrimer Materials: Designer Photophysics and Electrodynamics. *J Mater Res* **2012**, *27*, 627-638.
14. Hasselman, G. M.; Watson, D. F.; Stromberg, J. R.; Bocian, D. F.; Holten, D.; Lindsey, J. S.; Meyer, G. J., Theoretical Solar-to-Electrical Energy-Conversion Efficiencies of Perylene-Porphyrin Light-Harvesting Arrays. *J Phys Chem B* **2006**, *110*, 25430-25440.
15. Frisch, M. J.; Trucks, G. W.; Schlegel, H. B.; Scuseria, G. E.; Robb, M. A.; Cheeseman, J. R.; Scalmani, G.; Barone, V.; Mennucci, B.; Petersson, G. A., et al. *Gaussian 09a02*, Gaussian, Inc.: Wallingford, CT, USA, 2009.
16. Lee, C. T.; Yang, W. T.; Parr, R. G., Development of the Colle-Salvetti Correlation-Energy Formula into a Functional of the Electron-Density. *Phys Rev B* **1988**, *37*, 785-789.
17. Reed, A. E.; Weinstock, R. B.; Weinhold, F., Natural-Population Analysis. *J Chem Phys* **1985**, *83*, 735-746.
18. Rappe, A. K.; Casewit, C. J.; Colwell, K. S.; Goddard, W. A.; Skiff, W. M., Uff, a Full Periodic-Table Force-Field for Molecular Mechanics and Molecular-Dynamics Simulations. *J Am Chem Soc* **1992**, *114*, 10024-10035.
19. Leem, G.; Keinan, S.; Jiang, J. L.; Chen, Z.; Pho, T. A.; Morseth, Z. A.; Hu, Z. Y.; Puodziukynaite, E.; Fang, Z.; Papanikolas, J. M., et al., Ru(Bpy)(3)(2+) Derivatized Polystyrenes Constructed by Nitroxide-Mediated Radical Polymerization. Relationship between Polymer Chain Length, Structure and Photophysical Properties. *Polym Chem-Uk* **2015**, *6*, 8184-8193.
20. Tachibana, Y.; Moser, J. E.; Gratzel, M.; Klug, D. R.; Durrant, J. R., Subpicosecond Interfacial Charge Separation in Dye-Sensitized Nanocrystalline Titanium Dioxide Films. *J Phys Chem-US* **1996**, *100*, 20056-20062.
21. Fleming, C. N.; Jang, P.; Meyer, T. J.; Papanikolas, J. M., Energy Migration Dynamics in a Ru(II)- and Os(II)-Based Antenna Polymer Embedded in a Disordered, Rigid Medium. *J Phys Chem B* **2004**, *108*, 2205-2209.
22. Fleming, C. N.; Dupray, L. M.; Papanikolas, J. M.; Meyer, T. J., Energy Transfer between Ru(II) and Os(II) Polypyridyl Complexes Linked to Polystyrene. *J Phys Chem A* **2002**, *106*, 2328-2334.
23. Fleming, C. N.; Maxwell, K. A.; DeSimone, J. M.; Meyer, T. J.; Papanikolas, J. M., Ultrafast Excited-State Energy Migration Dynamics in an Efficient Light-Harvesting Antenna Polymer Based on Ru(II) and Os(II) Polypyridyl Complexes. *J Am Chem Soc* **2001**, *123*, 10336-10347.

24. Yoshimura, A.; Hoffman, M. Z.; Sun, H., An Evaluation of the Excited-State Absorption-Spectrum of Ru(Bpy)₃(2+) in Aqueous and Acetonitrile Solutions. *J Photoch Photobio A* **1993**, *70*, 29-33.
25. Zigler, D. F.; Morseth, Z. A.; Wang, L.; Ashford, D. L.; Brennaman, M. K.; Grumstrup, E. M.; Brigham, E. C.; Gish, M. K.; Dillon, R. J.; Alibabaei, L., et al., Disentangling the Physical Processes Responsible for the Kinetic Complexity in Interfacial Electron Transfer of Excited Ru(II) Polypyridyl Dyes on TiO₂. *J Am Chem Soc* **2016**, *138*, 4426-4438.

CHAPTER 5. LIGHT-HARVESTING AND CHARGE SEPARATION IN A π -CONJUGATED ANTENNA POLYMER BOUND TO TiO₂

This chapter contains work that previously appeared as an article in The Journal of Physical Chemistry C. The original citation is as follows: Leem, G.; Morseth, Z.A.; Puodziukynaite, E.; Jiang, J.; Zhen, F.; Gilligan, A.T.; Reynolds, J.R.; Papanikolas, J.M.; Schanze, K.S. "Light-Harvesting and Charge Separation in a π -Conjugated Antenna Polymer Bound to TiO₂," **2014**, *118*, 28535-28541.

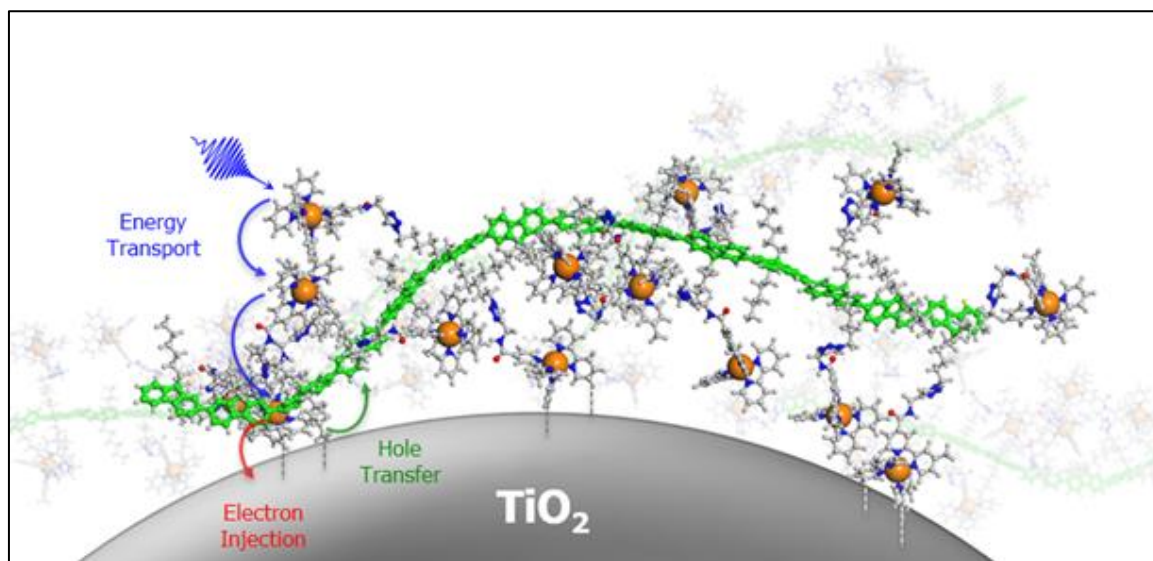
5.1. INTRODUCTION

The development of molecular assemblies that mimic the characteristics of photosynthetic systems is central to the realization of solar fuel technologies. Using natural photosynthesis as a guide, artificial photosynthetic assemblies must be able to perform multiple functions spanning light harvesting, charge separation, and charge transfer of the redox equivalents to catalytic sites that drive multi-electron reactions such as water oxidation or CO₂ reduction.¹⁻² Coupling of light-harvesting to charge-separation has been successfully demonstrated in a number of solution phase systems employing a broad range of sensitizers.³⁻⁵ Although these molecular systems elegantly demonstrate proof-of-concept principles regarding the photophysical mechanisms of directional energy flow, they are typically limited to a single or small group of chromophores and are difficult to synthesize, limiting their scalability to practical solar energy conversion applications. Multi-chromophore light-harvesting assemblies based on polymers,⁶⁻⁸ dendrimers⁹ and peptides¹⁰ are less challenging to synthesize and thus provide a potentially scalable architecture, but only a few examples exist in which multiple functions (e.g. light-harvesting, energy transport, charge separation) are incorporated into a single assembly.^{10,11}

We previously reported the synthesis and photophysical study of a poly(fluorene) (pF)-based Ru^{II} polypyridyl assembly (pF-Ru), where selective photoexcitation of the pF backbone gives rise

to a kinetic competition between ultrafast energy and electron transfer to the pendant Ru^{II} sites, producing a charge-separated state that persists for approximately 6 ns.⁶ In the present investigation, we describe an approach that anchors a structurally similar pF-based assembly through ionic carboxylate functionalized Ru^{II} chromophores to metal oxide (TiO₂) films (Scheme 5.1). When bound to TiO₂, the polymer exhibits multifunctional characteristics in which light absorption is coupled with energy transport and charge separation. Through pump-probe transient absorption methods we follow the photophysical events on time scales ranging from 100s of femtoseconds to 100s of microseconds. Photoexcitation of one of the Ru^{II} complexes is followed by energy transport through site-to-site hopping to the interface, where electrons inject (i.e. charge separation) into the TiO₂. Hole transfer from the oxidized Ru complex to the pF backbone regenerates the chromophore at the interface on the picosecond time scale. The holes that reside on the pF backbone are stable for > 100 μs, implying that the pF serves not only as a structural scaffold, but also as a functional element that can transport and potentially store multiple oxidative equivalents, for consumption by relatively slow catalytic cycles.

Scheme 5.1. Cartoon of pF-Ru-A anchored onto a TiO_2 surface.



5.2. EXPERIMENTAL SECTION

5.2.1. Sample Preparation

Thin films of ZrO_2 and TiO_2 deposited on FTO glass were soaked for 48 hours in a solution containing the sensitizer dissolved in acetonitrile and were placed in a home-made 1 cm quartz cuvette at a 45 degree angle relative to the front face of the cuvette. All transient absorption experiments were performed with the sensitized films immersed in argon-saturated solutions of 100 mM LiClO_4 dissolved in acetonitrile and were raster-scanned to prevent photodegradation of the samples.

5.2.2. Steady State Techniques

UV-Visible spectra were recorded on an HP 8543 Diode Array Spectrophotometer. UV-Visible spectra were recorded on all samples before and after excited state measurements to ensure that samples did not undergo photodecomposition.

Emission spectra were measured on Photon Technology International (PTI 4SE-NIR) Quantamaster™ spectrofluorometer equipped with a continuous xenon arc lamp as the excitation source. The emitting light was collected at 90° to the excitation beam and detected by a Multi-mode 814 photomultiplier tube (PMT) in photon counting mode (digital).

5.2.3. Transient Absorption Spectroscopy

Transient absorption measurements were performed using a home-built transient absorption spectrometer. The spectrometer is based on a commercially available ultrafast laser system (Clark MXR CPA-2210). The system consists of an erbium-doped fiber ring oscillator pumped by a solid-state fiber coupled laser diode operating at 980 nm and a chirped pulse Ti:Sapphire regenerative amplifier pumped by a frequency-doubled, Q-switched Nd:YAG laser. Following pulse compression, the amplifier produces pulses centered at 775 nm with 120 fs fwhm duration at 1

kHz with pulse energies of 1.6 mJ/pulse. The 450 nm pump pulse was generated in a 2 mm BBO crystal by sum frequency generation of the 775 nm fundamental and the second harmonic of the 1070 nm signal from an optical parametric amplifier (Light Conversion TOPAS-C). The femtosecond probe pulse is generated by focusing 3 mW of the 775 nm amplifier output into a translating 5 mm thick CaF₂ window. The pump beam is focused onto the sample using a 300 mm lens and the probe beam is focused and overlapped with a 250 mm spherical aluminum mirror. Spectra were collected on a shot-by-shot (1 kHz) basis over the range of 350 to 820 nm with a sensitivity of up to 0.1 mOD. The angle between the pump and probe polarization vectors was set to magic angle ($\sim 54.7^\circ$) to avoid polarization effects and ensure that only excited-state population dynamics were being monitored and the sample was raster scanned to provide for a fresh sample between laser pulses. Following data collection, the frequency chirp in the probe pulse was characterized using the optical Kerr response of liquid CCl₄ in a 2 mm cuvette in a polarization gating geometry. The spectra were chirp-corrected using a data processing program written in LabVIEW.

Sub-nanosecond transient measurements were performed with an Ultrafast Systems EOS spectrometer, in which the probe pulse is generated by continuum generation from a photonic crystal fiber and detected by a fiber optic coupled multichannel spectrometer with a CMOS sensor. The pump-probe delay is electronically controlled. The kinetic window ranges from 500 ps – 400 μ s and the time resolution of the instrument is around 500 ps, dictated by the width of the probe pulse and the timing electronics.

For transient absorption sample preparation, thin films of TiO₂ deposited on FTO glass were soaked for 48 hours in a solution containing the sensitizer dissolved in a 1:2 (v/v) mixture of acetonitrile: methanol and were placed in a home-made 1 cm quartz cuvette at a 45 degree angle

relative to the front face of the cuvette. All transient absorption experiments were performed with the sensitized films immersed in argon-saturated solutions of 100 mM LiClO₄ dissolved in acetonitrile and were raster-scanned to prevent photodegradation of the samples.

Injection yield calculations were determined by comparing the intensity of the 385 nm bpy^{•-} absorption to the 450 nm ground state bleach. The maximum absorbance at 385 nm occurs when $\Phi_{inj} = 0\%$, which is observed from the transient absorption spectrum on ZrO₂, where injection is not possible due to the location of the conduction band edge. The minimum absorbance at 385 nm occurs when $\Phi_{inj} = 100\%$, in which the transient absorption spectrum represents Ru(III) on TiO₂. This is approximated as the inverse of the ground state absorption spectrum, normalized to the Ru^{II} bleach. By comparing the amplitude of the 385 nm band with respect to these two limits, we can estimate Φ_{inj} as a function of pump-probe delay times.

5.2.4. Transient Absorption Kinetics Fitting Parameters.

The fsTA kinetics traces at 385 nm were fit to a bi-exponential function with an x and y -offset as implemented in Origin 9.0. The instrument response function (IRF) at 385 nm from the cross-correlation determined the earliest time point in the fitting function. The fitting function was minimized using the Levenberg-Marquardt method until a reduced Chi-Square value of $1e^{-9}$ was achieved.

5.2.5 Molecular Dynamics Simulations.

The polymer structures for the MD simulations were constructed using the Materials Studio suite (Accelrys Software, Inc., San Diego, 2011). The ground-state geometry of the monomer was optimized using the B3LYP DFT functional and the LANL2DZ basis set, as implemented in Gaussian09 version 09a02.¹² After optimizing the gas-phase monomer structures, the homopolymer was constructed in Materials Studio. The gas-phase geometries of the polymers

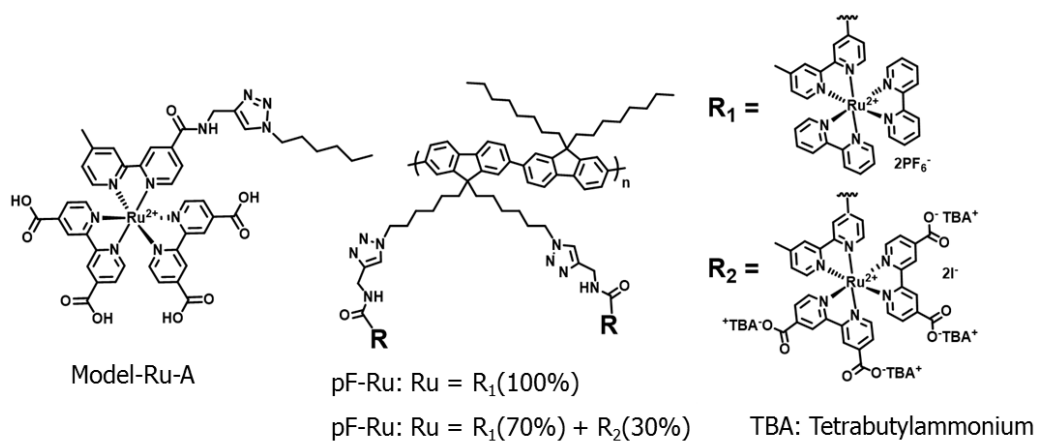
were then optimized and annealed with atomic charges (NPA) obtained from the Gaussian09 QM calculations. The annealing step consisted of 5 temperature cycles using the Universal Force Field with the temperature ranging from 300 K to 700 K in a time step of 1 fs, with 5 heating ramps per cycle and 200 dynamics steps per ramp for a total of 1 ns. The simulation cell consisted of a 8-repeat unit polymer, 32 PF_6^- (counter ion), and 1180 CH_3CN molecules. The cell was then annealed using the same force field as the gas phase polymer with the temperature ranging from 300 K to 1200 K in a time step of 1 fs with 2 heating ramps per cycle and 100,000 dynamics steps per ramp for a total of 800 ps. The annealed simulation cells were then used for molecular dynamics calculations with the canonical ensemble, NVT, at a temperature of 298 K controlled by the Nose thermostat with a Q-ratio of 0.01. Dynamics were calculated for a total of 1 ns in each polymer system and snapshots were collected every 1 ps, giving a trajectory with 1,000 snapshots for analysis for each annealed simulation cell.

5.3. RESULTS AND DISCUSSIONS

5.3.1. Polymer Structures

The chemical structures of the molecular systems studied are shown in Figure 5.1 which include the model Ru^{II} complex (Model-Ru-A), and polymer assemblies pF-Ru and pF-Ru-A. pF-Ru was previously studied⁶ in solution leading us to design pF-Ru-A to allow anchoring of the assembly to metal oxide surfaces. Scheme 5.1 schematically illustrates a pF-Ru-A structure obtained from solution molecular dynamics (MD) simulations anchored onto a TiO₂ surface (pF-Ru-A//TiO₂), with surface attachment facilitated by interaction of the polar carboxylate units with the oxide interface, revealing that the polymer coating is approximately 6 nm in diameter. Within the pF-Ru-A assembly, 30% of the pendant Ru^{II} chromophores feature the 4,4'-(dicarboxylate)-2,2-bipyridine ligands allowing for multiple surface binding points randomly positioned along the chain, leaving 70% of the unsubstituted Ru^{II} 2,2-bipyridine chromophores to participate as antennas that transfer excited state energy to surface bound Ru^{II} centers.¹³

Figure 5.1. Chemical structures of Model-Ru-A, pF-Ru and pF-Ru-A



5.3.2. Photoexcitation of pF-Ru-A

The ground-state absorption spectrum of pF-Ru-A//TiO₂ in MeCN is characterized by several distinct features in the visible region (Figure 5.2). This includes the intense visible transition centered at 395 nm along with a weaker, broad transition centered near 450 nm. The 395 nm transition is ascribed entirely to a $\pi \rightarrow \pi^*$ transition delocalized along the pF backbone, while the 450 nm transition is attributed to the metal-to-ligand charge transfer (MLCT) band of the Ru^{II} chromophores. Emission from pF-Ru-A following excitation into the Ru^{II} MLCT band is broad and featureless, consistent with triplet Ru^{II} MLCT emission. The overall attainment of distinct absorption bands suggests that the electronic coupling between the polymer backbone and pendants chromophores is weak.

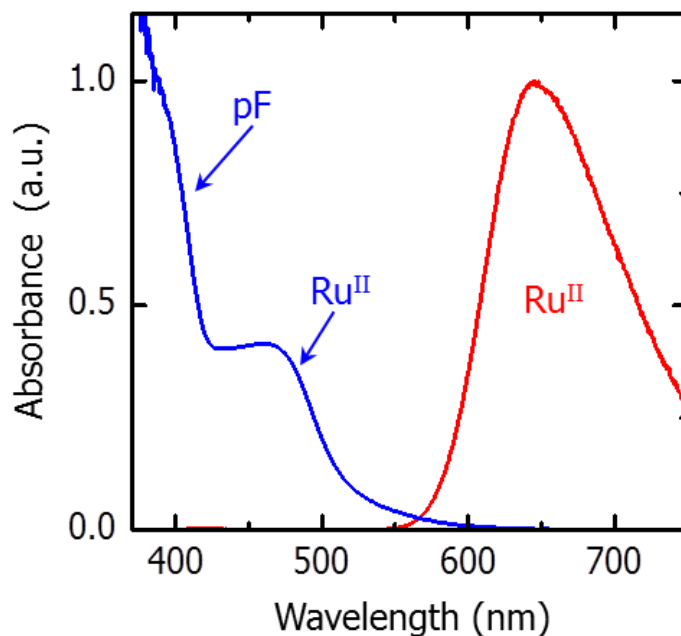


Figure 5.2. Ground-state absorbance spectrum of pF-Ru-A on TiO₂ (blue) and emission spectrum of pF-Ru-A on ZrO₂ in MeCN with 0.1 M LiClO₄. The emission spectrum was acquired following excitation at 450 nm.

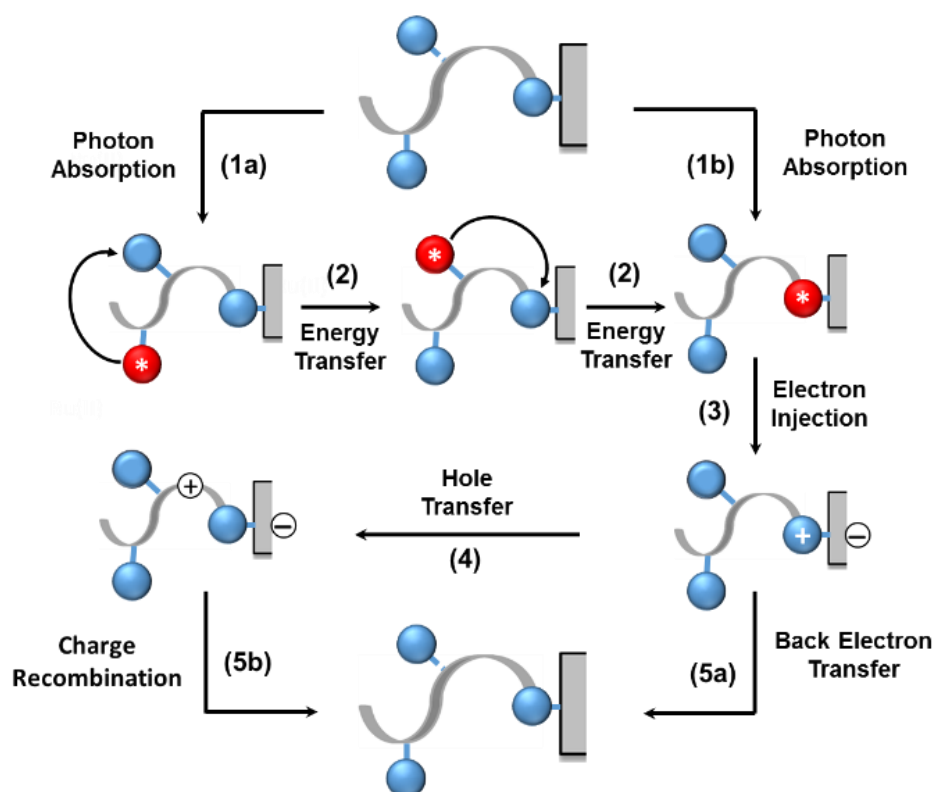
5.3.3. Interfacial Dynamics of pF-Ru-A

Transient absorption measurements performed on Model-Ru-A//TiO₂ and pF-Ru-A//TiO₂ films reveal a cascading series of energy and electron transfer events that occur following photoexcitation, as illustrated in Scheme 5.2. Photoexcitation of a surface-bound (proximal) Ru^{II} chromophore (1b) results in rapid electron injection into TiO₂ (3), followed by the transfer of the hole on the oxidized Ru(III) complex to the pF backbone (4). Excitation of a Ru^{II} chromophore that is distal with respect to the interface (1a) can lead to multiple Ru^{*}→Ru energy hopping events (2). Transport of the energy to surface bound chromophores is followed by electron injection (3) and hole transfer to the polymer (4). On longer time scales, back electron transfer between Ru^{III}

and $\text{TiO}_2(\text{e}^-)$ (5a) or charge recombination between pF^+ and $\text{TiO}_2(\text{e}^-)$ (5b) give the original ground state Ru^{II} species.

Scheme 5.2. Schematic representation of photophysical events of pF-Ru-A on the surface of TiO_2 .

Balls represent $\text{Ru}(\text{L})_3^{2+}$ chromophores, and the grey ribbon the poly(fluorene) backbone.



The electron injection process (3) is monitored by fs-ps transient absorption on the Model-Ru-A/ TiO_2 film. Spectra acquired shortly after 450 nm excitation of the Model-Ru-A/ TiO_2 film (Figure 5.3A) show the characteristic $\pi \rightarrow \pi^*$ absorption at 385 nm of the reduced polypyridyl radical anion ($\text{bpy}^{\bullet-}$) along with a prominent ground-state bleach at 450 nm and a ligand-to-metal charge transfer (LMCT) and $\text{bpy}^{\bullet-}$ band that extends to the red of 500 nm.¹⁴ Loss of the $\text{bpy}^{\bullet-}$ absorption at 385 nm without loss of the ground state bleach at 450 nm is the spectral signature of

electron injection into the TiO₂. By monitoring the loss of the 385 nm excited state absorption (Figure 5.3B), the decay is described well by fast ($\tau_1=60$ ps) and slow ($\tau_2=500$ ps) components. Photoinduced electron injection has been shown to be a multi-exponential process, owing to the intrinsic heterogeneity and dynamic relaxation processes following excitation.¹⁵⁻¹⁶ These slower decay components most likely reflect electron injection from a thermalized ³MLCT excited state, as reported for other Ru^{II} dyes.¹⁵ The presence of multiple kinetic components has been observed for other related sensitizers and arises from a number of factors, including the dye-binding motifs, electronic coupling and overlap of the dye donor levels with the TiO₂ acceptor states.^{8, 17-18} Furthermore, based on the analysis of the transient spectra¹⁹ there is negligible ultrafast ($\tau<200$ fs) electron injection in this complex, and by 1.4 ns the overall injection yield is 45%.²⁰

Photoexcitation of the pF-Ru-A//TiO₂ film at 450 nm gives rise to similar spectral features as seen for the Model-Ru-A//TiO₂ film at early times (Figure 5.3C). The intensity of the 385 nm absorption decays with time components that are similar to the Model-Ru-A complex ($\tau_1=60$ ps and $\tau_2= 500$ ps) (Figure 3D), but the overall injection yield is significantly lower based on inspection of the transient spectra.¹⁹ In addition, the transient spectra for the pF-Ru-A//TiO₂ assembly show additional bleach and absorption features at 400 and 580 nm, respectively (Figure 5.3C), and a concomitant loss of the MLCT ground state bleach at 450 nm. The 400 nm bleach and the 580 nm absorption are both attributed to oxidized pF polymer (pF⁺) on the basis of spectroelectrochemical observations.⁶

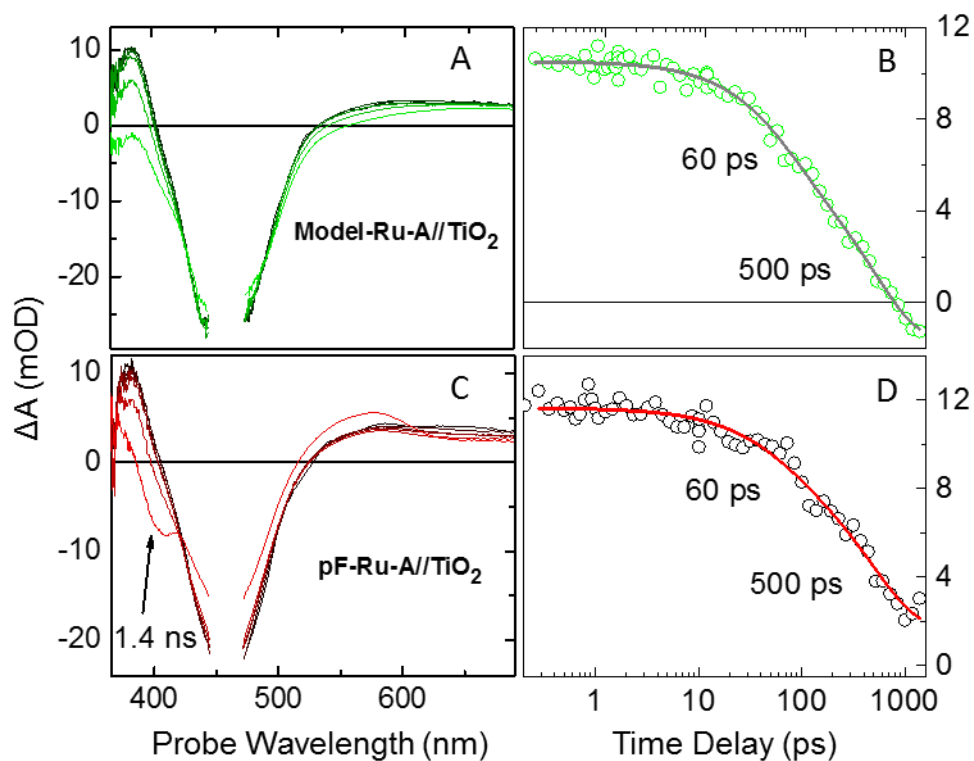


Figure 5.3. (A) Transient absorption spectra following 450 nm laser excitation for the Model-Ru-A complex on TiO₂ at 0.25, 1, 5, 10, 100, and 1400 ps. (B) Model-Ru-A//TiO₂ kinetics trace at 385 nm. (C) Transient absorption spectra of pF-Ru-A//TiO₂ at 0.25, 1, 5, 10, 100, and 1400 ps. (D) pF-Ru-A//TiO₂ kinetics trace at 385 nm. The films were immersed in argon-saturated acetonitrile with 0.1 M LiClO₄.

The absence of these two features in the transient spectra for pF-Ru-A//ZrO₂ (Figure 5.4) indicate that formation of pF⁺ is a consequence of charge injection, most likely due to hole transfer from Ru(III), produced by charge injection, to the pF backbone (Scheme 5.2, step 4). Furthermore, the loss of the bpy•- absorption at 385 nm occurs simultaneously with appearance of the pF⁺ feature at 400 nm, suggesting that hole transfer takes place on a time scale that is short compared to the longer injection components.

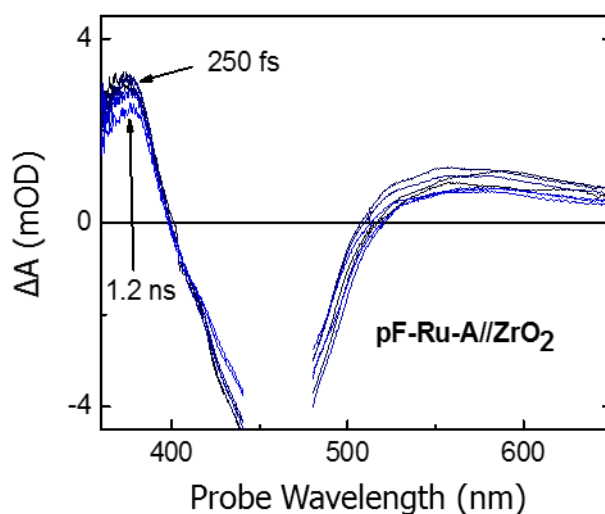


Figure 5.4. Transient absorption spectra of pF-Ru-A//ZrO₂ following photoexcitation at 450 nm on time scales of 250 fs to 1.2 ns. The slight spectral changes that are observed between 450 and 600 nm are not observed in the Model-Ru-A//ZrO₂ transient spectra and are attributed to Ru^{II*}→Ru energy hopping.

The spectral features associated with the formation of pF^+ at 400 and 580 nm become increasingly pronounced on longer time scales, as seen in Figs 5.3A and 5.3C. Their continued growth during the first 200-300 ns is consistent with triplet-triplet energy transport from unbound Ru^{II} complexes through site-to-site hopping to a chromophore bound to the TiO_2 surface, which then undergo electron injection and hole localization on the pF (Scheme 5.2, steps 2, 3). Thus, the time scale associated with the growth of the pF^+ features at 400 and 580 nm reflects the total time needed for the Ru^* created by photoexcitation to reach the interface, which in turn depends upon the $\text{Ru}^* \rightarrow \text{Ru}$ hopping time, as well as the number of hops. Work on a related polymer assembly²¹⁻²³ suggests that the $\text{Ru}^* \rightarrow \text{Ru}$ hopping time is <10 ns. Thus, the growth of pF^+ over 200-300 ns implies that some $\text{Ru}^{\text{II}*}$ excited states may make as many as 20-30 hops prior to charge injection, underscoring the antenna-like nature of the pF-Ru-A polymer assembly.

By 200-300 ns after photoexcitation, the transient spectrum contains both the prominent features associated with the pF^+ , as well as a significant Ru^{II} bleach at 450 nm. Since hole transfer to form the positive polaron repopulates the Ru^{II} ground state, the bleach must arise from Ru^{III} complexes that have not undergone hole transfer, or $\text{Ru}^{\text{II}*}$ excited states that remain. Although it is difficult to distinguish between these two contributions, the rapid hole transfer time would suggest that it is the $\text{Ru}^{\text{II}*}$ that is responsible for the bleach.

Furthermore, the Ru^{II} ground state bleach decays before the pF^+ features (Fig 5.3B, 5.3C), indicating that the transient spectrum observed at the longest times arises almost entirely from the positive polaron, pF^+ . A small population of Ru^{III} still exists at 150 μs , most likely a result of the similar oxidation potentials for pF and non-carboxylated Ru^{II} chromophores, leading to an equilibrium between the hole residing on the polymer backbone and the pendant chromophores. The charge-separated state decays through recombination of the injected electron in the TiO_2 with

holes on the pF backbone (Scheme 5.2, 5b). Its lifetime ($\sim 150 \mu\text{s}$) is significantly longer than that of Model-Ru-A//TiO₂ (Figure 5.6), consistent with a greater separation between the pF positive polaron and the surface.

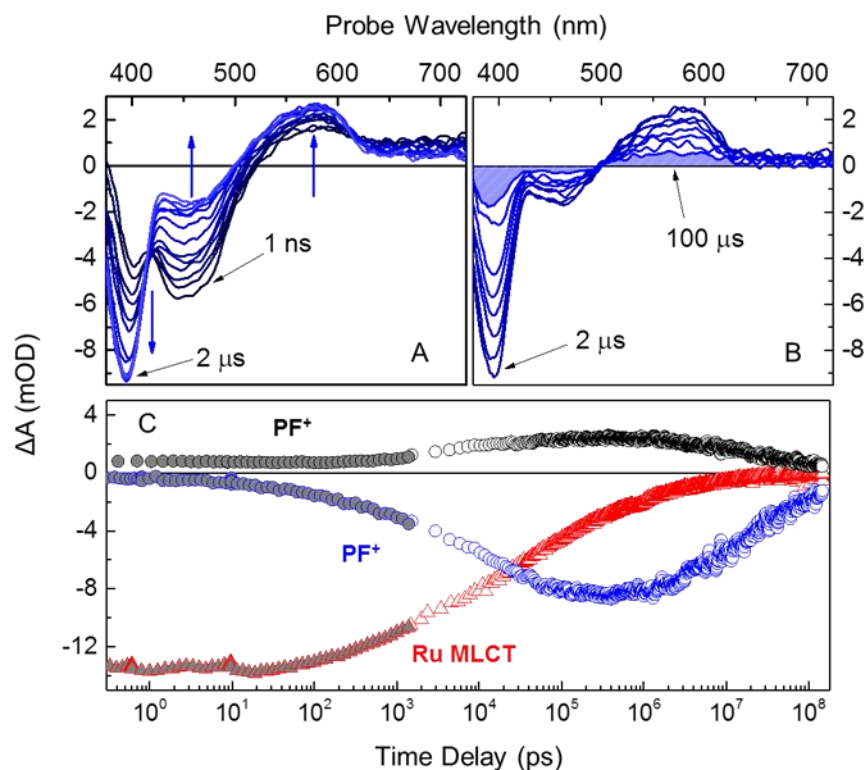


Figure 5.5. (A) Nanosecond transient absorption spectra of pF-Ru-A//TiO₂ films following excitation at 450 nm from 1 ns to 2 μs . (B) Nanosecond transient absorption spectra of pF-Ru-A//TiO₂ films from 2 μs to 100 μs . The shaded region is the spectrum at 100 μs . (C) Kinetics traces for pF-Ru-A//TiO₂ films at probe wavelengths 400 nm (blue), 485 nm (red) and 580 nm (black) from 250 fs to 150 μs following 450 nm excitation. The gray-filled points represent the femtosecond and picosecond kinetic traces. The films were immersed in argon-saturated acetonitrile with 0.1 M LiClO₄.

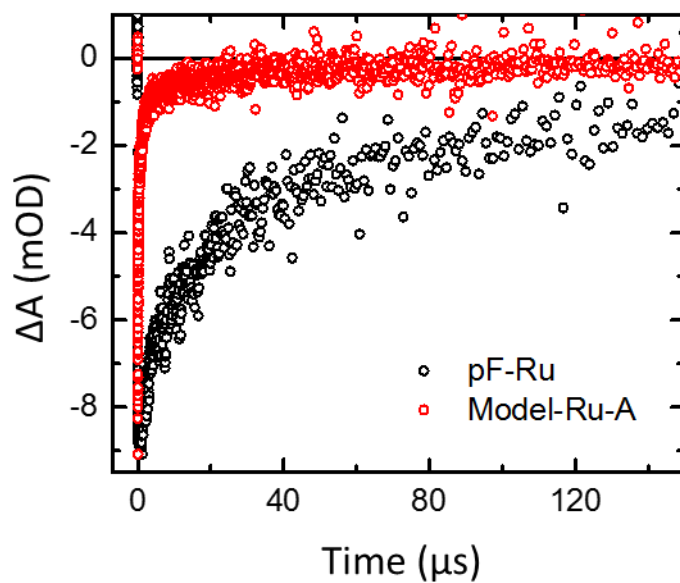


Figure 5.6. Kinetics trace monitored at 430 nm for Model-Ru-A//TiO₂ (red) and 400 nm for the pF-Ru-A//TiO₂ assembly (black) following 450 nm excitation. Charge recombination between the polaron on the PF backbone is much longer lived than back electron transfer in Model-Ru-A//TiO₂.

5.4. CONCLUSIONS

pF-Ru chromophores functionalized with a small fraction of ionic carboxylate moieties have been prepared by “click” chemistry to attach the mixture of Ru^{II} polypyridyl complexes and ester-containing Ru^{II} polypyridyl complexes, following the deprotection step to form ionic carboxylate functionalized Ru^{II} polypyridyl complexes. With the successful synthesis of pF-Ru-A, the polymer-based chromophores were anchored to TiO₂ films. The solar characteristics demonstrate TiO₂ surface anchoring and light-harvesting ability when applied in solar photoelectrochemical cells. These light harvesting mechanisms were studied with femtosecond pump probe spectroscopy, where direct excitation of the Ru^{II} chromophores leads to rapid and efficient electron injection for chromophores directly bound to the TiO₂ surface. This event is followed by ultrafast hole transfer to the polyfluorene chain, thereby facilitating repopulation of the ground state Ru^{II} species and avoiding deleterious charge recombination processes. The pendant Ru^{II} chromophores undergo energy transfer to surface-bound chromophores on the nanosecond time scale, where electron injection can precede hole transfer to the polymer backbone. Charge recombination for the Ru^{II} chromophores occurs on the microsecond time scale, where injected electrons recombine with oxidized chromophores that have not undergone hole transfer, whereas charge recombination involving the oxidized polymer occurs on longer time scales. This study reveals the promise for coupling polymeric assemblies to a semiconductor interface for light harvesting, charge separation and transient charge storage. Future work seeks to include oxidation catalyst centers into the assemblies with the objective of accomplishing water oxidation at the photoanode of a dye-sensitized photoelectrosynthesis cell.

REFERENCES

1. Ashford, D. L.; Song, W.; Concepcion, J. J.; Glasson, C. R. K.; Brennaman, M. K.; Norris, M. R.; Fang, Z.; Templeton, J. L.; Meyer, T. J., Photoinduced Electron Transfer in a Chromophore–Catalyst Assembly Anchored to Tio₂. *J Am Chem Soc* **2012**, *134*, 19189-19198.
2. Song, W.; Glasson, C. R. K.; Luo, H.; Hanson, K.; Brennaman, M. K.; Concepcion, J. J.; Meyer, T. J., Photoinduced Stepwise Oxidative Activation of a Chromophore–Catalyst Assembly on Tio₂. *J. Phys. Chem. Lett.* **2011**, *2*, 1808-1813.
3. Tomizaki, K.; Loewe, R. S.; Kirmaier, C.; Schwartz, J. K.; Retsek, J. L.; Bocian, D. F.; Holten, D.; Lindsey, J. S., Synthesis and Photophysical Properties of Light-Harvesting Arrays Comprised of a Porphyrin Bearing Multiple Perylene-Monoimide Accessory Pigments. *J Org Chem* **2002**, *67*, 6519-6534.
4. Gust, D.; Moore, T. A.; Moore, A. L., Mimicking Photosynthetic Solar Energy Transduction. *Accounts Chem Res* **2001**, *34*, 40-48.
5. Wasielewski, M. R., Photoinduced Electron Transfer in Supramolecular Systems for Artificial Photosynthesis. *Chemical Reviews* **1992**, *92*, 435-461.
6. Wang, L.; Puodziukynaite, E.; Vary, R. P.; Grumstrup, E. M.; Walczak, R. M.; Zolotarskaya, O. Y.; Schanze, K. S.; Reynolds, J. R.; Papanikolas, J. M., Competition between Ultrafast Energy Flow and Electron Transfer in a Ru(II)-Loaded Polyfluorene Light-Harvesting Polymer. *J. Phys. Chem. Lett.* **2012**, *3*, 2453-2457.
7. Wang, L.; Puodziukynaite, E.; Grumstrup, E. M.; Brown, A. C.; Keinan, S.; Schanze, K. S.; Reynolds, J. R.; Papanikolas, J. M., Ultrafast Formation of a Long-Lived Charge-Separated State in a Ru-Loaded Poly(3-Hexylthiophene) Light-Harvesting Polymer. *J. Phys. Chem. Lett.* **2013**, *4*, 2269-2273.
8. Chen, Z.; Grumstrup, E. M.; Gilligan, A. T.; Papanikolas, J. M.; Schanze, K. S., Light-Harvesting Polymers: Ultrafast Energy Transfer in Polystyrene-Based Arrays of Pi-Conjugated Chromophores. *J Phys Chem B* **2014**, *118*, 372-378.
9. Adronov, A.; Gilat, S. L.; Frechet, J. M. J.; Ohta, K.; Neuwahl, F. V. R.; Fleming, G. R., Light Harvesting and Energy Transfer in Laser-Dye-Labeled Poly(Aryl Ether) Dendrimers. *J Am Chem Soc* **2000**, *122*, 1175-1185.
10. Ma, D.; Bettis, S. E.; Hanson, K.; Minakova, M.; Alibabaei, L.; Fondrie, W.; Ryan, D. M.; Papoian, G. A.; Meyer, T. J.; Waters, M. L., et al., Interfacial Energy Conversion in Ru-II Polypyridyl-Derivatized Oligoproline Assemblies on Tio₂. *J Am Chem Soc* **2013**, *135*, 5250-5253.
11. Sykora, M.; Maxwell, K. A.; DeSimone, J. M.; Meyer, T. J., Mimicking the Antenna-Electron Transfer Properties of Photosynthesis. *PNAS* **2000**, *97*, 7687-7691.

12. Frisch, M. J.; Trucks, G. W.; Schlegel, H. B.; Scuseria, G. E.; Robb, M. A.; Cheeseman, J. R.; Scalmani, G.; Barone, V.; Mennucci, B.; Petersson, G. A., et al. *Gaussian 09*, Gaussian, Inc.: Wallingford, CT, USA, 2009.
13. The 30% loading of the bis(dicarboxy)bpy Ru(II) on the pF chain reflects the stoichiometry in the click reaction used to attach the acetylene functionalized Ru(II) chromophores to the azide functionalized pF.
14. Rack, J. J., Electron Transfer Triggered Sulfoxide Isomerization in Ruthenium and Osmium Complexes. *Coordination Chemistry Reviews* **2009**, *253*, 78-85.
15. Koops, S. E.; O'Regan, B. C.; Barnes, P. R. F.; Durrant, J. R., Parameters Influencing the Efficiency of Electron Injection in Dye-Sensitized Solar Cells. *J Am Chem Soc* **2009**, *131*, 4808-4818.
16. Juozapavicius, M.; Kaucikas, M.; van Thor, J. J.; O'Regan, B. C., Observation of Multiexponential Pico- to Subnanosecond Electron Injection in Optimized Dye-Sensitized Solar Cells with Visible-Pump Mid-Infrared-Probe Transient Absorption Spectroscopy. *J Phys Chem C* **2013**, *117*, 116-123.
17. Giokas, P. G.; Miller, S. A.; Hanson, K.; Norris, M. R.; Glasson, C. R. K.; Concepcion, J. J.; Bettis, S. E.; Meyer, T. J.; Moran, A. M., Spectroscopy and Dynamics of Phosphonate-Derivatized Ruthenium Complexes on TiO₂. *J Phys Chem C* **2013**, *117*, 812-824.
18. Asbury, J. B.; Anderson, N. A.; Hao, E. C.; Ai, X.; Lian, T. Q., Parameters Affecting Electron Injection Dynamics from Ruthenium Dyes to Titanium Dioxide Nanocrystalline Thin Film. *J Phys Chem B* **2003**, *107*, 7376-7386.
19. Wang, L.; Ashford, D. L.; Thompson, D. W.; Meyer, T. J.; Papanikolas, J. M., Watching Photoactivation in a Ru(II) Chromophore-Catalyst Assembly on TiO₂ by Ultrafast Spectroscopy. *J. Phys. Chem. C* **2013**, *117*, 24250-24258.
20. This injection yield is substantially lower than those observed for similar Ru(II) complexes on TiO₂. It is most likely a result of the chemical modification needed to attach the complex to the polymer, which could lead to low-energy MLCT excited states associated with the ancillary ligands that slow electron injection and diminish the overall injection yield.
21. Fleming, C. N.; Maxwell, K. A.; DeSimone, J. M.; Meyer, T. J.; Papanikolas, J. M., Ultrafast Excited-State Energy Migration Dynamics in an Efficient Light-Harvesting Antenna Polymer Based on Ru(II) and Os(II) Polypyridyl Complexes. *J Am Chem Soc* **2001**, *123*, 10336-10347.
22. Fleming, C. N.; Jang, P.; Meyer, T. J.; Papanikolas, J. M., Energy Migration Dynamics in a Ru(II)- and Os(II)-Based Antenna Polymer Embedded in a Disordered, Rigid Medium. *J Phys Chem B* **2004**, *108*, 2205-2209.

23. Fleming, C. N.; Brennaman, M. K.; Papanikolas, J. M.; Meyer, T. J., Efficient, Long-Range Energy Migration in Ru-II Polypyridyl Derivatized Polystyrenes in Rigid Media. Antennae for Artificial Photosynthesis. *Dalton Trans.* **2009**, 3903-3910.

CHAPTER 6. INTERFACIAL DYNAMICS WITHIN AN ORGANIC CHROMOPHORE-BASED WATER OXIDATION MOLECULAR ASSEMBLY

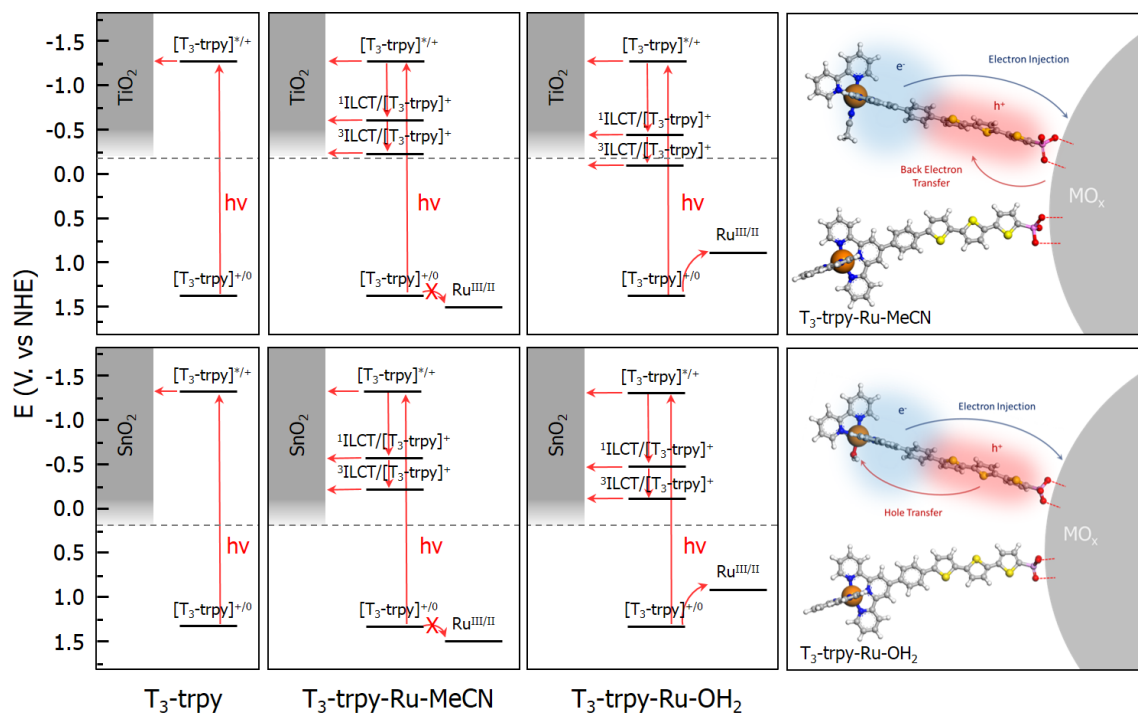
6.1. INTRODUCTION

The dye-sensitized photoelectrochemical cell (DSPEC) is an artificial photosynthetic system that converts sunlight into chemical fuels (e.g., hydrogen or carbon-based fuels), thus circumventing energy storage problems facing conventional photovoltaics.¹⁻² In the DSPEC, the water oxidation and CO₂ reduction half reactions occur at separate electrodes. Water oxidation is accomplished by a chromophore-catalyst assembly bound to the surface of a metal oxide semiconductor. Here, light absorption by the chromophore is followed by electron injection into the conduction band of the semiconductor, and transfer of the redox equivalent to the catalyst, which drives the catalytic cycle for splitting water into O₂ and H⁺.³

Several chromophore-catalyst assemblies have been demonstrated for light-driven water oxidation that incorporate Ru-based complexes to perform both the light absorption and catalytic functions.⁴⁻⁶ However, the use of rare metals, like Ru, present problems with scaling to meet energy demands and economic feasibility, prompting efforts to find less expensive components based on earth abundant materials. We have pursued a strategy that replaces the Ru^{II} chromophore with an organic chromophore. A previous report described the synthesis and photoelectrochemical characterization of a terthiophene chromophore (T₃-trpy) coupled to a Ru^{II} water oxidation catalyst to form the T₃-trpy-Ru-L (L = MeCN or H₂O) chromophore-catalyst assembly on TiO₂.⁷

In this chapter, we describe the ultrafast dynamics of this assembly in solution and at the surface of metal oxides (Scheme 6.1). In comparison to the Ru^{II}-based systems, we find several distinct differences. The weak electronic coupling between the Ru^{II}-Ru^{II} sites results in electronic states that remain largely intact, with fast electron injection (fs-ps) and fast (<500 ps) intra-assembly catalyst photoactivation. In contrast, the strong electronic coupling between the T₃ chromophore and Ru^{II} catalyst in T₃-trpy-Ru-L give rise to a new, low energy intra-ligand charge transfer (ILCT) excited state. The energy of this state depends on the identity of the ligand 'L' in the active site. In MeCN (i.e., T₃-trpy-Ru-MeCN), the ILCT state undergoes ps-ns electron injection and ns-μs back electron transfer. Photoactivation is not observed due to the large driving force for hole transfer. In H₂O, (i.e., T₃-trpy-Ru-OH₂), we observe slow (ns) electron injection and photoactivation on TiO₂, suggesting that electron injection is the rate limiting activation step. On SnO₂, however, the 0.4 V positive shift of the conduction band results in ultrafast electron injection (fs-ps) and ultrafast photoactivation (<35 ps).

Scheme 6.1. (Left) Energy level diagram of the relevant states present in the T₃-trpy chromophore and T₃-trpy-Ru-L assemblies in relation to the metal oxide conduction band density of states for TiO₂ (top) and SnO₂ (bottom). (Right) Illustration of the interfacial dynamics within the T₃-trpy-Ru-MeCN (top) and T₃-trpy-Ru-OH₂ (bottom) assemblies.



6.2. EXPERIMENTAL METHODS

6.2.1. Sample Preparation

Solution spectroscopic experiments were performed in spectroscopic grade dimethyl sulfoxide or acetonitrile. Ground-state absorption and emission measurements were performed in 1 cm quartz cuvettes whereas transient measurements were performed in 2 mm quartz cuvettes in sufficiently dilute solution (optical density (OD) between 0.3 and 0.4 at the excitation wavelength). All samples were sparged with argon for 20 minutes and sealed prior to use.

Thin films of TiO_2 and SnO_2 deposited on FTO glass were soaked for 24 hours in a solution containing the sensitizer dissolved in acetonitrile or methanol and were placed in a home-made 1 cm quartz cuvette at a 45 degree angle relative to the front face of the cuvette. All transient absorption experiments were performed with the sensitized films immersed in argon-saturated solutions of 100 mM LiClO_4 dissolved in acetonitrile or 100 mM HClO_4 in H_2O and were raster-scanned to prevent photodegradation of the samples.

6.2.2. Steady State Techniques

UV-Visible spectra were recorded on an HP 8543 Diode Array Spectrophotometer. UV-Visible spectra were recorded on all samples before and after excited state measurements to ensure that samples did not undergo photodecomposition.

Emission spectra were measured on Photon Technology International (PTI 4SE-NIR) Quantamaster™ spectrofluorometer equipped with a continuous xenon arc lamp as the excitation source. The emitting light was collected at 90° to the excitation beam and detected by a Multi-mode 814 photomultiplier tube (PMT) in photon counting mode (digital).

6.2.3. Transient Absorption Spectroscopy

Femtosecond-picosecond transient absorption measurements were performed using a home-built transient absorption spectrometer. The spectrometer is based on a commercially available ultrafast laser system (Clark MXR CPA-2210). The system consists of an erbium-doped fiber ring oscillator pumped by a solid-state fiber coupled laser diode operating at 980 nm and a chirped pulse Ti:Sapphire regenerative amplifier pumped by a frequency-doubled, Q-switched Nd:YAG laser. Following pulse compression, the amplifier produces pulses centered at 775 nm with 120 fs fwhm duration at 1 kHz with pulse energies of 1.6 mJ/pulse.

The amplified output is initially split into two fractions, where the larger fraction (80%) is further split to pump several optical parametric amplifiers (OPA) for frequency tunability. 50% (650 μ J/pulse) of this fraction pumps a collinear near-IR OPA (White Light Conversion TOPAS-C) that is tuned to 1070 nm and mixed with the residual fundamental in a 1 mm thick BBO crystal to produce 450 nm pulses by sum-frequency generation with energies of approximately 1 μ J/pulse. A smaller portion (20%) is used to drive a home-built collinear near-IR OPA tuned to 1200 nm. The femtosecond probe pulse is generated by focusing either the 1200 nm signal output or 775 nm fundamental (5 μ J/pulse) into a translating 5 mm thick CaF_2 window, giving spectral coverage across the visible region. The smaller fraction of the amplifier output (20%) is further split using a 90:10 window, where the larger fraction is frequency doubled in a 1 mm BBO crystal and coupled into a home-built, hollow fiber waveguide filled with argon at 20 psig for spectral broadening. Prism compression results in 388 nm pump pulses (200 nJ/pulse) with a duration of approximately 35 fs fwhm.

The pump beam is directed through a mechanical chopper to modulate between pump-on and pump-off spectra and focused onto the sample using a 300 mm lens. The probe beam is focused

and overlapped with the pump pulse using a 250 mm spherical aluminum mirror. After the sample, the probe beam is dispersed by a 0.15 m spectrograph with a 600 g/mm grating and detected on a diode array. Time-resolved spectra were collected by varying the delay between pump and probe pulses using a computer controlled delay stage with a resolution of 1 μ m. Spectra were collected on a shot-by-shot (1 kHz) basis over the range of 350 to 820 nm with a sensitivity of up to 0.1 mOD. The angle between the pump and probe polarization vectors was set to magic angle ($\sim 54.7^\circ$) to avoid polarization effects and ensure that only excited-state population dynamics were being monitored. The sample was stirred with a magnetic stirrer to provide for a fresh sample volume between laser pulses and a steady-state absorbance spectrum was acquired before and after transient experiments to confirm the absence of photoproduct formation. Following data collection, the frequency chirp in the probe pulse was characterized using the optical Kerr response of liquid CCl_4 in a 2 mm cuvette in a polarization gating geometry. The spectra were chirp corrected using a data processing program written in LabVIEW.

Sub-nanosecond transient measurements were performed with an Ultrafast Systems EOS spectrometer. The probe pulse is generated by continuum generation from a photonic crystal fiber and detected by a fiber optic coupled multichannel spectrometer with a CMOS sensor. The pump-probe delay is electronically controlled and the kinetic window ranges from 500 ps – 400 μ s. The time resolution of the instrument is around 500 ps, dictated by the width of the probe pulse and the timing electronics.

5.2.4. Electronic Structure Calculations

The ground-state geometry of T₃-trpy complex was optimized using the B3LYP DFT functional and the 6-31G** basis sets, as implemented in Gaussian09 (v09e01).¹ Solvation effects for dimethyl sulfoxide (DMSO) were included with a polarizable continuum model in Gaussian. A vibrational analysis was performed to verify that the optimized structure was at a potential energy minimum.

Time-dependent density functional theory (TD-DFT) calculations were performed on the optimized ground-state geometry using the B3LYP DFT functional and the 6-31G** basis sets, as implemented in Gaussian09 (v09e01), with solvation effects for dimethyl sulfoxide included with a polarizable continuum model. A total of 10 singlet states were computed and the geometry of the lowest energy excited-state was computed.

6.3. RESULTS AND DISCUSSION

6.3.1 Photoexcitation and Electronic Structure of T₃-trpy and T₃-trpy-Ru-L.

The ground-state absorption spectrum of T₃-trpy in DMSO is characterized by a broad, intense visible transition centered at 410 nm along with several weak transitions in the UV (<400 nm) region (Figure 6.1). The 410 nm transition is ascribed entirely to a $\pi \rightarrow \pi^*$ transition delocalized along the T₃ moiety. Emission from T₃-trpy is broad and featureless (Figure 6.1), with a fluorescence quantum yield, Φ_{Fl} , of 0.30, consistent with previous reports for related oligothiophenes.⁸ DFT and TD-DFT calculations suggest the ground-state exhibits a small degree of torsional disorder while the excited-state adopts a planar geometry (Figure 6.2). This geometrical distortion arises from the shift in electron density as the bonding adopts a quinoidal arrangement along the T₃ unit in the excited state, planarizing the thiophene units and phenyl bridge along the length of the chromophore.⁹

The absorbance spectrum of the T₃-trpy-Ru-L assembly (Figure 6.1) exhibits multiple overlapping transitions across the visible region with prominent peaks at 383 nm and 470 nm and a low energy shoulder near 520 nm.⁷ The 383 nm transition is assigned to the $\pi\text{-}\pi^*$ transition on the T₃ fragment and the weak, low-energy shoulder near 520 nm is consistent with the Ru^{II} metal-to-ligand charge transfer (MLCT) transition on the Ru^{II} catalyst.^{6, 10} The transition centered at 470 nm, which is only observed in the assembly, is assigned based on TD-DFT calculations to correspond to excitation of an intra-ligand charge transfer (ILCT) state, where electron density shifts from the T₃ to the trpy ligand (i.e., T₃^{*}-trpy-Ru-L \rightarrow T₃⁺-trpy⁻-Ru-L).⁷ The lack of fluorescence from T₃-trpy-Ru-L suggests that the ILCT state is dark and lies lower in energy than both the ³MLCT and ³T₃^{*} states.

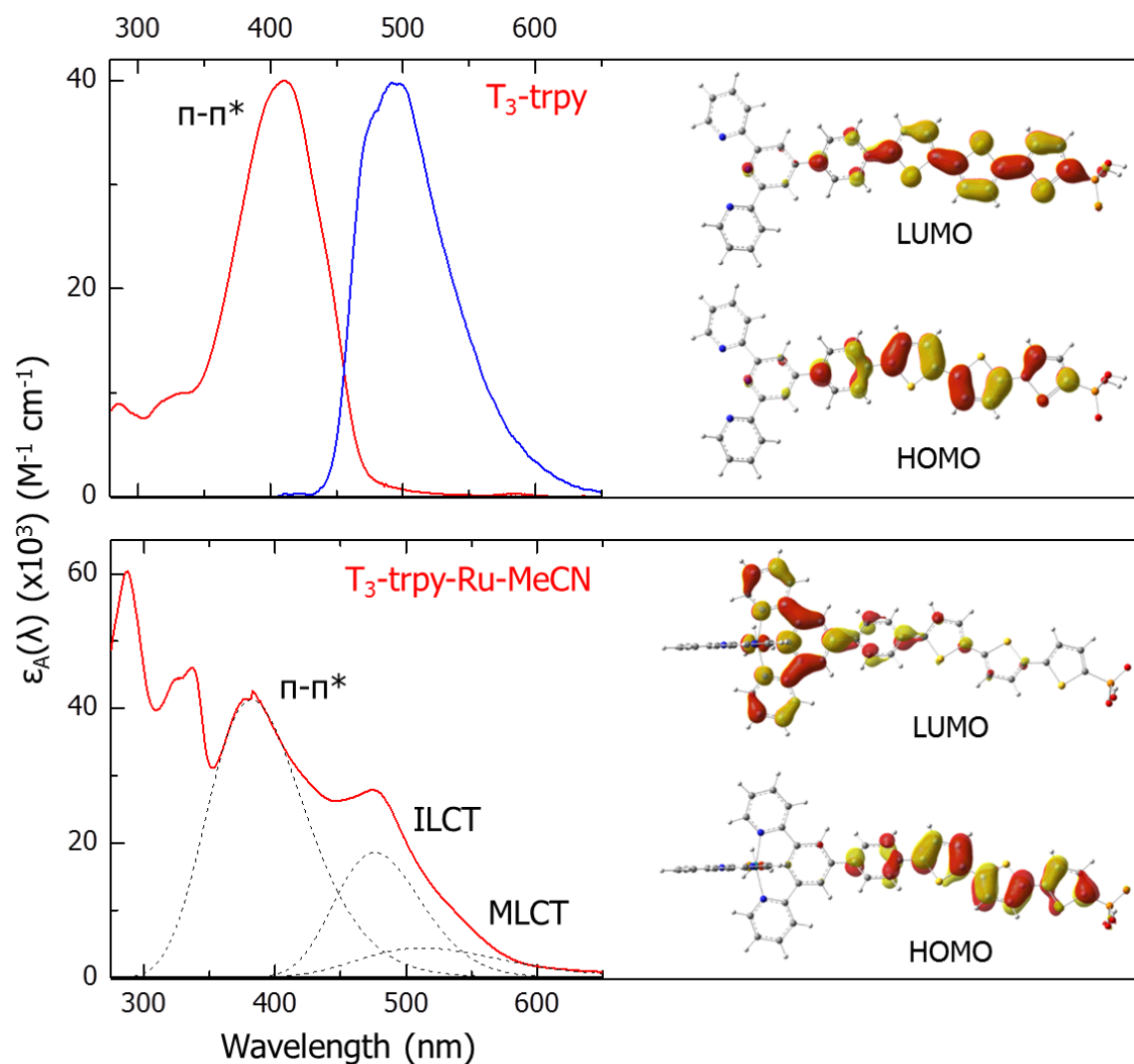


Figure 6.1. (Top) Ground-state absorption (red) and emission (blue) spectra for T_3 -trpy in DMSO. The emission spectrum was collected following 390 nm excitation. Frontier orbitals corresponding to the lowest energy $\pi \rightarrow \pi^*$ transition in T_3 -trpy computed by DFT (isovalue = 0.03). (Bottom) Ground-state absorption spectrum (red) for T_3 -trpy-Ru-L in MeCN. Frontier orbitals corresponding to the lowest energy intra-ligand charge transfer (ILCT) transition in T_3 -trpy-Ru-MeCN computed by DFT (isovalue = 0.03).

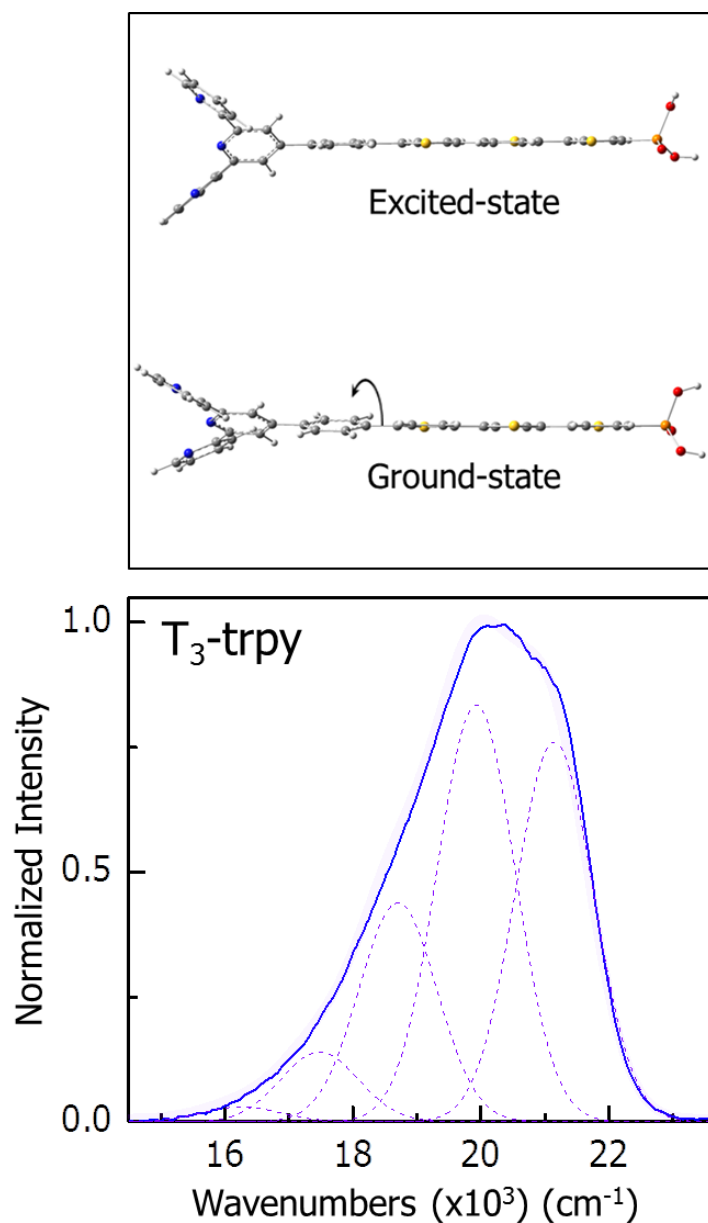


Figure 6.2. (Top) Optimized ground-state (bottom) and excited-state (top) geometries of T₃-trpy. (Bottom) Emission spectrum of T₃-trpy in DMSO following 390 nm excitation. The light purple spectrum corresponds to the simulated fit of a one-mode Franck-Condon progression with a mode-spacing of 1,220 cm⁻¹ and E₀₋₀ energy of 21,150 cm⁻¹.

6.3.2. Photophysics of the T₃-trpy Chromophore

6.3.2.1. T₃-trpy Solution Photophysics

Photoexcitation of T₃-trpy produces a singlet π - π^* excited state that exhibits complex excited state relaxation dynamics. At early times, the transient spectra exhibit negative features centered at 410 and 500 nm along with a broad excited-state absorption (ESA) that peaks at 760 nm (Figure 6.3). The 410 nm band is ascribed to the ground state bleach (GSB) of the π - π^* transition while the 760 nm band is assigned to the manifold of singlet ESAs ($S_1 \rightarrow S_n$). The 500 nm band corresponds to stimulated emission (SE). The maximum of this feature shifts to the red during the first 5-10 ps after excitation, which could be the result of torsional relaxation to a more planar excited state, as suggested by DFT. On longer time scales, there is a correlated loss of the SE and ESA bands that occurs in conjunction with the growth of an ESA feature centered at 620 nm. This spectral feature persists into the microsecond time domain ($\tau=58 \mu\text{s}$), suggesting that it corresponds to the formation of the triplet π - π^* state, $^3\text{T}_3\text{-trpy}^*$.

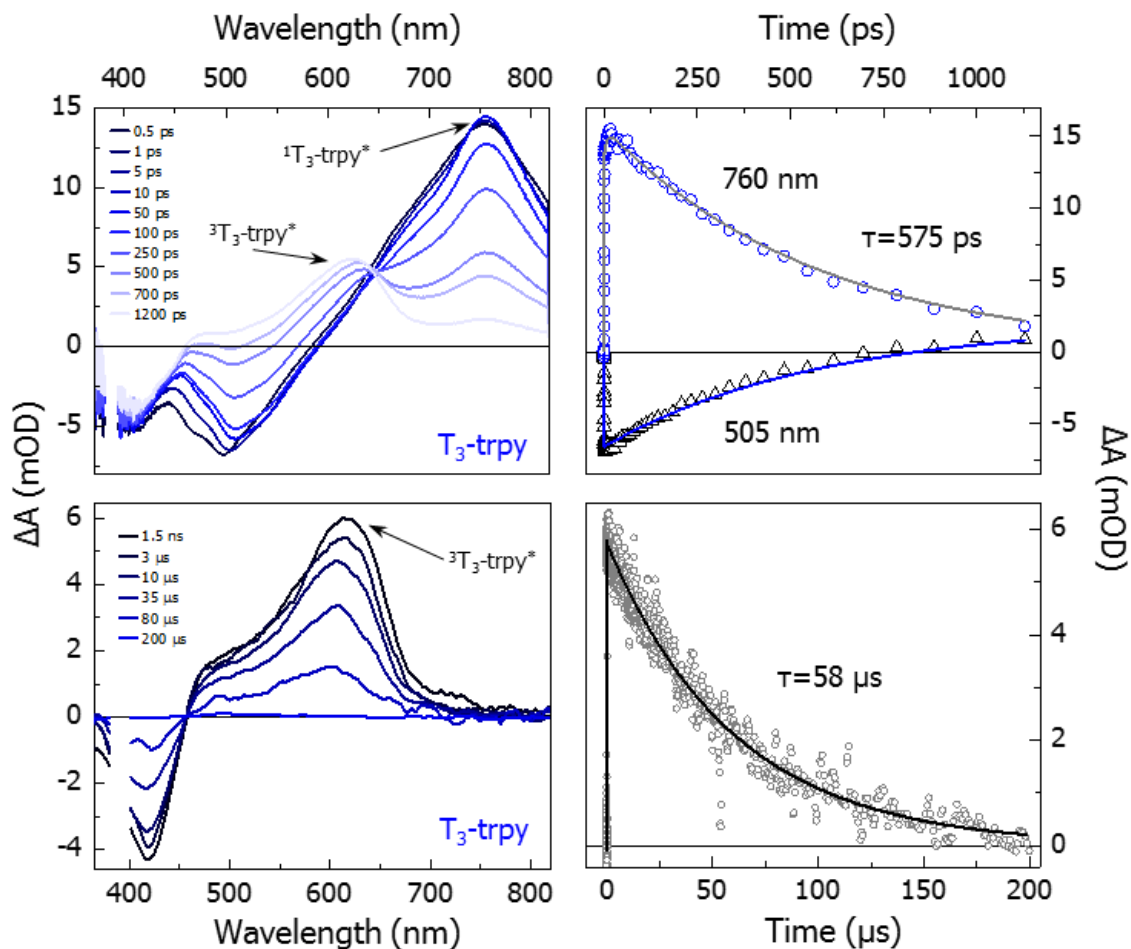


Figure 6.3. (Top Left) Transient absorption difference spectrum of T_3 -trpy in DMSO on time scales ranging from 0.5 ps to 1.2 ns. (Top Right) Kinetic traces at 505 (black triangles) and 760 nm (blue circles) fit to a single exponential function with $\tau=575$ ps. (Bottom Left) Transient absorption difference spectrum of T_3 -trpy in DMSO on time scales ranging from 1.5 ns to 200 μ s. (Bottom Right) Kinetics trace at 620 nm with $\tau=58$ μ s.

6.3.2.2. Interfacial Dynamics on TiO_2

Electron injection from $\text{T}_3\text{-trpy}^*$ into the TiO_2 conduction band is marked by several distinct features in the transient spectra (Figure 6.4A). First, there is a noticeable absence of the SE band, even in the earliest spectra, indicating the rapid loss of $\text{T}_3\text{-trpy}^*$. Second, the shape of the ESA in the red is blue-shifted and narrower than it is in solution. Spectroelectrochemistry of similar oligothiophenes suggests that this change in the ESA is due to the oxidized chromophore, $\text{T}_3^+\text{-trpy}$, that is formed following electron injection into TiO_2 .¹¹ The presence of $\text{T}_3^+\text{-trpy}$ is evident in the earliest spectra, suggesting electron injection within the instrument response (i.e., $\tau < 0.2$ ps). This ultrafast injection is likely the result of the $\text{T}_3^*\text{-trpy}$ excited-state oxidation potential lying about 1.33 V above the conduction band edge where the excited state has access to a large number of acceptor states within the TiO_2 (Scheme 6.1).

The back electron transfer (BET) process is followed through decay of the $\text{T}_3^+\text{-trpy}$ spectral feature on the ps- μs time scale. Loss of the $\text{T}_3^+\text{-trpy}$ absorption is multi-exponential with time constants that range from picosecond to microseconds. A significant fraction (~60%) of $\text{T}_3^+\text{-trpy}$ is lost to BET in less than 100 ps, while the remaining 40% undergo recombination on time scales that extend out to 50 μs . While the exact origin of the extraordinary heterogeneity in the BET kinetics is unknown, one possibility is that after injection, the hole is localized on the T_3^+ fragment, resulting in fast BET, but over time delocalizes onto the trpy fragment as it twists with respect to the thiophene units (i.e., $\text{T}_3^+\text{-trpy} \rightarrow [\text{T}_3\text{-trpy}]^+$). This localization away from the surface would then lead to the slow microsecond BET component (Figure 6.4D).

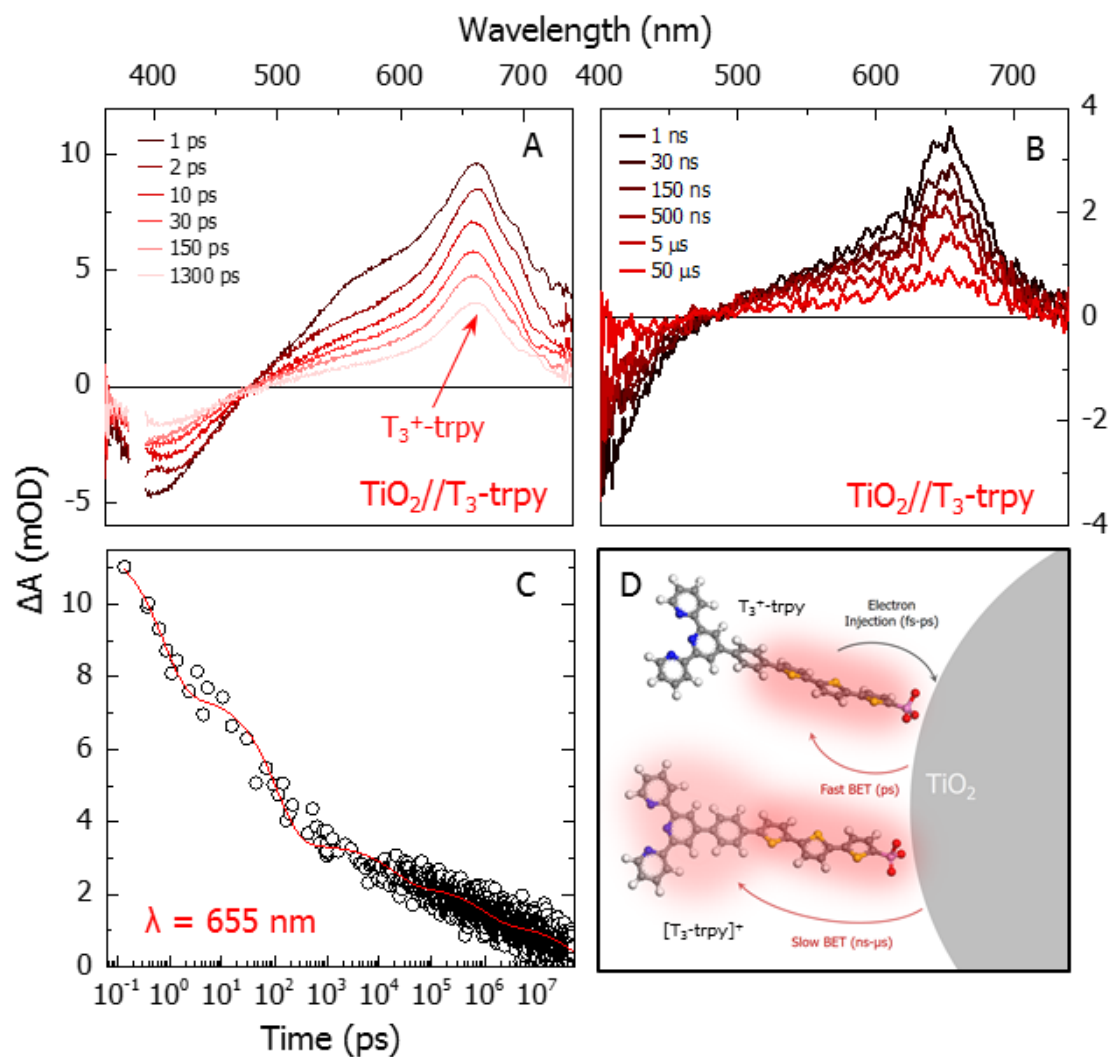


Figure 6.4. (A) Transient absorption difference spectrum of $\text{TiO}_2//\text{T}_3\text{-trpy}$ in H_2O with 0.1 M HClO_4 on time scales ranging from 1 to 1300 ps. (B) Transient absorption difference spectrum of $\text{TiO}_2//\text{T}_3\text{-trpy}$ on TiO_2 in H_2O with 0.1 M HClO_4 on time scales ranging from 1 ns to 50 μs . (C) Kinetics trace monitoring the $\text{T}_3^+\text{-trpy}$ absorption centered at 655 nm. The decay, which spans 9 decades of time, exhibits five distinct time components: $\tau_1=0.79 \text{ ps}$, $\tau_2=114 \text{ ps}$, $\tau_3=20 \text{ ns}$, $\tau_4=1 \mu\text{s}$, and $\tau_5=50 \mu\text{s}$. (D) Illustration of the primary photophysical events in the $\text{TiO}_2//\text{T}_3\text{-trpy}$ assembly, where electron injection is followed by either fast or slow BET.

6.3.3.3. *Interfacial Dynamics on SnO₂*

Electron injection from T₃-trpy is markedly slower on SnO₂ compared to TiO₂, even though its conduction band edge lies 0.4 V lower in energy (Scheme 6.1).¹²⁻¹⁵ The SnO₂//T₃-trpy transient spectra at early times are similar to those observed from the solvated T₃-trpy in DMSO, with a GSB at 400 nm, SE centered near 520 nm, and a broad ESA in the red (Figure 6.5). While the SE is completely absent for T₃-trpy bound to TiO₂, on SnO₂ it is still visible at early times, albeit significantly reduced in amplitude relative to solution. On the 10-100 ps time scale, there is continued SE quenching with concomitant evolution of the ESA to form the sharp T₃⁺-trpy band centered at 655 nm. The decay of the transient signal associated with the SE at 520 nm indicates that electron injection occurs with both 2.3 ps and 15 ps time components (Figure 6.5). The slower electron injection on SnO₂ compared with TiO₂ is attributed to a smaller density of states for SnO₂.¹⁶⁻¹⁷ Following electron injection into the SnO₂ conduction band, the decay of the GSB at 400 nm indicates that ~50% of the charge separated states are lost to BET within ~1 ns after photoexcitation, similar to TiO₂//T₃-trpy.

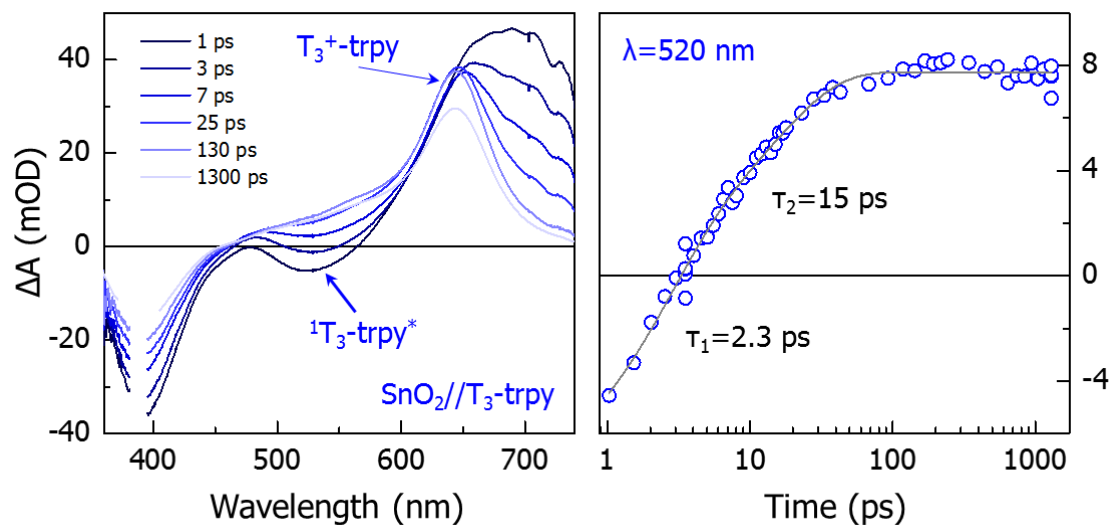


Figure 6.5. (Left) Transient absorption difference spectrum of SnO₂//T₃-trpy in H₂O with 0.1 M HClO₄ on time scales ranging from 1 ps to 1300 ps. (Right) Kinetics trace at 520 nm monitoring the SE band of T₃^{*}-trpy. The band decays with two distinct time components: $\tau_1=2.3$ ps and $\tau_2=15$ ps.

6.3.3. Photophysics of the T₃-trpy-Ru-L Assembly

6.3.3.1. Solution Dynamics

Photoexcitation of the T₃-trpy-Ru-MeCN assembly in solution is followed by rapid relaxation to a low energy, ¹ILCT excited state that is localized on the T₃-trpy ligand. The transient spectra consist of two GSB features at 375 and 475 nm along with a broad ESA extending across the visible and near-infrared (Figure 6.6). The shape of the ESA at longer times appears to be a superposition of a narrow feature on top of a broader absorption. This overall shape is dissimilar from that of both T₃-trpy* ESA (Figure 6.3) and the weak ESA absorption associated with the Ru^{II} catalyst.⁶ Spectroelectrochemistry on related trpy-containing Ru^{II} complexes show that ESA of the reduced trpy ligand is characterized by a broad band that extends across the visible and near-infrared,¹⁸ whereas the T₃⁺-trpy spectrum is a sharp feature centered near 655 nm (Figure 6.4). Qualitatively, the ESA observed for the T₃-trpy-Ru-MeCN assembly appears to contain characteristics of both of these absorptions, suggesting the broad ESA at longer times corresponds to the formation of an ILCT state in which the photoexcited electron resides primarily on the trpy fragment of the T₃-trpy ligand, i.e. T₃⁺-trpy^{•-}. During the first 5 ps the ESA increases in amplitude and narrows, consistent with relaxation from the optically prepared Franck-Condon state into the lower energy ¹ILCT state.

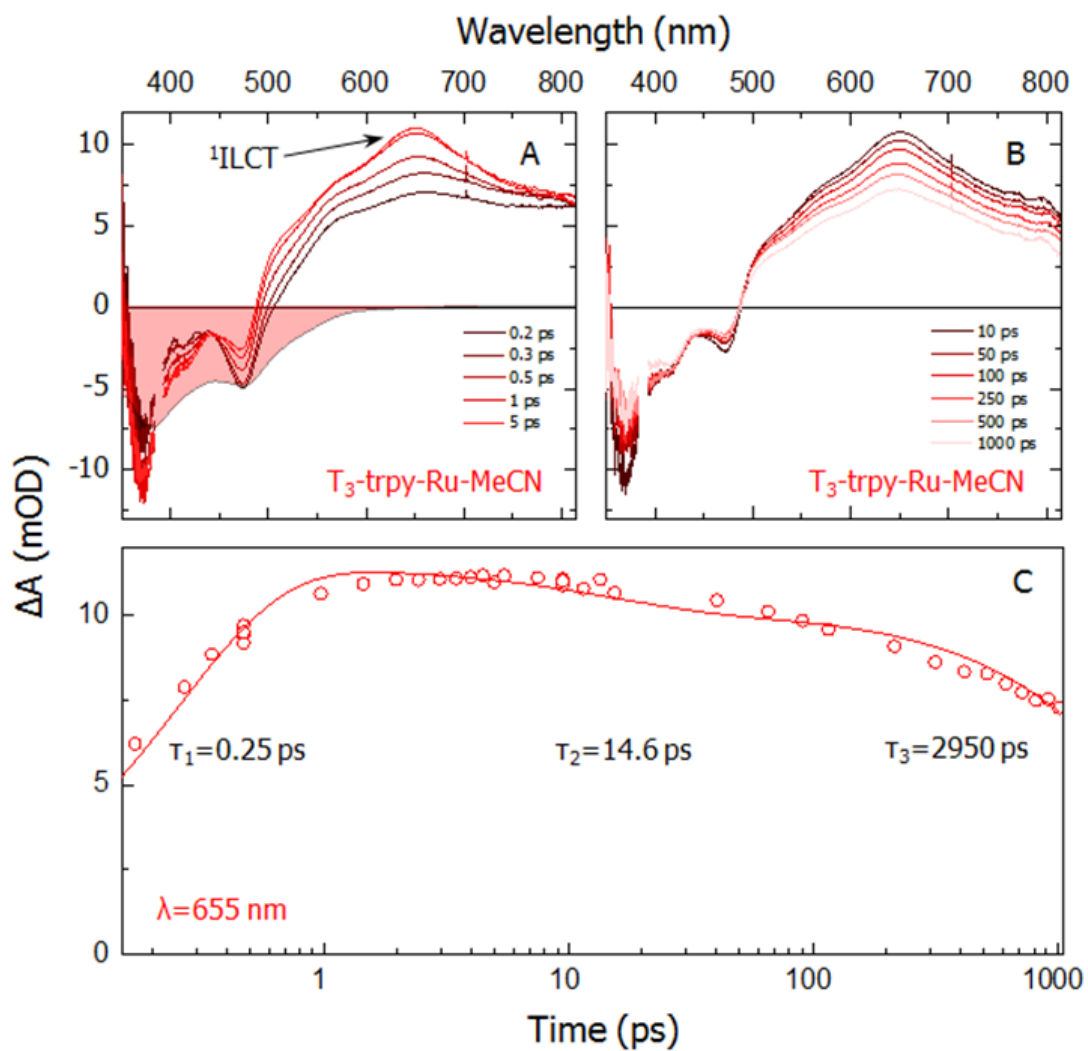


Figure 6.6. (A) Transient absorption difference spectrum of T_3 -trpy-Ru-MeCN on time scales ranging from 200 fs to 5 ps. (B) Transient absorption difference spectrum of T_3 -trpy-Ru-MeCN on time scales ranging from 10 ps to 1000 ps. (C) Kinetics trace at 655 nm fit to a tri-exponential function with characteristic time constants of $\tau_1=0.25 \text{ ps}$, $\tau_2=14.6 \text{ ps}$, and $\tau_3=2950 \text{ ps}$.

The ESA associated with the ILCT state decays with time constants of 2.3 ns, 47 ns, and 4.2 μ s (Figure 6.7). The long time component (4.2 μ s) is shorter than the lifetime of the 3T_3 -trpy* chromophore, but significantly longer than the lifetime of the 3 MLCT state for the trpy-Ru-L catalyst ($\tau \sim 4$ ns),⁶ suggesting that it corresponds to the ligand-localized 3 ILCT state. We thus attribute the 2.3 ns component to intersystem crossing into the triplet manifold from the singlet state, 1 ILCT \rightarrow 3 ILCT, while the slower time components reflect relaxation of the 3 ILCT state back to the ground state.

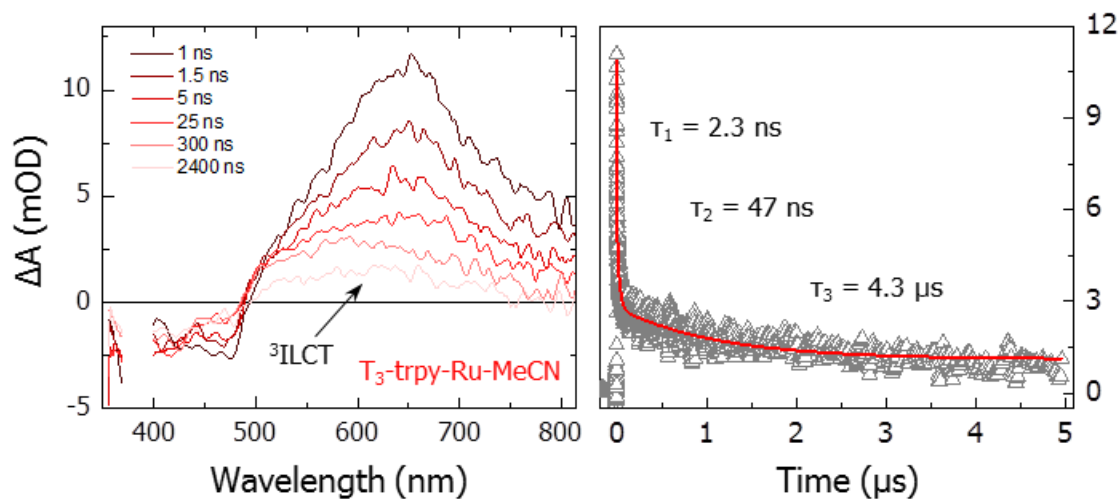


Figure 6.7. (Left) Transient absorption difference spectrum of T_3 -trpy-Ru-MeCN on time scales ranging from 1 ns to 2400 ns. (Right) Kinetics trace at 655 nm fit to a tri-exponential function with $\tau_1=2.3$ ns, $\tau_2=47$ ns, and $\tau_3=4.3$ μ s.

6.3.3.2. *Interfacial Dynamics on TiO₂*

The identity of the ligand 'L' in the active site of the catalyst in T₃-trpy-Ru-L has a dramatic effect on the interfacial dynamics for the assembly on TiO₂. While the transient spectra for T₃-trpy-Ru-MeCN in solution (Figure 6.6) and adsorbed on TiO₂ (Figure 6.8) are similar in shape, their evolution is significantly different. The most notable change is in the TiO₂//T₃-trpy-Ru-MeCN spectra, where the narrow band centered at 655 nm similar to the sharp T₃⁺-trpy absorption in the TiO₂//T₃-trpy spectra (Figure 6.4A). This spectral feature is observed in the earliest spectra (0.9 ps), indicating the presence of rapid electron injection to form TiO₂(e⁻)/T₃⁺-trpy-Ru-MeCN. This T₃⁺-trpy-Ru-MeCN feature decays with time constants that are similar to those observed for T₃-trpy on TiO₂ (Figures 6.8), implying that the oxidative equivalent (i.e. the hole) remains localized on the T₃-trpy ligand. The absence of hole transfer to the catalyst is most likely a consequence of the MeCN in the active site, which makes oxidation of the catalyst by T₃⁺-trpy uphill by 0.21 eV (Scheme 6.1).

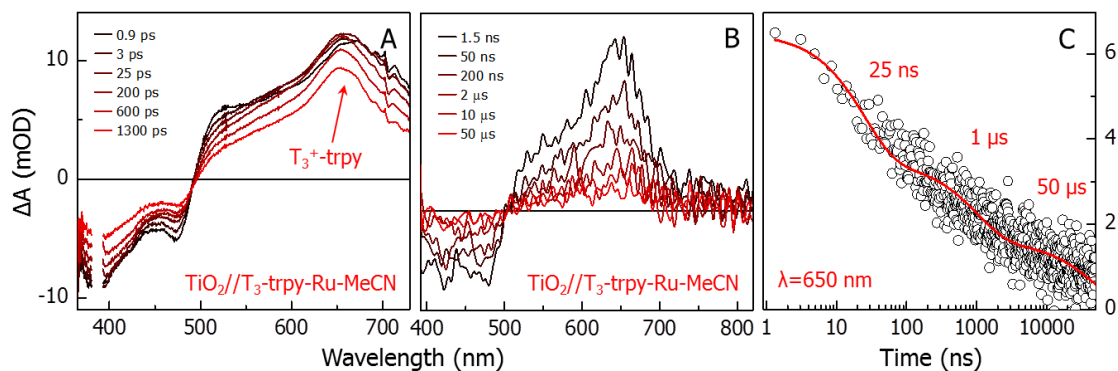


Figure 6.8. (A) Transient absorption difference spectrum of $\text{TiO}_2//\text{T}_3\text{-trpy-Ru-MeCN}$ in MeCN with 0.1 M LiClO_4 on time scales ranging from 0.9 ps to 1300 ps. (B) Transient absorption difference spectrum of $\text{TiO}_2//\text{T}_3\text{-trpy-Ru-MeCN}$ in MeCN with 0.1 M LiClO_4 on time scales ranging from 1.5 ns to 500 ns. (C) Kinetics trace at 650 nm. The transient is fit to a tri-exponential function with $\tau_1=25$ ns, $\tau_2=1$ μs , and $\tau_3=50$ μs .

Photoactivation of the Ru^{II} catalyst becomes thermodynamically favored when the MeCN is replaced with H_2O in active site ($\Delta G = -0.35$ eV), which pushes the oxidation potential of the catalyst more negative by ~ 500 meV. While hole transfer to the catalyst is possible, electron injection from the assembly is suppressed. Indeed, the transient spectra with H_2O in the active site show no evidence for the formation of the sharp T_3^+ -trpy absorption during the first 1 ns following excitation, and instead show an ESA that resembles the broad absorption associated with the $^1\text{ILCT}$ state (Figure 6.9A). The suppressed injection in H_2O compared to MeCN is most likely a result (at least in part) of the aqueous solvent environment in the $\text{TiO}_2//\text{T}_3\text{-trpy-Ru-OH}_2$ system, which destabilizes the metal oxide conduction band.¹⁹ As discussed below, the spectra on longer time scales indicate that electron injection is not shut off completely. Rather it is slowed to the point that no significant buildup of T_3^+ -trpy-Ru-OH₂ occurs, suggesting that the $^1\text{ILCT}$ state lies near (or slightly below) the conduction band minimum.

The transient spectra observed on the ns to μ s time scales (Figure 6.9B) differ significantly with H₂O in the active site compared to MeCN, suggesting the formation of a long-lived transient photoproduct. The most notable difference is a new GSB feature at 520 nm that appears in conjunction with the loss of the ILCT state (i.e. 400 nm GSB and 655 nm ESA). Based on its spectral position, we attribute the 520 nm GSB to the loss of the Ru^{II} MLCT transition (Figure 1). Thus, the emergence of this spectral feature reflects the appearance of the oxidized catalyst by intra-assembly electron transfer from the Ru^{II} catalyst to the T₃⁺ moiety (i.e., TiO₂(e⁻)/T₃⁺-trpy-Ru^{II}-OH₂ \rightarrow TiO₂(e⁻)/T₃-trpy-Ru^{III}-OH₂, Scheme 6.1).

The kinetics associated with the growth and decay of this Ru^{III} population are reflected in the transient at 520 nm (Figure 6.9C). The oxidized catalyst appears with time constants of $\tau_1=2\pm1$ ns and $\tau_2=45\pm16$ ns. The absence of the T₃⁺-trpy spectral features in the TiO₂/T₃-trpy-Ru-OH₂ spectra suggest that hole transfer to the Ru^{II} catalyst from T₃ is fast ($\tau<1$ ns) following electron injection, with the hole transfer rate ultimately limited by electron injection into TiO₂ from the ILCT state. Once formed, the charge separated state in TiO₂(e⁻)/T₃-trpy-Ru^{III}-OH₂ decays by slow (μ s) BET ($\tau_1=3.2\pm0.3$ μ s and $\tau_2=88\pm7$ μ s). These time scales are consistent with the increased separation between the Ru^{III} catalyst and the TiO₂ surface compared to the TiO₂/T₃-trpy-Ru-MeCN system where the hole remains on the T₃-trpy ligand.

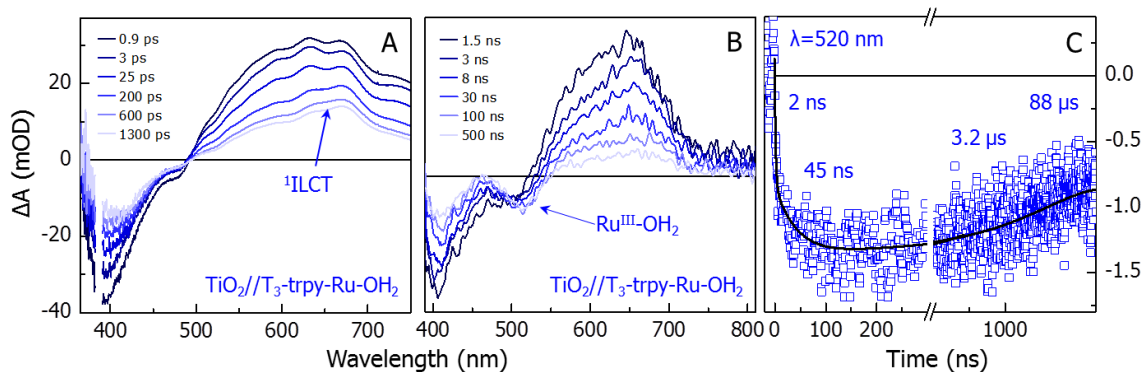


Figure 6.9. (A) Transient absorption difference spectrum of $\text{TiO}_2//\text{T}_3\text{-trpy-Ru-OH}_2$ in pH 1 HClO_4 on time scales ranging from 1.5 ps to 1300 ps. (B) Transient absorption difference spectrum of $\text{TiO}_2//\text{T}_3\text{-trpy-Ru-OH}_2$ in pH 1 HClO_4 on time scales ranging from 1.5 ns to 500 ns. (C) Kinetics trace at 520 nm for $\text{TiO}_2//\text{T}_3\text{-trpy-Ru-OH}_2$ in pH 1 HClO_4 . The transient spans 6 decades of time and exhibits four distinct time components: $\tau_1=2$ ns, $\tau_2=45$ ns, $\tau_3=3.2$ μs , and $\tau_4=88$ μs .

6.3.3.3. Interfacial Dynamics on SnO_2

The time scale for the photoactivation of the Ru^{II} catalyst can be determined by replacing the TiO_2 with SnO_2 , where the 0.4 V positive shift in the conduction band edge of SnO_2 relative to TiO_2 increases the electron injection rate (Scheme 6.1).^{14, 16, 20} At early times, the transient spectra of both surface-bound $\text{T}_3\text{-trpy-Ru-L}$ ($\text{L}=\text{MeCN}$ and H_2O) assemblies show the broad ESA and two GSB features centered at 400 and 490 nm that are characteristic of the ILCT state (Figure 6.10). With MeCN in the active site, the bands decay slowly in amplitude during the first 1300 ps, with a slight spectral narrowing of the ESA that is consistent with electron injection into the SnO_2 conduction band and formation of the oxidized chromophore, i.e. $\text{T}_3^+\text{-trpy-Ru-MeCN}$. The continued narrowing of the ESA suggests that injection occurs within 10-100 ps. Similar to

T_3 -trpy, injection from T_3 -trpy-Ru-MeCN on SnO_2 also appears to be slower than on TiO_2 . While the transient spectra show evidence of electron injection, they do not show evidence of photoactivation of the Ru^{II} catalyst, which is still energetically uphill. In contrast to the $\text{SnO}_2//T_3$ -trpy-Ru-MeCN assembly, the transient spectra of $\text{SnO}_2//T_3$ -trpy-Ru- OH_2 do show the appearance of the 520 nm GSB that signifies hole transfer from T_3^+ to the trpy- Ru^{II} - OH_2 catalyst following electron injection. The growth of the 520 nm GSB is multi-exponential, with $\tau_1=35$ ps and $\tau_2=130$ ps (Figure 9C). Given the 10-100 ps time scale for electron injection in T_3 -trpy-Ru-MeCN, this implies that the time scale for hole transfer is less than 35 ps in T_3 -trpy-Ru- OH_2 .

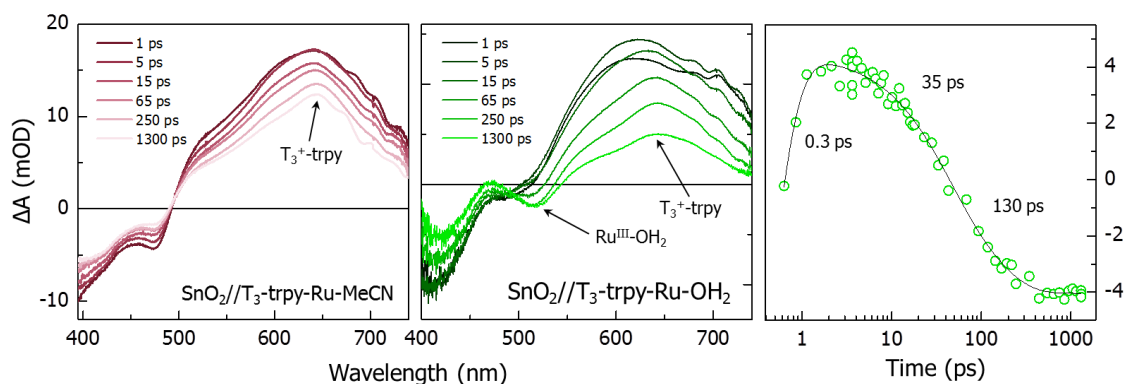


Figure 6.10. (Left) Transient absorption difference spectrum of $\text{SnO}_2//T_3$ -trpy-Ru-MeCN in MeCN with 0.1 M LiClO_4 on time scales ranging from 1 ps to 1300 ps. (Middle) Transient absorption difference spectrum of $\text{SnO}_2//T_3$ -trpy-Ru- OH_2 in 0.1 M HClO_4 on time scales ranging from 1 ps to 1300 ps. (Right) Kinetics trace at 520 nm for $\text{SnO}_2//T_3$ -trpy-Ru- OH_2 . The band exhibits an ultrafast growth ($\tau_1=0.3$ ps) followed by a bi-exponential decay ($\tau_1=35$ ps and $\tau_2=130$ ps).

6.4. CONCLUSIONS

We present here an investigation into the electronic structure and photoinduced dynamics of a terthiophene chromophore (T_3 -trpy) and a T_3 -trpy-Ru-L water oxidation molecular assembly. At the metal oxide surface, photoexcitation of the T_3 -trpy chromophore results in ultrafast (fs-ps) electron injection into the semiconductor conduction band, followed by BET on the ps- μ s time scales. In the T_3 -trpy-Ru-L molecular assembly, strong electronic coupling between the T_3 chromophore and Ru^{II} catalyst results in ultrafast relaxation to a low energy intra-ligand charge transfer (ILCT) state following excitation. The T_3 -trpy-Ru-MeCN assembly undergoes electron injection into the semiconductor conduction band on the ps-ns time scales, with BET kinetics similar to the T_3 -trpy chromophore. Meanwhile, replacement of the MeCN ligand with H_2O results in slower electron injection kinetics overall, but lowers the $Ru^{II/III}$ oxidation couple such that hole transfer from the oxidized T_3 moiety to the Ru^{II} catalyst (i.e., $T_3^+-trpy-Ru^{II}-OH_2 \rightarrow T_3-trpy-Ru^{III}-OH_2$) is energetically favorable. We find that the catalyst photoactivation step is limited by electron injection and occurs with a time constant of $\tau < 35$ ps following electron injection.

REFERENCES

1. Alstrum-Acevedo, J. H.; Brennaman, M. K.; Meyer, T. J., Chemical Approaches to Artificial Photosynthesis. 2. *Inorg Chem* **2005**, *44*, 6802-6827.
2. Ashford, D. L.; Gish, M. K.; Vannucci, A. K.; Brennaman, M. K.; Templeton, J. L.; Papanikolas, J. M.; Meyer, T. J., Molecular Chromophore-Catalyst Assemblies for Solar Fuel Applications. *Chem Rev* **2015**, *115*, 13006-13049.
3. Concepcion, J. J.; Jurss, J. W.; Brennaman, M. K.; Hoertz, P. G.; Patrocinio, A. O. T.; Iha, N. Y. M.; Templeton, J. L.; Meyer, T. J., Making Oxygen with Ruthenium Complexes. *Accounts Chem Res* **2009**, *42*, 1954-1965.
4. Bettis, S. E.; Hanson, K.; Wang, L.; Gish, M. K.; Concepcion, J. J.; Fang, Z.; Meyer, T. J.; Papanikolas, J. M., Photophysical Characterization of a Chromophore/Water Oxidation Catalyst Containing a Layer-by-Layer Assembly on Nanocrystalline Tio₂ Using Ultrafast Spectroscopy. *J Phys Chem A* **2014**, *118*, 10301-10308.
5. Bettis, S. E.; Ryan, D. M.; Gish, M. K.; Alibabaei, L.; Meyer, T. J.; Waters, M. L.; Papanikolas, J. M., Photophysical Characterization of a Helical Peptide Chromophore-Water Oxidation Catalyst Assembly on a Semiconductor Surface Using Ultrafast Spectroscopy. *J Phys Chem C* **2014**, *118*, 6029-6037.
6. Wang, L.; Ashford, D. L.; Thompson, D. W.; Meyer, T. J.; Papanikolas, J. M., Watching Photoactivation in a Ru(II) Chromophore-Catalyst Assembly on Tio₂ by Ultrafast Spectroscopy. *J Phys Chem C* **2013**, *117*, 24250-24258.
7. Pho, T. V.; Sheridan, M. V.; Morseth, Z. A.; Sherman, B. D.; Meyer, T. J.; Papanikolas, J. M.; Schanze, K. S.; Reynolds, J. R., Efficient Light-Driven Oxidation of Alcohols Using an Organic Chromophore-Catalyst Assembly Anchored to Tio₂. *Acs Appl Mater Inter* **2016**, *8*, 9125-9133.
8. Facchetti, A.; Mushrush, M.; Yoon, M. H.; Hutchison, G. R.; Ratner, M. A.; Marks, T. J., Building Blocks for N-Type Molecular and Polymeric Electronics. Perfluoroalkyl-Versus Alkyl-Functionalized Oligothiophenes (Nt; N=2-6). Systematics of Thin Film Microstructure, Semiconductor Performance, and Modeling of Majority Charge Injection in Field-Effect Transistors. *J Am Chem Soc* **2004**, *126*, 13859-13874.
9. Banerji, N.; Cowan, S.; Vauthey, E.; Heeger, A. J., Ultrafast Relaxation of the Poly(3-Hexylthiophene) Emission Spectrum. *J Phys Chem C* **2011**, *115*, 9726-9739.
10. Ashford, D. L.; Song, W. J.; Concepcion, J. J.; Glasson, C. R. K.; Brennaman, M. K.; Norris, M. R.; Fang, Z.; Templeton, J. L.; Meyer, T. J., Photoinduced Electron Transfer in a Chromophore-Catalyst Assembly Anchored to Tio₂. *J Am Chem Soc* **2012**, *134*, 19189-19198.

11. Hill, M. G.; Penneau, J. F.; Zinger, B.; Mann, K. R.; Miller, L. L., Oligothiophene Cation Radicals - Pi-Dimers as Alternatives to Bipolarons in Oxidized Polythiophenes. *Chem Mater* **1992**, *4*, 1106-1113.
12. Fessenden, R. W.; Kamat, P. V., Rate Constants for Charge Injection from Excited Sensitizer into SnO_2 , ZnO , and TiO_2 Semiconductor Nanocrystallites. *J Phys Chem-Us* **1995**, *99*, 12902-12906.
13. Gratzel, M., Photoelectrochemical Cells. *Nature* **2001**, *414*, 338-344.
14. Asbury, J. B.; Hao, E.; Wang, Y. Q.; Ghosh, H. N.; Lian, T. Q., Ultrafast Electron Transfer Dynamics from Molecular Adsorbates to Semiconductor Nanocrystalline Thin Films. *J Phys Chem B* **2001**, *105*, 4545-4557.
15. Katoh, R.; Furube, A.; Yoshihara, T.; Hara, K.; Fujihashi, G.; Takano, S.; Murata, S.; Arakawa, H.; Tachiya, M., Efficiencies of Electron Injection from Excited N_3 Dye into Nanocrystalline Semiconductor (ZrO_2 , TiO_2 , ZnO , Nb_2O_5 , SnO_2 , In_2O_3) Films. *J Phys Chem B* **2004**, *108*, 4818-4822.
16. Tiwana, P.; Docampo, P.; Johnston, M. B.; Snaith, H. J.; Herz, L. M., Electron Mobility and Injection Dynamics in Mesoporous ZnO , SnO_2 , and TiO_2 Films Used in Dye-Sensitized Solar Cells. *ACS Nano* **2011**, *5*, 5158-5166.
17. Pijpers, J. J. H.; Ulbricht, R.; Derossi, S.; Reek, J. N. H.; Bonn, M., Picosecond Electron Injection Dynamics in Dye-Sensitized Oxides in the Presence of Electrolyte. *J Phys Chem C* **2011**, *115*, 2578-2584.
18. Hewitt, J. T.; Vallett, P. J.; Damrauer, N. H., Dynamics of the (Mlct)-M-3 in R(Li) Terpyridyl Complexes Probed by Ultrafast Spectroscopy: Evidence of Excited-State Equilibration and Interligand Electron Transfer. *J Phys Chem A* **2012**, *116*, 11536-11547.
19. Watson, D. F.; Meyer, G. J., Electron Injection at Dye-Sensitized Semiconductor Electrodes. *Annu Rev Phys Chem* **2005**, *56*, 119-156.
20. Bauer, C.; Boschloo, G.; Mukhtar, E.; Hagfeldt, A., Ultrafast Studies of Electron Injection in Ru Dye Sensitized SnO_2 Nanocrystalline Thin Film. *Int J Photoenergy* **2002**, *4*, 17-20.